University of Southampton

Direct Liquid Crystal Templating of Mesoporous Metals

by

Stéphane Alfred André Leclerc

A dissertation submitted in partial fulfilment of the requirements of the degree of Doctor of Philosophy at the University of Southampton

Department of Chemistry

October 2000

UNIVERSITY OF SOUTHAMPTON

ABSTRACT

FACULTY OF SCIENCE

CHEMISTRY

Doctor of Philosophy

DIRECT LIQUID CRYSTAL TEMPLATING OF MESOPOROUS METALS

by

Stéphane Alfred André Leclerc

The preparation of mesoporous platinum has been studied by the reduction of a platinum salt in the aqueous domains of the hexagonal phases of Brij surfactant systems. A detailed study of the synthesis of mesoporous platinum from such mixtures revealed the ability to increase the regularity of the nanostructure and surface area of the materials by varying the amount of surfactant in the templating mixture or varying the reduction temperature. The most successful method of preparing H_I material employed reduction with iron metal from Brij 76 lyotropic H_I phase at 40 ^{o}C. BET surface area analysis showed the mesoporous platinum to have a surface area of 46 m^2g^{-1}. The pore size of the H_I materials was found to be ~3nm with ~3.5 nm thick walls.

The templating mechanism was then extended to the chemical preparation of mesoporous palladium and lead materials from the H_I phase of Brij 76. The electrochemical reduction of lead precursors within the H_I domain of Brij 56 on Au support was also shown to be a successful method to obtain nanostructured lead films. Direct liquid crystal templating of Pt-based alloys was also investigated. The co-reduction of binary mixture of platinum and ruthenium metal compounds dissolved in the H_I phase of Brij 76 leads to bimetallic alloy powders that have a long range nanostructure and high surface areas. Investigations into the electrochemical preparation of the same materials showed that nanostructured bimetallic films could be obtained.

Finally, the catalytic activity of mesoporous platinum and platinum/ruthenium alloys was assessed in hydrogenation reactions and in the formulation of electrodes for CO and methanol oxidation. When compared to the equivalent commercial catalysts, kinetic data for the heterogeneous reactions showed that the catalytic activity of H_I platinum and H_I platinum/ruthenium was significantly higher from that of the equivalent catalysts and that this difference cannot be explained only by differences in the specific surface area. Preliminary results showed that mesoporous Pt and Pt based alloys could play an important role in the development of effective catalysts for CO and methanol electrooxidation.

Contents

Acknowledgements

I would like to thank Dr George Attard for his supervision throughout this work, for his constant support, for his enthusiasm as progress were made and especially for giving me the opportunity to come back to Southampton. I would also like to thank Prof. Phil Bartlett for his advice concerning the electrochemical part of the project.

Acknowledgements also go to Dr Andrea Russell for proof reading and help concerning the EXAFS analysis and Dr Barbara " TEM " Cressey for numerous hours spent helping me in front of the microscope.

I would like to thank City Technology for their financial support and especially Dr John Chapples for his continued interest in the project and welcome when carrying experiments in his laboratory.

This section would not be complete without acknowledgements addressed to all those who have helped me throughout the past 3 years: various members of the chemical physics group: Dr Fiona Farrand for keeping in touch over the years and warm welcome when I first arrived homeless in Southampton, Dr Nick Coleman for his help and good laughs shared in Quebec City, Dr S Perkins for his fair comment about the typical french behaviour, all the members of George' group: Marcus for numerous entertaining discussions in the lab just to remember that Chemistry was not everything, M.Perkins, Toby, Jason and Paolo "the God father". Acknowledgements also go to Matt, Martin and Yannick for the lunch time entertainment and Jackie for the good times spent together and endless support. I would like also to thank my french compatriots Sam "Sammy" for his reading patience and choice of music in his lab and Stephanie for coping with my questions without forgetting Anne " Tea expert" for cheering me up from time to time.....Merci beaucoup!!!!!!

Finally but not the least important, I want to acknowledge my parents Daniel and Mireille because I know they are responsible for what I have become and my brother David whose support has been really important too!! Words can not express my gratitude to Claire whose love and care have been tremendous! Merci Beaucoup!!

Abbreviations

Brij	registered trademark of ICI Americas Inc.
Brij 76	$C_{18}EO_n$ n~20
Brij 56	$C_{16}EO_n$ n~10
$C_{16}EO_8$	Octaethlyeneglycol monohexadecylether
EO	one ethylene oxide unit $-CH_2CH_2O-$
HCPA	hexachloroplatinic acid (H_2PtCl_6)
ATCP	ammonium tetrachloropalladate $(NH_4)_2PdCl_4$
PbTFB	Lead tetrafluoroborate
POE	polyoxyethylene
HCl	hydrochloric acid
TEM	transmission electron microscopy
SEM	scanning electron microscopy
BET	Brunauer-Emmett-Teller
EXAFS	extended x-ray absorption fine structure
EDE	energy dispersive EXAFS
XRD	x-ray diffraction
DMFC	Direct Methanol Fuel Cell
H_I	hexagonal phase
L_α	lamellar phase
I_1	micellar cubic phase
V_1	cubic phase
L_1	micellar solution
L_2	inverse micellar solution
cmc	critical micelle concentration

Chapter 1

Introduction to synthetic nanoporous materials

1.1 Introduction

1.1.1 Microporous and mesoporous materials

Ordered nanoporous/microporous solids are exemplified by zeolites and their related compounds. Zeolites are aluminosilicates with a periodic three-dimensional framework structure containing voids; related compounds possess similar structures but differ in the chemical composition of the framework (e.g. aluminophosphates). The early history of ordered microporous materials is to be found in the field of mineralogy. Prior to 1900 there were 24 zeolite minerals that had been discovered in nature [1]. With the advent of x-ray diffraction many more zeolite minerals were characterised. The discovery of the first novel synthetic zeolite in 1948 [2] and the realisation of their catalytic properties led to a long period of industrial research in the field.

The highly crystalline nature of zeolites results in ordered channel systems and very narrow pore size distributions. However, pore sizes are restricted to cage and channel diameters of about 1.5 nm [3]. For many applications in catalysis this limits the size of species that can be utilised. For example, cracking of the heavier fractions of crude oil [4], sieving of biomolecules, and anchoring of metals with bulky ligands [5] all require larger channels than those currently found in zeolites.

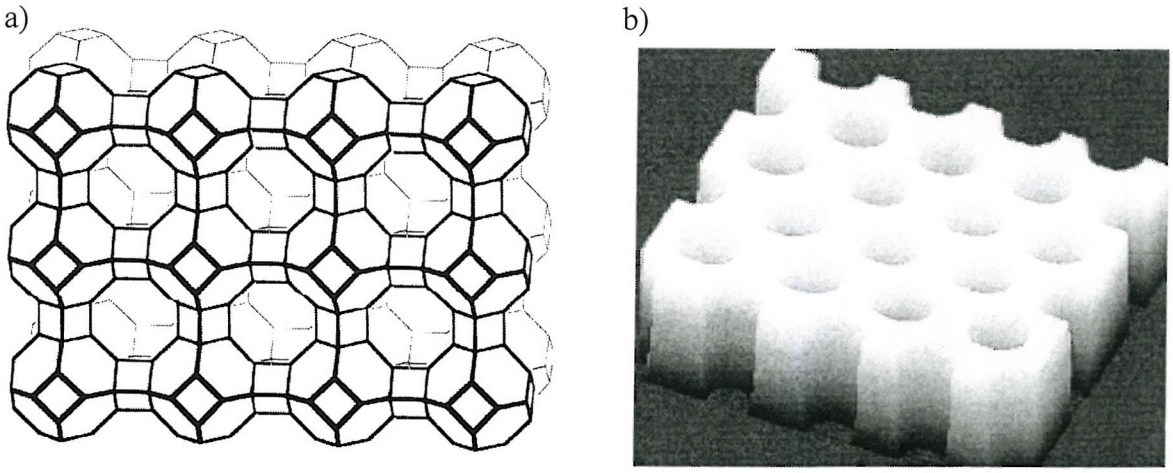

Figure 1.1 a) The organised 3 dimensional pore structure of a crystalline microporous material (zeolite A [LTA]), b) The organised 2 dimensional pore structure of an amorphous mesoporous silica (MCM-41).

Extension of pore sizes into the mesoporous domain (2-50 nm according to IUPAC definition [6]) has received a great deal of interest over the last few years. In 1992 a new family of mesoporous silicas (M41S) was reported by researchers at Mobil R&D

Corporation [7-8]. These materials contain highly ordered pore structures with channels greater than 2 nm in diameter and narrow pore size distributions. They differ from zeolites in that their channel walls are not crystalline but amorphous (figure 1.1). Already M41S materials have been shown to have potential applications in catalysis [9-10].

More recently, work carried out by Attard *et al.* has shown that it is possible to produce mesoporous metals as well as inorganic oxides [11-13]. Metals with ordered arrays of nanometer sized pores are of particular interest for not only catalytic applications but also for battery, sensor and fuel cell technologies. The following sections describe some of the general background to surfactants and mesoporous materials. To place the novel area of mesoporous metals in context a discussion of existing high surface area metals is also presented. An introduction to fuel cell technology and catalysis by the platinum group metals, two of the possible applications of the mesoporous metals prepared, is finally given.

1.1.2 Surfactants and liquid crystal phases

The types of pore structures observed in mesoporous materials always resemble the aggregate structures observed on mixing surfactants with water. This is no coincidence as surfactants are an essential component of the synthesis mixtures for preparing mesoporous materials. In order to understand the mechanisms by which these ordered structures form it is necessary to understand how surfactants behave in aqueous solutions. What follows is an overview of the aqueous phase behaviour of surfactants [14-16].

Surfactant molecules consist of a water soluble (hydrophilic) component and a water insoluble (hydrophobic) component. As these molecules display characteristics of both hydrophilic and hydrophobic molecules they are also known as amphiphiles (loving both kinds). The solubility of the hydrophilic headgroup arises from its polar nature whereas the hydrophobic tail is nonpolar and insoluble in water. Table 1.1 shows the structures of some common amphiphiles used to prepare mesoporous materials.

Surfactant	Structure	Notes
$C_{16}EO_8$	$CH_3(CH_2)_{15}(OCH_2CH_2)_8OH$ Octaethylene glycol monohexadecyl ether	Nonionic surfactant Very expensive as a pure material [11]
Brij 76	$CH_3(CH_2)_{17}(OCH_2CH_2)_{10}OH$ (average chain length)	Nonionic surfactant Very Cheap [17]
Brij 56	$CH_3(CH_2)_{15}(OCH_2CH_2)_{10}OH$ (average chain length)	Nonionic surfactant Very Cheap [17]
Triton X-100	$CH_3C(CH_2)_2CH_2C(CH_3)_2C_6H_4(OCH_2CH_2)_{10}OH$ (average chain length)	Nonionic surfactant Very Cheap [17]
Pluronics	$HO(OCH_2CH_2)_x(OCH_2CH_2CH_2)_y(OCH_2CH_2)_xOH$ variations on.	Nonionic surfactant Long chain block copolymer [17,18]
CTAB	$CH_3(CH_2)_{15}N(CH_3)_3Br$ Cetyltrimethylammonium Bromide	Ionic surfactant Cheap Commonly used to prepare M41S materials [7,8]

Table 1.1 Examples of some surfactants that have been used to prepare mesoporous materials. References refer to studies of their use in the synthesis of mesoporous silicas.

The most important commercial nonionic surfactants are the polyoxyethylene (POE) compounds. A long polyoxyethylene chain exists in the middle of these molecules, a hydrocarbon chain is attached at one end, and a hydroxy group is present at the other end. These compounds are easily and inexpensively prepared on a commercial scale. For example, Brij 56 is prepared by the addition of ethylene oxide to a fatty alcohol. Commercial surfactants, such as Brij, invariably display a distribution in the number of oxyethylene groups. Individual POE surfactants (eg $C_{16}EO_8$), are much more difficult to prepare and consequently more expensive.

If a small amount of one of the surfactants shown above is mixed with water, it is possible for the molecules to go into solution. As the concentration of amphiphilic material increases, however, the amphiphilic molecules begin to form aggregates, with the polar head groups on the outside and the hydrocarbon tails towards the centre (figure 1.2a) reproduced from reference [19]. This structure is called a micelle and is

stable as long as the surfactant is above a certain concentration (called the critical micelle concentration or cmc). Typically the value of the cmc is less than 1 wt% of surfactant with respect to the total water content.

It is easy to see why micelles are stable structures because the hydrophobic components of the molecules are shielded from the water by the hydrophilic headgroups. As the amount of surfactant in solution is increased, more micelles form until eventually a point is reached where the micelles combine to form larger structures. One such aggregate is called the hexagonal phase (H_I), in which long cylindrical rods of amphiphilic molecules arrange in an hexagonal array (figure 1.2c). Another common structure that forms at even higher concentrations is the lamellar phase (L_α), in which the amphiphilic molecules form flat bilayers separated from each other by water (figure 1.2e). A less common phase is the cubic phase (V_I), which often lies between the H_I and L_α phase and has a complex interconnecting three-dimensional structure (figure 1.2d). At the extremes where there is very little water in the system the surfactant molecules revert to the spherical micelles but with the headgroups on the inside, surrounding small amounts of water (figure 1.2f). The range of aggregate structures shown in figure 1.2 only represents the phases commonly found for POE surfactant systems. There are a number of other lyotropic phases but for the purposes of this thesis only the structures shown below are of interest.

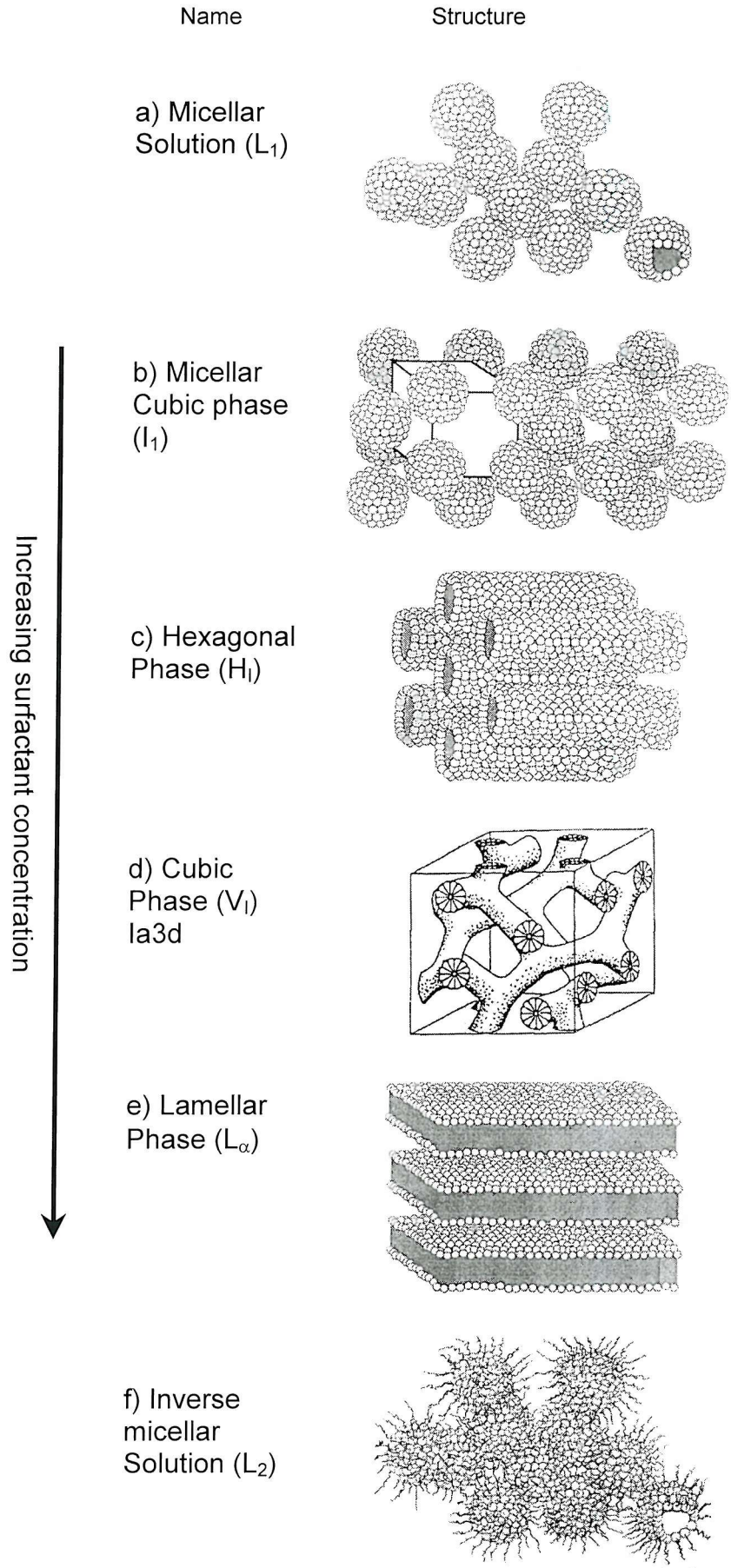

Figure 1.2 Examples of surfactant aggregate structures formed in lyotropic systems [19].

The larger structures, formed beyond the concentrations of surfactant required for micelles, are said to be liquid crystalline. This is because the molecules are oriented on average along some preferred direction, producing fluid but structurally anisotropic phases. The molecules in a liquid crystal phase do not have the positional and orientational order of a solid nor do they have the total disorder associated with a liquid but tend to lie somewhere between the two extremes. The liquid crystal phases formed by mixtures of surfactant and water are termed lyotropic phases. As with thermotropic liquid crystals altering the temperature can alter the phase. However, in lyotropic systems, as was explained previously, altering the water content can also change the structure of the phase. The variables of temperature and composition are commonly used to plot phase diagrams for amphiphilic molecules. Phase diagrams are constructed, from observations made by polarised light microscopy, X-ray diffraction and NMR [14, 15, 20].

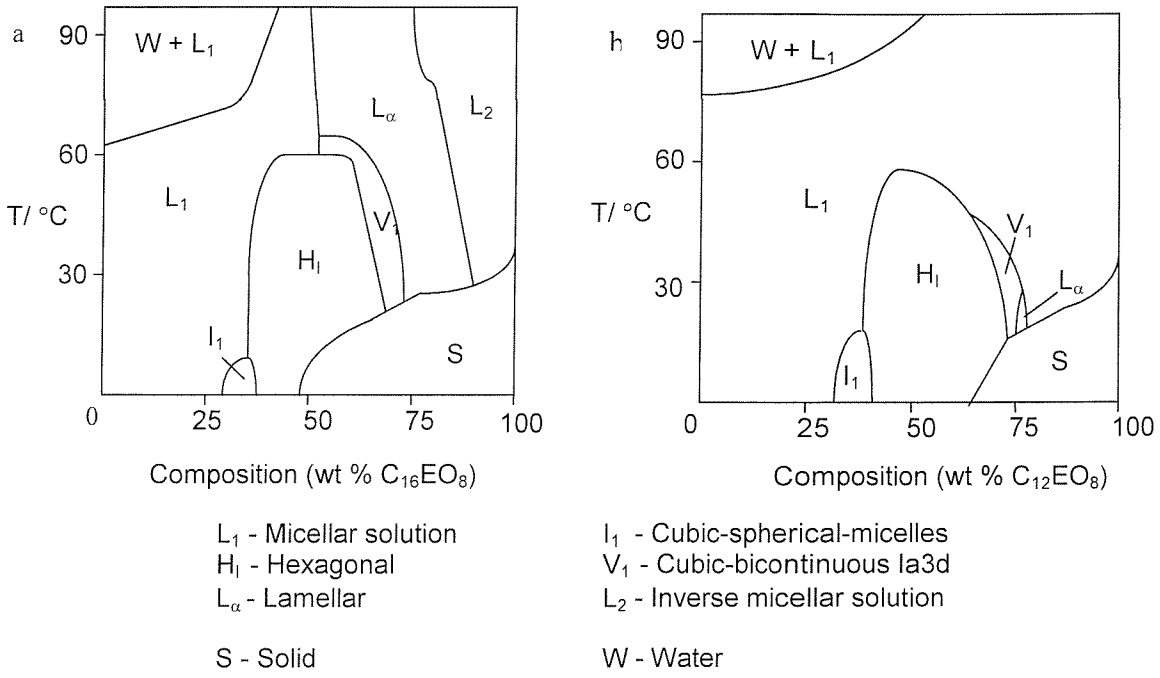

Figure 1.3 Liquid crystal phase diagrams for two POE surfactants in water, a) $C_{16}EO_8$ and b) $C_{12}EO_8$. Redrawn from reference 21.

The phase diagram for $C_{16}EO_8$ shows that the liquid crystalline behaviour of this material is diverse, with large regions over which the H_I and L_α phases are stable (figure 1.3a). In addition to the lyotropic phases and micellar solution domains, the phase diagram also exhibits a biphasic region (L_1 + W), which is characterised by a solution containing areas rich in micelles surrounded by water. The temperature at which a micellar solution phase separates is known as the cloud point. The name arises from the turbid nature of an L_1+ W solution. A further region of the phase diagram, at low temperatures, consists of solid surfactant that is not in solution. The line that separates the lyotropic phases from the solid region is known as the Krafft boundary and defines the crystal solubility boundary of the surfactant. Below the boundary the surfactant is present as crystals of surfactant surrounded by water [15].

Phase behaviour in lyotropic systems is not purely a function of composition-temperature space but is also strongly influenced by the molecular structure of the surfactant. Comparison of the phase diagram of $C_{16}EO_8$ with that for $C_{12}EO_8$ (figure 1.3) reveals considerable differences in the phase behaviour of the two surfactants, in particular the reduced size of the L_α and V_1 domains for $C_{12}EO_8$ compared to $C_{16}EO_8$. A complete analysis of how phase behaviour is effected by molecular structure is a complex subject. However, at a basic level, headgroup interactions, tail interactions and interfacial forces determine the shapes of aggregate structures (figure 1.4).

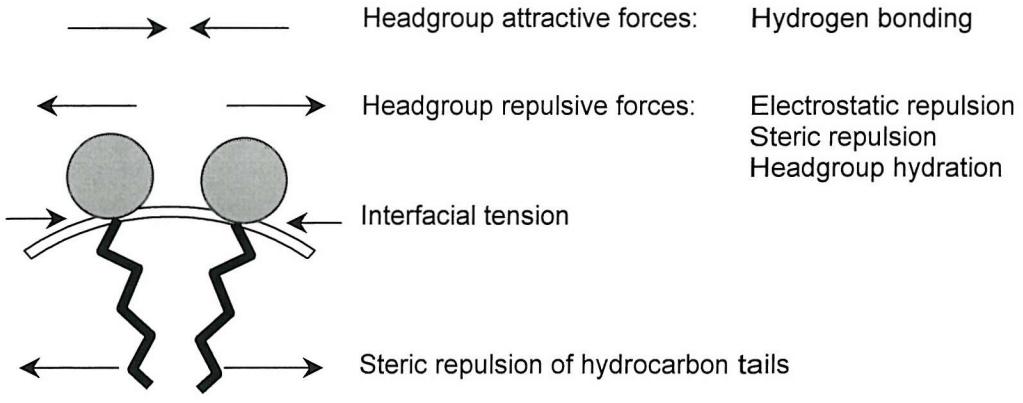

Figure 1.4 Interactions between surfactant molecules in aqueous systems

In the CTAB + water system, electrostatic repulsion between the positively charged ionic headgroups dominates. Consequently structures with a high positive mean curvature, where the headgroups are well spaced in comparison to the hydrocarbon tails, are favoured. As a result, a large hexagonal domain dominates the phase diagram of CTAB (figure 1.5) [22].

Returning to the non-ionic POE surfactants, the balance between the headgroup and tail interactions is more delicate and a small change in either end of the molecule can result in significant changes in phase behaviour. By increasing the size of the headgroup, steric repulsion increases between headgroups and the space required by the headgroup increases relative to the hydrocarbon tail. This is shown by a shift too more curved structures such as the micelles in the I_1 phase. Decreasing the length of the hydrocarbon tail, as in the $C_{16}EO_8$ versus $C_{12}EO_8$ case has a similar effect on the phase behaviour as increasing the size of the headgroup. Consequently, $C_{12}EO_8$ exhibits hardly any L_α behaviour because a molecule with a short hydrocarbon tail and large headgroup does not favour such a flat structure.

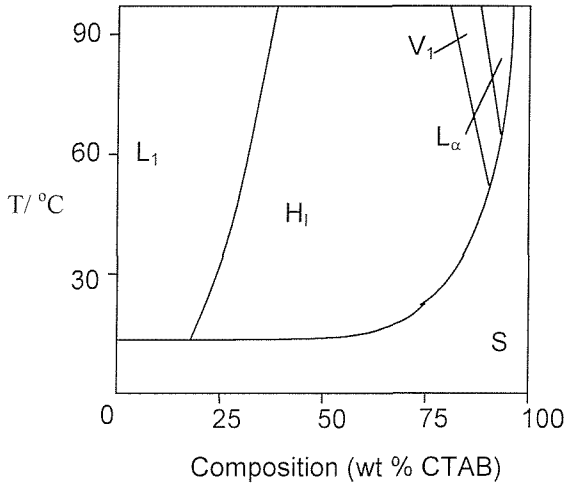

Figure 1.5 Liquid crystal phase behaviour of CTAB + water mixtures. Redrawn from reference 221.

1.2 The synthesis of mesoporous materials

1.2.1 Structure, nomenclature and composition

The field of ordered mesoporous materials is relatively new. In 1992, Beck and co-workers synthesised a range of mesoporous silicate materials known as M41S [7-8]. Characteristically these materials have highly ordered channel systems with narrow pore size distributions. However, unlike zeolites the channel walls are made up of amorphous silica and pore diameters are greater than 2 nm. The M41S family consists of three structure types. The first of these, MCM-41 (Mobil Corporation Material 41), contains a hexagonal arrangement of channels. A second material, MCM-48, has a complex interconnecting, 3-dimensional, channel system. Finally MCM-50 has a lamellar structure. Later Attard *et al.* showed that similar structures could be prepared directly from liquid crystal phases [23] and these materials were labelled according to the liquid crystal phase from which they were formed (hexagonal (H_I), cubic (V_I) and lamellar (L_α)). Figure 1.6 shows the range of pore mophologies observed for such mesoporous materials.

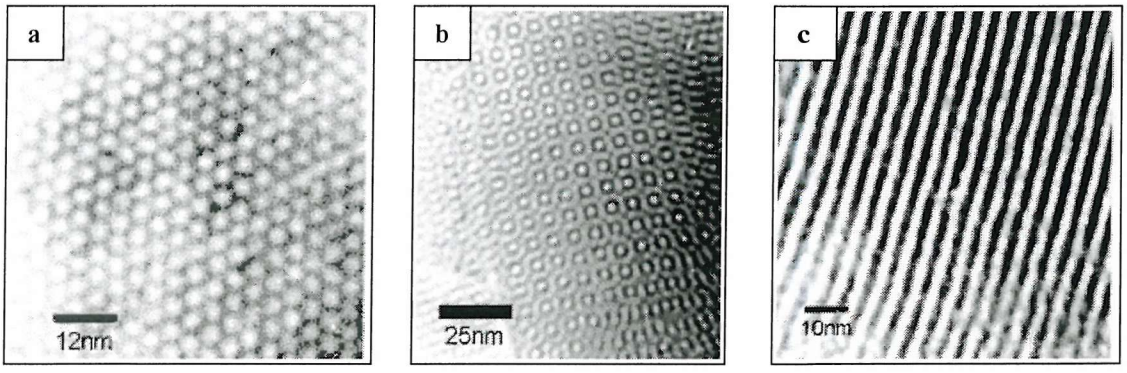

Figure 1.6 TEM images of mesoporous silicas. a) Hexagonal pore morphology (hexagonal array of cylindrical holes), b) Cubic pore morphology (complex interconnecting channel system with the Ia3d space group), c) Lamellar pore morphology (sheets of silica) [23].

Partial exchange of silica for alumina, in M41S materials, results in a mesoporous aluminosilicate. In a similar manner it is possible to include transition metals in the framework of the walls [24]. Ordered mesoporous materials are not only limited to silicas but extend to a variety of other inorganic oxides [25].

More recently it has been shown that mesoporous metals can be prepared with an hexagonal pore structure [11-13].

As described above, common to all preparations of ordered mesoporous materials is the presence of a surfactant. The concentration at which the surfactant is present predetermines the mechanism that results in a porous structure. In the Mobil synthesis, of M41S materials, the surfactant concentration is characteristically low (1-10 wt%) [7, 8]. This rules out the existence of a homogeneous liquid crystal phase in the synthesis mixture. In 1995 it was shown that regular mesoporous silicas could be prepared at much higher surfactant concentrations, such that lyotropic liquid crystal phases were acting as structure directing agents [23].

What follows is a discussion of the two methods of preparing mesoporous materials and a description of how direct liquid crystal templating can be utilised to make high surface area metals such as platinum.

1.2.2 Mobil synthesis – low surfactant concentrations

The Mobil method of producing mesoporous materials employs alkyltrimethylammonium ions, with alkyl chain lengths of 8-18 carbon atoms (figure 1.7). These cationic molecules are surfactants that can self-assemble in aqueous solution into spherical micelles, rodlike micelles, a lamellar phase (L_α), a hexagonal array (H_I) or a bicontinuous cubic phase (V_I) depending on the length of the alkyl chain, the surfactant concentration, temperature and the type of counterion present [22]. The surfactant molecules are occluded in the pores of the inorganic product with the cationic micellar headgroups adjacent to the silicate channel walls. The radius of the uniformly sized pores that result upon removal of the surfactant by calcination or solvent extraction is directly correlated to the length of the alkyl chain. Larger pores can be synthesised if an additional hydrophobic organic species is added to swell the self assembled structures [26].

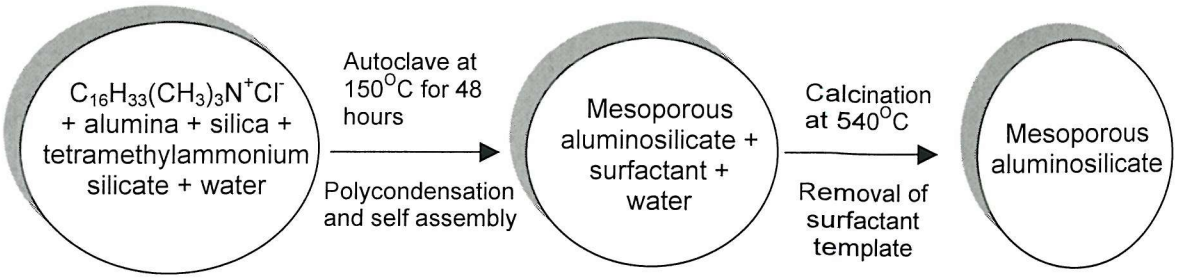

Figure 1.7 Mobil synthesis of mesoporous materials employing low surfactant concentrations [7, 8].

There is a clear resemblance between the hexagonal array of surfactant-filled pores found in these materials and the hexagonal topology of the H_I liquid crystal phase. This suggests that surfactant aggregates act as structure-directing agents in the synthesis of MCM-41. However, in the binary surfactant-water phase diagram the H_I phase is not present at the low surfactant concentrations used. This apparent paradox has stimulated a considerable amount of work on M41S materials [27]. It is now generally accepted that some sort of self-assembly of the micelles in the synthesis mixture is responsible for the pore topology. It is well known that the addition of inorganic salts to cationic surfactant-water systems results in phase separation of micelles and water [28]. In the synthesis of MCM-41, it is proposed that electrostatic interactions between the micellar headgroups and the silicate species results in a biphasic reaction mixture. This biphasic mixture contains a large quantity of water with small regions rich in silicate-encapsulated, rodlike, micelles. These inorganic-organic composite species are arranged in the hexagonal order of MCM-41. To facilitate the production of rod like micelles, the surfactant must be present in concentrations greater than the critical micelle concentration [29].

There are a large number of variations on the Mobil method, but they all rely on self-assembly of micelles at low surfactant concentration. Critical to the method is the charge interaction between the surfactant head group and the forming material. This limits the materials, which can be produced, to inorganic oxides such as silicas and metal oxides. To date most of the mesoporous materials have been prepared using variations on the Mobil method. The large majority of preparations of M41S silicas use ammonium based ionic surfactants such as CTAB. One reason for this is that, as explained above, charge is thought to be important in obtaining the ordered structures. However, it has been shown that non-ionic surfactants such as Brij, Tween, Triton, Tergitol and block copolymers can be used to prepare ordered mesoporous silicas [30]. The range of surfactants indicates that it is the phase forming properties of surfactants that control the formation of M41S materials.

1.2.3 Liquid crystal templating – high surfactant concentrations

Direct liquid crystal templating of mesoporous materials is possible by the use of high surfactant concentrations. The characteristic phase of the surfactant-water system can be used as a direct mould for the forming oxide ceramic or metal. In 1995 it was shown that mesoporous silicas, with pore morphologies identical to the M41S materials, could be produced in the homogeneous lyotropic liquid crystal phases of non-ionic POE surfactants ($C_{16}EO_8$ and $C_{12}EO_8$) [23].

In the direct liquid crystal templating method, a source of silica is provided by a silicon alkoxide (tetramethyl orthosilicate, TMOS) which is hydrolysed by acidified water. The reaction of water with TMOS results in a sequence of hydrolysis and condensation reactions, which eventually leads to the formation of amorphous silica. The final silica material is known as a gel because the silica can be thought of as a single molecule, which extends throughout the solution. If the smallest dimension of the gel is greater than a few millimetres, the object is generally called a monolith. The area of materials chemistry, which involves the preparation of gels from alkoxides is known as sol-gel science [31]. Many applications of sol-gel materials arise from the ability to form fibres, films and mould various shapes and it is the moulding properties of sol-gel materials that make them attractive for direct liquid crystal templating. Not only can the pore structure be moulded by the surfactant aggregates but also the shape of the container in which the reaction is carried out can predetermine the macroscopic structure.

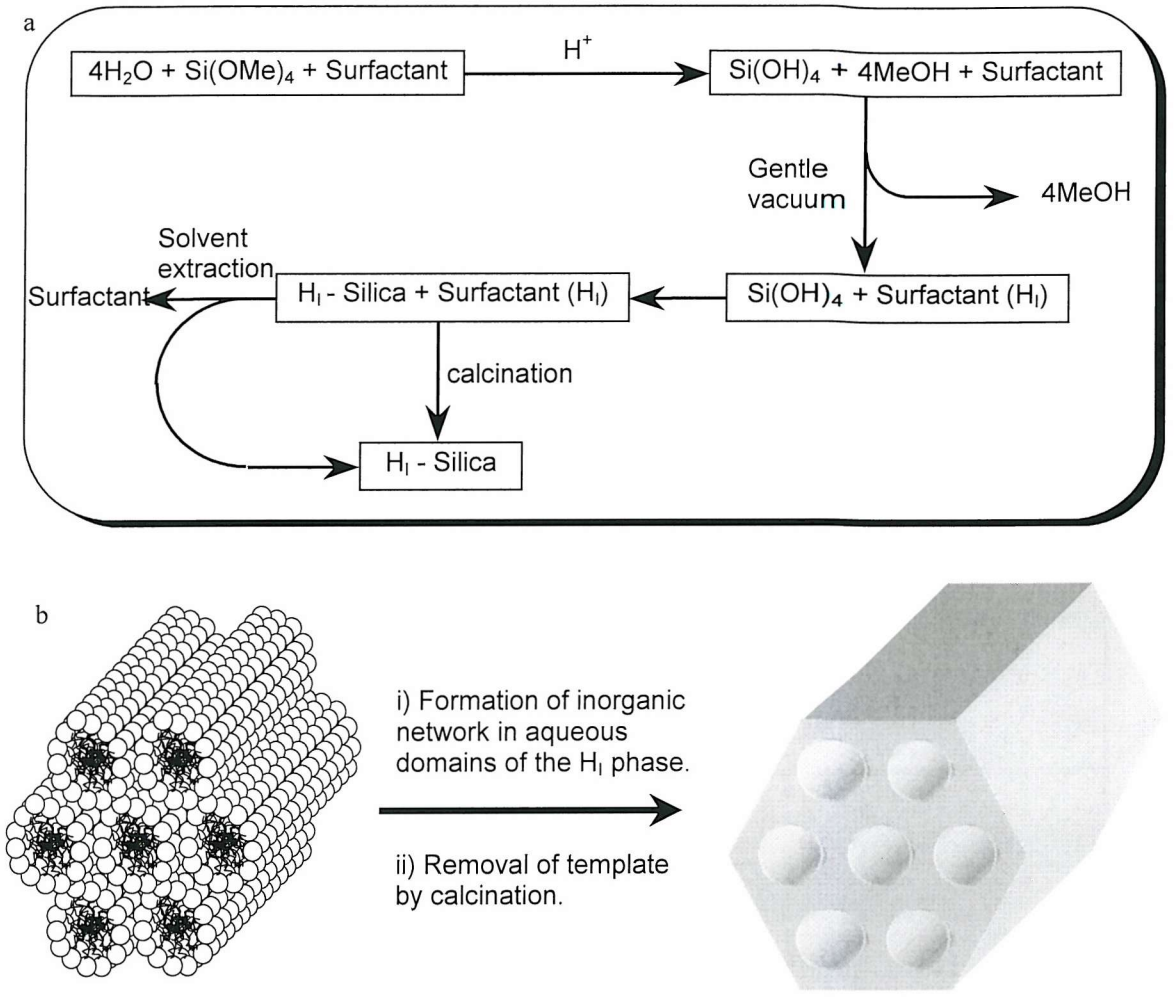

Figure 1.8 The preparation of H_I mesoporous silica, a) schematic of the whole process and b) a general scheme for the formation of inorganic mesoporous materials in the hexagonal phase of a surfactant-water system [19].

The preparation of a mesoporous silica directly from a liquid crystal phase involves addition of TMOS to a surfactant (> 50 wt%) + water + acid mixture. Initially, a large amount of methanol is produced which destroys the liquid crystal phase, but removing the methanol under a gentle vacuum can regenerate the phase. After leaving the mixture to gel, the surfactant is removed by calcination. The aqueous domains of the surfactant phases determine the regions in which condensation of the silica network occurs. Consequently, the structure of the calcined silica is a cast of the supramolecular architecture of the liquid crystal phase. Figure 1.8 shows a general scheme for the production of hexagonal, normal topology, silicas.

1.2.4 Direct liquid crystal templating vs. Mobil methods

There are a number of distinct advantages of using the liquid crystal templating route over the Mobil method:

Predictability and variation in the phase

The pore morphology can be predicted from the phase in which the reaction is carried out. In the Mobil method there is no simple way of predicting the type of material produced. In addition, the direct template method is not limited to hexagonal, lamellar and cubic phases but has the possibility of being extended to inverse phases. For example, an inverse hexagonal phase would result in a material that consists of long cylinders (figure 1.9).

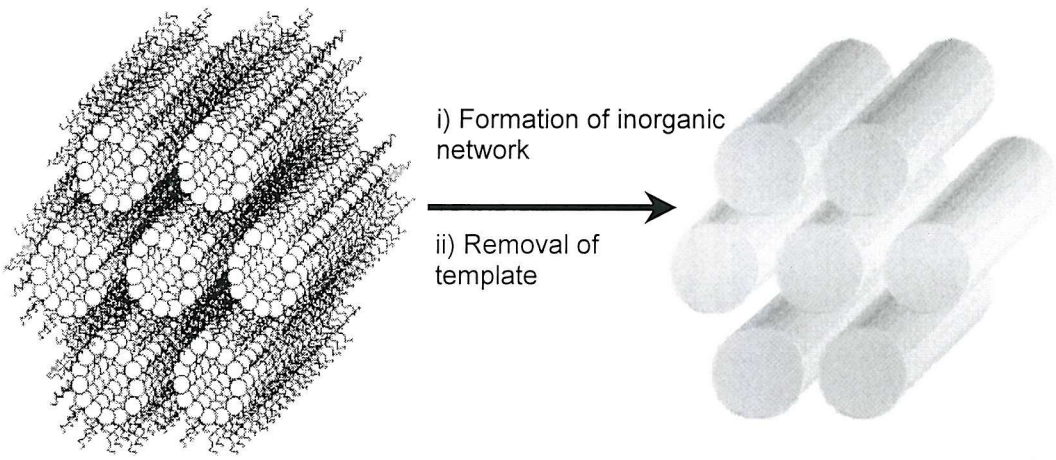

Figure 1.9 Synthesis of an inverse hexagonal material (H_{II}) from the aqueous domains of a surfactant that forms inverse phases.

Particle size

The direct templating route produces silicas whose overall particle size is much larger than those produced by the Mobil method. Typically, materials prepared using low surfactant concentrations consist of micron sized particles [7, 8]. In the direct liquid crystal templating method a continuous solid gel is produced rather than a precipitate [23, 30].

Extending the range of Mesoporous materials

The method is not limited to inorganic oxides as there is no necessity for an interaction between the precursor and the surfactant system. The use of a non-ionic surfactant, in the direct templating method, means that charge interactions are not important. Non-ionic surfactants have been used in adaptations of the Mobil method but it appears that the silicate species induce the phase separation to form an hexagonal structure [32]. By suitable choice of a precursor it should be possible to produce a variety of mesoporous materials, from polymers to metals, directly in the liquid crystal phase.

1.3 High surface area metals and mesoporous platinum

1.3.1 Conventional high surface area platinum materials

Traditionally, high surface area platinum powders are produced by warming a solution of KOH and $PtCl_2$ in ethanol [33]. The velvety black material obtained is known as platinum black and has a relatively high surface area (25-35 m^2g^{-1}) compared to other forms of platinum. Nanometer sized platinum particles can also be prepared, as colloidal dispersions, in the presence of surfactants. Typically, a platinum salt, such as hexachloroplatinic acid (H_2PtCl_6, HCPA), is reduced in a solution rich in surfactant micelles [34] or soluble polymers [35]. The organic additives stabilise the resulting platinum colloid, which contains 1-15 nm sized platinum particles.

High surface area platinum is important in catalytic and electrochemical applications. However, processing of nanometer sized platinum particles is complex. For example, separation of a colloidal platinum catalyst from reagents and products can be difficult. Often platinum nanoparticles on a catalyst support are preferred to colloidal systems [36].

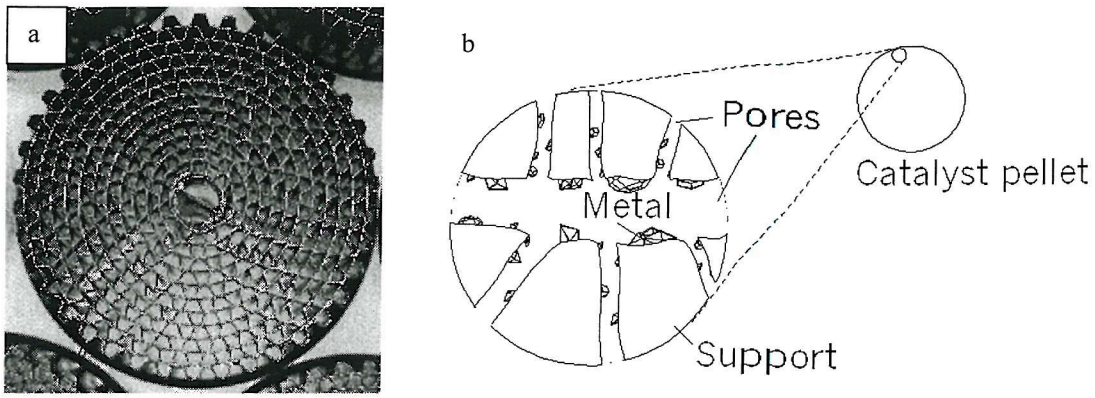

Figure 1.10 Supported platinum catalysts a) catalytic converter reproduced from reference 37, b) platinum metal supported on an alumina pellet.

The automotive catalytic converter uses an alumina support, which is loaded with platinum by soaking the alumina in a solution of a platinum salt and reducing the platinum ions to platinum metal (figure 1.10). Mesoporous silicas, prepared using the Mobil method, have also been loaded with platinum in a similar manner [38]. The mesoporous host is particularly attractive as a catalyst support because of its inherently high surface area and the potential to limit the size of the platinum nanoparticles.

For electrochemical applications, high surface area, platinum materials are of particular interest. Conventional methods of preparing high surface area platinum electrodes involve electroplating from an HCPA solution under conditions such that a rough platinum black deposit is obtained. The high surface area is obtained through the surface roughness of the material. These platinised platinum electrodes form the basis of the hydrogen reference electrode [39].

1.3.2 Palladium

Next to platinum, palladium is the most abundant of the platinum metals. Palladium is the chief rival of platinum in alloys for dentistry, jewellery and catalysis. In fact, palladium imparts to some alloys properties which are much more desirable than those imparted by platinum. An outstanding property of palladium is its ability to adsorb hydrogen. Gas occlusion takes place at ordinary temperatures and is accelerated by a rise in temperature.

The physical structure of the metal affects the absorption [40]. Freshly ignited palladium foil, for example takes up more than 370 volumes of hydrogen at room temperature, and when heated to 100 °C about 650 volumes of gas are absorbed. Spongy palladium and finely divided palladium black both have an enormous capacity for holding hydrogen. Hydrogen combines with palladium to form palladium hydride, a compound which exists in solid solution in the palladium metal remaining when the reaction with hydrogen is incomplete. The reaction of hydrogen with palladium is important in chemical processing: palladium and palladium hydride causes the decomposition of hydrocarbons at temperatures far below those which would otherwise decompose them [40]. When heated to several hundred degrees in contact with a hydrocarbon, the palladium swells and carbon is liberated from the hydrocarbon. Finely divided sponge palladium and palladium black act as a catalyst. Palladium oxide (Adam 's catalyst) prepared in the same manner as platinum oxide [40], is much used in hydrogenation. Carriers of various kinds may be employed as a base for colloidal palladium [40]. The number of reactions catalysed by palladium is extremely large, they include oxidation, chlorination, reduction, polymerisation, and synthesis but the most notable reactions are the hydrogenation of oils and other organic substances [41]. There are numerous patents dealing with palladium catalysis: applications such as petroleum cracking, gas sensors [42], production of hydrocyanic acid from ammonia and acetylene [43] and purification of rare inert gases such as Krypton and Xenon have been reported. In the field of gas sensor, palladium has been recognised as the best catalyst for methane oxidation [44]: commercial pellistors use, to fulfill this task, palladium particles on γ- alumina (porous type of alumina). The surface area of the catalyst influenced the sensitivity, lifetime and poison resistance of the gas sensor.

Recently, pellistors based on high surface area nanostructured palladium films prepared from direct liquid crystal templating were also proved to be suitable for methane detection [42].

1.3.2 High surface area Pt based alloys

The ability to produce binary intermetallic materials that have a uniform dispersion of the constituent metals is of considerable importance for the development of new catalysts, since in principle for such system, catalytic activity can be related to a well-defined and reproducible surface chemistry [45,46]. Furthermore, in many cases, alloying afford materials whose catalytic activity/performance is enhanced significantly in comparison to that of the constituents metals [47]. For example, platinum alloys catalysts can be less susceptible to poisoning by sulphur containing species or by carbon monoxide. Watanabe *et al.* reported that ruthenium when mixed with platinum group metals displays a synergistic effect for the direct oxidation of methanol: the Pt/Ru catalyst increased the specific activity over pure platinum by more than a factor of 10 at an atomic ratio of Pt/Ru of about 1/1 [48]. Because the catalyst is nevertheless expensive, the catalyst was used highly dispersed on a proper support having a high specific surface area (carbon black in that case) from the standpoint of its cost performance. The preparation of the highly dispersed Pt/Ru alloy clusters was based on the co-deposition of fine oxides of platinum and ruthenium in atomic scale of these metals followed by reduction with hydrogen bubbling [48]. This method provided a simple way of obtaining a specific surface area of around 80 m^2g^{-1} more than 3 times larger than that obtained by conventional methods [48].

For the development of fuel cell technology, the preparation of supported bimetallic catalysts has been extensively studied. Of the many procedures that have been employed to prepare bimetallic supported metal catalyst, the most commonly used has been an impregnation of the support material with aqueous solutions of the metal salts. Following a drying procedure, the support is heated under a gas-phase reductant, usually hydrogen, to give the metals. The interaction of the metal salts in solution with the surface of the support is of great importance in determining the size of the metal particles obtained as are the conditions used during adsorption of the metal salts on the catalyst support [49].

In a study of the effect of different reducing methods employed during catalysts deposition together with the effect of a drying-in process, Goodenough *et al.* showed that electrodes of highest activities were obtained from platinised carbons prepared by in- situ reduction of the metal salts with strong reducing agents such as formaldehyde and hydrazine rather than sodium formate [50]. The higher activities attained by those electrodes was related to the smaller particle size which led to an increase in surface area. A number of catalyst deposition techniques have also been investigated for the efficient dispersion of high surface area bimetallic catalysts on conducting carbon substrates [49]. The ability to produce supported binary intermetallic materials that have a uniform dispersion of the constituent metals combined with high specific surface area is of extreme importance to meet future challenges in fuel cell development.

Severe restrictions on the content of pollutant contained in car engine exhausts gases has also motivated the development of bimetallic catalysts for the purification of exhaust gas from CO, NO and hydrocarbons. The catalysts based on Pt/Rh and Pd/Rh in three way catalysis are commonly used for the simultaneous purification of gases from all the 3 components of exhaust gases [51]. By the electrochemical deposition of rhodium ions on a clean platinum surface, Sasahara *et al.* showed that a small amount of rhodium is an indispensable component of the platinum based catalyst for NOx reduction [52].

1.3.3 Novel nanoporous metals

For a wide variety of applications it would be particularly attractive to have platinum with a higher surface area than conventional platinum materials. Potentially, this not only increases the activity/efficiency of the metal, through increasing the number of surface platinum atoms, but also has the benefit of decreasing the amount of platinum required. Another interesting area is the production of ordered pore systems within metals. Such systems would be useful for size exclusion of certain molecules if the holes were sufficiently small and of a particular size.

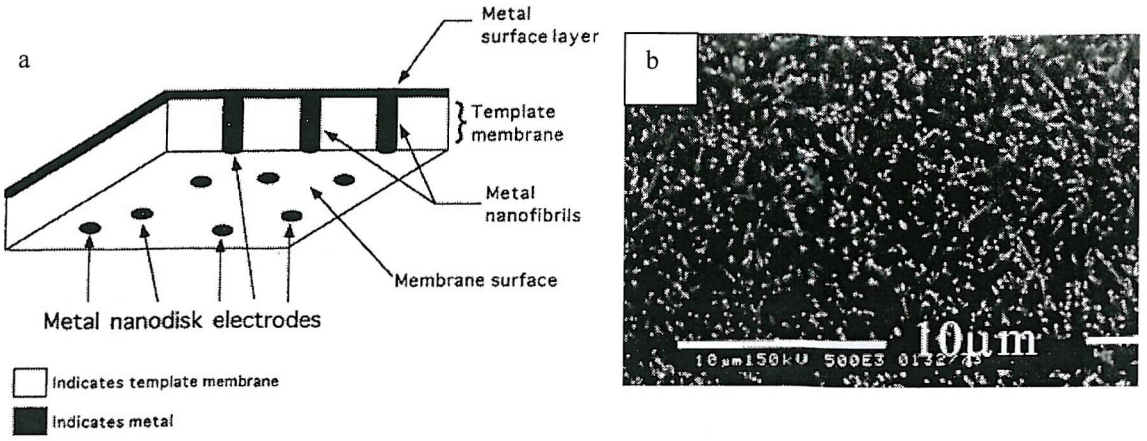

Figure 1.11 The electrodeposition of gold nanowires in track etched polycarbonate membranes a) schematic of the polycarbonate membrane containing nanowires, b) SEM image of the nanowires. Pictures reproduced from reference 53.

One method that has been successfully used to prepare ordered high surface area metals is to deposit a metal within an ordered membrane made of a polymer. For example, 100 nm diameter gold nanowires have been prepared by using track etched polycarbonate membranes [53]. The membranes are prepared by exposing polycarbonate to nuclear fission fragments to create damage tracks in the material, and then chemically etching these tracks into pores. The resulting cylindrical pores are distributed randomly but are of a uniform diameter (>10 nm). Formation of gold in the pores of the membrane is carried out by electroless deposition from a gold plating solution (figure 1.11).

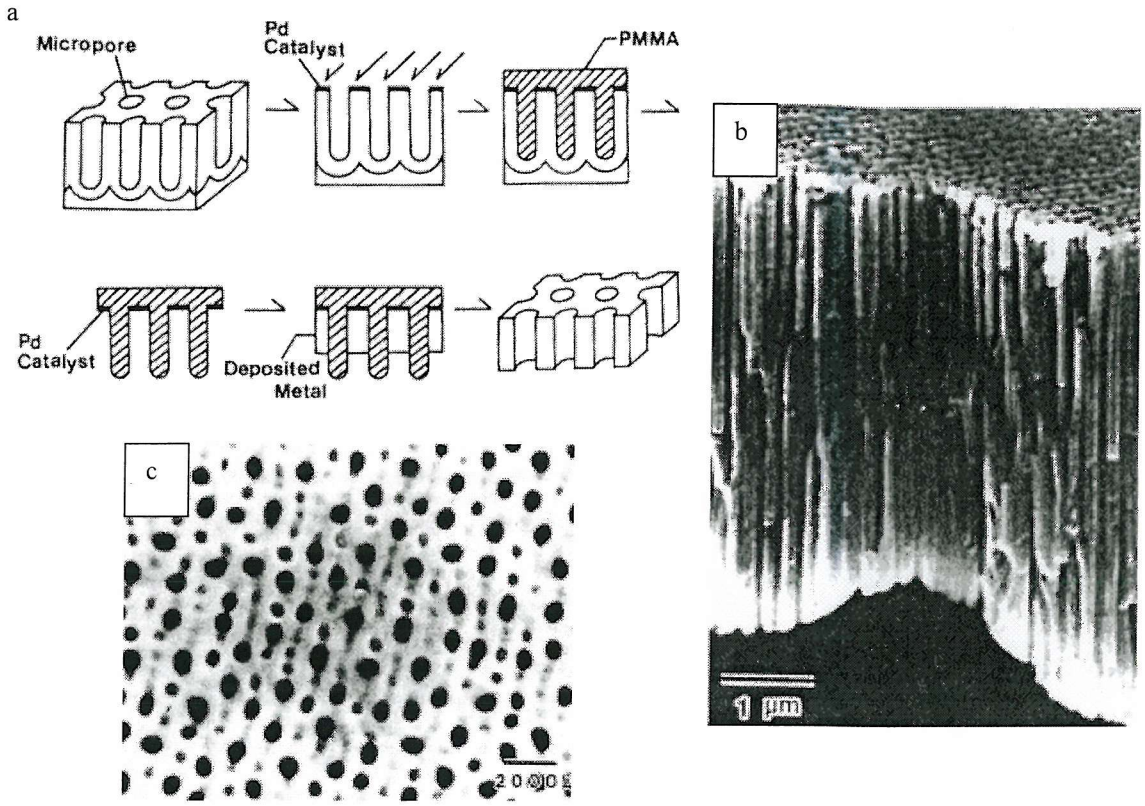

Figure 1.12 The generation of porous nickel films by a double replica moulding technique using a polymethylmethacrylate intermediate a) schematic of the process b) SEM image of the pore structure as viewed side on b) SEM image of the holes viewed end on. Reproduced from reference 54.

Another method that has been used is to prepare a porous alumina membrane via the anodisation of aluminium metal in acidic solution. These membranes contain cylindrical pores, which can be tailored in size from about 5 nm to 200 nm. Masuda *et al.* used an alumina membrane, in a double templating method, for the preparation of porous nickel [54]. Methylmethacrylate monomer was polymerised in the pores of the alumina membrane and the alumina dissolved in sodium hydroxide. Electroless deposition of nickel around the polymethylmethacrylate structure resulted in a porous nickel once the polymer had been selectively dissolved in acetone (figure 1.12). Similar methods were also used to prepare porous platinum and gold.

1.3.4 Direct liquid crystal templating of mesoporous platinum

In 1995 it was shown that an unsupported mesoporous platinum could be prepared by the reduction of HCPA in the aqueous domains of lyotropic liquid crystal phases [12]. The method used the same POE surfactant ($C_{16}EO_8$) that was employed for the direct templating of mesoporous silica [23]. Platinum produced in the hexagonal phase was shown to have an ordered H_I pore structure with ca. 3 nm diameter pores and ca. 3 nm thick walls. The material was a fine black powder with particles ranging in size from 90-500 nm. In addition, extended x-ray absorption fine structure (EXAFS) and x-ray diffraction revealed that the mesoporous platinum had the same face centred cubic crystal structure as a platinum foil. However, the average coordination of the platinum atoms was significantly less for H_I platinum than platinum foil indicating a high number of surface platinum atoms in the mesoporous material.

Chemical reduction of HCPA in a micellar solution of $C_{16}EO_8$ (or CTAB) resulted in dense unstructured platinum. This ruled out the self assembly/phase separation mechanism that has been shown to be important in the preparation of M41S silicas. The presence of a liquid crystal phase before chemical reduction was critical to the formation of mesoporous platinum.

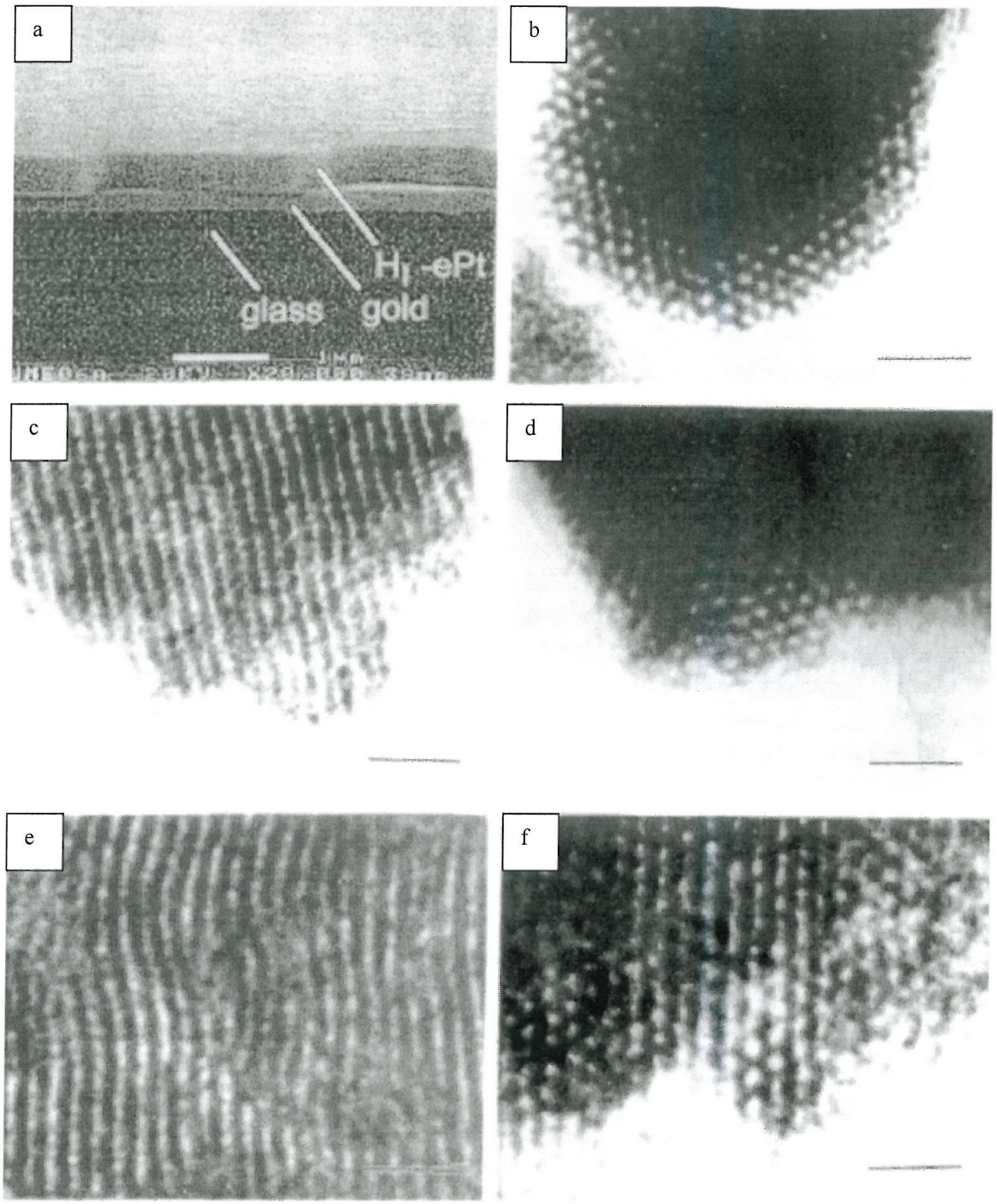

Figure 1.13 a) Scanning electron micrograpgh of H_I platinum electrodeposited on a gold-coated glasss slide (scale bar: 1 μm). Transmission electron micrographs showing the hexagonal nanostructure of: b) chemically produced platinum from a $C_{16}EO_8$ H_I phase, electrodeposited platinum from a $C_{16}EO_8$ H_I phase c) side on view of pores, d) end on view of pores, electrodeposited platinum from a $C_{16}EO_8$ H_I phase containing 1 mole equivalent of *n*-heptane e) side on view of pores, f) end on view of pores (scale bars: 25 nm).

Following on from the work on chemically produced mesoporous platinum it was reported that H_I platinum could be electrodeposited on gold electrodes [11]. The method used exactly the same $C_{16}EO_8$ + water + HCPA mixtures used to prepare H_I platinum chemically. Again, the materials were shown to have a high surface area and an ordered pore structure. However, unlike the chemically produced H_I platinum, which was a black sub-micron sized powder, the electrodeposited materials were uniform coherent films that were highly reflective and metallic in appearance (figure 1.13a). Scanning tunnelling microscopy studies of the electrodeposited films showed them to be remarkably flat (surface roughness ±10 nm over 1 cm^2) and this accounted for the high reflectance of the films. By adding a hydrocarbon (n-heptane) to the H_I phase, containing the platinum salt, it was possible to swell the hydrocarbon domains of the phase and increase the pore diameter from 2.5 nm to 4.0 nm (figure 1.13) [13].

There is another example in the literature where liquid crystal phases have been used as structure directing agents in the formation of noble metals. Palladium metal nanoparticles were prepared by the reduction of a tetrachloropalladate solution mixed with a glycerol monooleate surfactant [55]. Reduction of the palladium was facilitated by the oxidation of the surfactant headgroups. The monooleate surfactant formed cubic phases in the 60-70 wt% surfactant regime that was used in the synthesis. However there was no evidence for a liquid crystalline structure in the resulting material and only small crystallites of palladium were observed in the transmission electron microscope.

1.4 Fuel cell technology

Energy conservation has become a worldwide objective because the natural resources of fossil fuels are becoming depleted, hence the search for alternative energy sources has become important. Fuel cells represent a possibility for the future: although fuel cell systems are more expensive to install, they provide lower running costs and greater fuel efficiencies than existing power plant as very little waste heat is produced. The main application in the future for fuel cells is to provide energy for car to ultimately replace the internal combustion engine.

A fuel cell is a primary electrochemical cell in which the reactants are continuously supplied from outside while the cell is in use. The free energy of the reactants is converted into electrical energy directly via the flow of electrons through the circuit. A reaction taking place at fuel electrode will produce the electrons which will then be able to flow through the eternal circuit to reach the other electrode and an electrical current is generated [56]. The recent success of fuel cell powered demonstration vehicles using the proton exchange membrane fuel cell developed by the Canadian company Ballard Power Systems and by Daimler Chrysler, suggests that fuel cells have come of age. At the heart of these developments lie vital advances in catalyst technology, without which this technology would not have progressed to its current state [56].

1.4.1 Type of fuel cell and proton exchange membrane fuel cell

There is now a whole family of fuel cells which are commonly characterised by the electrolyte used. They all function in the same way. At the anode a fuel (usually hydrogen) is oxidised into electrons and protons and at the cathode , oxigen is reduced to oxide species. Depending on the electrolyte, either protons or oxide ions are transported through the ion-conducting but electronically insulating medium to combine with oxygen or hydrogen respectively to generate water and electrical current [56]. The proton exchange membrane fuel cell PEMFC takes it name from the special plastic membrane that uses as its electrolyte. All the key parts of a fuel cell are combined in a very compact unit. This membrane electrode assembly (MEA) not thicker than a few hundred microns is the heart of the PEMFC and, when supplied

with fuel and air, generates electric power at cell voltages up to 1 V and power densities of up to about 1 Wcm^{-2}. The MEA is a five layer structure consisting of the proton exchange membrane, anode and cathode electrocatalysts layers either side, with gas diffusion substrates making up the outside of the sandwich. The membrane relies on the presence of liquid water to be able to conduct protons efficiently, and this limits the temperature at which a PEMFC can operate (below 100 °C). Therefore, to achieve good performance, effective electrocatalyst is required. At present this is based on Pt electrocatalyst materials. The catalysts form thin (several microns to several tens of microns) gas porous electrode layers on either side of the membrane [56]. The MEA is typically located between a pair of current collector plates with flow fields for distributing fuel and oxidant to anode and cathode respectively as shown on figure 1.14.

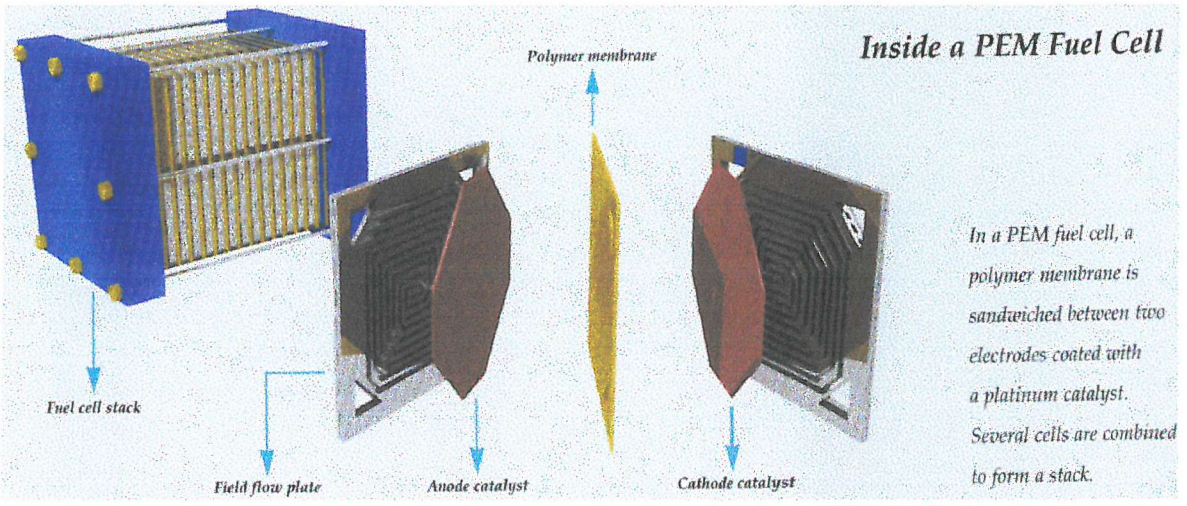

Figure 1.14 Membrane electrode assembly in a PEMFC consisting of three main components: two electrodes, each consisting of a carbon -based substrate coated with a platinum catalyst, and a solid electrolyte in the form of a polymer membrane. Reproduced from reference [57].

1.4.2 Direct Methanol Fuel Cell DMFC

Methanol is a particularly promising organic substance for fuel cell research; being relatively non-toxic, easy to store and handle, and possessing a high energy density of the order of 1 kWh/kg [56]. Methanol can readily be generated from biomass and, because of its simple structure, it should have a straight forward reaction mechanism when oxidised to produce CO_2 and H_2O. The direct methanol fuel cell oxidises methanol directly without transforming it into a hydrogen rich gas, meaning that the expensive reformer is eliminated.

Acid solution : $CH_3OH + H_2O \longrightarrow CO_2 + 6H^+ + 6\ e^-$

Alkaline solution: $CH_3OH + 1\ ½\ O2 \longrightarrow CO_3^{2-} + 3\ H_2O$

The methanol is introduced into the cell as a solution of the electrolyte, eliminating the 3-phase contact of a gas diffusion electrode. Typically, the methanol cell utilises a plate fuel anode and a normal diffusion or oxygen or air cathode.

So far the use of methanol as fuel has been considered more convenient than the conventional H_2 reformate as methanol is directly oxidised at the anode and is noted as transportable. However, the deactivation of the direct methanol fuel cell (DMFC) [58] may occur at the anode by formation of CO because of the electrosorption of methanol or by methanol crossover due to high permeability in the membrane towards the cathode, which causes polarisation losses [59]. Hence the anode requires a highly efficient methanol oxidation catalyst.

1.4.3 Fuel cell catalysis

To ensure that a fuel delivers maximum efficiency, both the oxidation of hydrogen (or methanol) and the reduction of oxygen need to take place as close to their thermodynamic potentials as possible. For these processes to occur at effective rates, they need to be catalysed. Therefore, the development of fuel cell technology has been intimately linked to the development of effective electro-catalyst technology. Research over several decades have shown that platinum or platinum containing catalysts are the best materials for both anode and cathode reactions [56].

The underlying difficulty with all fuel cell catalyst development is the identification of electrochemically active materials which are stable in the very corrosive, proton rich environment inside the membrane electrode assembly (MEA) over long periods of operation. The catalysts used for advanced low loading MEAs for PEMFCs, are carbon supported Pt-based catalysts where the loading of active metal can be very high. For a cathode catalyst, this can range from 10 to at least 40 wt % Pt supported on a conductive carbon black substrate. The carbon supports used are characterised by a high surface area (> 75 m^2g^{-1}), high electronic conductivity, relatively low oxygen content and a semi- graphitic nature [56].

In general precipitation methods are used to prepare fuel cell catalysts with typical particle sizes of less than 4 nm, even at 40 wt % loading. These approaches give catalysts with active surface areas of 70 to 120 m^2g^{-1} (Pt). The use of bimetallic catalysts demands the deposition of the two metals in intimate contact, so alloy formation can be achieved, with similar dispersion found for Pt-only catalysts. This is usually achieved by co depositing Pt and the second metal onto the carbon substrate as hydrous oxide /hydroxide precipitates, followed by thermal reduction at elevated temperature under inert gas flow [56].

Selectivity is the key to a successful design strategy for anode catalyst development. The number of H_2 oxidation sites on a given catalyst needs to be maximised, while CO coverage need to be minimised. Two types of modifications to the Pt electrocatalyst corresponding to two basic mechanisms have been reported [60] as described below.

1.4.3.1 Modification of platinum by alloying: intrinsic mechanism

This mechanism corresponds to a modification of a H_2 oxidation catalyst such as Pt by a second metal, in the form of an alloy, which modifies H_2 and CO chemisorption properties, so as to reduce CO coverage with respect to H_2 oxidation sites. The most elegant solution to overcome anode poisoning is the development of CO tolerant electrocatalysts, capable of operating in the presence of at least 100 ppm CO [61]. Much effort has been spent modifying Pt electrocatalytic properties by alloying with transition metals such as Ru, Rh, Cr, Ni, to produce catalysts with improved CO tolerance. The modification of platinum electrocatalytic properties by alloying with other metals is well established for both anodic and cathodic applications [62,64].

It has been shown by a number of authors that the modification of platinum by ruthenium in the form of an alloy does improve CO tolerance compared with pure platinum over a range of conditions [65,69], the ruthenium alloyed catalyst exhibits lower overpotentials and extended life times compared to the platinum. However, it is not clear by what mechanism this is achieved. Based on early work from Watanabe *et al.* [69] (on methanol oxidation), a bifunctional mechanism involving H_2O activation by Ru and subsequent CO oxidation on a neighbouring Pt atom has been postulated based on CO stripping voltammetry[65] and infrared spectroscopy[67]. The bifunctional character of Pt-Ru (adsorption of O-species at low potential and oxidation of CO migrating to these sites from Pt to Ru sites nearby has been recognised by Gasteiger *et al.* [71], they based their conclusions on the observation that the onset for CO stripping from Pt:Ru (~50:50) alloy electrodes lies at potentials lower than for pure platinum or ruthenium. Even though many studies have shown the improvement of the tolerance of electrocatalysts by alloying Ru to Pt, future challenges relie on the development of more efficient electrocatalysts for low temperature fuel cells.

1.4.3.2 Modification of platinum by metal oxides: promoted mechanism

The second strategy to increase the selectivity for anode catalyst development is to promote a H_2 oxidation catalyst by a metal or metal oxides which catalyses the oxidation of chemisorbed CO at low potentials by the activation of H_2O. This has the effect of reducing CO coverages and consequently increasing the number of H_2 oxidation sites. Many efforts have been spent modifying Pt electrocatalytic properties by using dopants such as tin oxide and tungsten oxide to compare with the alloy catalysts. Oxide dopants of both metals have been reported for CO activation with Pt containing system: early work by Niedrach and Weinstock showed that mixing of Pt black with various oxides led to remarkable CO electrooxidation activity in acid electrolyte [72]. More recently, Sn and W have been investigated as promoters to Pt for methanol electrooxidation [73,74] and CO electrooxidation [75].

1.5 Catalysis by the platinum group metals and heterogeneous catalysis

The uses of platinum group metals in catalysis are very varied and constitue important applications. These includes the oxidation of ammonia for the production of nitric acid [76] the hydrogenation of olefins [36] and the reduction of Nox in the control of car exhaust emissions [77]. In the following, a few of the most important catalytic applications of platinum group metals are described and the potential uses of the mesoporous metals prepared assessed.

1.5.1 Heterogeneous catalysis, catalytic hydrogenations

Heterogeneous catalysts are solids which increases the rates of chemical reactions by virtue of the specific properties of their surfaces. All catalytic processes possess certain common physico-chemical characteristics and the definition of a catalyst as a substance which increases the rate at which a chemical system attains equilibrium without itself undergoing chemical change is broadly applicable [78]. It has long been appreciated that the activity of a heterogeneous catalyst resides at the interface between the solid and the less dense phase and that the reactant must be adsorbed at this interface. The role of the catalyst surface is to lower the potential barrier between reactants and products (stabilisation of the transition state) and to activate the reactants [79]. Of the many methods available for reduction of organic compounds catalytic hydrogenation is one of the most convenient. Reaction is easily effected simply by stirring or shaking the substrate with the catalyst in a suitable solvent in an atmosphere of hydrogen. At the end of the reaction, the catalyst is filtered off and the product is recovered from the filtrate, often in a high state of purity [80]. Many different catalysts have been used for catalytic hydrogenations ; they are mainly finely divided metals, metallic oxides or sulphides. The most commonly used in the laboratory are the platinum metals (platinum, palladium and to a lesser extent rhodium and ruthenium). Platinum group metals are exceptionally active catalysts and promote the reduction of most functional groups under mild conditions with the notable exception of the carboxyl, carboxylic esters and amide group [81]. They are used either as the finely divided metal or, more commonly supported on a suitable carrier such as asbestos, activated carbon or alumina.

In general, supported metal catalysts, since they have a larger surface area, are more active than the unsupported metal but the activity is influenced strongly by the support and the method of preparation, and this provides a means of preparing catalysts of varying activity. Platinum is very often used in the form of PtO_2, " Adams catalyst", which is reduced to metallic platinum by hydrogen in the reaction medium [80]. It has been also found that very effective catalysts can be obtained by reduction of various metal salts with either sodium borohydride [82] or a trialkylsilane [83].

Palladium is also very important in organic reactions. Modern palladium chemistry started in 1960 with the ingenious invention of an industrial process for acetaldehyde production by the air oxidation of ethylene, catalysed by $PdCl_2$ and $CuCl_2$, which is called the Wacker process (homogeneous catalysis [84]. In heterogeneous catalysis, palladium is often the mildest reducing agent in the metal form and this was exploited in producing more selective catalysts [85]. The popularity of this catalyst is due to the fact that it is the best catalyst to use for the hydrogenation of olefins and acetylene. Palladium is usually used supported on a carrier but is occasionally used as palladium oxide or the finely divided palladium black. Palladium oxide is prepared by the fusion of chloropallidic acid with sodium nitrate in a procedure similar to that used for the preparation of platinum oxide [86]. Common palladium metal catalysed reactions includes the decarbonylations of aldehydes and reductions of unsaturated aldehydes, aromatic compound and various nitrogen containing compounds. [87,88,89].
Palladium catalystare also used in small scale hydrogenations [88] and in the selective removal of acetylene from ethene streams [90]. The requirement for this latter process is for a catalyst (typical catalyst 0.03% on Al_2O_3) which will hydrogenate acetylene to ethene but not through to ethane [91].

1.5.2 Platinum based catalysts for the control of automotive pollutants

The past quarter century has witnessed a growing awareness of the hazards of atmospheric pollution and of the role that catalysis has to play in combating it.
Without doubt the largest single contributor to atmospheric pollution is the internal combustion engine, emitting carbon monoxide, nitric oxide and unburnt hydrocarbons [92]. The first is highly toxic while the last two have been held largely responsible for the photochemical smog that has afflicted number of major cities. Moves began in the United States in the early 1970 's to limit exhaust emissions, first simply by catalytic oxidation of CO and unburnt fuel. Subsequently, it became mandatory to reduce emissions of nitrogen oxides (Nox); this could only be done by causing them to react catalytically with CO in the absence of oxigen, which implied control over the air/fuel ratio, and the use of lead free petrol. Any excess of reductant was then oxidised in a second catalyst bed to which additional air was fed [92].
More recently it has been proved possible to combine these functions into a single " three way catalyst" by the use of catalytic monoliths [93]: a monolith is just a honeycomb structure made from a low area and thermally stable ceramic substance (cordierite for instance). It is well suited as a catalyst support for vehicle exhaust treatment as it is light in weight, quiet rugged and creates very little resistance to gas flow. Although non porous it is possible to fix the active metal directly by firstly applying a washcoat of high area alumina suitably stabilised at high temperature against sintering at high temperature, to which the metal can adhere [94].A three way catalyst can convert CO, hydrocarbons and Nox simultaneously into harmless product: CO_2, H_2O and N_2. The main reactions occuring at a three way catalytic converter are summarised on figure 1.15. This conversion was first observed in 1968 by Weaver and Lassen who found that a platinum catalyst was able to reduce simultaneously these pollutants close to the stoichiometric point [95].

Three- way catalytic converter

Noble metals (Pt, Pd, Rh) dispersed on porous (surface area ~ 100 m^2g^{-1}) metal -oxide ($Ce\text{-}ZrO_2$, Al_2O_3)

Main reactions:

- Reduction of Nox

$$2\ NO + 2\ CO \longrightarrow N_2 + 2\ CO_2$$
$$2\ NO + 2\ H_2 \longrightarrow N2 + 2\ H_2O$$

- Oxidation of CO and hydrocarbons: e.g.,

$$2\ CO + O_2 \longrightarrow 2\ CO_2$$
$$Hydrocarbons + O_2 \longrightarrow CO_2 + H_2O$$

Figure 1.15 Main reactions observed during the three way catalytic process. Reproduced from reference [96].

It was not until 1978 that a three way catalyst was actually implemented , when Volvo used it in conjunction with electronically controlled fuel injection [97]. The three way catalyst system has been developed as a result of the strict automobile emission regulations (especially for NOx) which came into force in the USA in 1981[98].
Initially, platinum and palladium were used but platinum /rhodium soon became the standard catalyst; Pt/Rh three way catalysts have been the most extensively studied to lower emissions from automobiles. Pt is used as the catalyst for hydrocarbons and CO oxidation while Rh is recognised as the best catalyst to promote the reduction of NO to N_2 [99]. The performance of the Pt/Rh TWC has been described in terms of a Pt/Rh synergism [100]. Three way catalysts need to withstand high temperature operations. Exposure of catalysts to oxidising conditions at high temperature results in activity decrease, particularly for NO reduction and CO oxidation which are generally attributed to Rh deactivation through transformation to the hard to reduce Rh-aluminate.

In the Pt/Rh bimetallic catalyst, Pt facilitates regeneration of the inerte Rh-aluminate species to active Rh metal particles in the exhaust cycling between net oxidising and reducing compositions through a H_2 spillover mechanism [101,102]. To obtain highly active catalyst, the preparation method was shown to be crucial: stepwise metal impregnation of the two noble metals on the alumina support was shown to be more effective than the simultaneous impregnation of the noble metals (physical mixture of Pt and Rh monometallic catalysts, same amount of noble metal) [102]. The synergystic enhancement of activity in the bimetallic catalyst can be rationalized by visualising the catalyst surface structure as a statistical mixture of Pt and Rh sites [102]. Formulations have reached a high level of sophistication. A very small amount of noble metal is used in the washcoat (1 wt % Pt , 99 wt % Al_2 O_3) and when Rhodium is used, it is added in even smaller quantity (1/5 Rh/Pt for example).Further development have lead to the use of base metal promoters such as cerium additives. A ceria containing three way catalytic converter is described on figure 1.16.

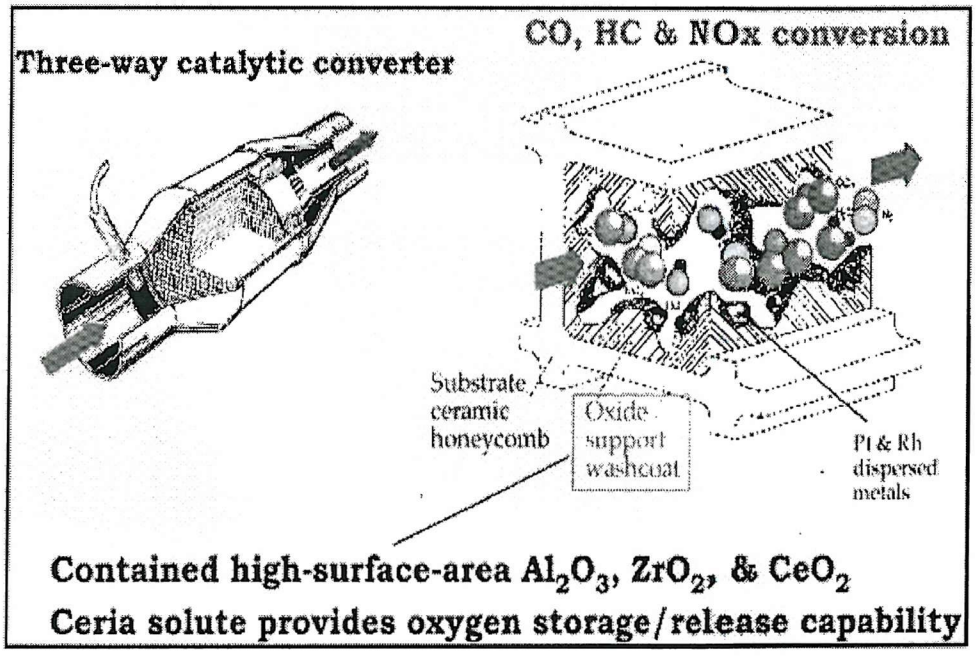

Figure 1.16 Ceria containing three way catalytic converter reproduced from reference [96].

Ceria can be incorporated into the TWC formulation to enhance CO and NOx performance: ceria improves indeed the stability of noble metals, promotes some

catalytic reactions, particularly the Nox reductions and allows the catalyst to work in oscillatory regime as a consequence of its oxigen storage capacity: the noble metals are continuously fed in oxygen species even when the ox/red ratio decreases in the gas phase [103, 104]. While significant advances in Pt/Rh TWC formulations have been accomplished, the use of Pd containing catalysts for 3 way emission control are currently of interests for overall noble metal cost reduction, lower Rh usage and potential durability improvements [105, 107].

Future technology in TWC relies on the development of more effective catalysts formulations to meet the more stringent emissions targets; the development and use of mesoporous Pt and Pt based alloys catalysts can be considered as an alternative to existing materials for future applications.

1.5.3 Application of mesoporous metals to heterogeneous catalysis and fuel cells development

As shown previously, noble metals especially platinum and palladium are extensively used in heterogeneous catalysis. Because of their exceptional activity, particularly for reactions involving hydrogen, their uses are very varied. In the catalytic processes reported, it is evident that adsorption on the surface and surface area of the different catalysts used are key factors for conversion or selectivity in the reactions investigated. The possibility of producing mesoporous platinum and palladium powders with inherently high surface areas is particularly attractive in the vast field of heterogeneous catalysis.

The development of fuel cell technology is linked to the development of effective electro-catalyst technology. Research over decades has shown that Pt or Pt containing catalysts are the best materials. The ability to produce high surface area mesoporous materials with ordered pore systems makes mesoporous platinum or platinum-based alloys a very attractive alternative to current porous platinum based materials used in fuel cell technology.

1.6 References

1. G Gottardi and E Galliv, *Natural zeolites*, (Springer, Berlin, 1985).
2. D E W Vaughan, Molecular Sieve Zeolites: A Historical Perspective, in *Comprehensive Supramolecular Chemistry,* Volume 7 Solid-state Supramolecular Chemistry: Two and Three-dimensional inorganic networks, chapter 13, (Elsvier Science, Oxford, 1996).
3. M E Davies and R F Lobo, *Chem. Mater.*, **4**, 756-768 (1992).
4. B A Lerner, *Chemistry and industry*, 1, 16-20 (1997).
5. P Behrens, *Adv. Mater.*, **5**, No 2, 127-132 (1993).
6. I Nettleship, *Key. Eng. Mater.*, **122**, 305-324 (1996).
7. C T Kresge, M E Leonowicz, W J Roth, J C Vartuli and J S Beck, *Nature*, **359**, 710-712 (1992).
8. J S Beck *et al. J. Am. Chem. Soc.*, **114**, 10834-10843 (1992).
9. F Schuth, *Ber. Bunsenges. Phys. Chem.*, **99**, 11, 1306-1315 (1995).
10. J C Vartuli, S S Shih, C T Kresge and J S Beck, *Studies in surface science and catalysis,* **117**, 13-22 (1998).
11. G S Attard, P N Barttlett, N R B Coleman, J M Elliott and J R Owen , *Science,* **278**, 838-840 (1997).
12. G S Attard, C G Goltner, J M Corker, S Henke and R H Templer, *Angew. Chem. Int. Ed. Engl.*, **36**, 1315-1317 (1997).
13. G S Attard, N R B Coleman and J M Elliott, *Studies in surface science and catalysis,* **117**, 89-94 (1998).
14. R G Laughlin, *The Aqueous Phase Behaviour of Surfactants,* (Academic Press, London, 1996).
15. M J Schick, *Non ionic surfactants: physical chemistry,* surfactant science series, vol. 23, (Marcel Dekker, New York, 1987).
16. P J Collings and M Hird, *Introduction to liquid crystals*, (Taylor and Francis, London, 1997).
17. D Zhao, Q Huo, J Feng, B F Chmelka and G D Stucky, *J. Am. Chem. Soc.*, **120**, 6024-6036 (1998).
18. D Zhao, J Feng, Q Huo, N Melosh, G H Fredrickson, B F Chmelka and G D Stucky, *Science,* **279**, 548-552 (1998).

19. N Coleman, PhD thesis, Department of Chemistry, University of Southampton (1999).
20. C E Fairhurst, M C Holmes and M S Leaver, *Langmuir,* **13**, 4964-4975 (1997).
21. D J Mitchell, G J T Tiddy, L Waring, T Bostock and M P Mc.Donald, *J. Chem. Soc. Faraday Trans. I,* **79**, 975-1000 (1983).
22. X Auvray, L Petipas, R Anthore, I. Rico and A. Lattes, *J. Phys. Chem.* **93**, 7458-7464 (1989).
23. G S Attard, J C Glyde and C G Göltner, *Nature*, **378**, 366-368 (1995).
24. D H Park, C Cheng, H He and J Klinowski, *J. Mater. Chem.*, **7,** No 1, 159-162 (1997).
25. Q Huo *et al.*, *Nature*, **368**, 317-321 (1994).
26. N Ulagappan and C N R Rao, *J. Chem. Soc. Chem. Commun.*, 2759-2760 (1996).
27. A Firouzi, A Atef, A G Oertli, G D Stucky and B F Chmelka, *J Am Chem Soc,* **119**, 3596-3610 (1997). Q Huo, D I Margolese and G D Stucky, *Chem Mater*, **8**, 1147-1160 (1996). J C Vartuli *et al.*, *Chem Mater*, **6**, 2317-2326 (1994). C A Fyfe and G Fu, *J Am Chem Soc*, **117**, 9709-9714 (1995), N K Raman, M T Anderson and C J Brinker, *Chem Mater*, **8**, 1682-1701 (1996).
28. E Jungerman, Cationic Surfactants, *Surfactant Science Series,* vol 4, 203-288 (Marcel Dekker, New York, 1970).
29. C Cheng Z Luan and J Klinowski, *Langmuir*, **11**, 2815-2819 (1995).
30. C G Göltner, S Henke, M C Weissenberger and M Antionietti, *Angew. Chem. Int. Ed.*, **37**, No. 5, 613-616 (1998).
31. C J Brinker and G W scherer, *Sol-gel Science : The Physics and Chemistry of Sol-gel Processing* (Academic Press, Boston, 1990).
32. S A Bagshaw, E Prouzet and T J Pinnavaia, *Science,* **269**, 1242-1244 (1995).
33. N N Greenwood and A Earnshaw, *Chemistry of the Elements*, First edition, p1331 (Pergamon Press, Oxford, 1985).
34. N Toshima and T Takahashi, *Bull. Chem. Soc. Japan*, **65**, 400-409 (1992), M V Seregina, L M Bronstein, O A Platonova, D M Chernyshov and P M Valetsky, *Chem. Mater.*, **9**, 923-931 (1997).
35. L D R Rampino and F F Nord, *J. Am. Chem. Soc.*, **63**, 2745-2749 (1941). T S Ahmadi, Z L Wang, A Henglein and M A El-Sayed, *Chem. Mater.*, **8,** 1161-1163 (1996).

36. Kirk-Othmer Encyclopedia of chemical technology, 3rd Edition, Vol 18, p254-270 (Wiley, New York, 1980).
37. Johnson Matthey, *Platinum 1998,* (Johnson Matthey, United Kingdom,1998).
38. R Long and R T Yang, *Catal. Lett.*, **52**, 91-96 (1998). U Junges, W Jacobs, I Voigt-Martin, B Krutzsch, F Schuth, *J. Chem. Soc. Chem Commun.*, 2283-2284 (1995).
39. A M Feltham and M Spiro, *Chem. Rev.*, **71**, No. 2, 177-193 (1971).
40. J. De Ment; *Rarer metals Chapter VII*, Temple Press Limited (1949).
41. Baker and CO; *Bibliography of patents on palladium as a catalyst*, Newark (1939).
42. S.Guerin, PhD thesis, Department of Chemistry, University of Southampton (1999)
43. US patent 1,934,838
44. C.F. Cullis; B.M. Willat; *J.of Catalysis*, **83**, 267 (1983)
45. H.A. Gasteiger; N. Markovic; P.N.Ross; E.J.Cairns; *Electochimica Acta*, **39**, 1825 (1994).
46. S. Murkerjee; S. Srinivasan; M.P. Soriaga; J. Mc Breen; *J.Electrochem.Soc.*; **142**, 1409 (1995).
47. Z.Hu; et al.; *J.of Catalysis*, **13**, 174 (1998).
48. M. Watanabe; M. Uchida; s.Motoo; *J.Electroanal.Chem*, **229**, 395 (1987).
49. M.P. Hogarth PhD thesis, Department of Chemistry, University of Newcastle upon Tyne (1995).
50. J.B. Goodenough; A. Hamnett; B.J. Kennedy; R. Manoharan; S.A. Weeks; *Electrochimica Acta* ,**35**, 199 (1990).
51. N.M. Poponova; N.A. Antonova; S.A. Sass; E.M. Moraz; V.A. Ushakoo; D.I. Kochubei; S.G. Degtyarev; *Kinetics and Catalysis*, 38,**5**, 685,(1997).
52. A. Sasahara; H. Tamura; K.Tanaka; *Catalysis Letters*, **28**, 161 (1994).
53. J C Hulteen and C R Martin, *J. Mater. Chem.*, **7**, 1075-1087 (1997).
54. H Masuda, K Nishio and N Baba, *Thin Solids Films,* **223**, 1-3 (1993).
55. S Purvvada, S Baral, G M Chow, S B Qadri and B R Ratna, *J. Am. Chem. Soc.*, **116**, 2135-2136 (1994).
56. G Hoogers, D thompsett, *Cattech*, 3, **2**, 106-124 (2000).

57. Johnson Matthey, *Platinum 1998*, p30 (Johnson Matthey, United Kingdom, (1998).
58. MP Hogart, GA Hards, *Platinum Metal Rev.*, 40,**4**, 150-159 (1996).
59. HA Gasteiger, N Markovic, PN Ross Jr, EJ Cairns, *J. Phys. Chem*, **98**, 617-625 (1994).
60. SJ Cooper, AG Gunner, G Hooger, D Thompsett, *New materials for fuel cell and battery systems II*, O Sarvadago and RR Roberger Eds (1997).
61. TR Ralph, GA Hards, D Thompsett, JM Gascogne, *1994 Fuel cell seminar Extended Abstracts*, p199 (1994).
62. PN Ross, K Kinoshita, AJ Scarpelino, P Stonehart, *J. Electranal.Interfacial Electrochem.*,**59**,177 (1975).
63. V Jalan, D Landsman, US Patent 4,186,110
64. D Landsman, F Luckzak, US Patent 4,316,944
65. H A Gasteiger, N Markovic, PN Ross Jr, EJ Cairns, *J.Phys.Chem.*, **98**,617 (1994).
66. H A Gasteiger, N Markovic, PN Ross Jr, J.Phys.Chem., **99**, 16757 (1995).
67. K A Friedrich, K P Geizers, U Linke, U Stimming, JStumper, J.Electroanal.Chem., **402**,123 (1996).
68. HF Oetjen, VM Schmidt, U Stimming, F Trila, J.Electrochem.Soc., **143**,3838 (1996).
69. M Iwase, S Kawatsu, *Proceedings of the Fist International Symposium on Proton Conducting Membrane Fuel Cells*, S Gottesfeld, G halpert, A Landgrebe (Eds), The Electrochemical Society, Pennington, NJ, Vol.95-23, p12.
70. M Watanabe, S Motoo, *J.Electroanal.chem.*, **60**,275 (1975).
71. H A Gasteiger, N Markovic, P N Ross Jr, *J.Phys.Chem.*, **97**, 12020-12029 (1993).
72. L W Niedrach, I B Weinstock, *Electrotech.Technol.*, **3**, 270 (1965).
73. P K Shen, A C C Tseung, *J.Electrochem. Soc.*, **141**,3082 (1994).
74. A S Arico, Z Poltarzewski, H Kim, A Morana, N Giordano, V Antonucci, *J. of Power Sources*, **55**, 159 (1995).
75. P K Shen, KY Chen, A C C Tseung, *J. Electochem. Soc.*, **142**, L85 (1995).
76. N Greenwood and A Earnshaw, *Chemistry of the Elements*, 1st Edition, p537-538 (Pergamon Press, Oxford, 1985).
77. Kirk-Othmer Encyclopedia of chemical technology, 3rd Edition, Vol 9, p494-509 (Wiley, New York, 1980).

78. G. C. Bond, *Catalysis by metals*, p. 1, Academic Press, London and New York, (1962).
79. G. C. Bond, *Catalysis by metals*, p. 4, Academic Press, London and New York (1962).
80. W Carruthers, *Some modern methods of organic synthesis*, 3rd Edition, Cambridge University Press, (1986).
81. P N Rylander, *Catalytic hydrogenation over platinum metals*, London Academic Press (1967).
82. H C Brown , C A Brown, *J. Am. Chem. Soc.*, **84**, 2827, (1962).
83. C Eaborn, B C Pant, E R A Peeling, S C Taylor, *J. Chem. Soc.* (C) 2823 (1969).
84. J. Tsuji, *Palladium Reagents and Catalysts, Innovations in organic synthesis*, p.1, John Wiley & Sons Ltd (1995).
85. V Ponec, T C Bond, *Catalysis by metals and alloys*, Elsevier, 38-41, p. 238-257, (1995).
86. D Starr and R M Hixon, *Catalytic hydrogenation over platinum metals*, Org. Syntheses, Coll. Vol. 2, 566 (1943).
87. J Tsuji, *Palladium Reagents and Catalysts*, Innovations in organic synthesis, p.528-545, John Wiley & Sons Ltd (1995).
88. Mulleron, Handbook of palladium catalysed organic reactions, Vol. 106, Academic Press (1997).
89. P N Rylander, *Catalytic hydrogenation over platinum metals*, Marcel Dekker, Inc, 283 (1965).
90. P N Rylander, *Catalytic hydrogenation in organic synthesis*, Academic Press, New York (1979).
91. M L Derrien, *Catalytic hydrogenation*, L. Ceveny (Ed.), Elsevier, Amsterdam, p. 613 (1986).
92. G C Bond , *Heterogeneous Catalysis: Principles and applications*, 2 nd Edition, Clarendon Press, Oxford (1987).
93. F R Hartley, *Chemistry of the platinum group metals: Recent developments, Studies in inorganic Chemistry 11*, p56 Elsevier (1991).
94. F R Hartley, *Chemistry of the platinum group metals: Recent developments, Studies in inorganic Chemistry 11*, p 49,50 Elsevier (1991).
95. J T Kunmer, *Prog.Energy Combust.Sci*, **6**, 177-190 (1980).

96. J T Woestman, E M Logothetis, *Industrial Physicist*, p 20 (1995).

97. I S Al-Mutaz, Y S Al-Seghayer, A S F Al-Koryshy, *The Arabian Journal for Science and Engineering*, 22, **1B**, 43-49 (1997).

98. K Wark, C F Warner, *Air Pollution: its Origin and Control*, 2 nd Edition, Harper and Row (1981).

99. KC Taylor, *The catalytic chemistry of Nitrogen Oxides*, R Klimish , J G Latson Eds, Plenum (1975).

100. Z Hu, *J.Chem.Soc.Chem.Commun.* 879 (1996).

101. Z Hu et al., *Journal of Catalysis*, **174**, 13-21(1998).

102. Se H. Oh, JE Carpenter, *Journal of Catalysis*, **98**, 178-190 (1986).

103. S Tagliaferri, R A Koppel, A Baiker, *Catalysis and Automotive Pollutants Control IV, Studies in Surface Science and Catalysis*, **116** , 61, (1998).

104. T Chafik, O Dulaurent, JL Gass, D Bianchi, *Journal of Catalysis*, **179**, 503-514 (1998).

105. Williamson et al.; *Strategies for future emission systems, Chapter 3:Automotive catalyst strategies for future emission systems*, p 27-41, ACS (1992).

106. R Van Yperen, D Lindmer, L Mussman, E S Lox, T Kreuzer, *Catalysis and Automotive Pollutants Control IV, Studies in Surface Science and Catalysis*, **116**, 51-60 (1998).

107. RW Mc Cabe, RK Usmen, 11 th International Congress on Catalysis 40 th Anniversary, *Studies in Surface Science and Catalysis*, 101, 355-368, JW Hightower, WN Delgass, E Iglesia, AT Bell Eds (1996).

Chapter 2

The preparation of mesoporous platinum

2.1 Background and objectives

Extending the range of mesoporous materials beyond inorganic oxides has been little studied. Some exceptions to this include the preparation of mesoporous CdS, CdS_2 [1] and Pt [2-7] from lyotropic liquid crystal phases. A new family of metal germanium sulphide mesostructured materials prepared by a non-aqueous surfactant templated assembly of cluster precursors has also been reported [8]. Mesoporous metals are of particular interest because they offer a whole new range of materials that have potential applications as catalysts, battery materials and sensors. In 1997 Attard et al reported that mesoporous platinum powders could be prepared by the chemical reduction of hexachloroplatinic acid (HCPA) in the aqueous domains of $C_{16}EO_8$ + H_2O mixtures [2]. Subsequently it was shown that these same mixtures could be used to electrodeposit platinum films that had an ordered mesoporous structure [3-6]. Following this work, a detailed study of the chemical synthesis and characterisation of mesoporous platinum from $C_{16}EO_8$ and $C_{12}EO_8$ was reported recently [7].

The subject of the work described in this chapter is an in depth study of the chemical synthesis, characterisation and properties of mesoporous platinum prepared from Brij surfactant systems. The objectives of the work are described below:

1. To characterise the liquid crystal phase behaviour of polyoxyethylene surfactant (Brij 56, Brij 76 and Brij 78) + HCPA + H_2O mixtures. This was important to optimise the conditions for the preparation of mesoporous platinum and also to gain some insight into the way in which platinic acid interacts with the surfactant.

2. To investigate methods of preparing mesoporous platinum from cheap surfactants and assess how easy it would be to scale up the processes. For any future work on the application of mesoporous platinum it will be important to be able to produce a high quality material in gram quantities.

3. To show that it was possible to prepare micellar cubic (I_1) and cubic (V_1) mesoporous platinum in addition to H_1 platinum. V_1 platinum was of particular interest because of the total 3D interconnectivity of the structure resulting in a more accessible surface than the 2D pore structure of H_1 platinum.

4. To characterise the mesoporous platinum in terms of structure on a micron and nanometer scale, surface area, regularity of the structure and crystal structure.

5. To compare the surface area and nanostructure of mesoporous platinum over commercially available, high surface area, materials such as platinum black.

2.2 Experimental

The experimental work was divided into four sections. The first of these was the determination of the phase behaviour of ethylene oxide based surfactants in platinic acid solutions. Following on from this the best method for preparing H_I mesoporous platinum was determined and H_I materials from different Brij surfactants prepared. I_I and V_I mesoporous platinum were also investigated and finally the materials were fully characterised.

2.2.1 Phase behaviour of ethylene oxide based surfactants in platinic acid solutions

Phase diagrams were constructed using polarised light microscopy as outlined in appendix 1. Ethylene oxide surfactants (Brij 56, 76 and 78) and HCPA ($H_2PtCl_6.xH_2O$, Pt 38-40%, purity = 99.9%) were used as supplied by Aldrich. For the purpose of these studies, the stoichiometry of the HCPA was assumed to be $H_2PtCl_6{\cdot}6H_2O$. Deionised water was used to make up the phases. In calculating the weight percentage of surfactant, with respect to the total water content, the water content of the HCPA acid was included. Mixtures containing HCPA, surfactant and deionised water were made up by adding the surfactant to a solution of HCPA. The phase diagrams that were prepared are summarised below and the exact compositions studied are given in appendix 2A.

- Phase diagram of Brij 76 + H_2O + HCPA where the concentration of HCPA was fixed with respect to the water content at 1.95M.

- Phase diagram of Brij 56 + H_2O + HCPA where the concentration of HCPA was fixed with respect to the water content at 1.95M.

- Phase diagram of Brij 78 + H_2O + HCPA where the concentration of HCPA was fixed with respect to the water content at 1.95 M.

- Phase diagrams of Brij 76+ H_2O + HCPA where the concentration of Brij 76 was fixed with respect to the water content at 40 wt % and 75 wt %.

2.2.2 *Investigating methods of preparing H_I platinum*

A number of different methods were used to prepare mesoporous platinum from surfactant + HCPA + H_2O mixtures. Essentially they all involved a reducing agent which reduced the Pt(IV) salt to platinum metal. The same chemicals were used as described in the phase diagram studies.

2.2.2.1 Steel reduction

The reduction of HCPA acid by a less noble metal than platinum was the basis for this method. By using a sheet of steel it was possible to maximise the exposed surface area of metal while still making it possible to remove unreacted metal after reduction was complete.

Steel sheets, as supplied by RS, were cleaned with acetone. An H_I phase containing HCPA (1.5 g), H_2O (1.42 g) and Brij 76 (4.5 g) was prepared. A thin layer of the phase (ca. 1-2 mm thick) was then spread onto a glazed ceramic tile and a thin sheet of steel placed over the top and weighted down. Reduction occurred at the interface between the phase and steel sheet (figure 1.1).

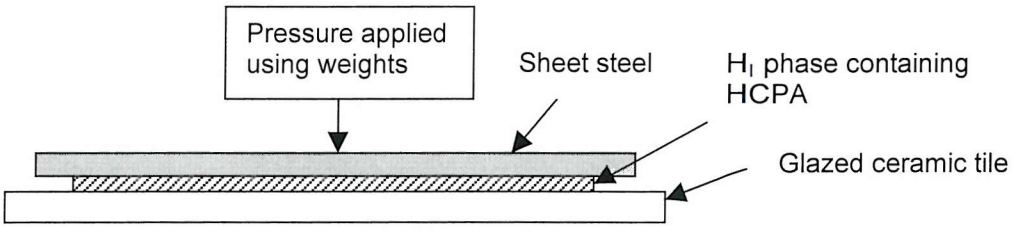

Figure 1.1 Reduction of HCPA, by steel, in the presence of an hexagonal phase.

Reduction of the HCPA to platinum, by the oxidation of iron, was complete within three hours at room temperature. The thick black mixture produced was scraped off the ceramic tile and steel sheet.

Removal of the template was carried out by stirring in acetone (200 ml) for 3 hours and decanting off the solution leaving platinum. This was followed by four washes in water (200 ml), 6M HCl (200 ml), water (200 ml) and acetone (200 ml). Separation of the platinum powder from the solutions was achieved by using a centrifuge. The purpose of the HCl wash was to remove any iron that may have been present in the mixture. Extraction of the template was also enhanced by the use of an ultrasound bath. Mixtures were placed in an ultrasound bath for 5 minutes before stirring for 3 hours. After the final extraction the black platinum powder was dried at 90°C for 24 hours. The yield of platinum after extraction and drying was ~500 mg and this equated to ~60 wt% of the platinum that was put into the reaction. This reaction was repeated four times to make 2g of mesoporous platinum.

2.2.2.2 Other metals reduction

To investigate the reduction of HCPA by a metal that is less noble than platinum, cadmium and zinc sheets were investigated. Cd and Zn as supplied by Aldrich were cleaned with acetone. The same experimental procedure was employed.

2.2.2.3 Hydrazine reduction

An H_I phase containing HCPA (1.5 g), water (1.42 g) and Brij 76 (4.5 g) was prepared, as described previously, by adding the surfactant to an aqueous solution of platinic acid. To this phase was added another H_I phase containing hydrazine hydrate (0.24 g, 55 wt% N_2H_4), water (0.72 g) and Brij 76 (1.00 g). The two phases were mixed using a glass rod for ca.1 minute before leaving to stand for 2 hours at room temperature. The orange HCPA rapidly reduced to platinum metal and the mixture turned black. The platinum was extracted by washing in water (200ml) followed by acetone (200ml).

2.2.2.4 Sodium citrate reduction

An H_I phase of Brij 76 (4.5g) containing platinic acid (1.5 g in 1.42 g water) was prepared and coated on the inside of a round bottom flask. An H_I phase of sodium citrate (citric acid trisodium salt dihydrate 50 % solution in water) with Brij 76 was prepared and mixed with the H1 platinic acid (2.78 g sodium citrate in 3.95 g Brij 76). The mixture was heated for 6 hours at 50 °C under mechanical stirring.

2.2.2.5 Preparation of I_I and V_I Platinum

Preparations of I_I and V_I materials were carried out by using the steel sheet reduction method outlined above. The only difference was the decrease of the amount of surfactant (Brij 78) used for the I_I material in the initial mixture or the elevated temperature of reduction used for the V_I material from Brij 76. Compositions were based on the phase diagrams reported. To prepare the micellar cubic I_I material from Brij 78, 1.5g HCPA was dissolved in 1.42g deioinised water and mixed with 1.5g Brij 78. Steel reduction was carried out at 20°C and 40 °C. The preparation of the cubic V_I material from Brij 76 was similar to the one reported for the H_I material (same composition) but the steel reduction was carried out at 85 °C.

2.2.2.6 Characterisation

Characterisation of the mesoporous platinum materials was carried out by nitrogen adsorption/desorption experiments to determine surface area and pore size, x-ray diffraction to deduce pore to pore distance and mesophase structure. TEM and SEM were used to determine structure on a nanometer and micron level respectively.

2.3 Results and discussion

2.3.1 The phase behaviour of ethylene oxide based surfactants in platinic acid solutions

2.3.1.1 Changes in phase behaviour for a fixed concentration of HCPA

The phase transition data obtained for the ternary mixture Brij 76 + HCPA + H_2O are shown schematically in figure 2.1a. The HCPA concentration was fixed at 1.95 M for all the compositions. As explained in the description of phase determination (appendix 1) the boundaries were drawn based on visual observations of the phases down the polarised light microscope. Consequently, the precise locations of the boundaries are only qualitative and this is reflected in the broad lines used to represent the boundaries. In any case, the transition between two homogeneous phases is likely to occur via a small biphasic domain.

Figure 2.1b shows the phase diagram for the binary Brij 76 + H_2O system. Comparison of the binary system with the HCPA containing system revealed that HCPA had a considerable effect on the phase behaviour of Brij 76. From the two diagrams it was observed that HCPA resulted in a dramatic increase in the temperature ranges over which the H_I phase was stable. Viscous I_1 and V_1 phases were also noted in the presence of HCPA. When viewed under a polarised light microscope these phases appeared isotropic, although a few small areas of weak birefringence were noticed, suggesting that residual H_I phase might have been present. On the phase diagram, the existence of a homogeneous I_1 phase was inferred from these observations although not observed directly. However, the biphasic H_I + I_1 domain, which was observed directly, made a large contribution to the phase diagram. In summary:

- The H_I phase, which was only stable up to 60°C in the binary phase diagram, was stable to temperatures greater than 95°C in the presence of HCPA and was present over a much wider range of compositions resulting in a much smaller lamellar region than the binary system.

- The V_1 phase not reported for the binary system was observed in the presence of HCPA (narrow region, viscous and isotropic between H_I and lamellar phases).

- The I_1 phase, which was not observed in the binary system over the composition and temperatures studied, was found in the presence of HCPA. In addition, a large biphasic $H_I + I_1$ region made up a considerable area of the phase diagram. This biphasic region was characterised on the polarized light microscope by a viscous isotropic phase (I_1) containing small regions of birefringence (H_I).

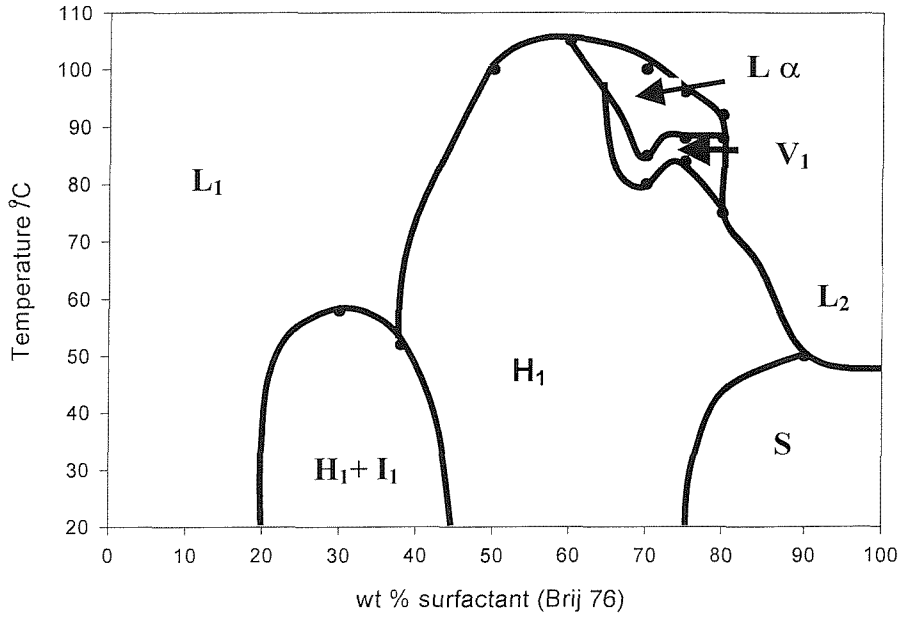

Figure 2.1a Phase diagram of Brij 76 + water + HCPA where the concentration of HCPA is kept fixed at 1.95 M

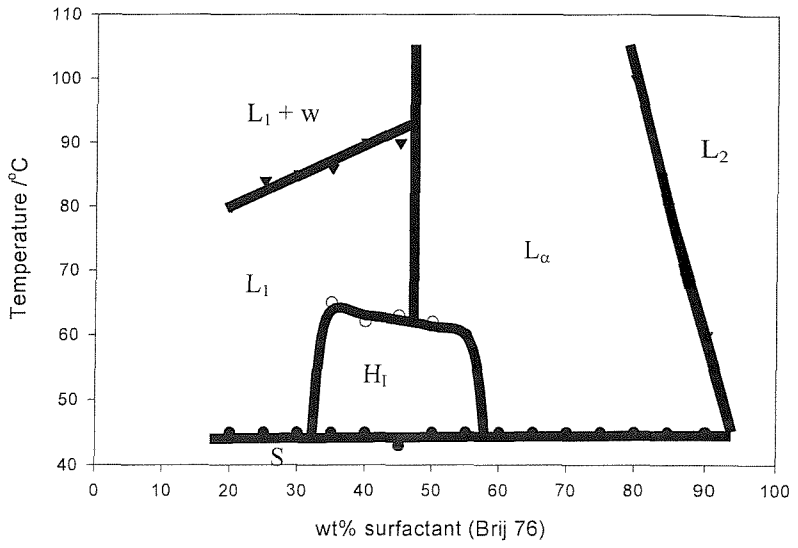

Figure 2.1b Phase diagram of the binary system Brij 76 + water reproduced from reference [7].

The effects of HCPA on the phase boundaries of Brij 76 in water were not just limited to this one surfactant. The phase transition data for the ternary mixture Brij 56 + HCPA + water are shown schematically in figure 2.2 a. The HCPA concentration was fixed at 1.95 M for all the compositions. Fig 2.2 b shows the phase diagram for the binary Brij 56 + water system reproduced from reference [7]. HCPA added to the Brij 56 lyotropic system resulted in significant stabilisation of the H_I phase.

In summary:

. The H_I phase, which was only stable up to 65 °C in the binary mixture, was stable to temperatures greater than 80 °C in the presence of HCPA.

. The V_1 phase was stable up to 70 °C in the presence of HCPA (65 °C in the binary system) but appeared at much higher surfactant concentration in the system (shift in phase boundary).

. The lamellar region in the presence of HCPA was also considerably smaller than the one observed for the binary mixture.

The overall effect of platinic acid in the phase behaviour of Brij 56 was again to stabilise the higher curvature structure such as H_I phase. Consequently the low curvature L_α phase which made up a considerable part of the binary phase diagram, occurred over a reduced range of temperatures and compositions in the HCPA system.

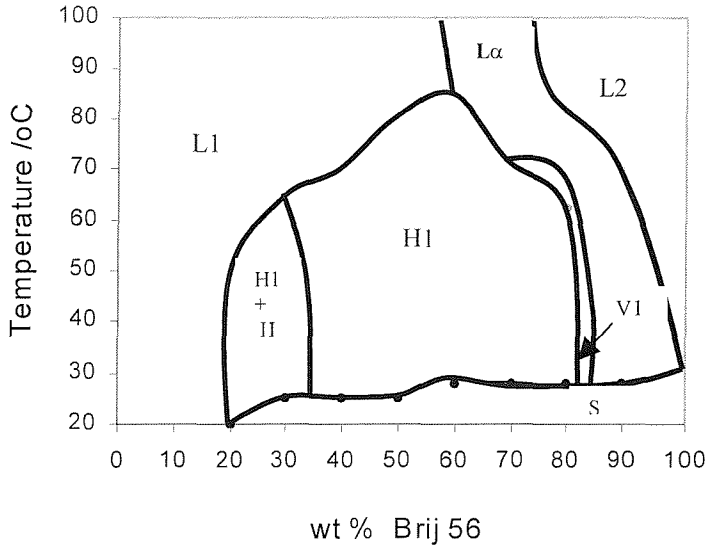

Figure 2.2a. Phase diagram of Brij 56 + water + HCPA where the concentration of HCPA in water is kept constant at 1.95 M.

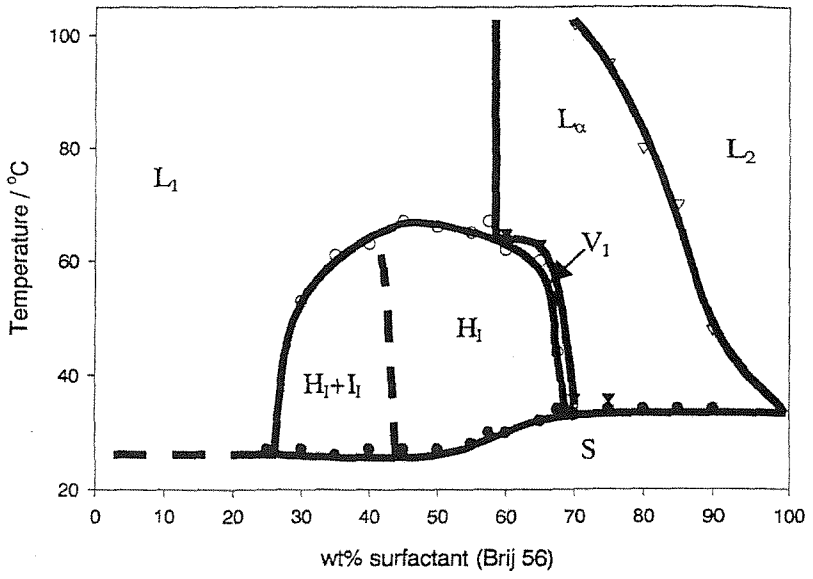

Figure 2.2b Phase diagram of the binary system Brij 56 + water redrawn from reference [7].

Changes in phase behaviour for a fixed concentration of HCPA were also studied for another surfactant from the Brij series; namely Brij 78. The HCPA concentration was again fixed at 1.95 M for all the compositions. Fig 2.3 a shows the phase diagram obtained for the ternary Brij 78+ HCPA + water. Comparison with the phase transition data for the binary Brij 78 + water system (fig 2.3 b) revealed the influence of HCPA on the phase behaviour of Brij 78.

In summary:

. A viscous I_1 phase was also observed in the presence of HCPA though this region is smaller than the one observed for the binary mixture.

• A larger H_I phase than the H_I phase observed in the binary system was identified in the presence of HCPA and consequently the L_2 phase is much smaller and observed only at temperatures higher than 75 °C.

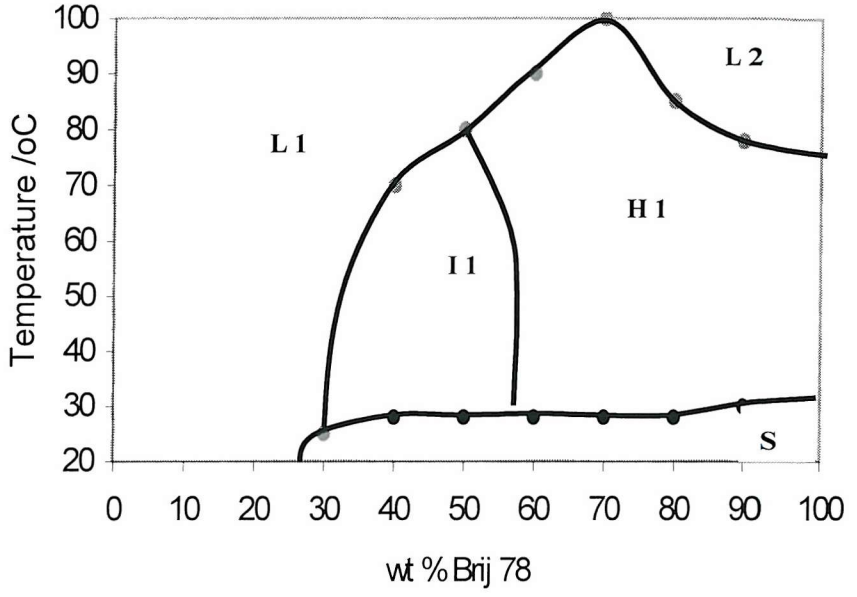

Figure 2.3a Phase diagram of Brij 78 + water + HCPA where the concentration of HCPA is kept constant at 1.95M.

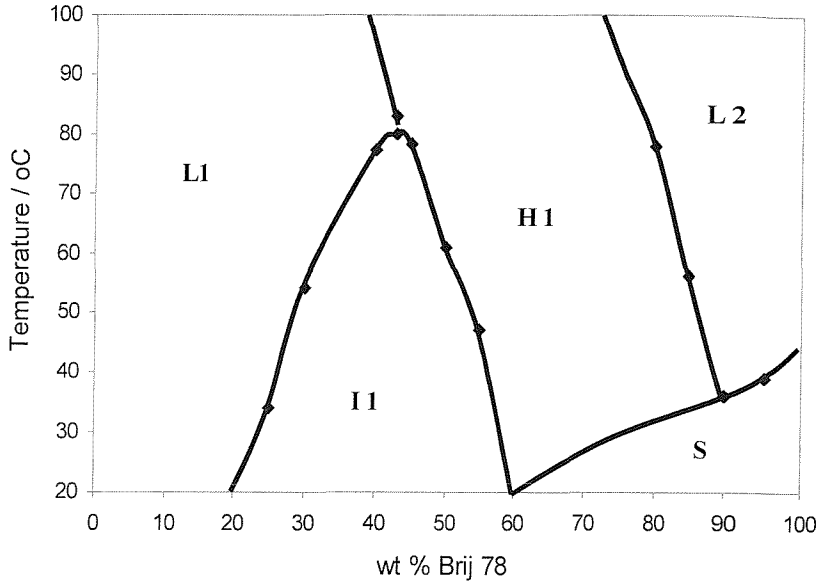

Figure 2.3b Phase diagram of the binary system Brij 78 + water.

2.3.1.2 Changes in phase behaviour for changing HCPA concentration

Changes in phase behaviour for a fixed concentration of HCPA were observed for the ethylene oxide surfactants studied. To complete the study, investigations were carried out as to how the phase boundaries changed as a function of HCPA concentration for two ternary mixtures made from Brij 76 in which the surfactant weight fraction was kept fixed at 40 % and 75 %. It must be noted that the HCPA was not included in the calculation of these weight fractions. The results are presented in figure 2.4 and 2.5. From these plots it was observed that when the amount of HCPA in the mixtures increased the transition temperatures of the phases increased. At high HCPA mole fractions the H_I and I_I phases dominated over the V_I and L_α.

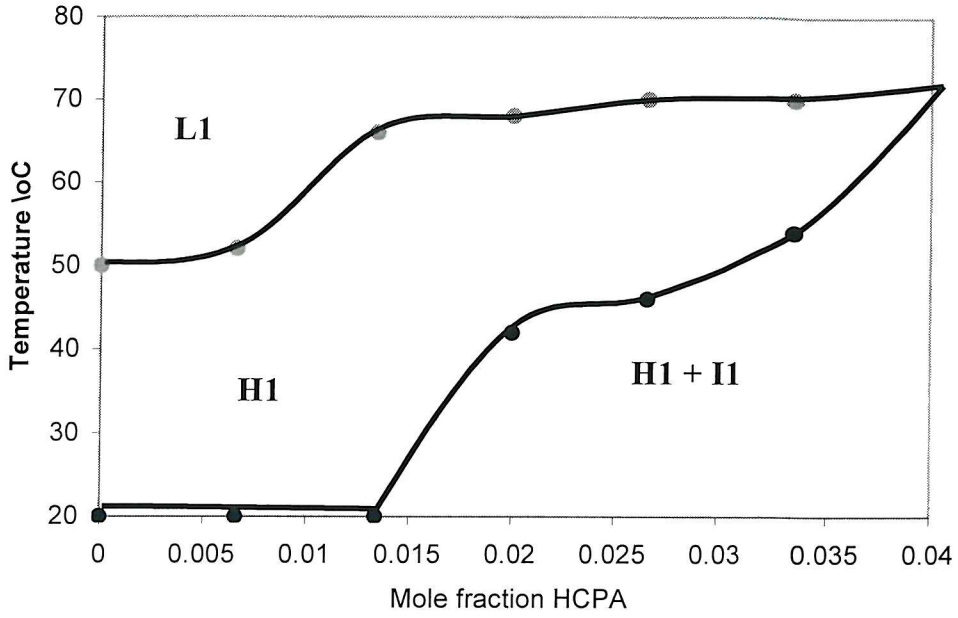

Figure 2.4 Phase diagram of Brij 76 + water + HCPA where the concentration of HCPA is varied and the Brij 76 content is fixed at 40 wt %. Both the HCPA and the surfactant contents are given with respect to the water content only.

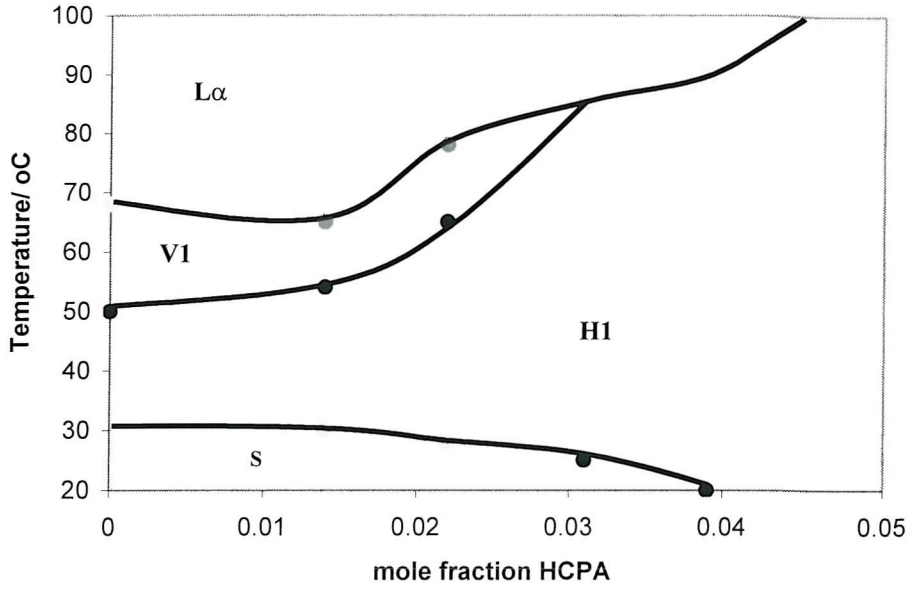

Figure 2.5 Phase diagram of Brij 76 + water + HCPA where the concentration of HCPA is varied and the Brij 76 content is kept fixed at 75 wt %. Both the HCPA and the surfactant contents are given with respect to the water content only.

2.3.1.3 Discussion of the phase behaviour of Brij surfactants + H_2O + HCPA mixtures

It was clear from the phase diagram studies that HCPA had a significant effect on the phase behaviour of Brij surfactants. While there have been a number of studies on the effects of ionic species on micellar solutions [9], the effects on liquid crystal phase behaviour have not been well documented. Generally the effect of adding an ionic species to a micellar solution of a POE surfactant is to induce phase separation. The phase separation is characterised by regions rich in surfactant and regions rich in water. A similar phase separation is found upon heating binary mixtures of surfactant and water. This behaviour has been interpreted in terms of a lowering of the activity of water. In other words, at a local level, the mixtures behave as if there was less water present. At the extreme, the surfactant can be sufficiently concentrated that the phase separated mixture contains small domains of H_I or L_α phases surrounded by water.

The observations that have been made for micellar solutions appear not to apply for the ternary mixtures that have been studied in this chapter. In fact, HCPA appeared to have the opposite effect from dehydrating the system. The more HCPA present in the mixture the greater the dominance of the higher curvature structures. One possible explanation for these observations is an interaction between the ethylene oxide headgroups of the surfactant and the HCPA. This results in an increase in the steric cross section of the headgroups, while at the same time increasing the electrostatic repulsion between headgroups. The net effect is to stabilise aggregates and phases with a high positive mean curvature (figure 2.6).

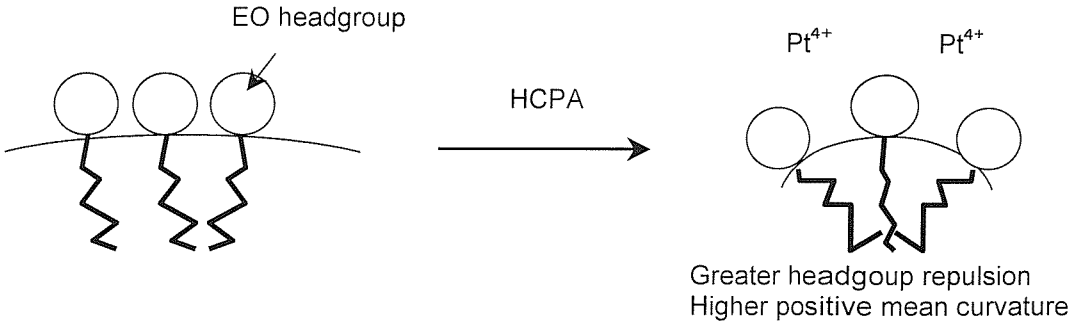

Figure 2.6 The interaction between HCPA and EO headgroups in the formation of high curvature aggregates.

Similar effects have also been reported and discussed while studying the effect of HCPA on the binary $C_{12}EO_8$ (or $C_{16}EO_8$) + water mixtures where the net effect was to stabilise aggregates and phases with a high positive mean curvature [7]. Clearly, this has important implications for the choice of formulations to be used in preparing mesoporous materials from liquid crystal phases. The phase diagrams, characterised above, were used as guides, in finding compositions, for the synthesis of mesoporous platinum.

2.3.2 The physical properties and structure of mesoporous platinum prepared from the H_I phase of Brij 76

The following describes the results that were obtained from the various analytical methods used to determine the nanostructure, chemical composition and porosity of the prepared H_I platinum materials. Commercially available platinum black was used as a reference material to compare with the properties of mesoporous H_I platinum.

2.3.2.1 General visual appearance

All the H_I platinum materials that were prepared were very dark grey/black powders. The appearance was slightly different from platinum black, which was pitch black in colour. In addition, a similar mass of platinum black to H_I platinum appeared to take up considerably more volume.

2.3.2.2 TEM

Transmission electron microscopy was useful in determining the morphology of the pore structure. For the material produced by zinc reduction of platinic acid in the H_I phase a dendritic platinum was produced which consisted of a disordered arrangement of elongated platinum crystals (figure 2.7a). The cadmium reduction produced a porous material which was not ordered (figure 2.7b). Both the hydrazine hydrate and steel reduction methods produced materials that were considerably more ordered than the one prepared by zinc or cadmium reductions (figure 2.7 c and d respectively). For the materials prepared from steel reduction, the H_I structure was clearly visible on the smaller platinum particles but only at the edges of the larger platinum particles (figure 2.7d). Transmission of the electron beam through the larger particles was poor because platinum absorbs or back-scatters the majority of the electrons in the beam. Particles ranged from 50-500 nm in size and tended to be elongated along the axis parallel to the cylindrical tubes of the H_I structure. The repeat distance between the pores was measured from the micrographs as ca. 6.0 nm.

The sodium citrate reduction method produced a platinum with a more ordered structure to that of the cadmium reduction method but less ordered than that of the iron reduction methods (figure 2.7e). In the TEM less than ~10 % of the sample was observed to have

an ordered H_I structure compared to the steel reduction case where greater than ~80 % of the sample was ordered. For comparison, the TEM of platinum black showed that this material was very finely divided crystallites of platinum (figure 2.7f). Typically the crystals were 2-10 nm in size and joined to other crystals to form larger structures.

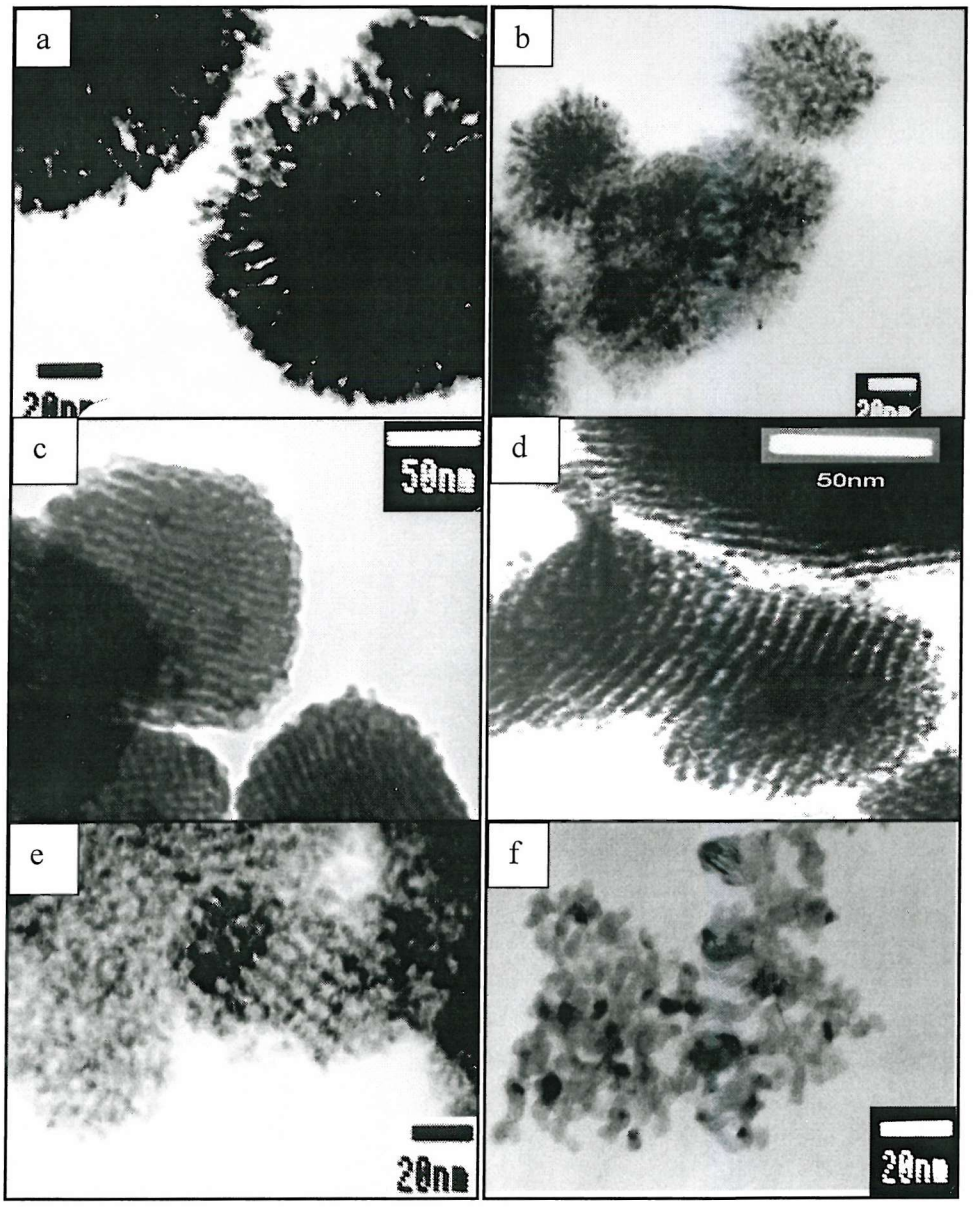

Figure 2.7.TEM micrographs of a) H_I Pt prepared by Zn reduction b) H_I Pt by Cd reduction c) H_I Pt by hydrazine hydrate reduction d) H_I Pt by steel reduction e) H_I Pt by sodium citrate reduction and f) Pt black as supplied by Aldrich.
Scale bars are given for each micrograph.

Of the different reduction methods investigated, reduction using steel appeared to be the most successful method to produce an ordered mesoporous Platinum. Using the steel reduction method at 40 °C, several compositions (wt % surfactant) were investigated and the materials characterised. Figure 2.8 and 2.9 show the TEM micrographs obtained for the various catalysts prepared when varying the amount of Brij 76 in the initial mixture.

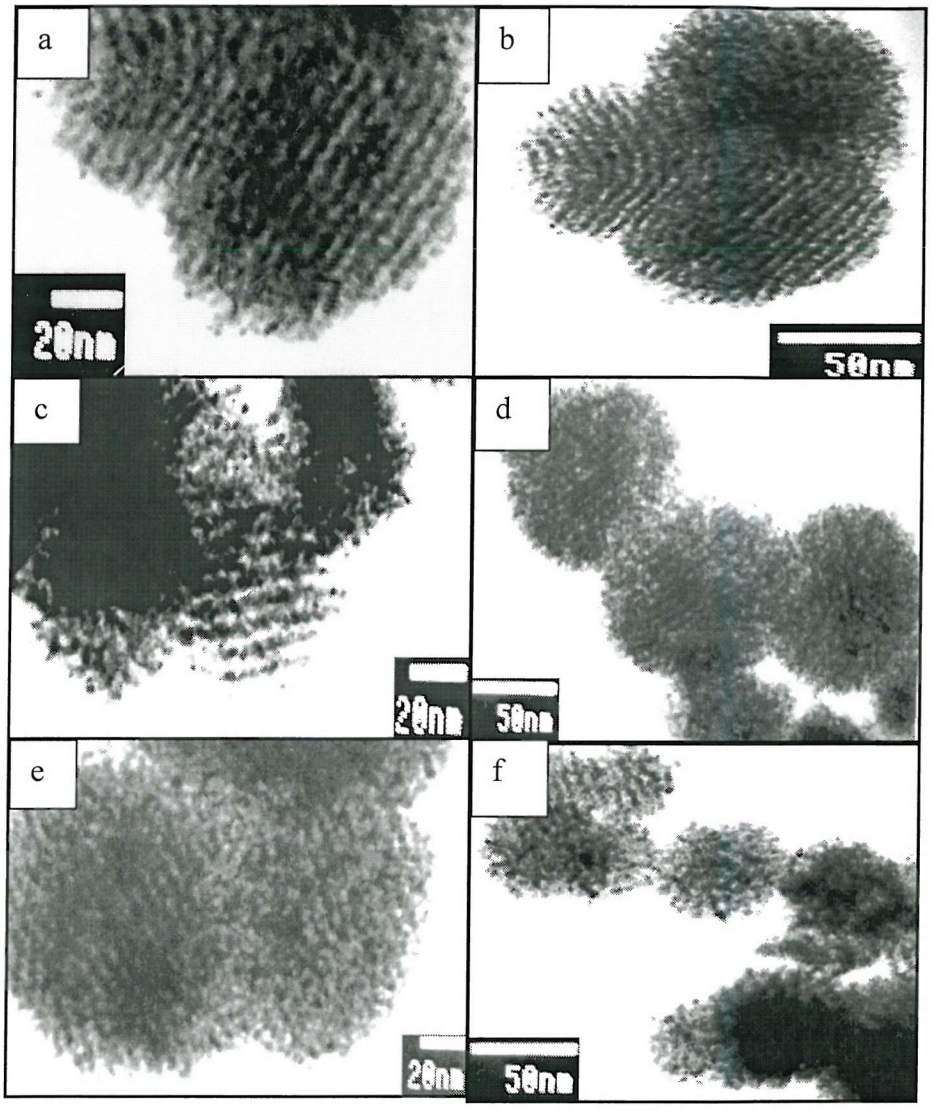

Figure 2.8. TEM micrographs of H1 Platinum prepared while varying the amount of surfactant in the templating mixture: a,b)50 wt %; c,d)60wt %; e,f) 70 wt % Brij 76.

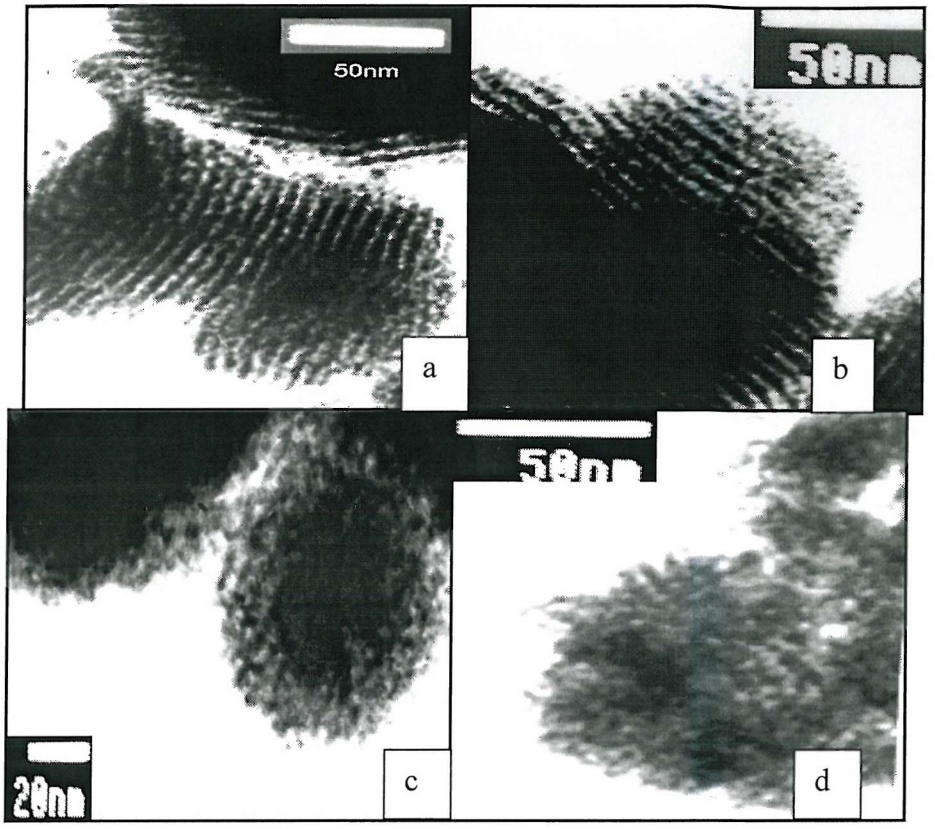

Figure 2.9. TEM micrographs of H_I Platinum prepared while varying the amount of surfactant in the templating mixture: a,b) 75 wt %; c,d) 80 wt % Brij 76.

These results demonstrate that ordered mesoporous platinum can be obtained from a precursor mixture with a range of composition. Nevertheless, it is important to note that only a small amount of material is characterised by microscopy and the ordered particles analysed are usually mixed with more disordered ones. Therefore, the higher surface area obtained for 75 wt % surfactant can be explained by a larger number of particles with high regularity of structure as seen from TEM studies.

The TEM micrographs analysis of the various H_I materials prepared while varying the amount of Brij 76 in the templating mixture are summarised in table 1.

Wt % Brij 76	**Pore diameter (nm +/- 1 nm)**	**Wall thickness (nm +/-1 nm)**
50	3	5
60	3	5
70	3	2.5
75	3	3.5
80	3	2.5

Table 1. Pore size and wall thickness of various H_I Platinum samples prepared while varying the amount of surfactant in the templating mixture.

2.3.2.3 SEM and EDAX

SEM pictures of the H_1 platinum prepared by the steel reduction method (Figure 2.11) were compared with those obtained for platinum black (as supplied by Aldrich, Figure2.12). At low magnification (X1000), no major difference in the structure was observed.

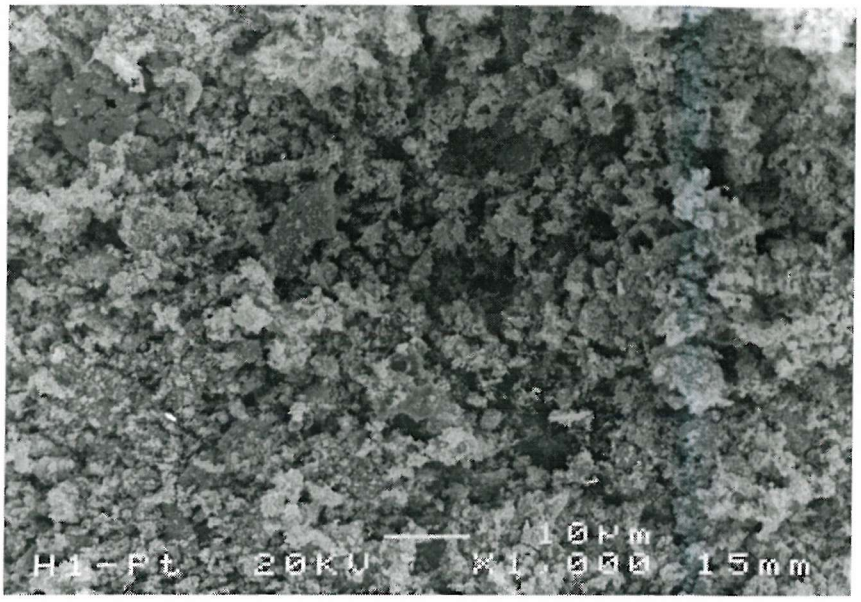

Figure 2.11 SEM images of H1 Platinum particles prepared by the steel reduction method (scale bar =10 μm).

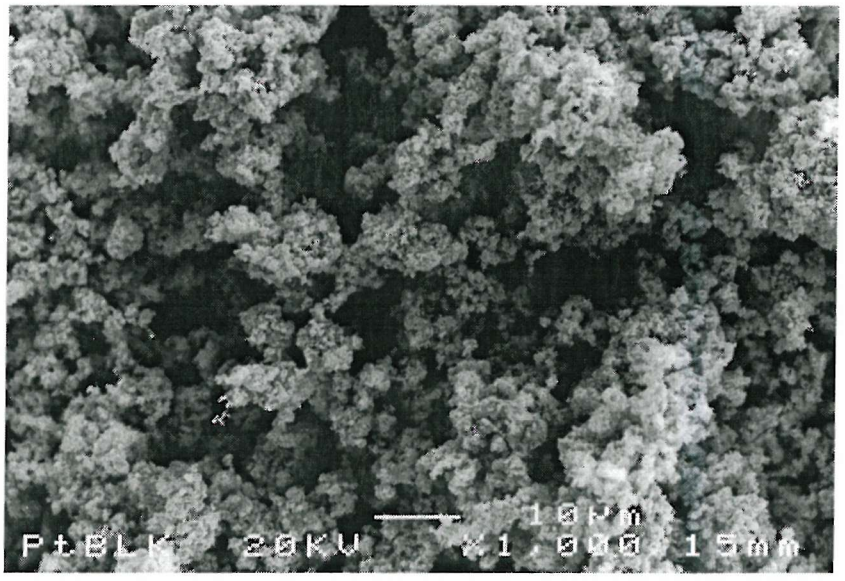

Figure 2.12 SEM image of Platinum black (scale bar=10 μm).

At higher magnification (X 10000), the SEM of the platinum black showed rough irregular particles which contrast with bigger regular particles observed for the H_I material.

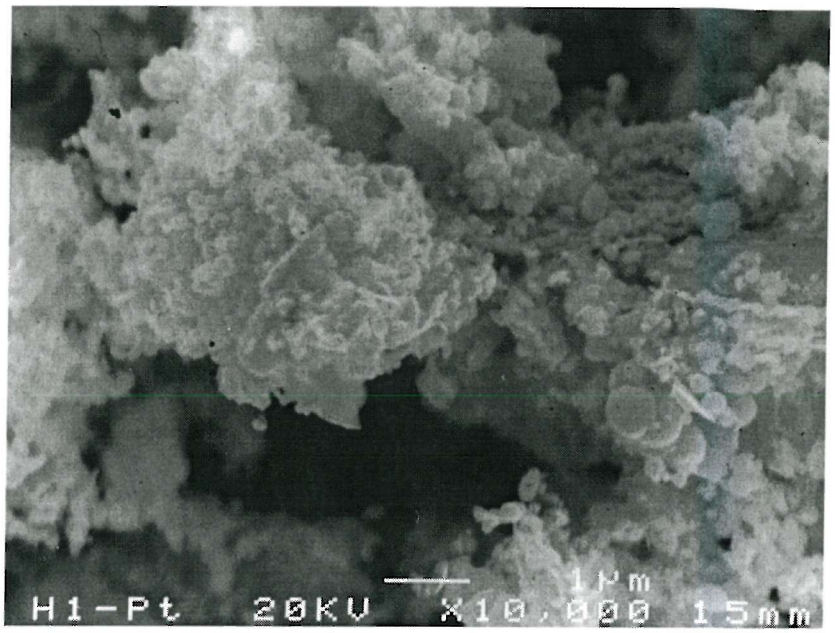

Figure 2.13 SEM image of H_I Platinum prepared by steel reduction (scale bar 1μm).

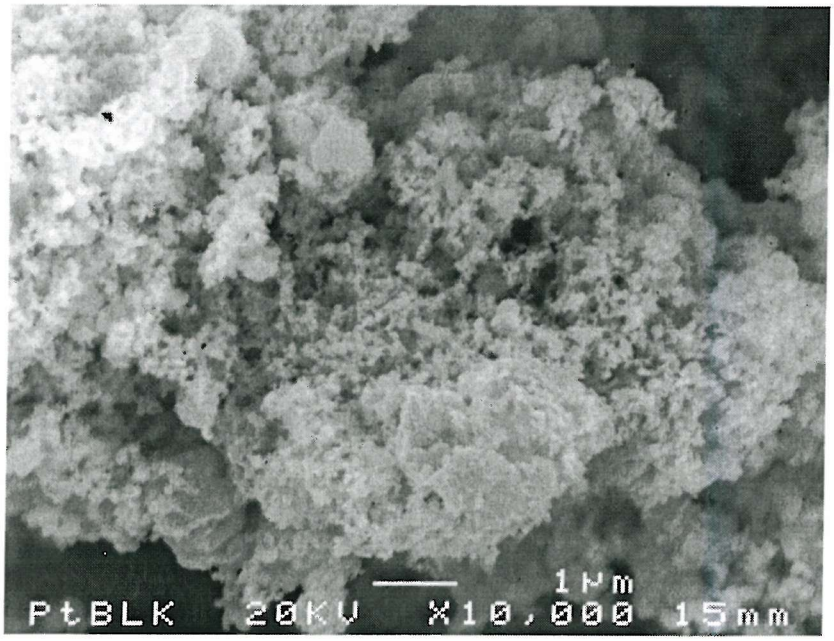

Figure 2.14 SEM image of Platinum black (scale bar 1μm).

X-ray microanalysis revealed that the H_i Platinum prepared by the steel reduction method contained small amount of iron impurities (figure 2.15). This showed that not all the iron is removed in the extraction process. For comparison, EDAX was also carried out on Platinum black and this showed no major impurities (figure 2.16).

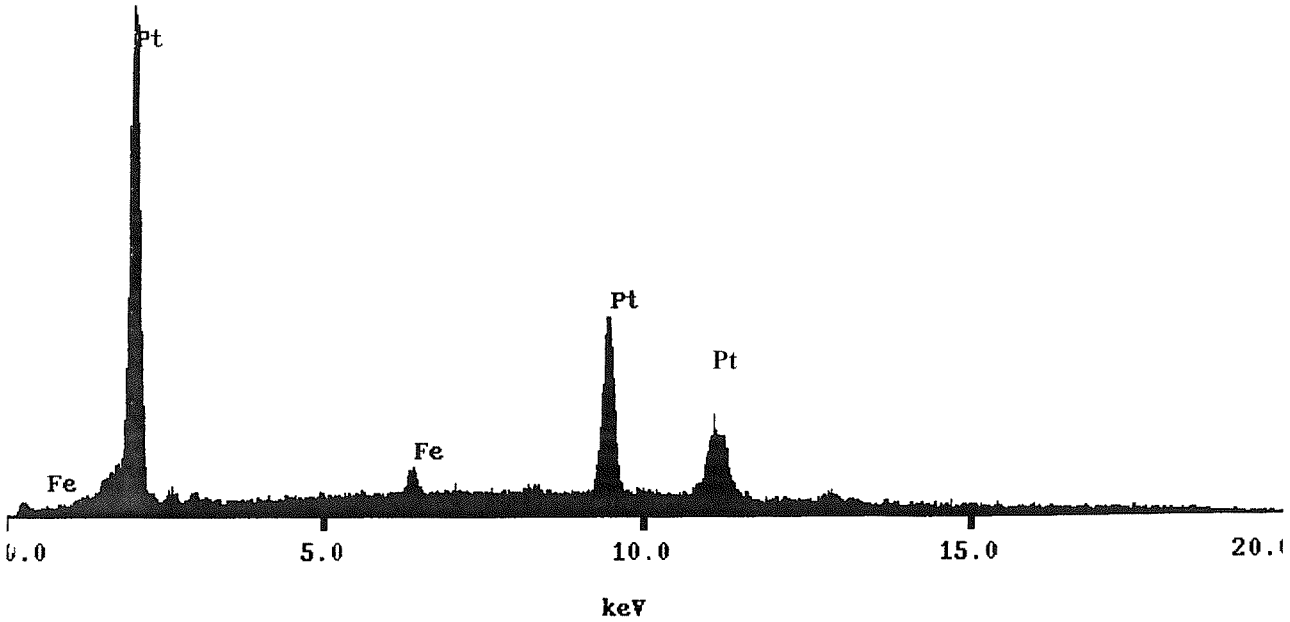

Figure 2.15 EDAX spectra for H1 Pt prepared by the steel reduction method.

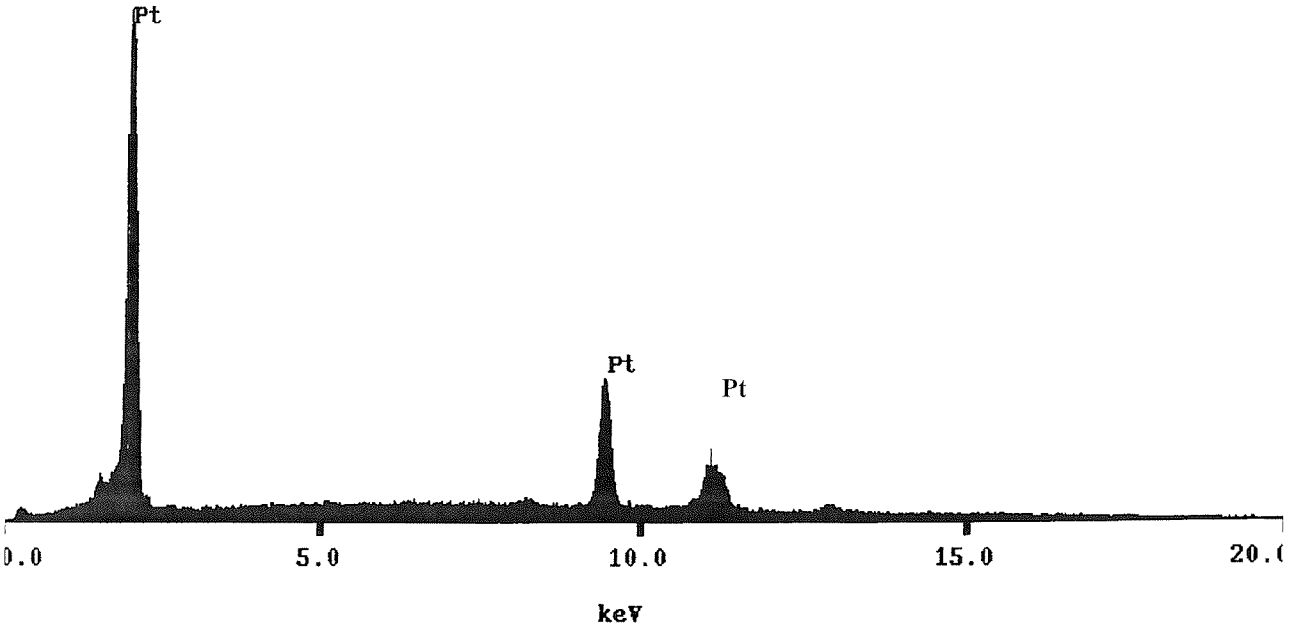

Figure 2.16 EDAX spectra for Pt black as supplied by Aldrich.

2.3.2.4 Small angle XRD

Small angle XRD was used to determine the repeat distance between pores and the order of the phase. For the H1 Platinum described in this chapter, only one peak was observed in the diffraction patterns. This corresponded to the 100 reflection. The X-ray diffractogram in figure 2.17 for H_I Pt (surface area 33 m^2g^{-1}) shows only one diffraction peak with a lattice parameter of 6nm which was in good agreement with the TEM results.

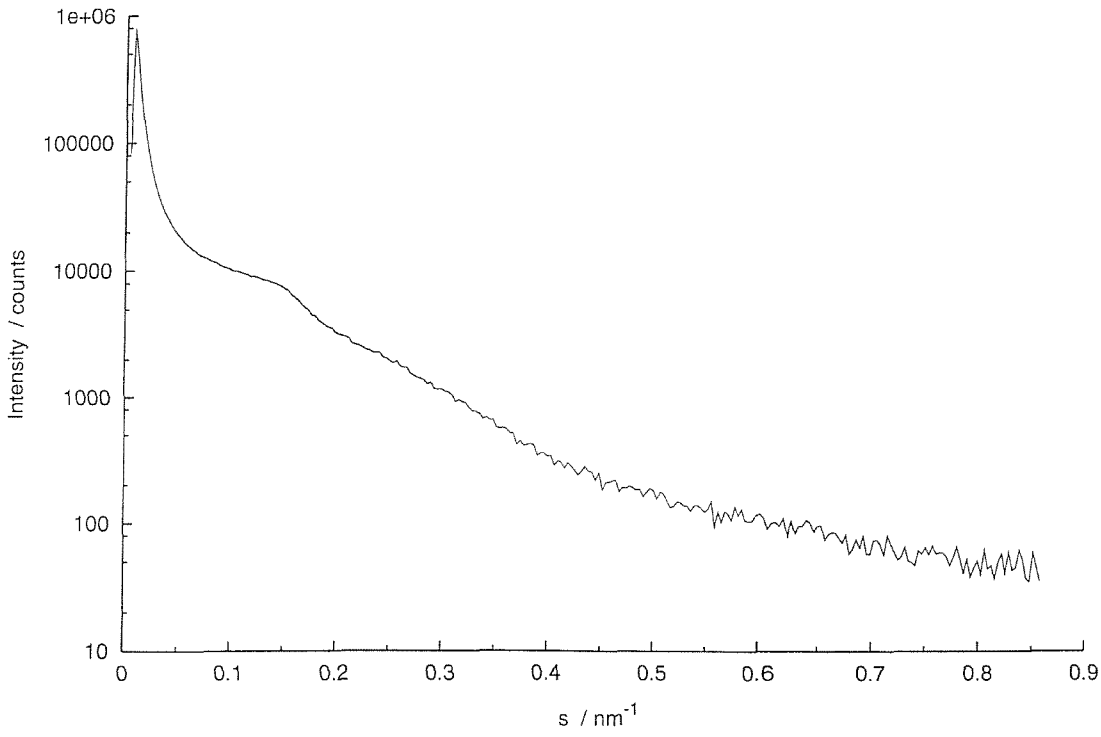

Figure 2.17 Small angle XRD pattern for H_I Pt prepared by steel reduction (surface area =33 m^2g^{-1}).

2.3.2.5 Wide angle XRD

In order to clarify our studies of the diffraction patterns and assess the broadness of the peaks observed (peak widths at half height) XRD results were plotted as intensity of the diffractions against 2 θ (diffraction angle), these eased the study of the reflections for comparison with database and Platinum black.

The wide angle XRD of mesoporous platinum, prepared by the steel reduction method, was recorded and compared with the one obtained for Platinum black (Figure 2.18).
The wide angle XRD of mesoporous Platinum confirmed the fcc crystal structure of the platinum (Figure 2.19).

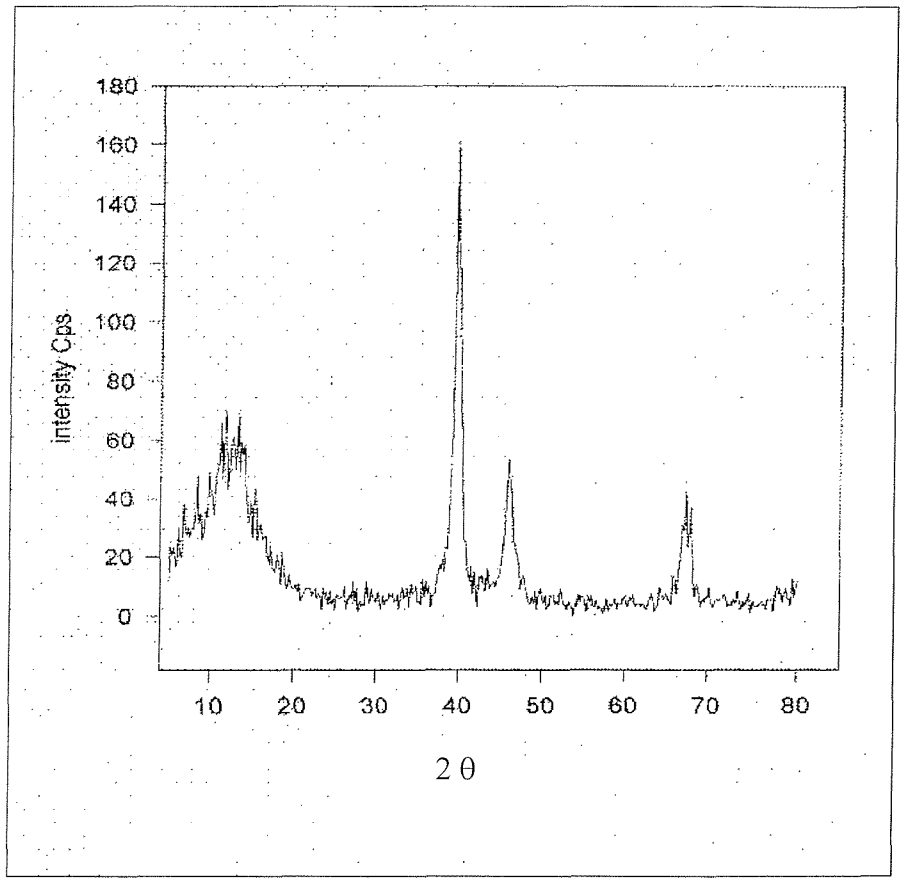

Figure 2.18 Wide angle powder XRD for Platinum black

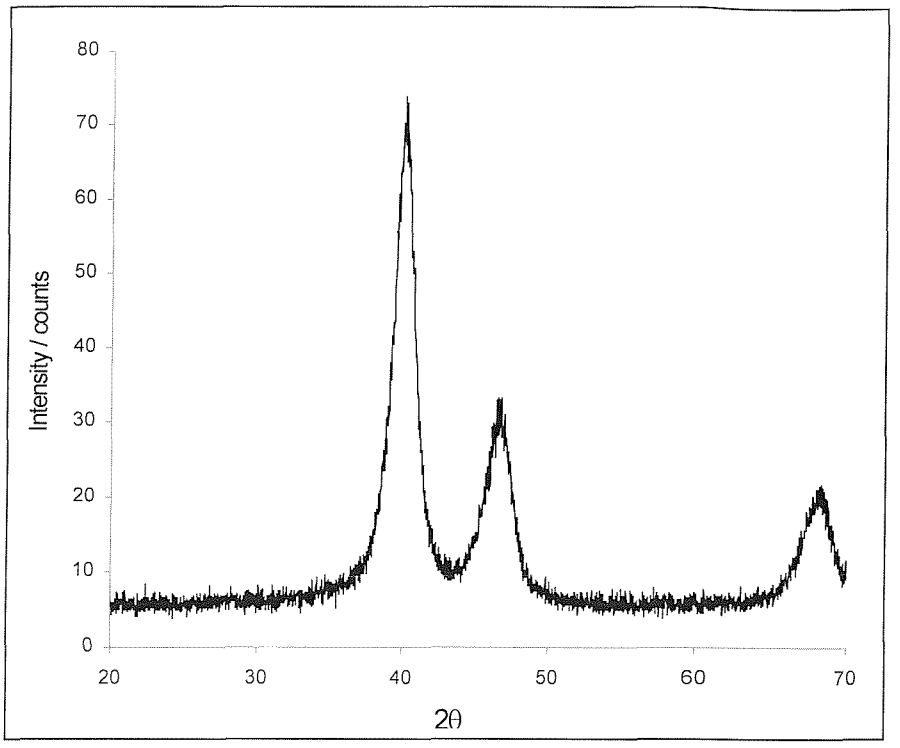

Figure 2.19 Wide angle powder XRD for H_I platinum prepared by the steel reduction of HCPA

Peaks (hkl)	ICDS platinum		Platinum black			H_I platinum		
	2θ /degrees	Relative Intensity	2θ /degrees	Relative Intensity	Peak width /degrees	2θ /degrees	Relative Intensity	Peak width /degrees
111	39.763	100	39.9	160	0.9	40.1	100	1.7
200	46.243	53	46.3	55	1.1	46.6	45	2.1
220	67.454	31	67.9	42	1.4	68.1	28	2.4
311	81.286	33	-	-	-	-	-	-
222	85.712	12	-	-	-	-	-	-

Table 2.1 XRD data for H_I platinum and platinum black compared to the ICSD values for crystalline fcc platinum. Note that the 311 and 222 diffraction data were not recorded for platinum black and H_I platinum.

For both mesoporous platinum and platinum black the diffraction peaks were broad. Generally, broadness of diffraction peaks is associated with a powder containing small crystallites and this is consistent with a mesoporous material with a polycrystalline wall structure. The breadth of a diffraction peak is related to the thickness of a crystal by the Sherrer equation:

$$t = \frac{0.9\lambda}{\sqrt{B_M{}^2 - B_S{}^2}Cos\theta}$$

where t is the crystallite thickness, λ the x-ray wavelength, θ the Bragg angle (half the measured diffraction angle) and B_M and B_S are the width, in radians, of the diffraction peaks of the sample and a standard at half height. For the value of B_S the half height width for the first reflection of a KCl sample was used. This gave the instrumental broadening of the peaks, which could be subtracted from the broadening due to crystallite size. For H_I platinum, the thickness of the crystallites, as calculated from the width of the (111) peak, was calculated as 5nm. For platinum black the crystallite size was almost double that for H_I platinum (table 2.2).

Reflections for Fm3m (hkl)	Platinum black			H_I platinum		
	θ /degrees	B_M /radians	Crystallite size (t) / nm	θ /degrees	B_M /radians	Crystallite size (t) /nm
111	20.0	0.016	9	20.1	0.030	5
200	23.2	0.019	8	23.3	0.037	4
220	34.0	0.024	7	34.1	0.042	4

Table 2.2 Crystallite size for high surface area platinum materials, λ=0.15406 nm, B_S = 0.0016 radians.

2.3.2.6 BET Nitrogen adsorption studies

Nitrogen adsorption studies were carried out on the mesoporous Platinum prepared from Brij 76 to study the surface area and the type of isotherms associated for different H_I Platinum.

Figure 2.20 shows the isotherms obtained for different mesoporous materials prepared using different reducing agents. For the H_I platinum prepared by the steel reduction method, there was a distinct inflection in the isotherm, which was characteristic of a mesoporous material. Mesoporous Platinum prepared by hydrazine hydrate reduction method resulted in an isotherm characteristic of a material with only a small amount of mesoporosity. At the extreme, the sodium citrate reduction method leads to Platinum with virtually no porosity of any form.

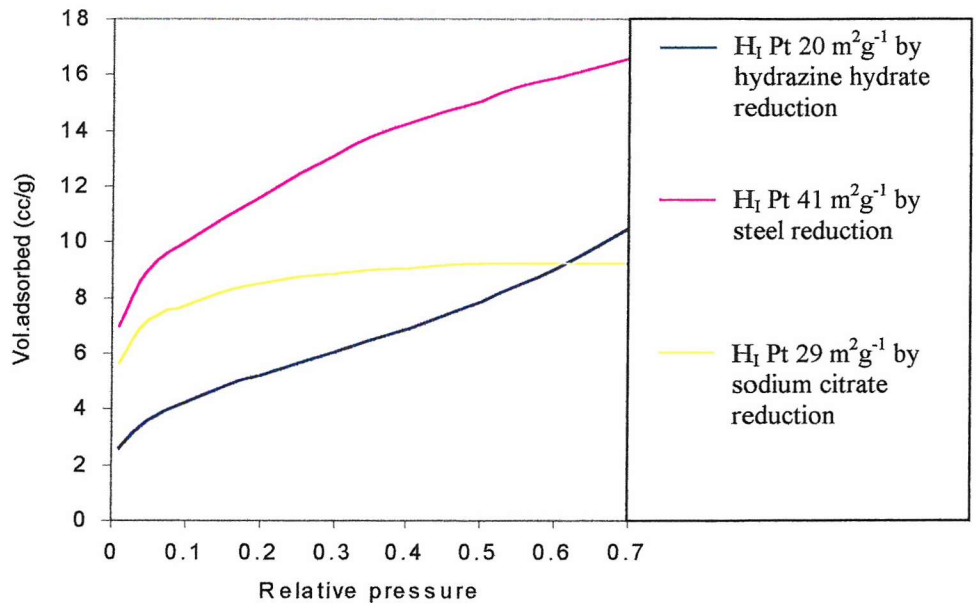

Figure 2.20 Nitrogen adsorption isotherms for different Platinum samples prepared using different reducing agents.

Figure 2.21 shows the isotherms for different Platinum prepared using different metals as reducing agents. The distinct inflection observed for the mesoporous Platinum prepared by steel reduction is not observed for the materials prepared using others metals such as cadmium and zinc. Cadmium reduction leads to a material with only a small degree of mesoporosity whereas virtually no porosity of any form was observed for the material prepared by Zn reduction.

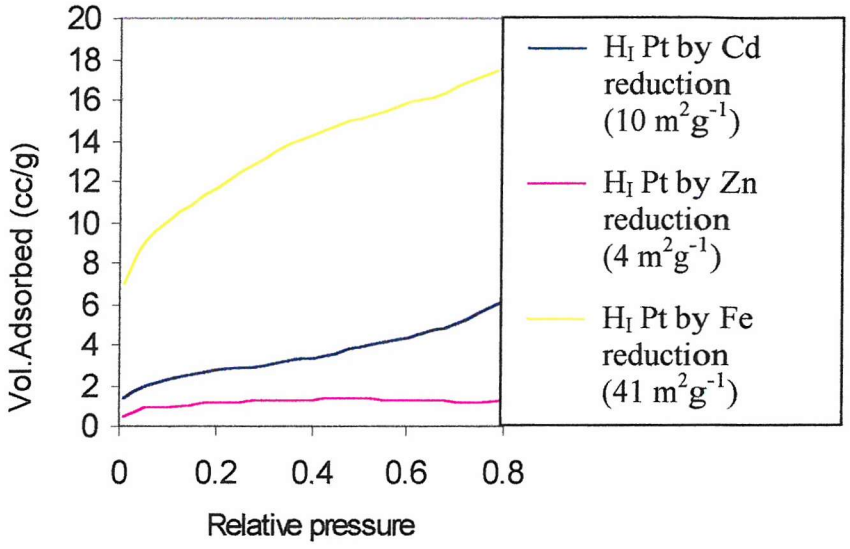

Figure 2.21 Nitrogen adsorption isotherm for different Platinum prepared using different metals as reducing agents

The phase diagram of Brij 76 + HCPA + water has been reported and exhibits large H_I region from ~45 to 85 wt% surfactant in water. Five different compositions 50, 60, 70, 75 and 80 wt % Brij 76 were investigated to prepare the mesoporous materials.

Figure 2.22 shows the isotherms for the mesoporous platinum prepared by steel reduction at 40 °C while varying the amount of surfactant in the H_I initial mixture according to these compositions.

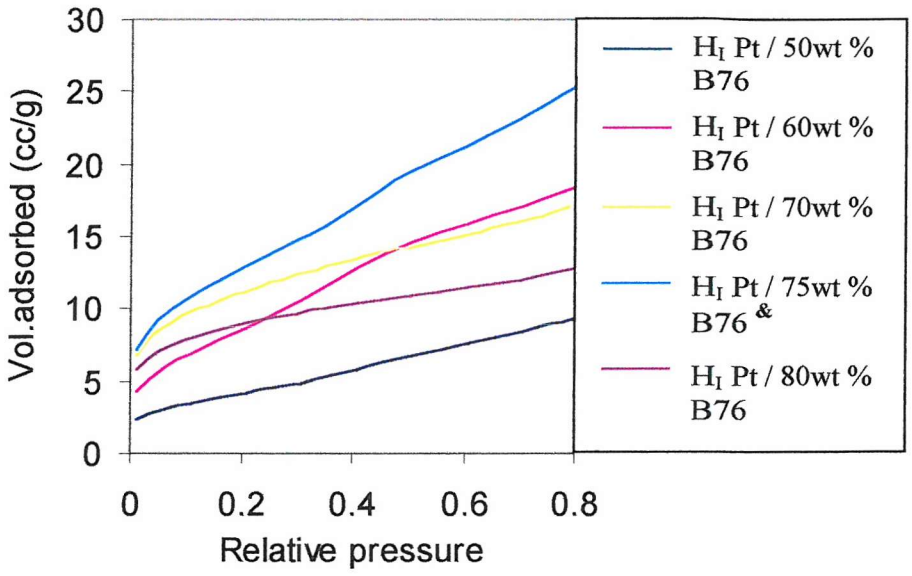

Figure 2.22 Nitrogen adsorption isotherms for different Platinum samples prepared at 40°C while varying the amount of Brij 76 in the templating mixture. & Highest surface area obtained 46 m^2g^{-1}; Average of 3 measurements each made from a different batch from the same material.

A distinct inflection in the isotherms is observed for the Platinum samples prepared from 60 and 75 wt% Brij 76 in the initial mixture but is less pronounced for the three other materials. As the concentration of surfactant in the initial mixture increases, the surface area of the material increases with a maximum for 75 wt% Brij 76. Then, as the concentration increases even more (80 wt%), the surface area decreases. The results obtained emphasise the importance of the stability of the H_I phase during the process. Optimum results were obtained when using 75 wt% Brij 76.

Hence although the precursor mixture may be in an H_I domain, if the amount of surfactant is lower or higher than 75 wt % in the initial mixture, the surface area of the material obtained is smaller.

Pore size distributions, calculated from the adsorption branches of the isotherms as explained in Appendix 1 (Dollimore and Heal pore size distibution), revealed a very broad distribution of pores characteristic of disordered mesoporous materials as shown in figure 2.23 and 2.24. In general, a maximum in the distribution was observed at around 3 to 3.5 nm for all the materials prepared from different Brij 76 compositions in the initial templating mixture which is in good agreement with the TEM studies. The peak observed at less than 2 nm in the pore size distribution of the material prepared from 70 wt % composition in the templating mixture can be explained as artefacts from the pore size calculation. Irregularity of the structure of the material obtained for this composition explained the strange distribution observed and confirmed the TEM studies.

From these results, it was interesting to note that the pore size distribution for the H_I material prepared from 75 wt % Brij 76 , which had the highest surface area, had the broadest distribution in all the compositions investigated. The high surface area measured is the result of a non homogeneous distribution of pores which confirmed the TEM studies.

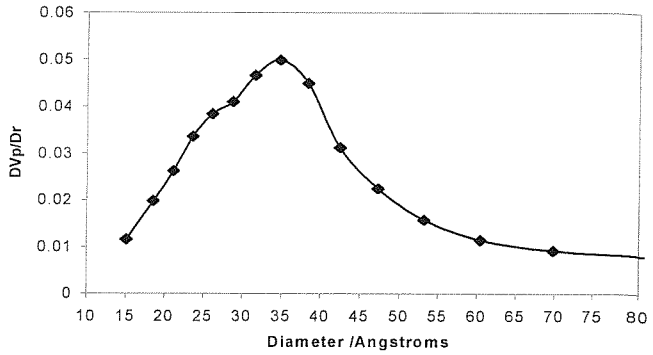

a) 50 wt % Brij 76

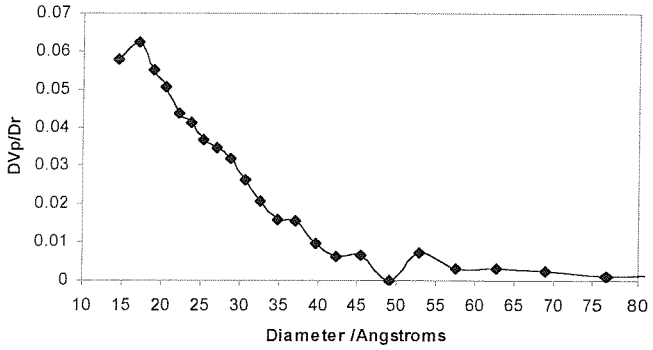

b) 60 wt % Brij 76

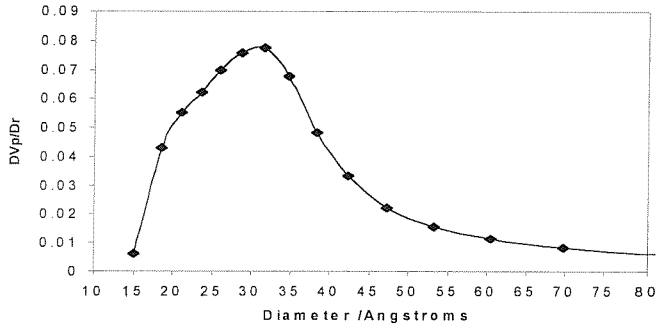

c) 70 wt% Brij 76

Figure 2.23 Pore size distribution for H_I platinum prepared by the steel reduction of HCPA while varying the amount of Brij 76 in the templating mixture. Pore size distributions were calculated from the adsorption branch of the isotherms.

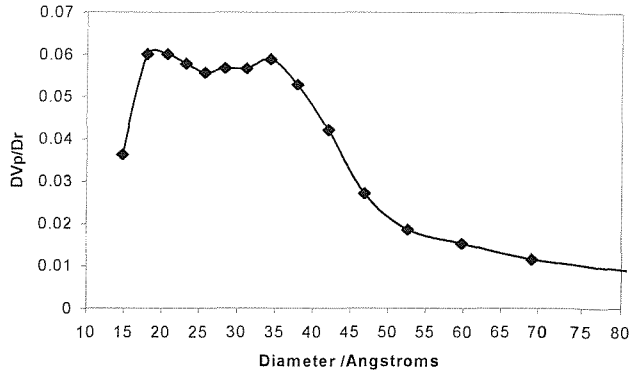

e) 75 wt % surfactant

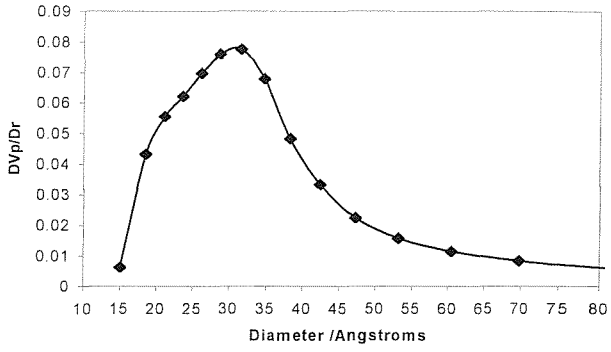

f) 80 wt % surfactant

Figure 2.24 Pore size distribution for H_I platinum prepared by the steel reduction of HCPA while varying the amount of Brij 76 in the templating mixture. Pore size distributions were calculated from the adsorption branch of the isotherms.

Studying various compositions at a given temperature was crucial to optimise the surface area of the materials prepared. With the most favorable composition obtained, investigating the influence of the reduction temperature was then the next step to optimise the results.

Figure 2.25 shows the isotherm and surface area measured for different platinum prepared by steel reduction at different temperatures while fixing the amount of surfactant at 75 wt% in the initial mixture. These reductions were carried out on the templating mixtures just after their preparations. Another set of experiments investigate the stability of the templating mixtures by leaving the prepared samples at room temperature for 2 days before carrying out the steel reduction at the same temperature (40 °C).An inflection in the isotherm is observed for the platinum prepared at 40 °C. Leaving the templating mixture at room temperature for 2 days before doing the reduction tend to produce a material with higher surface area. Carrying out the steel reduction at lower or higher (25 and 70 °C respectively) lead to platinum with smaller surface area (33 and 16 m^2g^{-1} respectively).

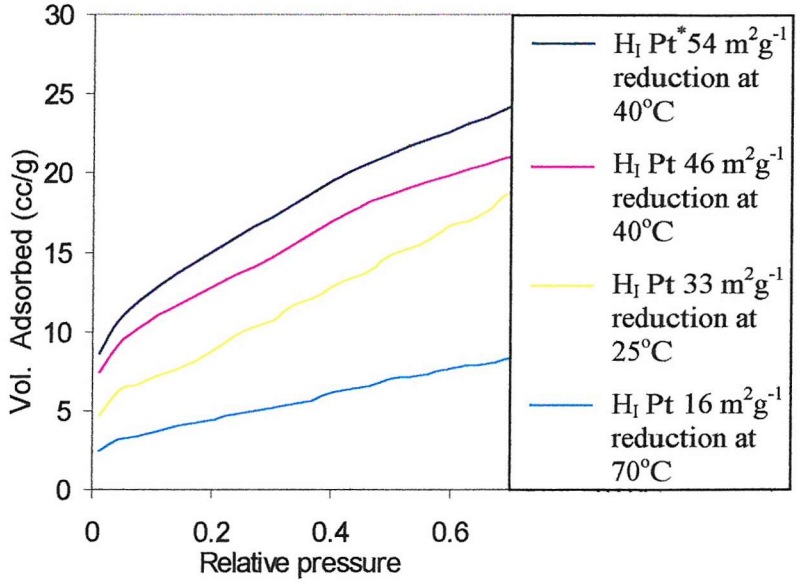

Figure 2.25 Nitrogen adsorption isotherm on different Platinum samples prepared at different temperatures

These results demonstrate the ability to optimise the preparations and obtain higher surface area materials while varying the amount of surfactant or changing the reduction temperatures.

2.3.3 The physical properties and structure of mesoporous Platinum prepared from the H_I phase of Brij 56

The following describes the results that were obtained from the various analytical methods used to determine the nanostructure and porosity of the H_I materials prepared while using Brij 56. Steel reduction was carried out on different templating mixtures at 40 °C since this was shown to be the most successful method investigated.

2.3.3.1 Visual appearance

All the materials prepared from Brij 56 were very dark grey/black powders similar to the one prepared from Brij 76.

2.3.3.2 TEM

Figure 2.26 shows the TEM micrographs for the various catalysts prepared by steel reduction at 40 °C while varying the amount of Brij 56 in the initial mixture.

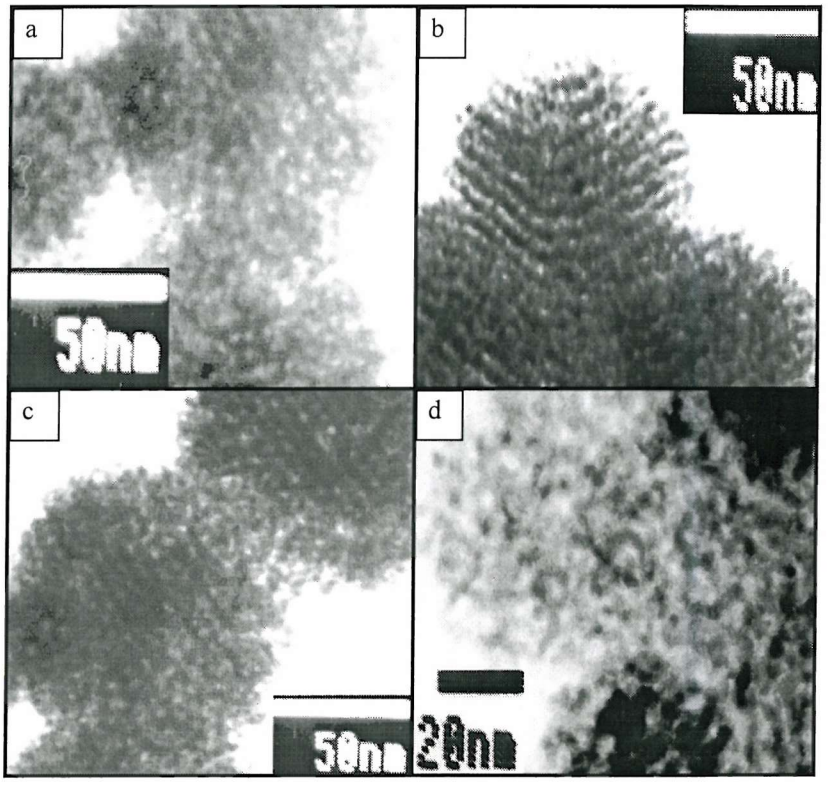

Figure 2.26 TEM micrographs of H_I platinum prepared while varying the amount of Brij 56 in the templating mixture: a) 50 wt %; b,c) 60 wt %;d) 75 wt % Brij 56.

As apparent from the TEM micrographs, the materials prepared from either 40 or 75 wt % Brij 56 in the templating mixture exhibit porous structures which were not ordered (figure 2.26 a and d respectively). Using 60 wt % in the initial mixture, the materials were considerably more ordered: the H_I structure was clearly visible at the edges of the platinum particles (figure 2.26 b and c). The repeat distance between the pores was measured from the micrographs as ca.6.0 nm, similar to the one reported for the H_I platinum powders prepared from Brij 76.

2.3.3.3 BET Nitrogen adsorption studies

Nitrogen adsorption studies were carried out on the materials prepared from Brij 56 to study the surface area and compared the type of isotherms associated for different H_I materials to the one obtained for the materials prepared from Brij 76.

In figure 2.27, a distinct inflection in the isotherm was observed for the H_I material with the highest surface area (60 wt % Brij 56, 31 m^2/g) whereas the other isotherms were characteristics of materials with only a small amount of mesoporosity (40 and 75 wt % surfactant).

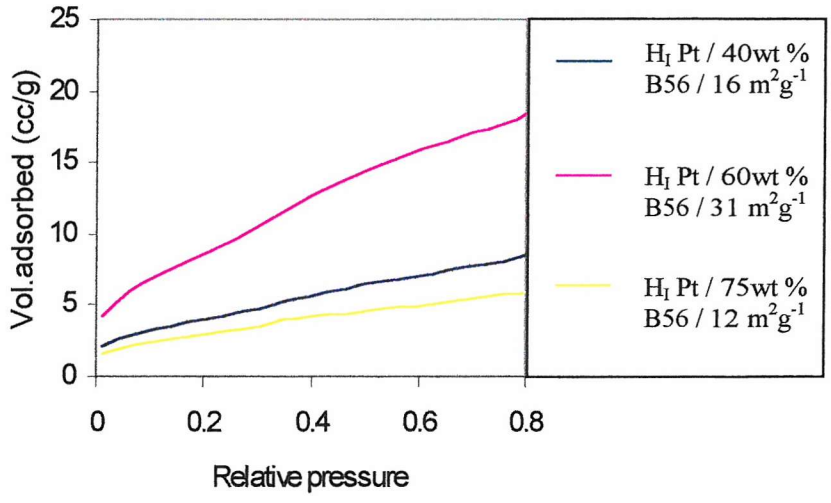

Figure 2.27 Nitrogen adsorption isotherms for different Platinum samples prepared at 40 °C while varying the amount of surfactant, Brij 56, in the templating mixture.

The effect of the temperature was then investigated using 60 wt % Brij 56 in the initial templating mixture (figure 2.28) but no major difference in surface area and type of isotherms was observed when the reduction was carried out at 40 or 60 °C (31 and 33 m^2/g respectively).

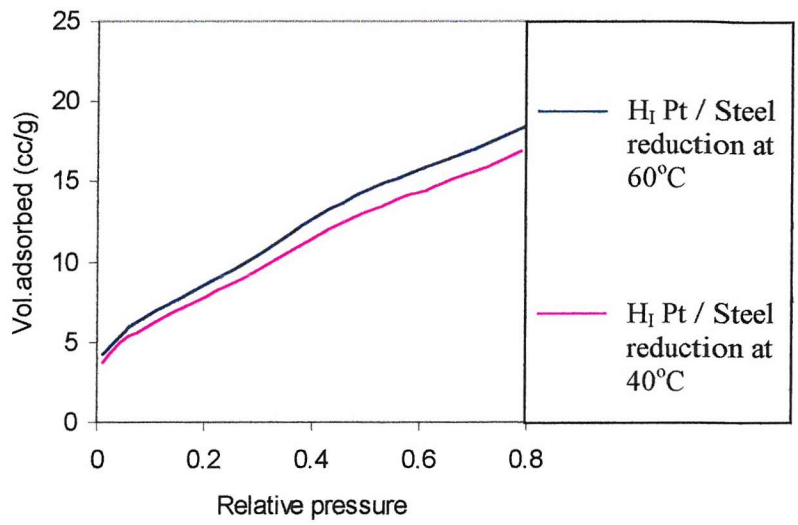

Figure 2.28 Nitrogen adsorption isotherms for different Platinum samples prepared at different temperatures.

The pore size distribution was calculated from the adsorption branches of the isotherms for the different materials prepared from different compositions and revealed pores of around 3nm. Pore size distribution as shown in figure 2.29 were similar to the one obtained for the materials prepared from Brij 76 and revealed a similar broad distribution characteristic of slightly disordered materials. As for Brij 76, pore size distribution was used to give insight into the range of pores obtained in the materials and used to confirm the TEM studies.

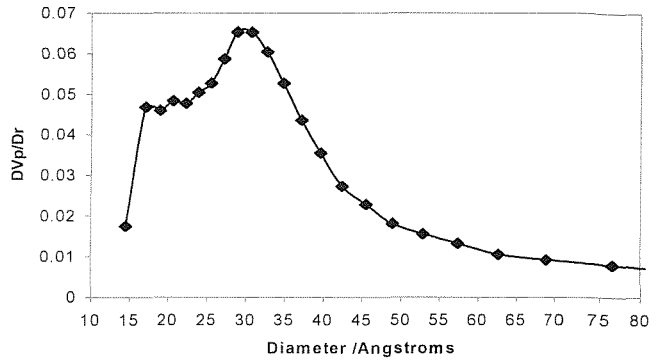

a) 40 wt % Brij 56

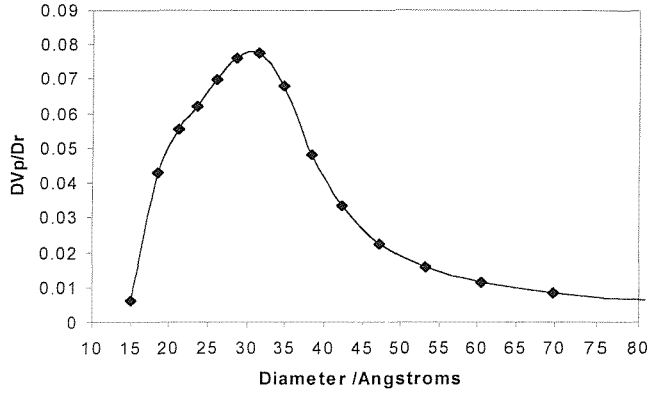

b) 60 wt % Brij 56

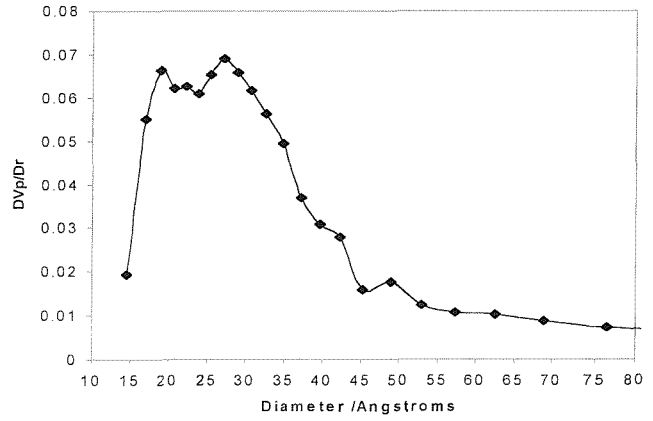

c) 75 wt % Brij 56

Figure 2.29 Pore size distribution for H_I platinum prepared by the steel reduction of HCPA while varying the amount of Brij 56 in the templating mixture. Pore size distributions were calculated from the adsorption branch of the isotherms.

2.3.4 The physical properties and structure of mesoporous Platinum prepared from the H1 phase of Brij 78

The following describes the results that were obtained from the various analytical methods used to determine the nanostructure and porosity of the prepared H1 materials. As reported previously, Steel reduction was carried out on different templating mixtures at different temperatures since this was shown to be the most successful method investigated.

2.3.4.1 General visual appearance

All the materials prepared from Brij 78 were dark grey/black powders similar to the one prepared from Brij 56 or 76.

2.3.4.2 TEM

Figure 2.30 shows the TEM micrographs of the various H_I platinum prepared while using Brij 78 in the initial mixture.

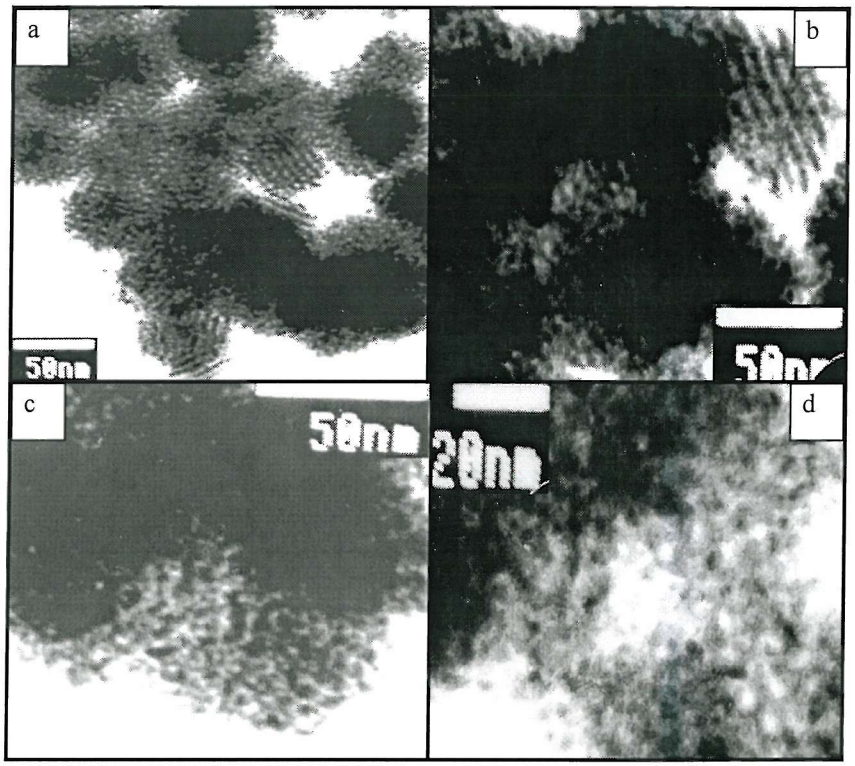

Figure 2.30 TEM micrographs of H_I platinum prepared while varying the amount of surfactant in the templating mixture a,b) 60 wt %;c)75 wt %;d) 85 wt% Brij 78

TEM micrographs revealed that the H_I platinum catalysts prepared while using 60 wt % Brij 78 in the templating mixture had a regular hexagonal nanostructure. The H_I structure was clearly visible on the smaller platinum particles but only at the edge of the larger platinum particles as shown on figure 2.30 (a ,b).Particles ranged from 50-500 nm in size and the repeat distance between the pores was measured from the micrographs as ca. 7 nm which is similar to the one reported for the materials prepared from Brij 56 and Brij 76 using the steel reduction method. Increasing the amount of Brij 78 in the templating mixture (75 and 85 wt % surfactant) produced porous materials with disordered structures as shown on figure 2.30 c and d respectively.

2.3.4.3 BET Nitrogen adsorption studies

Nitrogen adsorption studies were carried out on the material prepared from Brij 78 to study the surface area and compare the types of isotherms obtained with the one associated with the materials prepared from Brij 56 or 76. As shown in figure 2.31, a distinct inflection in the isotherm was observed for the material with the highest surface area (60 wt % Brij 78, 41 m^2g^{-1}) which was more attenuated for the other materials prepared from 75 or 85 wt % surfactant (13 and 20 m^2g^{-1} respectively).

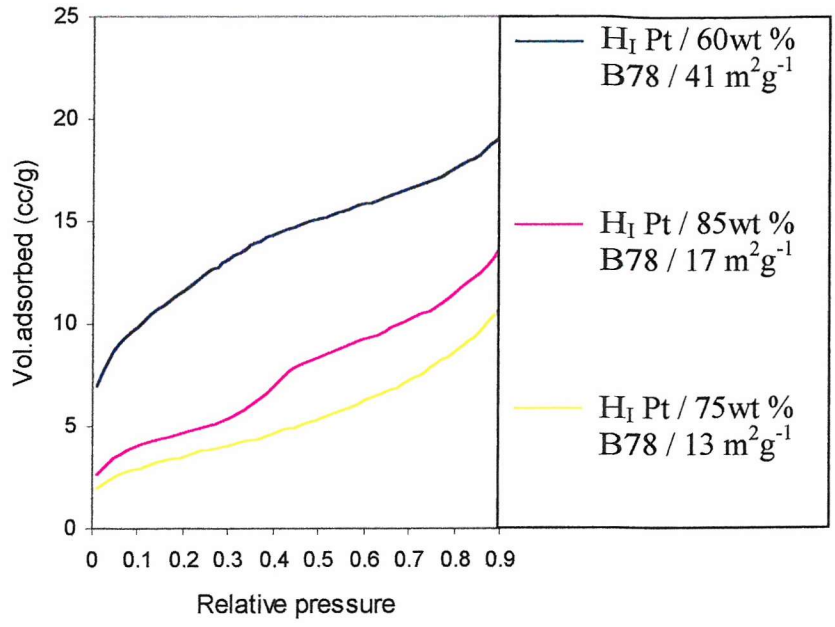

Figure 2.31 Nitrogen adsorption isotherms on Platinum samples prepared from Brij 78 while varying the amount of surfactant in the templating mixture.
(Steel reduction at 40 °C).

For 60 wt % in the templating mixture, the effect of the temperature on the reduction process was investigated (still in H_I phase) and the results in figure 2.32 showed that the surface area of the H1 material decreased as the reduction temperature increased with 40 °C giving the optimum results.

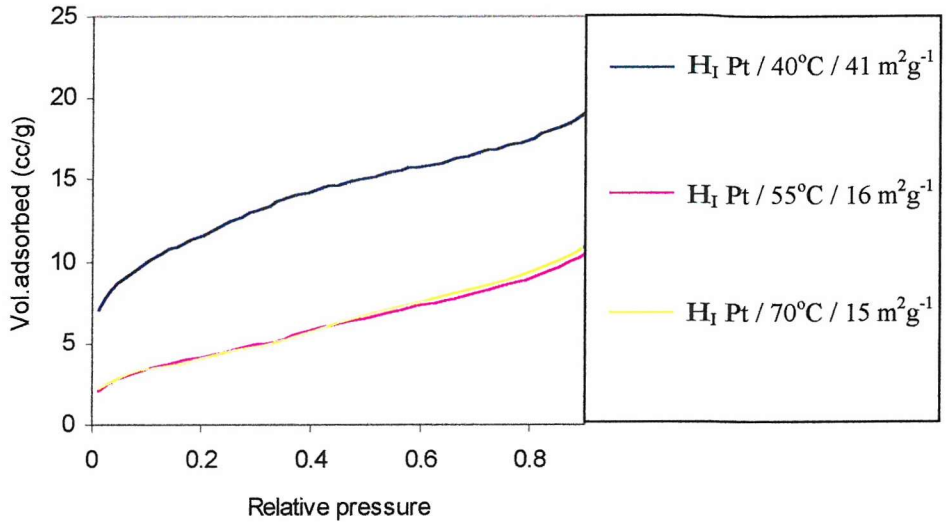

Figure 2.32 Nitrogen adsorption isotherms on different Platinum samples prepared at various temperatures (60 wt % Brij 78).

As previously, pore size distribution was calculated for the various materials prepared from different compositions at 40 °C and revealed a broad distribution of pores. In general, a maximum in the distribution is observed at around 2.5 to 3nm. For the material prepared from 75 wt % Brij 78, no distinct maximum from the pore size calculation was observed due to the lack of distinct inflection in the adsorption isotherm and lower surface area of the material prepared.

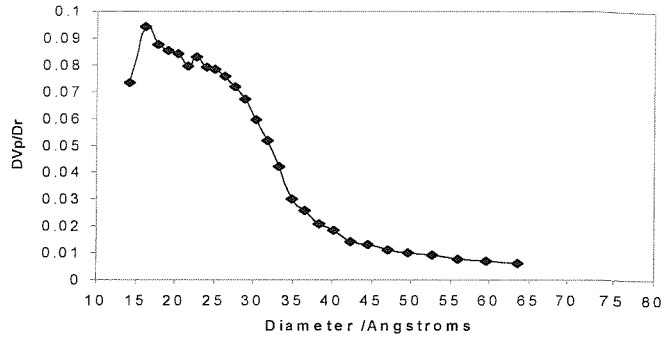

a) 60 wt % Brij 78

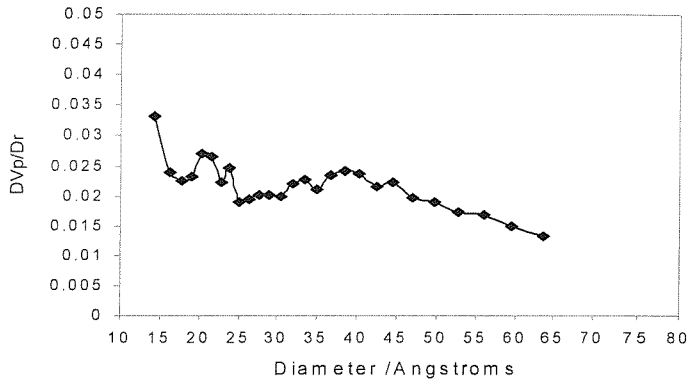

b) 75 wt% Brij78

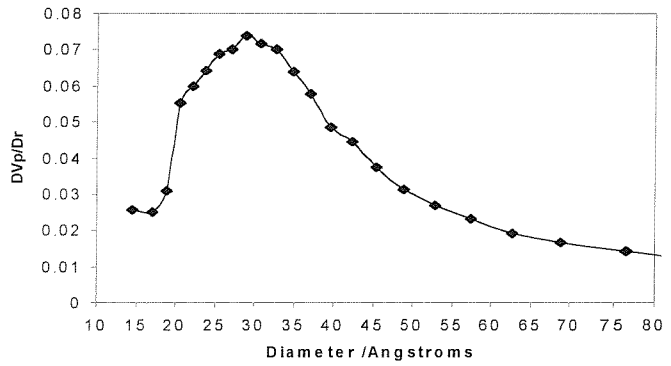

c) 85 wt% Brij 78

Figure 2.33 Pore size distribution for H_I platinum prepared by the steel reduction of HCPA while varying the amount of Brij 78 in the templating mixture. Pore size distributions were calculated from the adsorption branch of the isotherms.

2.3.5 Discussion on the preparation of H_I Platinum

2.3.5.1 Method of HCPA reduction

The most successful method for preparing mesoporous H_I platinum was the reduction of platinic acid using steel. This produced a material with a regular pore structure and a high surface area of 46 m^2g^{-1}. The sodium citrate reduced material was less ordered and had a lower surface area of 29 m^2g^{-1}. The hydrazine hydrate reduction and other metals methods produced the lowest surface area materials. There are two likely hypotheses as to why the different reduction methods produced very different materials:

i) Rate of reduction

All the different methods, that were tested, reduced the HCPA at different rates. The hydrazine reduction method was very fast whereas the sodium citrate reduction method was relatively slow. In the liquid crystal phase the surfactant aggregates are not in a rigid state and over short time scales the surfactant molecules can reorganise. If the platinum is forming slowly then it is likely that the structure becomes more disordered as the surfactant molecules reorganise. At the other extreme, where the platinum is being deposited very rapidly, the structure may grow regardless of the phase and produce a disordered material. The steel reduction method reduced the HCPA moderately quickly and so the pore structure of the resulting platinum was ordered.

ii) Effect of reducing agent on the phase

Although the phase behaviour of the different Brij surfactants studied in the presence of HCPA was well known, the effect of the reducing agent was not well characterised. For example, it would have been expected that hydrazine might significantly alter the phase behaviour of Brij 76. Under the conditions of the experiment the addition of hydrazine could have destroyed the H_I phase. Considering the dynamic state of all the species present in the reaction mixture further complicates the situation. During the reduction, the HCPA concentration is depleted and reaction by-products formed.
Therefore, at a local level, it is likely that the phase behaviour of the surfactant is changing throughout the reduction.

Steel reduction was shown to be the most successful method for reducing HCPA. Cadmium and Zinc produced materials much less ordered with a much lower surface area. Cadmium and zinc foils were mainly studied to compare their influence on the templating process and see if any correlation of their reducing activity with their redox potentials could be involved in the process.

Cadmium and iron have similar redox potentials –0.401 V and –0.441 V respectively (standard potential at 298K) but the platinum catalyst prepared by cadmium reduction at 20 or 40 ^{o}C (same initial composition) had much lower surface area than the H_I platinum prepared by steel reduction. Zinc is a strong reducing agent (-0.762, standard potential at 298K) and the catalyst obtained had an even smaller surface area. Compared to steel reduction, the kinetics of the reaction and the side products such as $ZnCl_2$ and $CdCl_2$ must play an important role in the templating process and are believed to be responsible for the lower surface area observed (reduction too quick with Zinc foil as stronger reducing agent, side products at interface between foil and H_I Phase).

iii)Effect of reduction Temperature

The results obtained while changing the reduction temperature at given compositions for the different surfactants studied demonstrated that precise control of the reduction was crucial for successful preparations of the H_I material. For the three surfactants studied, although in an H_I phase, if the reduction temperature is too high or too low, the material prepared is less ordered and exhibits a much lower surface area. This emphasises that the surfactant molecules are not in rigid state and can reorganise with changing temperature. As already mentioned, the rate of reduction is important and can also be considerably modified by altering the temperature. At lower temperature the platinum is forming slowly then it is likely that the structure becomes more disordered as the surfactant molecules reorganise. At the other extreme, at high temperature where the platinum is being deposited very rapidly, the structure may grow regardless of the phase and produce a disordered material.

2.3.5.2 Comparison of the different Brij surfactants used in the production of H_I Platinum

From the 3 different surfactant systems investigated, Brij 76 gave the best results in terms of producing mesoporous platinum with higher surface area and regularity of structures. From the polarising microscope studies in the presence of HCPA, the phase diagram reported for Brij 76 exhibits a wider and more stable hexagonal phase than the one depicted for Brij 56 or Brij 78 ternary mixtures. This greater stability could explain the higher surface area and regularity of structures produced using this surfactant. In the direct liquid crystal mechanism reported, it is evident that a right balance between alkane chain length and head group size of the surfactant is necessary to optimise the production of nanostructured platinum.

2.3.5.3 The polycrystalline structure of H_I platinum

Evidence from electron diffraction and wide angle XRD showed that the H_I platinum was polycrystalline. The size of the crystallites, as determined by peak broadening, was relatively small (average size ~ 4 nm) compared to platinum black (average size ~ 8 nm). In the H_I phase the growing platinum crystals were confined by the dimensions of the aqueous phase and this must limit the crystal size. It is proposed that the pore walls are made up of small crystallites of platinum that are heavily agglomerated. The possibility of a colloidal assembly of platinum particles, forming the H_I structure, can be ruled out because experience shows that the pore structures can survive harsh washing procedures and temperatures in excess of 100°C. If the H_I platinum were a result of a colloidal assembly then the structure would be susceptible to temperature and different solvent conditions. For the mesoporous structure to remain intact there must be a reasonable amount of cohesion between the platinum crystallites.

2.3.5.4 Surface area of H_I platinum

The surface area of H_I platinum (46 m^2g^{-1}) was considerably less than for example the analogous H_I silica materials (1400 m^2g^{-1}). This could partly be explained by the greater density of platinum (21.5 gcm^{-3}) compared to that of silica (2.2 gcm^{-3}). However, it was also necessary to consider the pore geometry's of the two materials to complete the study. The equivalent H_I silica was observed to have a wall thickness of only 1.2 nm, whereas H_I platinum had walls that were 3.5 nm thick.

In appendix B a model of the H_I structure is described that shows how density, pore size and wall thickness can effect surface area. From the model it was shown that as the wall thickness for H_I platinum was greater than for silica the predicted surface area was reduced for platinum. By combining this with the greater density of platinum it was possible to rationalise the surface areas of the H_I platinum materials. Ultimately, microporosity in the polycrystalline pore walls, and the external surface of the particles, were also important in determining the surface area.

2.3.6 Mesoporous Platinum from I_1 and V_1 phase

The following describes the results that were obtained from the various analytical methods used to determine the nanostructure and porosity of the prepared I_1 and V_1 materials. As reported previously, Steel reduction was carried out using different templating mixtures at different temperatures.

2.3.6.1 Visual appearance

All the I_1 and V_1 materials that were prepared were very dark grey powders similar to the H_1 Platinum prepared from Brij surfactants.

2.3.6.2 TEM

TEM provided the most direct method of examining the V_1 and I_1 mesostructures of Platinum. For the Platinum prepared from the V_1 Phase of Brij 76, there was evidence for a cubic mesoporous structure, with pore systems running at 90 degrees to one another as depicted in figure 2.34a. However, there was also a lot of disordered material (porous but disordered in the same samples, as shown on figure 2.34b).

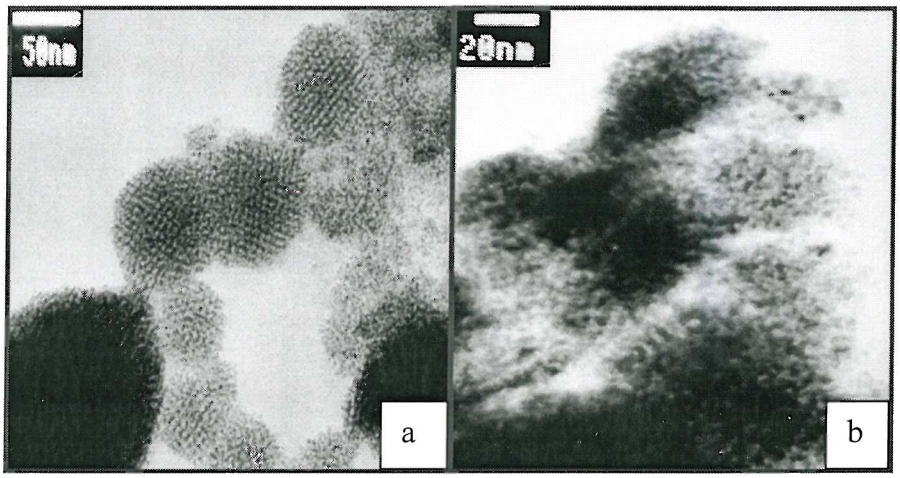

Figure 2.34 TEM micrographs of V_1 Platinum prepared from Brij 76 (75 wt % surfactant, steel reduction at 85 °C).

The TEM micrographs for the I_1 material depicted in figure 2.35 a and b show the porosity of the catalyst obtained characteristic of disordered structure (small pores with large walls).

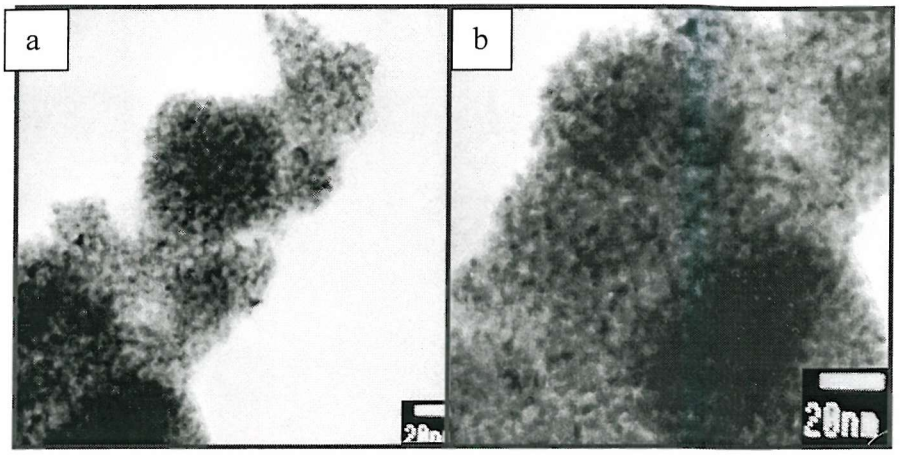

Figure 2.35 TEM micrographs of I_1 Platinum prepared from Brij 78 (50 wt % surfactant, steel reduction at 40 °C).

2.3.6.3 BET Nitrogen adsorption studies

BET nitrogen adsorption were carried out on the mesoporous V_1 Platinum prepared from Brij 76 and the I_1 materials prepared from Brij 78 to study the surface area and the type of isotherms associated for different Platinum powders. For the Platinum prepared from the V_1 Phase of Brij 76 (75 wt %, steel reduction carried out at 85 °C), BET nitrogen adsorption on the material obtained revealed a surface area of 38 m^2g^{-1} with a maximum in the pore size distribution of around 1.7 nm (figure 2.36).

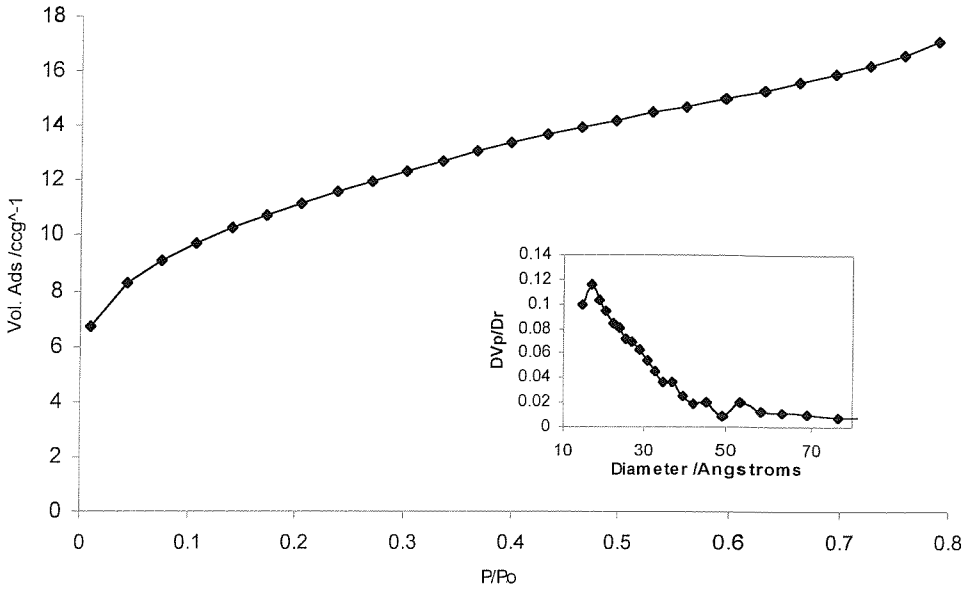

Figure 2.36 Nitrogen adsorption isotherm and pore size distribution for V_1 Platinum prepared from Brij 76

BET nitrogen adsorption on the I_1 material revealed a surface area of 11 m^2/g. Pore size distribution calculated from the adsorption branch of the isotherm (figure 2.37) was very broad and revealed pores of around 3.5 nm.

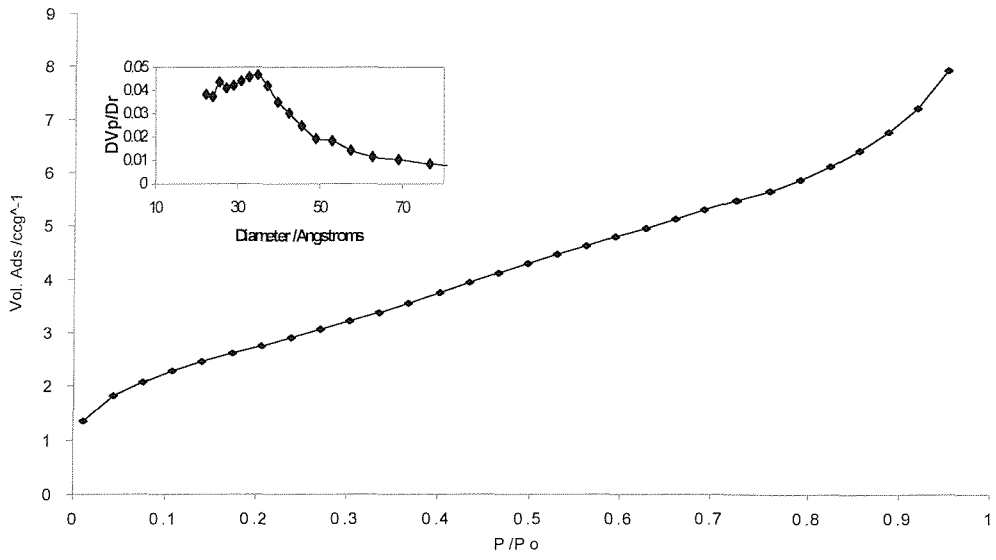

Figure 2.37 Nitrogen adsorption isotherm and pore size distribution for the I_I material prepared from Brij 78 at 40 °C.

2.3.6.4 Discussion of the results for the I_1 and V_1 preparations

By using the phase diagram constructed for Brij 76 + water + HCPA, it was possible to prepare V_I form of mesoporous Platinum. The total connectivity of the V_I stucture resulted in a surface area of 38 m^2g^{-1}, smaller than the one for the H_I Platinum prepared (46 m^2g^{-1}). A higher surface area was expected for the V_I material because the 3D interconnectivity should lead to a more accessible surface than the 2D pore structure of the H_I Platinum. Moreover, using purer surfactant such as $C_{16}EO_8$, this total connectivity resulted in an increased surface area of 74 m^2g^{-1} compared to the H_I Platinum prepared from the same surfactant (60 m^2g^{-1}) [7].

2.4 Conclusion and further work

The work described in this chapter showed that it is possible to use lyotropic liquid crystal phases as moulds for the formation of mesoporous platinum. Typically the materials had almost double the surface areas of commercially available, high surface area, platinums (e.g. platinum black).

Phase diagram studies of the HCPA + Brij surfactants + H_2O mixtures, that are used in the preparation of mesoporous platinum, revealed that platinic acid did not adversely effect the phase behaviour of the surfactant. In fact the stability of the H_I phase was increased considerably particularly at elevated temperatures. The predominance of the higher curvature structures such as the H_I aggregates was attributed to an interaction between the ethylene oxide headgroups of the surfactant and the HCPA.

In the synthesis of mesoporous H_I platinum it was shown that the method used to reduce HCPA to platinum metal was critical in obtaining an ordered mesopore structure. Reduction with steel sheet was shown to be the most successful method of preparing H_I materials and it was proposed that the method of reduction was important because the synthesis was sensitive to the rate of reduction. Generally, very fast and very slow methods of reduction resulted in disordered mesoporous platinum structures.

By using the phase diagram constructed for the HCPA + Brij 76 + water system it was possible to prepare V_I form of mesoporous platinum. The total connectivity of the V_I structure resulted in surface area of 38 m^2g^{-1} smaller than the H_I Platinum prepared (46 m^2/g). A higher surface area was expected for the V_I material because of the 3D interconnectivity resulting in a more accessible surface than the 2D pore structure of H_I material. Moreover, using purer surfactant such as $C_{16}EO_8$, an increased surface area for the V_I Platinum compared to the H_I material from the same surfactant was reported.
Using the phase diagram constructed for the HCPA + Brij 78 + water system, it was also possible to prepare I_I form of the mesoporous Platinum.

All the mesoporous platinum materials were micron sized black powders. Electron diffraction studies of one of the platinum particles revealed the structures to be made up of polycrystalline fcc platinum. XRD studies also confirmed that the platinum was fcc and that the crystallite size was very small at around 5 nm. From these observations, it was concluded that the pore walls were made up of polycrystalline fcc platinum and not a single platinum crystal containing pores. Although the material was polycrystalline the adhesion between crystallites must have been strong to resist thermal and chemical treatments. Studies of electrodeposited H_I platinum have shown that similar mesostructures can be formed but as metallic films rather than powders [3].

Mesoporous Platinum was only formed at high concentrations of surfactants. From these observations it is proposed that lyotropic phase acts purely as a structure directing agent or mould. Initially, reduction of the HCPA affords small colloidal platinum particles in the aqueous domains of the phase. Subsequently, these primary particles agglomerate and coalesce, until a wall thickness is reached at which the structure is mechanically stable. Although interactions between the HCPA and the surfactant were shown to be present in the phase diagram studies these are thought not to be important in the formation of the platinum structure. The HCPA only effects the phase behaviour of the surfactant and not the reduction process.

Table 3.1 summarises some of the major differences between our novel mesoporous H_I platinum and commercially available platinum black. The major advantage of H_I platinum over platinum black for catalytic applications is the much higher surface area of H_I platinum. In addition, the larger particle size of H_I platinum is also attractive because of the problems associated with separating finely powdered catalysts from reagents and products. As outlined in the introduction, it has also been possible to prepare mesoporous platinum films by electrodeposition. These mesoporous electrode materials may find applications where the tailored pore structure and size is important in addition to the inherently high surface area of the material.

Comment	H_I platinum	Platinum black
Method of formation	Reduction of HCPA in an H_I phase of Brij 76 + water mixture	Reduction of HCPA in a solution of ethanol
Structure		
On a mm scale	Fine black powder	Fine very dark black powder
On a μm scale	Oval shaped micron sized particles	Sub micron sized irregular particles
On a nm scale	Ordered H_I pore structure with Pores: 3 nm Walls: 3.5 nm	Partially agglomerated platinum crystals
Crystal structure	fcc polycrystalline platinum Crystallite size: 4 nm	fcc polycrystalline platinum Crystallite size: 8 nm
Surface area	~46 m^2g^{-1} Some external surface area with a large mesopore contribution	~30 m^2g^{-1} All external surface area

Table 3.1 A comparison of mesoporous H_I platinum and platinum black.

The major cost associated with preparing mesoporous H_I platinum was the platinic acid precursor. The use of Brij surfactant series offers an attractive route for the production of the mesoporous material when compared to the far more expensive $C_{16}EO_8$ reported.

In summary, it has been shown that in preparing a mesoporous metal it is important to consider the interactions between the surfactant and the metal salt, and the resulting effects on phase behaviour. Furthermore the method of reducing the metal salt is critical in obtaining an ordered mesoporous structure. The elements that make the mesoporous platinum system successful are the high solubility of HCPA, the positive effect of HCPA on the stabilisation of the H_I phase of the surfactant and the steel reduction method. It is also important note that platinum is a relatively inert metal and can withstand the extraction procedure used to remove the surfactant. For some of the more reactive metals, extraction of the surfactant may be more of a problem. Oxidation could also be an issue because of the materials inherently high surface area.

Further work

- Although the preparation of mesoporous platinum has been fairly exhaustive there are still a number of issues that need to be addressed. Firstly, confirmation of the phase diagram studies of HPCPA + Brij 76 + water by small angle XRD would help to identify the symmetry of the V_1 phase and provide more direct evidence of the I_1 phase (Brij 78). Small angle XRD studies of the HCPA mixtures before reduction should help in improving the order of the V_1 phases. Choice of a suitable surfactant, with a large V_1 domain, may also help in improving the order of the V_1 phase. Our work focused on the use of HCPA as the source of platinum because of its high solubility in water. Investigating other platinum sources could also considerably improve the quality of the catalysts prepared. $(NH_4)_2PtCl_6$ was investigated briefly as the platinum source for example but the material obtained had a smaller surface area.

In addition to the work on mesoporous platinum there are a number of applications where other mesoporous materials might find uses. The challenges in extending the range of mesoporous metals cover three major areas:

- Identifying suitable metal salts that are highly soluble in water but do not significantly disrupt the phase forming properties of the surfactant. Identifying suitable surfactants that on the water + surfactant + metal salt phase diagram have large domains containing the phase of interest.

- Identifying suitable methods of reducing the metal salt that do not disrupt the phase forming properties of the surfactant and carry out reduction at the correct rate to replicate the aggregate structures of the surfactant. In addition, the reaction by products must be easily removed from the final mesoporous metal.

In the last case, the reduction method, electrodeposition is perhaps the most attractive route as the rate of reduction can be controlled and the reaction by-products are minimised because the reaction is electrochemical. However, electrodeposition, does not produce gram quantities of material and the films that are deposited are only 1-100 μm thick. Work has already been carried out on the preparation of mesoporous tin films for lithium ion insertion batteries [10] and mesoporous palladium films for gas sensors [11].

2.5 References

1. P V Braun, P Osenar and S I Stupp, *Nature*, **380**, 325 (1996).
2. G S Attard, C G Goltner, J M Corker, S Henke ,R H Templer, *Angew. Chem. Int. Ed. Engl.*, **36**, 1315 (1997).
3. G S Attard, P N Bartlett, N R B Coleman, J M Elliott, J R Owen , J H Wang, *Science*, **278**, 838 (1997).
4. G S Attard, N R B Coleman and J M Elliott, *Studies in Surface Science and Catalysis*,**117**, 89 (1998).
5. G S Attard, P N Bartlett, N R B Coleman, J M Elliott and J R Owen, *Langmuir*, No 26, 7340 (1998).
6. J M Elliott, P R Birkin, P N Bartlett, G S Attard, Langmuir, No 22,7411 (1999).
7. N R B Coleman, PhD thesis, Department of Chemistry, University of Southampton (1999).
8. M J Maclachlan, N Coombs, G A Ozin, *Nature*, 397,681 (1999).
9. D J Mitchell, G J T Tiddy, L Waring, T Bostock and M P Mc.Donald, *J. Chem. Soc. Faraday. Trans. I,* **79**, 975 (1983).
10. A H Whitehead, J M Elliott, J R Owen and G S Attard, J. *Chem. Soc. Chem. Commun.*, **4**, 331 (1999).
11. S Guerin, PhD Thesis, University of Southampton (1999).

Chapter 3

The preparation of mesoporous palladium

3.1 Background and objectives

The most widely studied noble metal is certainly platinum; however the properties of other metals such as palladium have also received a great deal of interest.
Palladium has been recognized as one of the best catalysts for methane oxidation [1]. Unlike other noble metals, palladium has the ability to adsorb hydrogen in large quantities [2]; it adsorbs 935 times its own volume of hydrogen gas when heated [2]. Palladium forms divalent and tetravalent compounds and resembles platinum chemically [3]. Palladium is also very important in organic synthesis. Its major uses are typically in homogeneous catalysis, through complexes such as Pd $(PPh_3)_4$, are used in carbon-carbon bond forming chemistry. Metal salts, such as palladium chloride, are used in the Wacker process ($PdCl_2/CuCl_2$ catalyzed air oxidation of ethylene, 1960) [4,5]. Heterogeneous catalysis with Palladium metal is also used industrially, although more frequently it is supported on a carrier such as carbon (5-10%Pd). This form of the catalyst has high surface areas, typically of ca.120 m^2g^{-1} [6].
Of the platinum metals it is often the mildest reducing agent in metal form; while platinum and ruthenium are capable of reducing aldehydes to alcohols palladium does not. This property is exploited in producing more selective catalysts [5]. The most useful reactions of palladium metal are those involving absorption of C=C bonds leading to chemical reduction. Common palladium metal catalyzed reactions are decarbonylations of aldehydes and reductions of unsaturated aldehydes, aromatic compound and various nitrogen containing compounds [4,7,8].

The subject of the work described in this chapter is an investigation into the chemical preparation of mesoporous palladium from Brij surfactant system. The objectives of the work are descibed below:

1- To characterise the liquid crystal phase behaviour of polyoxyethylene surfactant Brij 76 + palladium acetate + water mixtures.

2- To characterise the liquid crystal phase behaviour of polyoxyethylene surfactant Brij 76 + ammonium tetrachloropalladate + water mixtures.

In both cases, it was important to optimize the conditions for the preparation of mesoporous palladium and to investigate the way in which the palladium precursors interact with the surfactant.

3- To investigate methods for the chemical preparation of mesoporous palladium in terms of palladium precursors and reducing agents.

4- To characterise the mesoporous palladium obtained in terms of structure on a nanometer scale, surface area and regularity of the nanostructure.

3.2 Experimental

The experimental work is presented in 3 sections. The first of these describes the study of the phase behaviour of Brij 76 that contains palladium acetate or ammonium tetrachloropalladate solutions. Following from this, the use of several reducing agents is described. This work was aimed at optimizing the reduction process. Finally the structural characterisation of the mesoporous palladium is presented.

3.2.1 Phase behaviour of Brij 76 in palladium acetate and ammonium tetrachloropalladate solutions.

Phase diagrams were constructed using polarised light microscopy as outlined in Appendix 1. Brij 76, palladium acetate and ammonium tetrachloropalladate were used as supplied by Aldrich. Deionised water was used to make up the phases. In all cases, mixtures were made up by adding the surfactant to a solution of the palladium precursor. Phase diagrams were constructed for the following systems: (Details of the compositions are given in appendix 2 B).

- Phase diagram of Brij 76 + water + palladium acetate where the concentration of palladium acetate was fixed with respect to the water content at 0.26M.

-Phase diagram of Brij 76 + water + ammonium tetrachloropalladate where the concentration of ammonium tetrachloropalladate was fixed with respect to the water content at 1.1M.

3.2.2 A study of the chemical preparation of H_I palladium

A number of different methods were used to prepare mesoporous palladium from Brij 76+ palladium precursors + water. Essentially they all involved the use of a reducing agent to reduce the palladium (II) precursors to palladium metal.

3.2.2.1 Steel reduction

As reported in the previous chapter, it is possible to prepare mesoporous platinum by the chemical reduction of HCPA by the steel sheet method. On a similar basis, the reduction of the palladium precursors by a less noble metal than palladium was therefore investigated. By using a steel sheet it was possible to maximise the exposed surface area of the metal while making the removal of unreacted metal possible after reduction.

Steel sheets as supplied by RS, were cleaned with acetone. An H_I phase containing ammonium tetrachloropalladate (ATCP) (1g), H_2O (3.25g) and Brij 76 (4g) was prepared by adding the surfactant to the ATCP solution. As for the reduction of HCPA, a thin layer of the phase was spread onto a glazed ceramic tile and a thin sheet of steel placed over the top and weighted down. Reduction occurred at the interface between the phase and steel sheet. Reduction of the palladium precursor to palladium by the oxidation of iron was complete within three hours at room temperature. The thick black mixture produced was scraped off the ceramic tile and steel sheet. Removal of the template was carried out by stirring in acetone (200 ml) for 3 hours and decanting off the solution leaving palladium. This was followed by three washes: water (2 X 200 ml) and acetone (200 ml). As previously, separation of the platinum powder from the solution was achieved by using a centrifuge. When comparing with the platinum washing process, no acid washing step was used in the palladium preparation because of potential problems with palladium dissolving in acidic conditions. After the final extraction the black palladium powder was dried at 90 ^{o}C for 24 hours. Using the same reduction method and the same palladium precursor, the preparation of mesoporous palladium was also investigated for an H_I phase of

$C_{16}EO_8$. The aim of this study was to compare the effect of using a purer surfactant on the templating process. An H_I phase containing ATCP (1g), deionised water (3.25 g) and $C_{16}EO_8$ (9.75g) was prepared by adding the surfactant to the ATCP solution (75 wt % $C_{16}EO_8$). Steel reduction was carried out at room temperature for 3 hours and the palladium material extracted as before.

The same experimental procedure was used for the production of palladium from the steel reduction of palladium acetate by preparing an initial templating mixture of palladium acetate (0.4g), H_2O (7g) and Brij 76 (10.95g) by adding the Brij surfactant to the palladium acetate solution (60 wt % Brij 76, H_I phase).

3.2.2.2 Hydrazine hydrate reduction

An H_I phase containing ammonium tetrachloropalladate (1g), H_20 (3.25g) and Brij 76 (4g) was prepared by adding the surfactant to an aqueous solution of the palladium precursor (60 wt % surfactant). To this phase was added another H_I phase made up from hydrazine hydrate (0.5g, 10 % solution), H_2O (3g) and Brij 76 (5g). This phase was obtained by adding the surfactant to the aqueous solution of reducing agent. The two phases were mixed using a glass rod for ca. 1 minute before leaving at to stand at room temperature for 3 hours. The brown palladium salt rapidly reduced to palladium metal and the mixture turned black. The palladium was extracted by washing in water (2X 200 ml), followed by acetone (200 ml).

3.2.3 Characterisation

Characterisation of the mesoporous palladium was carried out by nitrogen adsorption/ desorption experiment to determine surface area and pore size distribution, X- ray diffraction and TEM to determine structure on a nanometer level.

3.3 Results and discussion

3.3.1 The phase behaviour of ethylene oxide based surfactant in ammonium tetrachloropalladate solutions

The phase transition data obtained for the ternary mixture Brij 76 + ammonium tetrachloropalladate + H_2O are shown schematically in figure 3.1. The ammonium tetrachloropalladate concentration was fixed at 1.1 M for all the compositions. As explained in chapter 2 , the boundaries were drawn based on visual observations through a polarised light microscope. Consequently, the precise locations of the boundaries are only qualitative and this is reflected in the broad lines used to represent the boundaries. It should also be noted that the transition between two homogeneous phases is likely to occur via a small biphasic domain.

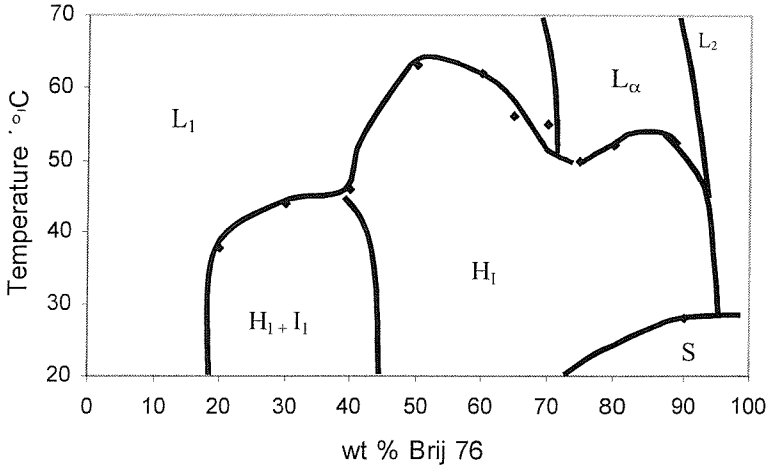

Figure 3.1 Phase diagram of Brij 76 + water + ammonium tetrachloropalladate where the concentration of the palladium salt is kept constant at 1.1 M.

In the previous chapter, the phase diagram of the binary Brij 76 + H_2O system was described (Figure 2.1b).

Comparison of the binary system with the ammonium tetrachloropalladate containing system revealed that the ammonium salt had a considerable effect on the phase behaviour of Brij 76. When compared to the binary Brij 76 + water system, it was observed that the presence of the ammonium tetrachloropalladate salt resulted in a dramatic increase in the composition range over which the lyotropic H_I phase was stable. The emergence of a viscous I_I phase was also noted. When view under the polarised light microscope, this viscous phase appeared isotropic with only a few small areas of birefringence suggesting that residual H_I phase was present. In summary:

- The H_I phase, which is stable up to 58 ^{o}C in the binary system from 30 to 60 wt% Brij 76, had a similar temperature stability in the presence of the additional salt but was present over a much wider range of compositions. (From 45 to 95 wt% brij 76).

- This larger H_I domain resulted in a much smaller $L\alpha$ region being observed only from 70 to 90 wt % brij 76 and at higher temperature than in the binary system.

- A viscous I_I phase in a significant $H_I + I_I$ domain was noted in the presence of the palladium salt. This was not observed for the binary system.

3.3.2 The phase behaviour of ethylene oxide based surfactant in palladium acetate solutions

The change of phase behaviour for Brij 76 in the presence of the ammonium tetrachloropalladate salt was not just limited to this palladium precursor. The transition data for the ternary Brij 76 + water + palladium acetate systems are shown schematically in figure 3.2.

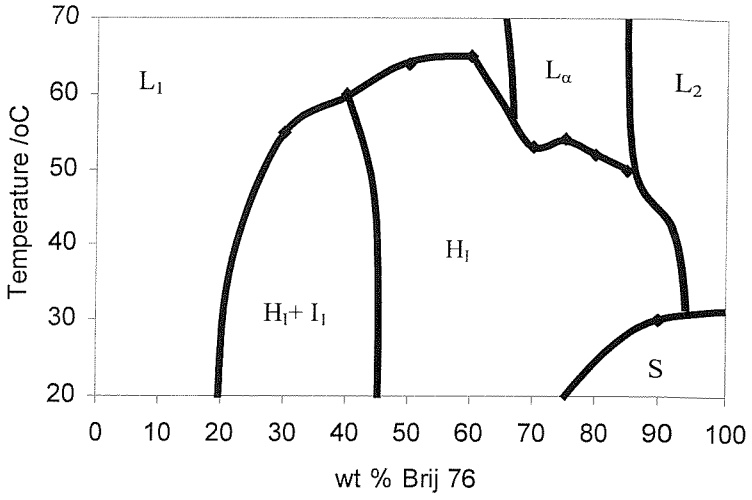

Figure 3.2 Phase diagram of Brij 76 + water + palladium acetate where the concentration of the palladium salt is kept constant at 0.26M.

The phase diagram for the ternary system that contained palladium acetate salt was very similar to the one reported previously for the ternary Brij 76 + ammonium tetrachloropalladate + water system. Addition of palladium acetate to the Brij 76 lyotropic system resulted in the stabilization of the H_I phase over a wider range of composition. In summary:

- When comparing to the binary system, the H_I phase was present over a wider range of compositions in the presence of palladium acetate resulting in an important contraction of the domain over which the $L\alpha$ was stable.

- The biphasic H_I + I_I domain was also observed in the presence of the palladium acetate precursor

3.3.3 Discussion of the phase behaviour of Brij 76+ H_2O+ palladium precursors

The phase behaviour of ethylene oxide based surfactants in platinic acid solutions has been reported in chapter 2.The results showed that the interactions between the platinum salt and the lyotropic systems led to a stabilisation of aggregates and phases with a high positive mean curvature. In the phase diagram of Brij 76 in platinic acid solution reported for example, the net effect was to stabilise the H_I phase over a wider range of compositions and temperatures than the one observed in the binary Brij 76 + water system. In the case of the ternary brij 76 + H_2O + Palladium precursors investigated, similar behaviour was observed. When compared to the binary Brij 76 + H_2O system, the ternary system containing ammonium tetrachloropalladate or palladium acetate show an H_I phase stability with temperature that is similar to the binary system, the lyotropic H_I phase was stabilised over a wider range of compositions when the palladium salt was added. One possible explanation for these observations is an interaction between the ethylene oxide headgroups of the surfactant and the palladium precursors. The overall effect is to stabilise the higher positive mean curvature phases such as the H_I phase resulting in a much smaller lamellar region, initially predominant in the binary system.

Phase studies of the ternary Brij 76 + H_2O + palladium precursors mixtures revealed that the phase forming properties of the Brij 76 + H_2O mixtures can be altered by the addition of a metal salt. This clearly has important implications for the choice of formulations to be used in the direct liquid crystal templating of mesoporous palladium.

3.3.4 The physical properties and structure of mesoporous palladium prepared from the H_I phase of Brij 76

The following describes the results that were obtained from the various analytical methods used to determine the nanostructure, chemical composition and porosity of the prepared H_I palladium materials.

3.3.4.1 General visual appearance

All the H_I palladium materials that were prepared were very dark grey powders which were very similar in appearance to the H_I platinum materials described in chapter 2.

3.3.4.2 TEM

As for the H_I platinum powders analyzed in chapter 2, TEM was used to determine the morphology of the mesopore structure. H_I palladium prepared by the steel reduction of ammonium tetrachloropalladate in the presence of $C_{16}EO_8$ (65 and 75 wt % surfactant had a characteristic hexagonal pore morphology as shown on figure 3.3a and 3.3b respectively. The wall thickness was found to be 4 nm and the diameter of the holes 4 nm. The materials prepared from the same precursor in the H_I phase of Brij 76 (50 and 60 wt %) were also characterized by TEM and the micrographs are shown of figure 3.3c,d and 3.3e,f respectively. Although the porosity of the catalyst was clearly visible, the structure of the H_I powders prepared from Brij 76 were less ordered than the materials prepared from $C_{16}EO_8$.

Although only visible on the edge of the sample, a more ordered mesoporous structure was obtained for 50 wt % Brij 76.

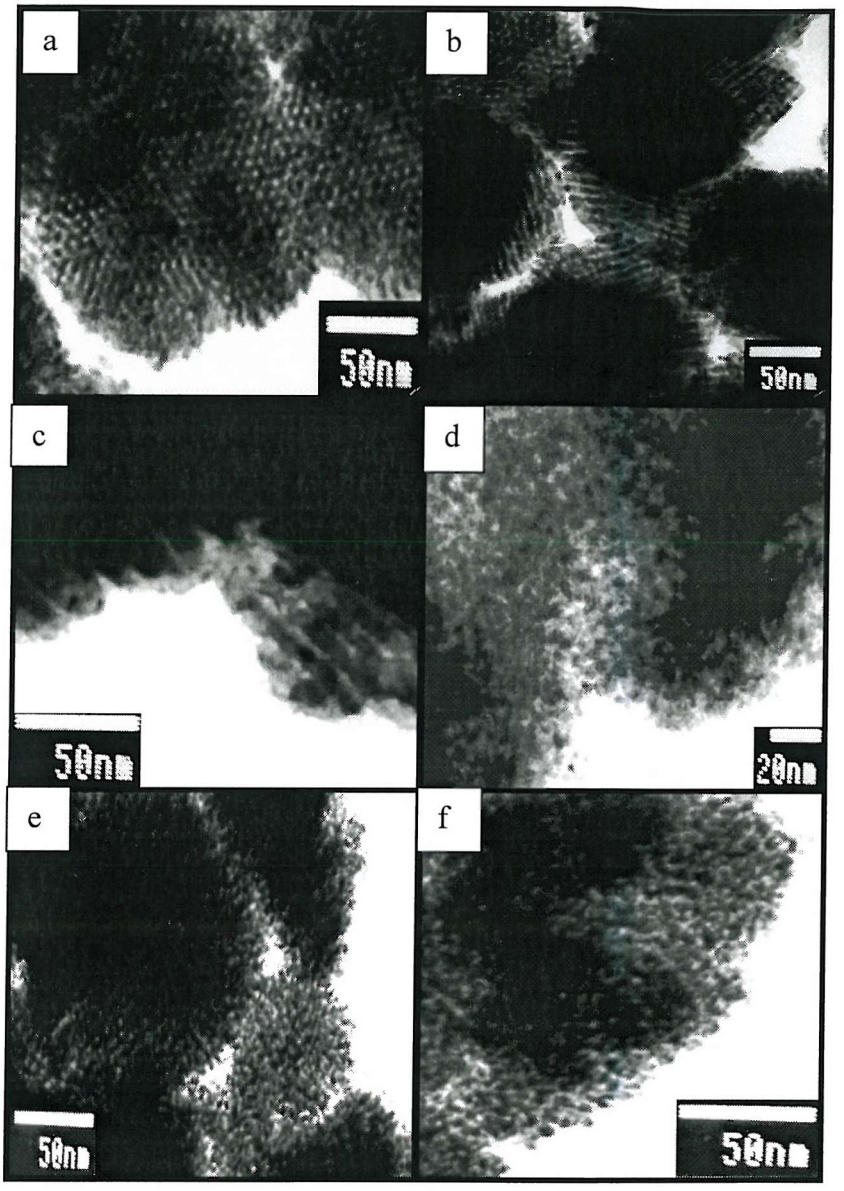

Figure 3.3 TEM micrographs of H_I Pd prepared by steel reduction of ammonium tetrachloropalladate at room temperature in H_I phases containing a) 65 wt % $C_{16}EO_8$; b) 75 wt % $C_{16}EO_8$; c)d) 50 wt % Brij 76;e)f) 60 wt % Brij 76 in the templating mixture. Scale bars are given for each micrograph.

The materials prepared from palladium acetate were investigated by TEM The results are shown on figure 3.4. A highly porous but disordered structure was observed for the material prepared from 50 wt % Brij 76 as shown on figure 3.4a and 3.4b. Although only visible on the edge of the sample, an ordered nanostructure was obtained when using 60 wt % of Brij 76 in the templating mixture, (figure 3.4 c,d). The wall thickness was found to be 3 nm and the pore diameter was found to be ~ 2nm, slightly smaller than the diameter of the hole observed for the materials prepared using the ammonium tetrachloropalladate precursor.

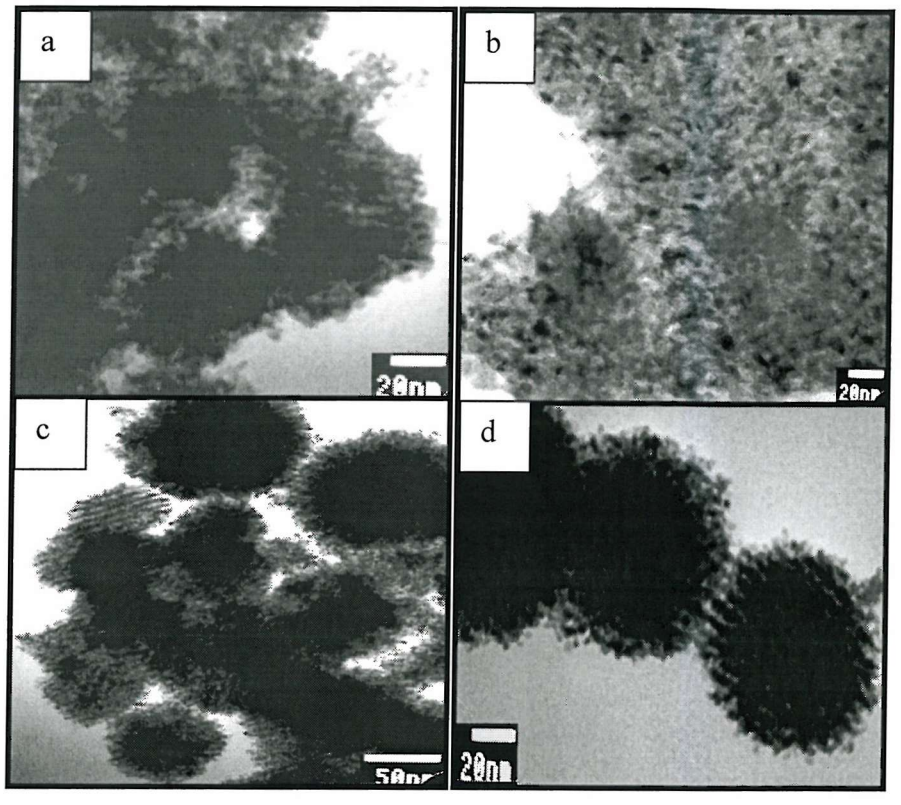

Figure 3.4 TEM micrographs of H_I Pd prepared by steel reduction of palladium acetate at room temperature in H_I phases containing a)b) 50 wt % Brij 76; c)d) 60 wt % Brij 76 in the templating mixture. All these materials were prepared while using palladium acetate as palladium precursor. Scale bars are given for each micrograph.

3.3.4.3 SEM and EDAX

Scanning electron microscopy was carried out on the H_I palladium prepared by steel reduction of ammonium tetrachloropalladate at room temperature. The results are shown on figure 3.4 and 3.5. At higher magnification, a sponge-like porosity of the H_I catalyst was visible.

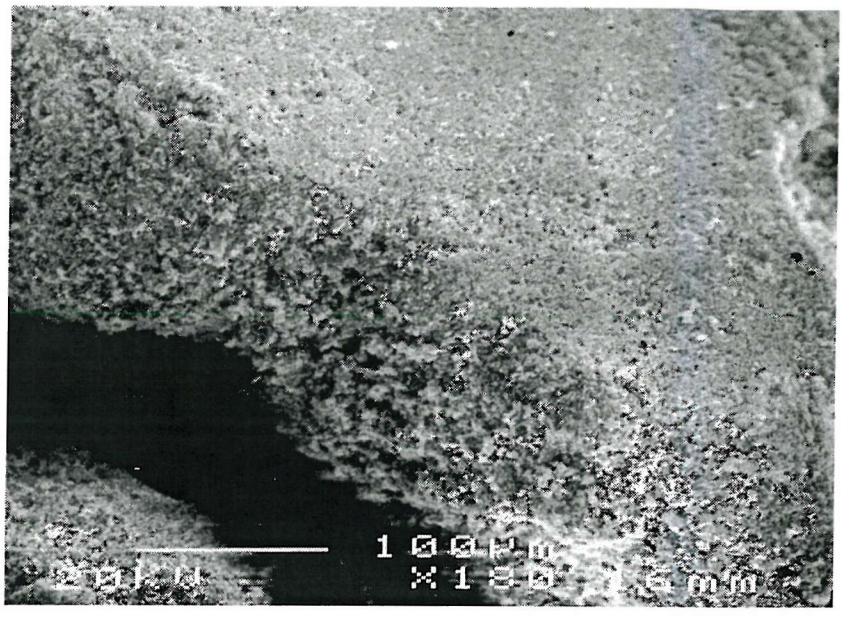

Figure 3.5 SEM picture of H_I Pd prepared by steel reduction. Scale bar 100 μm.

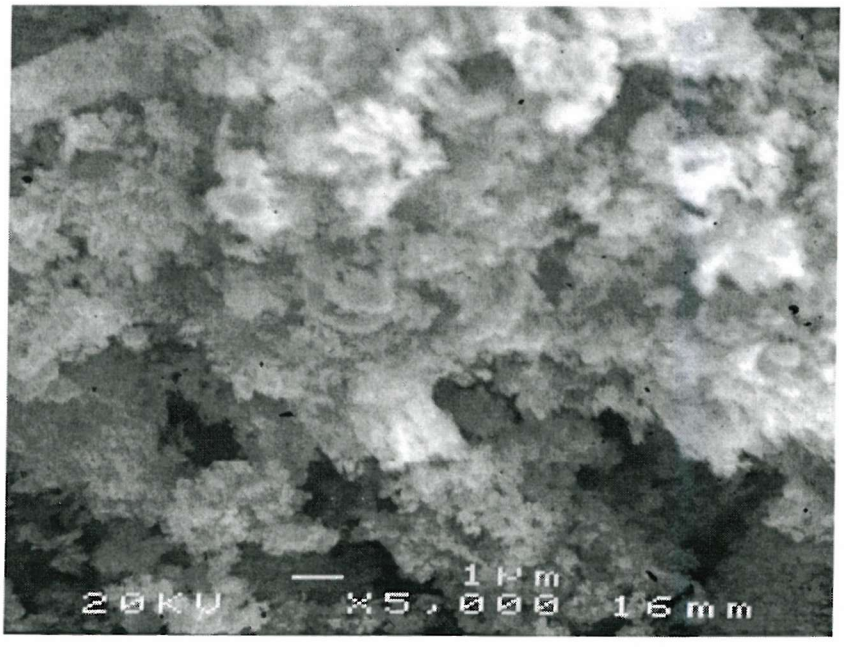

Figure 3.6 SEM picture of H_I Pd prepared by steel reduction. Scale bar 1 μm.

X-ray microanalysis was carried out on the H_I powders prepared from steel reduction and confirmed the purity of the palladium powders prepared as shown on figure 3.6. When comparing with the H_I platinum prepared by steel reduction where a small amount of iron impurities were present (chapter 2), no residual iron was detected in the H_I palladium powder.

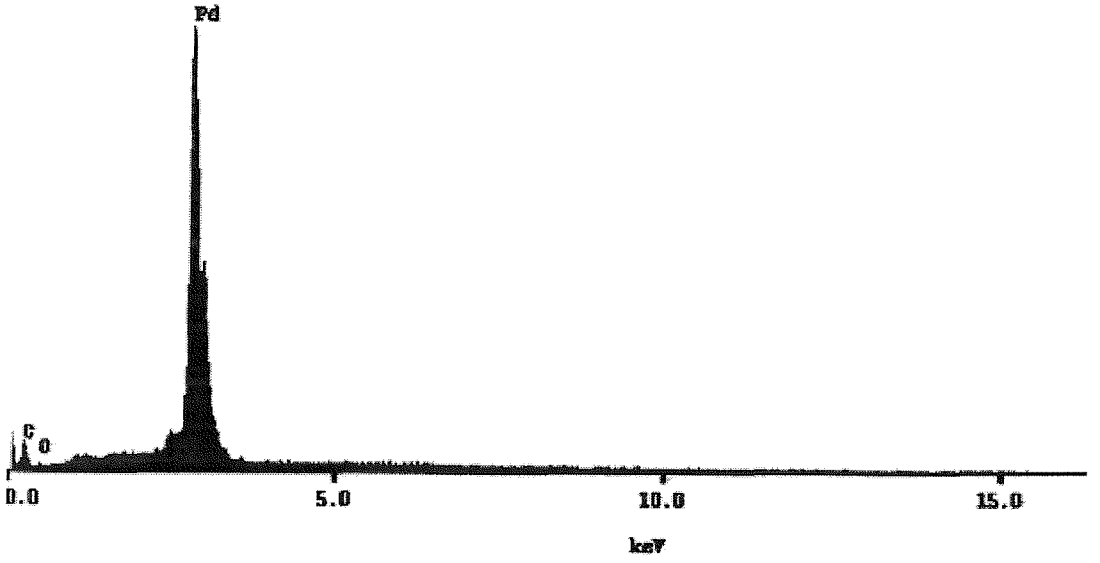

Figure 3.7 EDAX spectra of HI Pd prepared by steel reduction.

3.3.4.4 Small angle XRD

Small angle XRD was used to determine the repeat distance between pores and the order of the phase. The H_I Palladium prepared by steel reduction did not produce such a characteristic H_I (100) diffraction peak as the one observed for the H_I platinum reported in chapter 2. The X-ray diffractogram in figure 3.7 for H_I Pd (surface area 60 m^2g^{-1}) prepared from ammonium tetrachloropalladate as palladium precursor in the H_I phase of Brij 76 (60 wt%) shows only one weak and very broad diffraction peak The approximate position of the peak could be used to determine a hole to hole distance of ~8.5 nm which is in agreement with the TEM analysis.

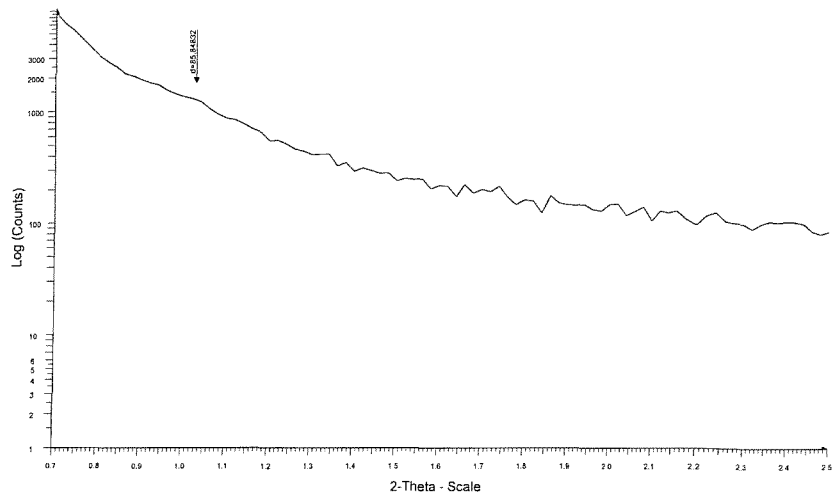

Figure 3.8 Small angle XRD pattern of the mesoporous palladium prepared by steel reduction. d_{100}= 85.8 angstroms. 60 wt % Brij 76, ATCP as palladium precursor.

3.3.4.5 Wide angle XRD

Wide angle XRD of mesoporous palladium prepared by steel reduction of ATCP in the H_I phase of Brij 76 (60 wt%) was recorded and compared to polycrystalline palladium (ICSD database). The diffractogram shown in figure 3.9 indicates that the H_I Pd has the same cubic structure as bulk palladium. The results are summarised in table 3.1.

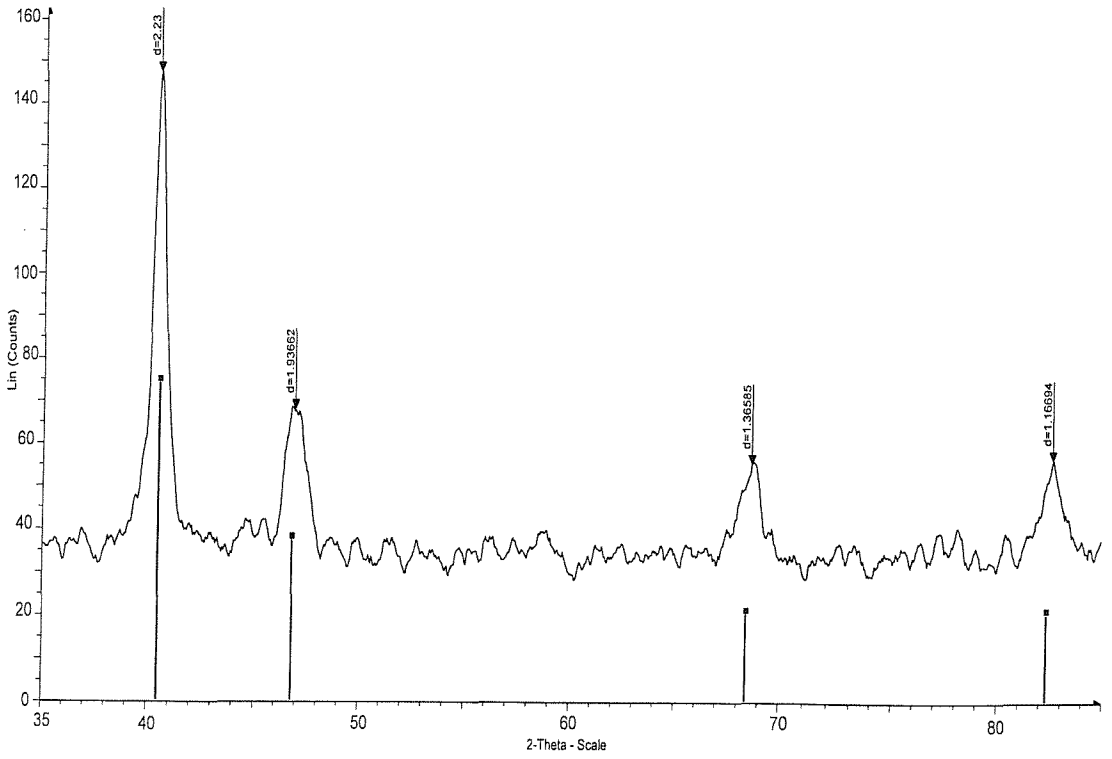

Figure 3.9 Wide angle XRD for mesoporous palladium, 60 wt % Brij 76, ATCP as palladium precursor (wider peaks) and polycrystalline palladium powders (straight line: ICDS data).

Peaks (hkl)	Polycrystalline Palladium		Mesoporous Palladium	
	2θ /degrees	Relative Intensity	2θ /degrees	Relative Intensity
111	40.119	100	40.05	100
200	46.659	60	46.9	47
220	68.121	42	68.2	37
311	82.100	55	82.2	39

Table3.1 XRD data for H_I Palladium prepared by steel reduction of ATCP in the H_I phase of Brij 76 (60 wt%) compared to ICDS values for polycrystalline cubic (Fm3m) palladium.

3.3.4.6 BET Nitrogen adsorption

Nitrogen adsorption studies were carried out on the mesoporous palladium prepared from Brij 76 using the two different palladium salts as precursors. In the case of ammonium tetrachloropalladate ATCP, the surface area and the type of isotherms associated for the different materials were compared to the isotherms obtained for the materials prepared while using the purer surfactant $C_{16}EO_8$ in the templating process.

Figure 3.10 shows typical adsorption/desorption isotherms for the mesoporous palladium prepared by the steel reduction of ATCP in the H_I phase of Brij 76(50 wt % room temperature) which is characteristic of a mesoporous material. Adsorption was small for low relative pressure and increased gradually at intermediate relative pressure. The presence of the hystresis loop, characteristic of a mesoporous material, indicates that the pore size and shape was not well defined.

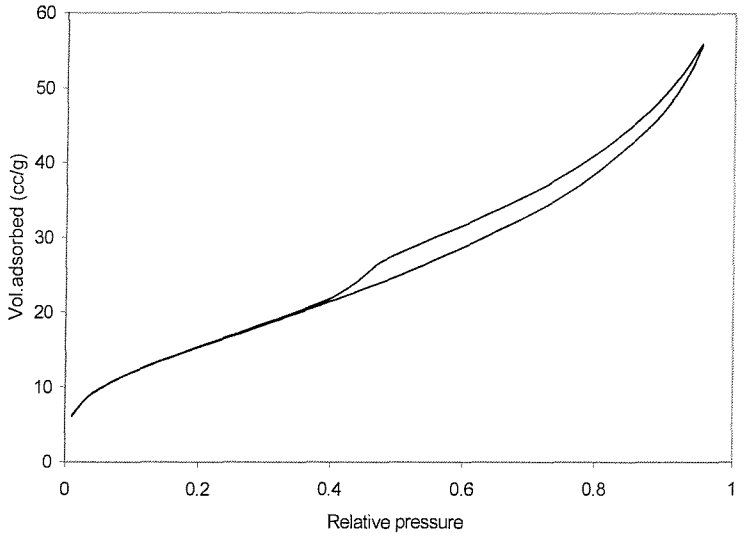

Figure 3.10 BET nitrogen adsorption/desorption isotherms for H_I Pd prepared by steel reduction of ATCP in the H_I phase of Brij 76 (50 wt %) at room temperature. Surface area = 60 m^2g^{-1} .

Using ATCP as palladium precursor, the influence of the initial templating composition and the reduction temperature were investigated to optimise the preparations and increase the surface areas of the materials. The results are reported on figure 3.11.

By increasing the reduction temperature from room temperature to 40 °C, an important decrease in surface area was observed for the compositions investigated. This can be explained by a much quicker reaction occuring at higher temperature. When the palladium is being deposited rapidly, the structure may grow regardless of the phase and produce a disordered material. At higher temperature, a change in the order of the H_I phase may also affect the direct liquid crystal mechanism.

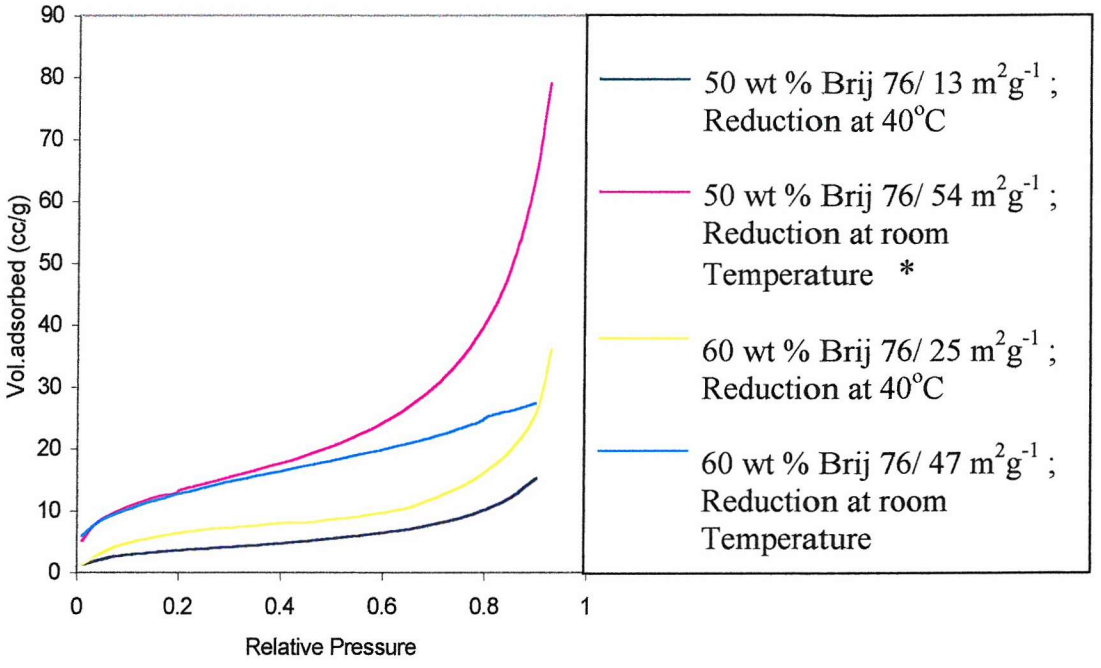

Figure 3.11 BET nitrogen adsorption on H_I Pd samples prepared using ATCP as palladium precursor while varying the amount of Brij 76 in the initial composition and the reduction temperature. * Average of 3 measurements each made from a different batch from the same material.

The material prepared from 50 wt % Brij 76 at room temperature was characterised by the highest surface area (54 m^2g^{-1}; average of 3 measurements made from a different batch). An inflection in the isotherm at intermediate relative pressure was observed characteristic of a material with a high degree of mesoporosity. Using ATCP as palladium precursor, the influence of using a purer surfactant such as $C_{16}EO_8$ on the chemical preparation of mesoporous palladium was investigated and the adsorption isotherms for the materials prepared are shown on figure 3.12.

For 65 and 75 wt % $C_{16}EO_8$ in the templating mixtures nitrogen adsorption studies revealed adsorption isotherms that are characteristic for materials with a high degree of mesoporosity. Surface areas of 44 and 60 m^2g^{-1} were obtained respectively.

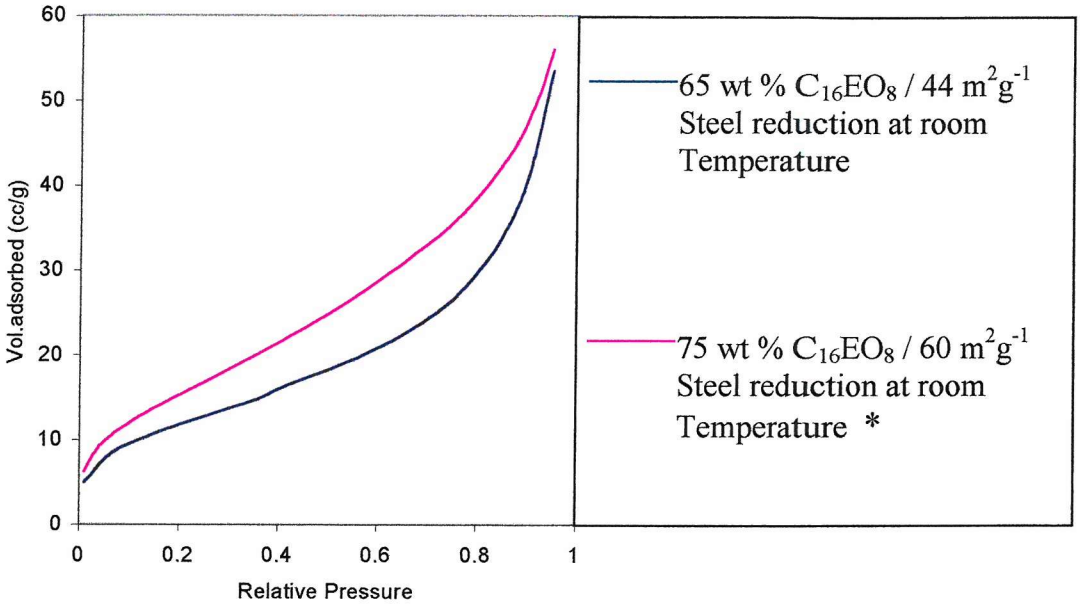

Figure 3.12 BET nitrogen adsorption on H_I Pd samples prepared using ATCP as palladium precursor and $C_{16}EO_8$ in the templating mixture.* Average of 3 measurements each made from a different batch from the same material.

For the material exhibiting the highest surface area 60 m^2g^{-1} prepared from 75 wt % $C_{16}EO_8$ in the templating mixture, the pore size distribution, calculated from the adsorption branch of the isotherm, showed a maximum in the distribution at 3.5 nm. (Dollimore and Heal pore size distribution; Appendix 1).

Figure 3.13 shows a narrow distribution of pores and indicates that the structure of the material obtained from $C_{16}EO_8$ is ordered.These results confirmed the TEM studies.

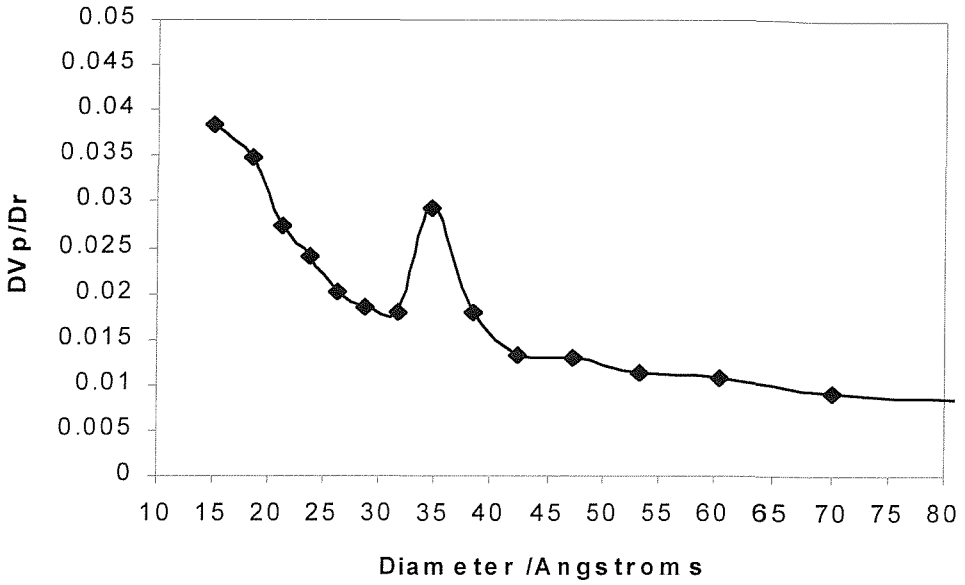

Figure 3.13 Pore size distribution for the H_I Pd powder prepared using ATCP as palladium precursors. 60 wt % C_{16} EO_8 in the templating mixture. Surface area of the H_I Pd material= 60 m^2g^{-1}.

When comparing the results obtained using $C_{16}EO_8$ to the results obtained for the H_I materials prepared from the much cheaper Brij 76 surfactant, similar surface areas were obtained; the H_I powder prepared from 50 wt % Brij 76 had a maximum surface area of 54 m^2g^{-1}, as reported on figure 3.11. This indicated that the purity of the surfactant was not the crucial parameter to optimise the preparation and increase the surface area of the material obtained. When compared to the production of mesoporous platinum described in chapter 2 where the purity of the surfactant was an effective parameter to increase the surface area of the HI Pt catalysts obtained, this tend to show that the preparation of mesoporous palladium was less affected by this parameter. This can be seen as an advantage for a relatively cheap production of high surface area Pd powders.

Figure 3.14 shows the nitrogen adsorption isotherms for the H_I palladium powders prepared by the chemical reduction of ATCP in the H_I phase of Brij 76 while using different reducing agents at room temperature. For the hydrazine hydrate reduction, the adsorption occurred at high relative pressure and the isotherms obtained were characteristic of materials with a small amount of mesoporosity. The maximum surface area of the material was measured to be 23 m^2g^{-1}. When compared to the H_I materials prepared from N_2H_4, the H_I Pd prepared by steel reduction was characterised by a much higher area (47 m^2g^{-1}) and the adsorption isotherm had a definite inclination at intermediate relative pressures characteristic of a mesoporous material. Steel reduction produces higher surface area materials than the hydrazine method.

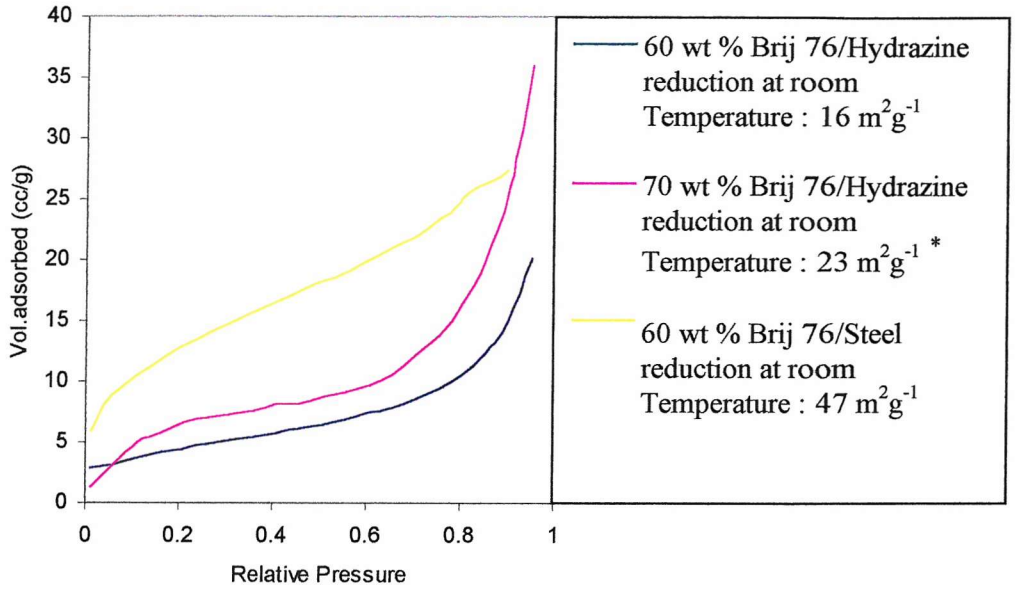

Figure 3.14 BET nitrogen adsorption isotherms for different palladium samples prepared by different reducing agents at room temperature.* Average of 3 measurements each made from a different batch from the same material.

Pore size distributions were calculated from the adsorption branches of the isotherms for the H_I materials prepared using the two reducing agents. The results are shown on figure 3.15.

When compared to the pore size distribution calculated for the HI Pd materials prepared from $C_{16}EO_8$ where a maximum was observed at 3.5nm, the distribution observed were characteristic of disordered materials with smaller pores. These results confirmed the TEM studies where smaller pores were observed when Brij 76 was used instead of $C_{16}EO_8$ in the templating mixture (steel reduction method).

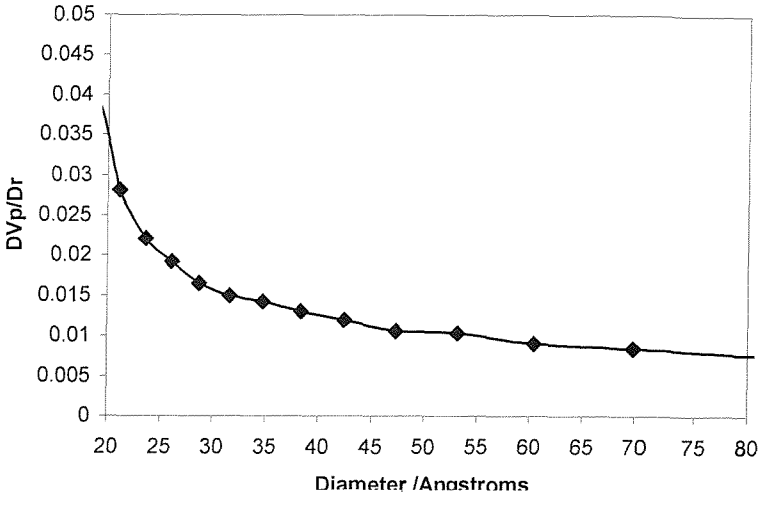

a) Hydrazine hydrate reduction. Surface area of H_I Pd =23 m^2g^{-1}

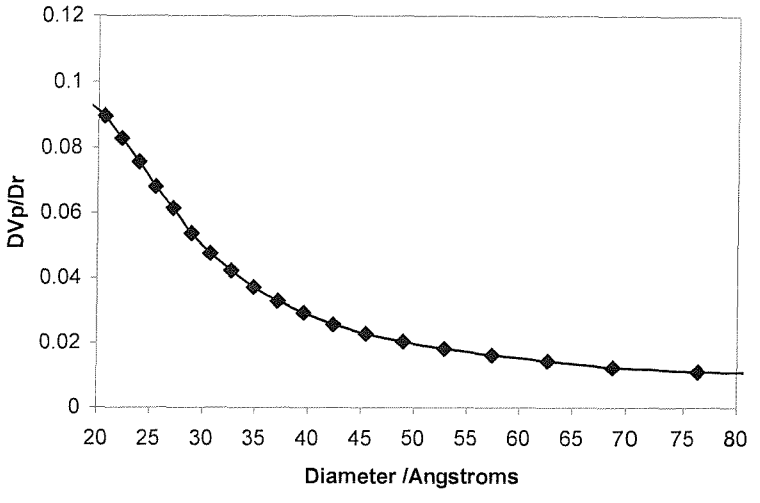

b) Steel reduction. Surface area of H_I Pd = 47 m^2g^{-1}

Figure 3.15 Pore size distribution for H_I palladium prepared using ATCP as palladium precursor. Reduction at room temperature by a) Hydrazine hydrate using 70 wt % Brij 76; b) Steel using 60 wt % Brij 76 in the templating mixture.

BET Nitrogen adsorptions were carried out on the mesoporous Pd catalysts prepared from Brij 76 while using palladium acetate as the palladium precursor. Using steel reduction, the influence of the initial templating composition and reduction temperature was investigated and the results are shown on figure 3.16. As for the production of H_I Pd from ATCP, increasing the reduction temperature from room temperature to 40 °C resulted in a smaller surface area of the powders prepared. The adsorption isotherms were characteristic of materials with a small degree of mesoporosity. (12 and 25 m^2g^{-1} for 50 and 60 wt % Brij 76 respectively).

The H_I materials prepared at room temperature from 50 and 60 wt % Brij 76 had much higher surface area, 49 and 63 m^2g^{-1} respectively with distinct inflections in the isotherms characteristic of materials with higher degree of mesoporosity.

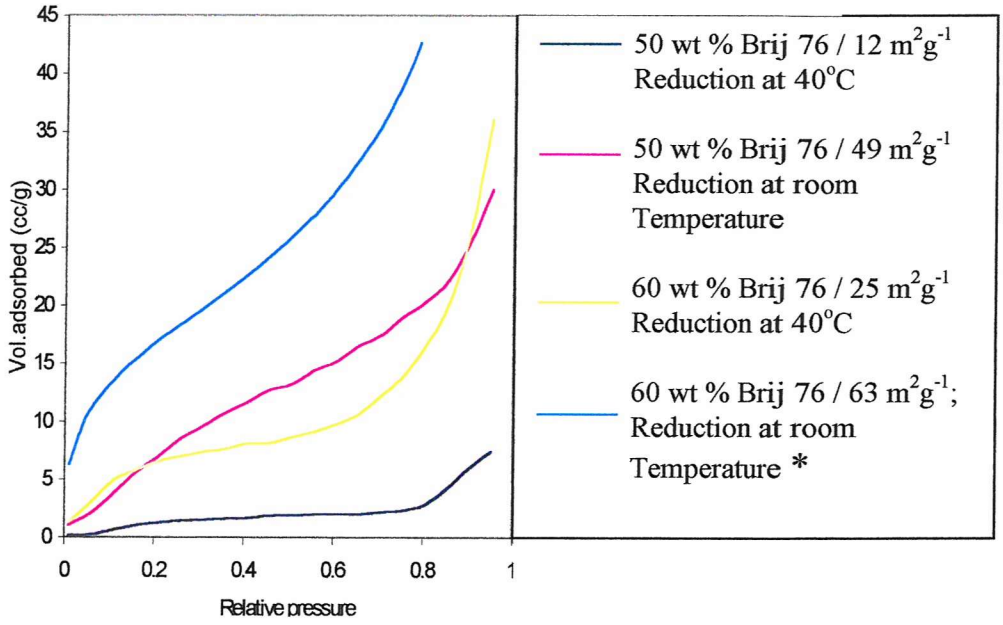

Figure 3.16 BET nitrogen adsorption on mesoporous Pd catalysts prepared from palladium acetate while varying the amount of Brij 76 in the templating mixture and the reduction temperature. * Average of 3 measurements each made from a different batch from the same material.

For the material with the highest surface area 63 m^2g^{-1} prepared from 60 wt % Brij 76 in the templating mixture, pore size distribution was calculated from the adsorption branch of the isotherm and revealed a maximum in the distribution at around 2 nm (figure 3.17) similar to the value calculated for the material prepared by steel reduction from ATCP. These results emphasised that similar materials were prepared by the steel reduction of either of the palladium precursors investigated in the HI phase of Brij 76.

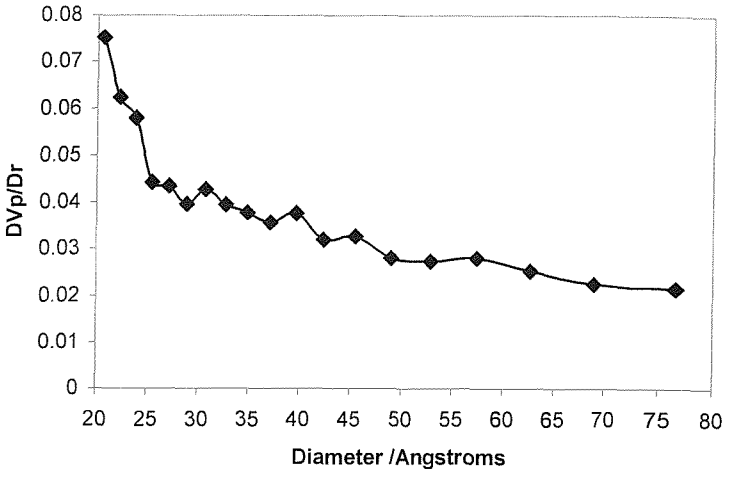

Figure 3.17 Pore size distribution for the HI Pd powder prepared using palladium acetate as palladium precursors. 60 wt % Brij 76 in the templating mixture. Surface area of the H_I Pd catalyst =63 m^2g^{-1}.

3.3.5 Discussion on the preparation of HI palladium

3.3.5.1 Methods of reduction

The most successful method for preparing mesoporous H_I palladium was the reduction of the palladium precursors by steel. In the presence of $C_{16}EO_8$, this produced a material with a regular pore structure and a surface area of 60 m^2g^{-1}. The materials prepared using the cheaper Brij 76 surfactant had a pore structure that was less ordered, but their surface area was similar in magnitude to the one obtained while using $C_{16}EO_8$ (63 m^2g^{-1} as optimum value). For comparison, BET nitrogen adsorption was carried out on commercially available palladium black and revealed a surface area of ~ 45 m^2g^{-1}. The hydrazine hydrate reduced material was porous but less ordered and had a lower surface area of 23m^2g^{-1}. As for the production of H_I platinum powders, a few hypotheses can be made as to why different materials were obtained by the different reduction methods investigated:

i) Rate of reduction

As mentioned in chapter 2 for the production of mesoporous platinum, the two methods investigated reduced the palladium precursors at different rates: the hydrazine reduction was very fast compared to the steel method. In the lyotropic phases used, the surfactant molecules are in a dynamic state and can reorganise over short time scales. Control of the reduction kinetic is believed to be a crucial parameter to obtain material with structure which is a cast of the host mesophase. In the case of hydrazine reduction (fast reduction even at room temperature), the structure may grow regardless of the phase and produce a disordered material.

ii) Effect of the reducing agent on the phase

Although the phase behaviour of the ethylene oxide based surfactant in the presence of the palladium precursors was known, the effect of the reducing agent was not characterised. As for the preparation of mesoporous platinum in the H_I phase of Brij 76, it would have been expected that hydrazine hydrate being strong reducing agent might alter the template mixture made of palladium precursor dissolved in the H_I phase of Brij 76 surfactant.

iii) Effect of reduction temperature

The results obtained while changing the reduction temperature for given Brij 76 compositions demonstrated that careful control of the reduction temperature was important for successful preparation of the H_I palladium catalysts for the palladium precursors investigated. This was already observed during the studies concerning the chemical reduction of a platinum salt (HCPA) in the H_I phase of the same surfactant. For the materials prepared from ATCP as palladium precursor, the surface areas of the H_I Pd powders were higher when steel reduction was carried out at room temperature for the various compositions studied. Increasing the reduction temperature to 40 °C tend to produce materials with much smaller surface areas. Similar behaviour was observed for the materials prepared from palladium acetate where the materials with higher surface areas were obtained by steel reduction at room temperature. As already noted, the rate of reduction during the templating process is important and can be modified by changing the temperature. Although in an stable H_I phase at 40 °C, the palladium is being deposited more rapidly at this temperature than at room temperature leading to materials with smaller surface areas. Altering the temperature was shown to be one of the key factor to optimise the reduction conditions in order to produce higher surface areas materials.

3.3.5.2 Comparison of the different surfactants investigated in the production of H_I palladium

Using the same palladium precursor (ATCP), H_I Pd materials were prepared while using Brij 76, a cheap commercially available surfactant, and the pure but very expensive $C_{16}EO_8$. These enabled us to investigate the effects of using a purer surfactant for the chemical preparation of mesoporous palladium. TEM studies showed that the material prepared from $C_{16}EO_8$ were nanostructured and BET adsorption revealed a maximum surface area of 60 $m^2g^{-1}$with a maximum in the pore size distribution at 3.5 nm which confirmed the TEM analysis (~ 4 nm pore diameter separated by ~ 4 nm walls). Although the H_I materials prepared from Brij 76 had a less ordered structure from the TEM micrographs, similar surface areas were obtained

using Brij 76 (54 m^2g^{-1} with smaller pores ~2nm separated by ~ 3nm walls from TEM measurements). Although the study was not exhaustive, these results demonstrated that it was possible to prepare high surface area Pd catalyst from cheap surfactant system and that the higher purity of $C_{16}EO_8$ did not have significant affects on the templating process. Moreover, using palladium acetate as precursor dissolved in the H_I phase of Brij 76, slightly higher surface area materials than the one prepared from $C_{16}EO_8$ were obtained (63 m^2g^{-1} as maximum value) which confirmed the ability to produce high surface area catalysts from cheap surfactant system which is an important criterion for a possible commercial production of palladium catalysts.

3.4 Conclusion and further work

In the previous chapter, the preparation of mesoporous platinum powders by direct liquid crystal templating was shown to be successful. The work described in this chapter showed that it is also possible to use lyotropic liquid crystal phases as moulds for the preparation of another mesoporous noble metal such as palladium.

Phase diagram studies of the palladium precursor (either ammonium tetrachloropalladate or palladium acetate) + Brij 76 + water, used in the preparation of mesoporous palladium, revealed that either ATCP or palladium acetate did not adversely affect the behaviour of the Brij 76 surfactant used. In fact the stability of the H_I phase was increased over a wider range of composition in the presence of the palladium precursor when compared to the binary Brij 76 + water system. Nevertheless similar stability was observed with temperature. The predominance of the higher curvature structure was attributed to an interaction between the ethylene oxide headgroups of the surfactant and the palladium precursor.

In the preparation of mesoporous palladium, numerous similarities to the preparation of mesoporous platinum were observed. It was shown that the method of reducing the palladium precursor was critical in obtaining a mesoporous structure. Reduction with steel sheet at room temperature was shown to be the most successful method of preparing high surface area H_I materials. The reduction method and the temperature were described as crucial parameters for the templating mechanism since the synthesis was sensitive to the rate of reduction Higher reduction temperature or stronger reducing agent tend to produce disordered mesoporous palladium materials characterised by smaller surface areas.

XRD studies confirmed that the palladium prepared was polycrystalline and had a cubic crystal structure which was in good agreement with the values for polycrystalline palladium (ICDS database). Studies of electrodeposited palladium have shown that similar mesostructures could be obtained as metallic films rather than powders [9].

Further work:

The aim of this chapter was to show that the chemical preparation of mesoporous palladium by direct liquid crystal templating is possible and was not an exhaustive study of the area. Indeed there are still a number of issues to be addressed:

- Both palladium precursors investigated were shown to be suitable precursors for the production of H_I Pd but other sources should be investigated. The criteria for being a suitable precursor is a high solubility in water without affecting the phase forming properties of the surfactant. Palladium(II)chloride could have been used for instance.

- As in the study of mesoporous platinum reported in chapter 2, other suitable methods of reducing the metal salt that do not disrupt the phase forming properties of the surfactant should be investigated. Reduction must be carried out at a correct rate for the direct templating process to occur and the reaction by products must be easily removed from the final mesoporous palladium.

- Our work concentrated on the production of mesoporous palladium from the H_I phase of Brij 76. Other surfactant from the brij series could be investigated (as reported for the preparation of the analogous mesoporous platinum). By varying the alkane chain length or the ethylene oxide head groups size of the surfactant, it should be possible to optimise the process and obtain nanostuctured palladium with higher surface area than the one reported.

3.5 References

1. C F Cullis, B M Willat, *J. of Catalysis*, 83, 267 (1983).
2. N Greenwood, A Earnshaw, *Chemistry of the Elements*, Pergamon Press (1997).
3. Microsoft Encarta-palladium, microsoft (1995).
4. J Tsuji, *Palladium reagents and catalysts*, J. Wiley and sons.528-545 (1995).
5. V Ponec, G C Bond, *Catalysis by metals and alloys*, Elsevier,38-41, 238-257 (1995).
6. R L Augustine, *Catalytic hydrogenation*, Marcel Dekker Inc., 36-39, 81-88 (1965).
7. Malleron, *Handbook of palladium catalysed organic reactions*, Academic Press,106 (1997).
8. P N Rylander, *Catalytic Hydrogenation over platinum metals*, Marcel Dekker Inc, 283 (1965)
9. S Guerin, Ph D thesis, Department of Chemistry, University of Southampton (1999).

Chapter 4

The preparation of mesoporous lead

4.1 Background and objectives

Mesoporous metals are of particular interests because of their potential applications as catalysts, sensors and batteries. As demonstrated in chapter 2, it is possible to prepare mesoporous platinum powders by the chemical reduction of platinic acid in the aqueous domain of cheap surfactants from the Brij series. The ability to electrodeposit platinum films that had an ordered mesoporous structure has led to considerable interests in investigating the electrochemical preparation of other metals. Recently, the preparation of mesoporous tin and palladium films have indeed been reported [1,2].

The subject of the work described in this chapter is an investigation into the chemical and electrochemical preparation of mesoporous lead from surfactants systems. The unique physical and chemical properties of lead make it one of the most widely used non ferrous metals [3]. Lead finds the major part of its uses in chemicals and compounds: most important are the lead alkyls used as antiknock additives in gasoline and the lead oxides used in acid storage batteries and pigments [3]. The continued dependence on lead is due largely to society's growing need for portable energy. At present it is the lead/acid battery which underpins the continued growth in lead consumption: more than 70 % of lead is consumed in the western world by this sector [4]. Analysis of the chemical properties of Pb and the commercial applications of its compounds indicate that the key properties of the element of commercial importance are:

- High ability to form carbon metal bonds useful in antiknock compounds
- Favorable oxidation-reduction potentials useful in electrochemistry or as catalysts for the unsaturated oils and chemicals used in coatings and inks
- Formation of crystal structures desirable in pigments
- Relatively low cost per mole despite its relatively high atomic weight

Finally, lead has also generated great interests because of its superconductivity properties. The metal has been used as a model in research on this phenomenon because it is relatively easy to prepare in very pure form and because its transition temperature to superconductivity is considerably higher than that of other metals [5]. The objectives of the work are described below:

1- To characterise the liquid crystal phase behaviour of polyoxyethylene surfactants Brij 76 + lead acetate + water mixtures. This is important to optimise the conditions for the preparation of mesoporous lead and to investigate the way in which lead acetate interacts with the surfactants. In a similar way, the ternary system $C_{16}EO_8$ + lead acetate + water was studied.

2- To investigate methods for the chemical preparation of mesoporous lead in terms of choice of lead precursors and reducing agents.

3- To investigate the electrochemical preparation of mesoporous lead.

4- To characterise the mesoporous lead obtained in terms of structure on a micron and nanometer scale, surface area, regularity of the structure for the chemical and electrochemical preparations. Quality of the deposit (uniformity, adhesion on the working electrode) was also important for the electrochemical method.

4.2 Experimental

The experimental work was divided into 4 sections.

The first of these was the study of the phase behaviour of ethylene oxide based surfactants in lead acetate solution. Following on from this, in order to optimise the process for the chemical reduction, several lead precursors and reducing agents were studied. Thirdly, the electrochemical preparation of mesoporous lead films was investigated and finally the materials were characterised.

4.2.1 Phase behaviour of ethylene oxide based surfactants in lead acetate solutions.

Phase diagrams were constructed using polarised light microscopy as outlined in Appendix 1. Ethylene oxide surfactants (Brij 76 and C16EO8) were used as supplied by Aldrich and Fluka respectively. Lead acetate (lead acetate trihydrate purity =99%) was used as supplied by Aldrich. Deionised water was used to make up the phases. In calculating the weight percentage of the surfactant with respect to the total water content, the water content of lead acetate was included. Mixtures containing lead acetate, surfactant and deionised water were made up by adding the surfactant to a solution of lead acetate. The phase diagrams that were prepared are summarised below and the exact compositions given in appendix 2 C.

- Phase diagram of Brij 76+ water+ lead acetate where the concentration of lead acetate was fixed with respect to the water content at 3.5 M.

- Phase diagram of $C_{16}EO_8$ +water + lead acetate where the concentration of lead acetate was fixed with respect to the water content at 3.5 M.

4.2.2 Chemical preparation of H_I lead

A number of different methods were used to prepare mesoporous lead from surfactant + lead precursor + water. Essentially they all involved the use of a reducing agent which reduced the lead (II) precursor to lead metal. Firstly the chemical preparation was used where different lead precursors and reducing agents were investigated. The electrochemical preparation of mesoporous was studied in the second approach.

4.2.2.1 Lead acetate as lead precursor

4.2.2.1.1 Hydrogen reduction

The first method was to use hydrogen gas which offered an attractive route to prepare lead because it was relatively cheap and easy to use. The same chemicals as the ones reported for the phase diagram were used.

An H_I phase containing lead acetate (0.5 g), water (0.4 g) and Brij 76 (0.5 g) was prepared by adding the surfactant to an aqueous solution of lead acetate. A homogeneous hexagonal phase was obtained by heating the mixture to ~70°C and cooling, while agitating on a vortex mixer. The reaction mixture was then flushed with argon several times before evacuating and placing under a hydrogen atmosphere at 40 °C for 4 hours.

4.2.2.1.2 Hydrazine hydrate reduction

Hydrazine hydrate was used as supplied by Aldrich. An H_I phase containing lead acetate (1.0 g), water (0.8 g) and Brij 76 (1.8 g) was prepared, as described previously, by adding the surfactant to an aqueous solution of lead acetate. To this phase was added another H_I phase containing hydrazine hydrate (0.24 g, 55 wt% N_2H_4), water (0.72 g) and Brij 76 (1.00 g). The two phases were mixed using a glass rod for ca.1 minute before leaving to stand for 2 hours at room temperature. The same experiment was repeated but only a few drops of hydrazine hydrate were added to the viscous H_I phase and left to stand for 2 hours at room temperature to check if the reduction was occuring.

4.2.2.1.3 Thiourea as reducing agent

In a electroless method for the deposition of lead on copper, thiourea was used as a complexing and reducing agent for the reduction of lead nitrate in water and DMSO [6]. Thiourea was used as supplied by Aldrich. An H_I phase containing lead acetate (1.0 g), water (0.8 g) and Brij 76 (1.8 g) was prepared by adding the surfactant to the aqueous solution of lead acetate. To this phase was added another H_I phase containing Thiourea (0.24 g, 55 wt% N_2H_4), water (0.72 g) and Brij 76 (1.00 g). The two phases were mixed using a glass rod for ca.1 minute before leaving to stand for 3 hours at 45 °C. The same experiment was repeated but thiourea was directly used as a powder added to the viscous H_I phase. In another set of experiments, the same procedure was followed while using $C_{16}EO_8$ (1.8g) to investigate the influence of this purer surfactant on the templating process. Thiourea was used in a similar way as reducing agent in an H_I phase with $C_{16}EO_8$ or as a powder (reduction for 3 hours at 45 °C)
Each time, the products were extracted and washed with acetone and water. The lead material obtained was then dried overnight at 40 °C.

4.2.2.1.4 Sodium borohydride as reducing agent

A 0.1M solution of sodium borohydride (Aldrich) was prepared by dissolving 3.78 g sodium borohydride in 10 ml deionised water. An H_I phase containing Brij 76 (13 g) 0.1M lead acetate solution (7g) was prepared by adding the surfactant to the aqueous solution of lead acetate (65 wt % surfactant). To this phase was added an H_I phase containing Brij 76 (8.6g), 0.1 M $NaBH_4$ solution (7g) which was separately prepared by adding the surfactant to the reducing agent solution (55 wt % surfactant). This mixture was added in tiny amounts with continuous mechanical stirring until the all mixture turned black and left for 3 hours at room temperature to make sure the reaction was completed. The surfactant was then extracted by acetone. The lead precipitate was then filtered, washed by water and left to dry overnight at 40 °C. The reduction of Pb^{2+} ions in the presence of $NaBH_4$ in the hexagonal domain of Brij 76 can be summarised as follows [7]:

$$Pb^{2+} + 2\ NaBH_4 + nL \longrightarrow (L)_nPb(BH_4)_2 + 2Na^+ \quad \{1\}$$

$$(L)_nPb(BH_4)_2 \longrightarrow Pb + H_2 + B_2H_6 + nL \quad \{2\}$$

where the surfactant molecule L acts as a ligand.

4.2.2.2 Lead nitrate as lead precursor

Lead nitrate was investigated as lead precursor (highly soluble in water) and was used as supplied by Aldrich (99% purity).

The same reducing agents as reported previously were investigated using the same experimental procedures. Before carrying out any reduction, the stability of the H_I phase lead nitrate + Brij 76 + water was checked under polarizing microscope to check that the change of lead precursor did not affect the H_I mixture.

4.2.2.3 Lead tetrafluoroborate as lead precursor

Lead tetrafluoroborate (50wt % solution in water) was finally investigated as lead precursor and used as supplied by Aldrich. Sodium borohydride was investigated as reducing agent. An H_I phase containing lead tetrafluoroborate (1.0 g), water (1.0 g) and Brij 76 (1.8 g) was prepared, as described previously, by adding the surfactant to an aqueous solution of lead acetate. To this phase was added another H_I phase containing sodium borohydride (0.24 g, 55 wt% NaBH4), water (0.72 g) and Brij 76 (1.00 g). The two phases were mixed using a glass rod for ca.1 minute before leaving to stand for 3 hours at 45 ^{o}C. The same experiment was repeated but only a few drops of sodium borohydrate were added to the viscous H_I phase.

4.2.3 Investigations into the electrochemical preparation of mesoporous lead

As mentioned before, Attard *et al.* [9] have developed a new method to obtain platinum thin films with a mesoporous structure. These films have been obtained by the electrodeposition of platinum on a gold electrode from a lyotropic liquid crystal templating solution. Reduction of the platinum on the gold electrode leads to the electrodeposition of a platinum film without losing the hexagonal structure of the liquid crystal. The authors claimed that the size of the pores and therefore the size of the wall thickness can be tailored by the choice of the surfactant, as well as the geometry of the liquid crystalline structure used for deposition.

Recently, the electrodeposition of mesoporous palladium films using the same templating mechanism has also been reported, hence our interest in using the electrochemical approach to produce thin mesoporous lead films.

Lead and lead alloy coatings can be applied to metallic substrates by a wide variety of techniques (dip coating, spray coating, hot and cold rolling, electrodeposition) and for a diversity of industrial purposes such as corrosion protection, architectural purposes, resists for printed circuit boards [9]. Lead may be electrodeposited from aqueous media at high cathodes efficiencies. Several electrolytes notably the fluoroborate, silicofluoride and sulphamate baths have achieved technical importance for commercial lead electrodeposition. Lead may be deposited from the aqueous solutions of its soluble salts such as the acetate and nitrate but the resultant electrodeposits have no technical usefulness because they are fibrous in texture and possess a degree of porosity. In fact, complex solutions (that is those containing complex anions such as the fluoroborate) are necessary to produce satisfactory smooth and coherent electrodeposits [9]. In our experiments, lead tetrafluoroborate was investigated as the lead precursor.

4.2.3.1 Experimental

Electrochemistry experiments were performed with a three electrode system under potentiostatic control, the cyclic voltammograms and current transients were recorded by computer using a software designed and written by P.R Birkin, Southampton University,UK.

4.2.3.2 Electrodes used

All counter electrodes were made of platinum gauze. They were washed with deionised water and flamed over a bunsen flame just before use in order to remove any contaminants.

The reference electrodes used were Saturated Calomel Electrodes (SCE). All electrochemical potentials are given with respect to the saturated calomel electrode. The SCE has a value of– 0.268 V comparatively to the widely used hydrogen reference electrode (RHE). The electrodes were checked against a commercial SCE electrode from Russel, a difference of less than +/- 4mV was tolerated for our experiments. All reference electrodes were stored in saturated potassium chloride solutions and rinsed with deionised water prior use.

The working electrode consisted of a 1mm ∅ Au disc electrode for the cyclic voltammetry studies. These electrodes were polished using sand paper and alumina with particle size ranging from 25 μm to 3 μm. After polishing the electrodes were rinsed with deionised water. Electrodeposition (current transient experiments) were performed on these electrodes and also on Au electrodes that were made by evaporating a thin layer of gold onto a glass substrate.

4.2.3.3 Cyclic voltammetry

Lead tetrafluoroborate PbTFB (50 % solution in water) was used as supplied by Aldrich. For the cyclic voltammetry in solution, 1 ml PbTFB solution was mixed with 1.75g deionised water to prepare a 0.77 M solution. For the cyclic voltammetry studies of the lead salt in the H_I phase of Brij 56, the templating mixtures were prepared by adding 3.25g Brij 56 to 2.75 g 0.77 M aqueous solution of PbTFB (55 wt% surfactant). The templating mixture was analysed using polarising microscopy to determine the phase. This was also confirmed by XRD studies. Cyclic voltammograms were recorded at room temperature at a scan rate of 20 mV/s.

4.2.3.4 Current transient experiments

During the electrodepositions, the current transients were carried out on the same templating mixture consisting of 55 wt % Brij 56 and 45 wt% (0.77 M) PbTFB in water at room temperature. Various deposition times depending on the geometry of the Au working electrode (surface area) were investigated.

4.3 Results and discussion

4.3.1 The phase behaviour of ethylene oxide based surfactants in lead acetate solutions

The phase transition data obtained for the ternary mixture Brij 76 + lead acetate + water are shown schematically in figure 4.1.The lead acetate concentration was fixed at 3.5 M for all the compositions. As previously, the boundaries were drawn based on visual observations of the phases down the polarised light microscope. The broad lines used to represent the boundaries reflect the only qualitative location of these boundaries.

Comparison of the binary system Brij 76 + water reported in chapter 2 (Figure 2.1a) with the lead acetate containing system revealed that lead acetate had a considerable effect on the phase behaviour of Brij 76. In the presence of lead acetate, no lamellar (L_α) nor cubic V_I phases were observed. The presence of a viscous H_I + I_I phase was also noted in the presence of lead acetate, this biphasic domain was observed directly and made a large contribution into the phase diagram. In summary:

- No lamellar (L_α) nor cubic V_I phases were observed in the presence of lead acetate.

- Presence of a viscous I_I phase in a significant biphasic H_I +I_I domain not observed in the binary system

- The H_I phase has similar stability with temperature as the H_I phase in the binary phase diagram but is stable over a wider range of composition (H_I domain shifts over a wider range of compositions when compared to binary mixtures).

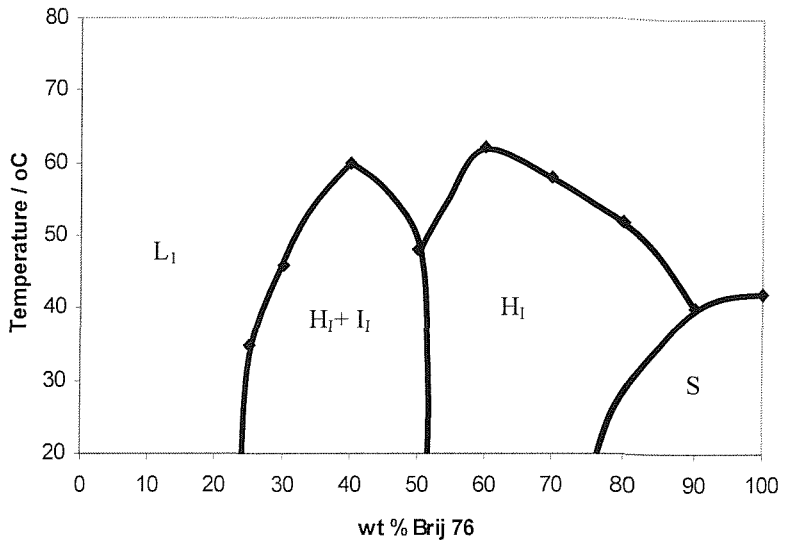

Figure 4.1 Phase diagram of Brij 76 + water + lead acetate where the concentration of lead acetate is kept constant at 3.5 M.

As reported previously, the change of behaviour for Brij 76 in the presence of lead acetate were not just limited to this surfactant. The transition data for for the ternary $C_{16}EO_8$ + lead acetate + water are shown schematically in figure 4.2. The lead acetate concentration was fixed at 3.5M for all the composition. Figure 4.3 shows the phase diagram for the binary system $C_{16}EO_8$ + water system reproduced from reference[10]. Addition of the lead precursor to the $C_{16}EO_8$ lyotropic system resulted in the stabilisation of the H_I phase over a wider range of composition.

In summary:

- The H_I phase was only stable up to 50 °C in the presence of lead stable (stable up to 60 °C in the binary system) but was stable over a wider range of composition (H_I domain shifted over a wider range of compositions when compared to the binary system).
- A small V_I domain was observed in the presence of lead acetate at higher compositions than the binary system, stable up to 50 °C.

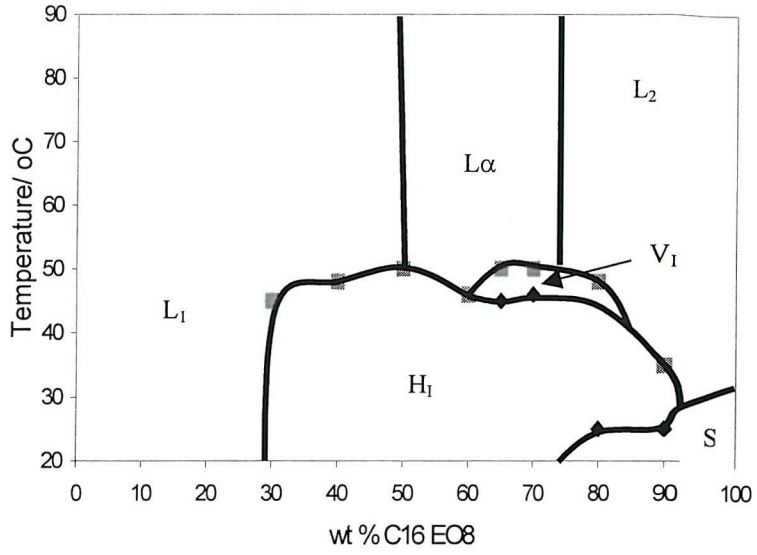

Figure 4.2 Phase diagram of the ternary system C16EO8+ lead acetate + water system where the concentration of lead acetate is kept constant at 3.5M.

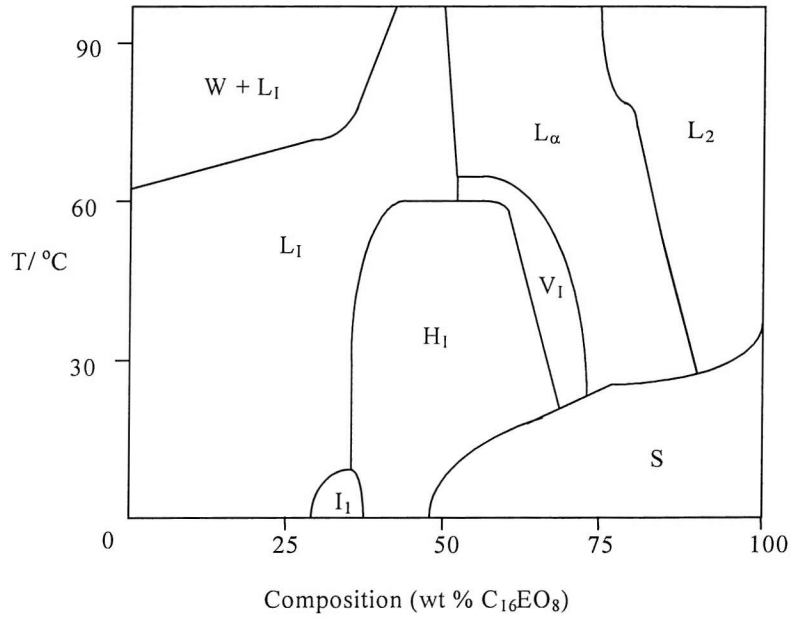

Figure 4.3 Phase diagram of the binary system C16EO8 + water system reproduced from reference [10].

4.3.2 Chemical preparation of mesoporous lead

The following describes the results that were obtained from the various chemical methods to prepare mesoporous lead. When the reduction was successful, the materials prepared were characterised by BET nitrogen adsorption, x-ray diffraction , SEM and TEM.

4.3.2.1 Chemical reduction investigations

Using lead acetate as lead precursor, Hydrogen gas and hydrazine hydrate were unsuccessful in reducing the lead precursor under the conditions used. Nevertheless, thiourea added as a powder reduced lead acetate in the lyotropic H_I phase of Brij 76 to produce after extraction an ordered mesoporous lead. Using the same reducing agent, the preparation of mesoporous lead by the chemical reduction of lead acetate in the lyotropic H_I phase of $C_{16}EO_8$ was successful.

Among the different reducing agents investigated, sodium borohydride dissolved in the H_I Phase of Brij 76 reduced successfully lead acetate but produce after extraction a porous but disordered material. This might be attributed to the gases evolved during the reduction process that affected the stability of the templating hexagonal phase or to the kinetics of the reduction (reaction very fast at room temperature).

Finally, the different reducing agents used for the chemical reduction of lead nitrate and lead tetrafluoroborate were unsuccessful in reducing the lead precursors under the conditions reported.

4.3.2.2 TEM

TEM was used to determine the order of the structure and pore morphology of the materials prepared and the results are shown in figure 4.4.

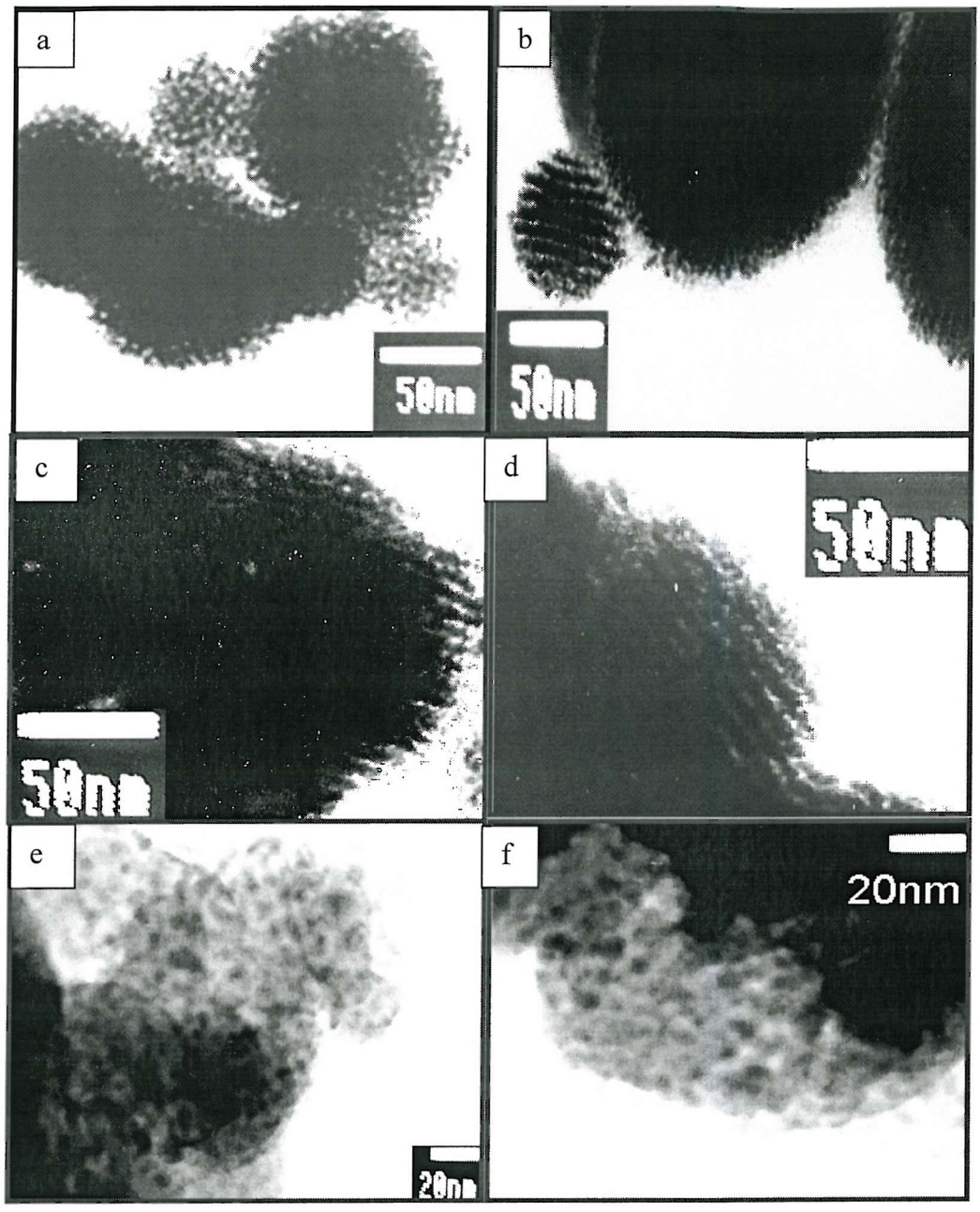

Figure 4.4 TEM micrographs of H_I Pb prepared by the chemical reduction of lead acetate a,b)in the H_I phase of Brij 76 using thiourea as reducing agent; c,d) in the H_I phase of $C_{16}EO_8$ using thiourea a reducing agent; e,f) in the H_I phase of Brij 76 (65 and 75 wt % surfactant respectively) using $NaBH_4$ as reducing agent.

The TEM micrographs depicted in figure 4.4(a,b) for the H_I Pb prepared from the chemical reduction of lead acetate in the H_I phase of Brij 76 (75 wt% surfactant) revealed a nanoporous structure with thick walls between the pores. Transmission of the electron beam through the larger particles was poor and the ordered H_I structure was only visible on the smaller particles. From the edge of the smaller particle observed on figure 4.4b, the repeat distance between the pores was measured from the micrographs as ca 9 nm. Nevertheless, as can be seen on figure 4.4a, the sample contained also disordered mesoporous structure.

The H_I Pb prepared from the lyotropic H_I phase of $C_{16}EO_8$ (75 wt % surfactant) revealed an ordered nanostructure (figure 4.4c,d), clearly visible on the edge of the sample. Particles ranged from 50-300 nm in size and tended to be elongated along the axis parallel to the cylindrical tubes of the H_I structure. As previously, other parts of the sample appeared porous but non ordered under the transmission electron microscope. The TEM micrographs depicted in figure 4.4 e,f) for the materials prepared from $NaBH_4$ while using the H_I phase of Brij 76 (65 and 75 wt% respectively) revealed a porous but non ordered structure. From the TEM analysis, the structure of the H_I lead powders produced by thiourea were much more ordered than the one obtained while using $NaBH_4$ as reducing agent.

4.3.2.3.SEM and EDAX

SEM pictures of the H_I Pb prepared by the chemical reduction of lead acetate dissolved in the H_I phase of Brij 76 using thiourea as reducing agent are shown on figure 4.5 a and b (magnification X 1000 and X10000 respectively). At high magnification, the SEM showed an average of small regular particles mixed with bigger irregular particles (left and bottom of the picture).

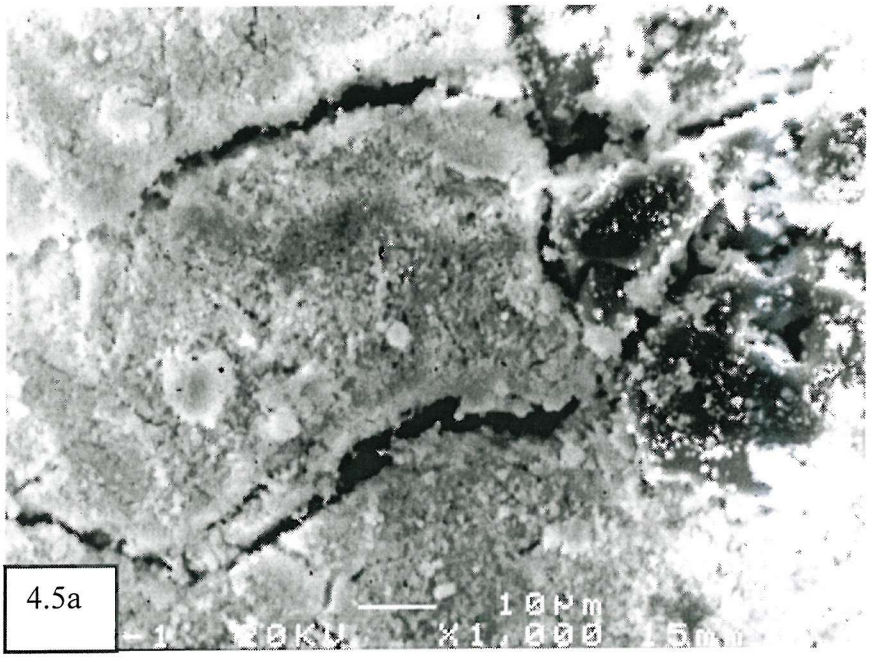

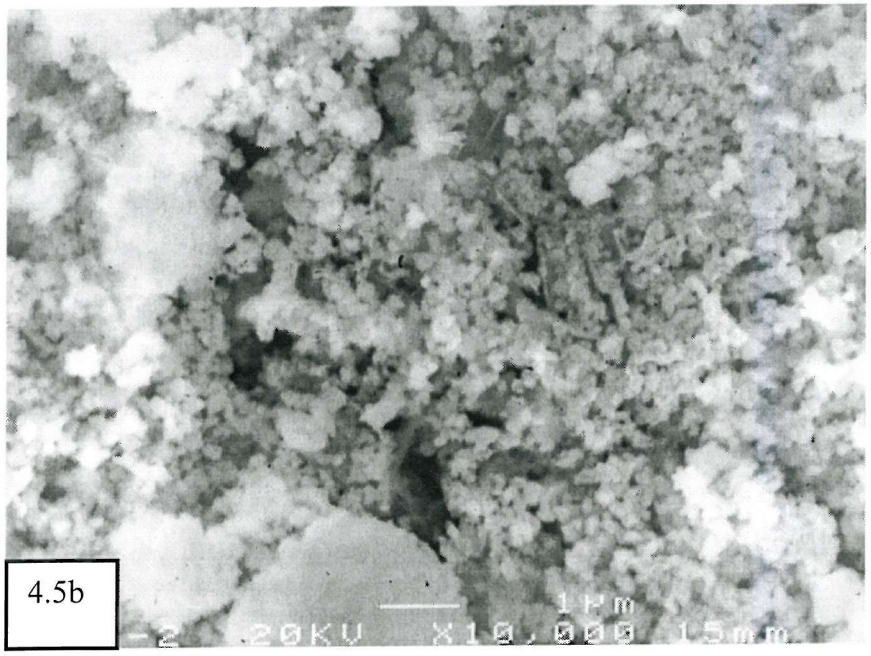

Figure 4.5 SEM picture of H_I Pb prepared while using thiourea as reducing agent
a) X 1000 b) X 10000

X- ray microanalysis revealed that the H_I lead prepared by thiourea method contained a small amount of oxygen on the surface (~ 3%) as depicted in figure 4.6 whereas the material prepared from $NaBH_4$ was more easily covered by oxygen (~ 10% as shown on figure 4.7).

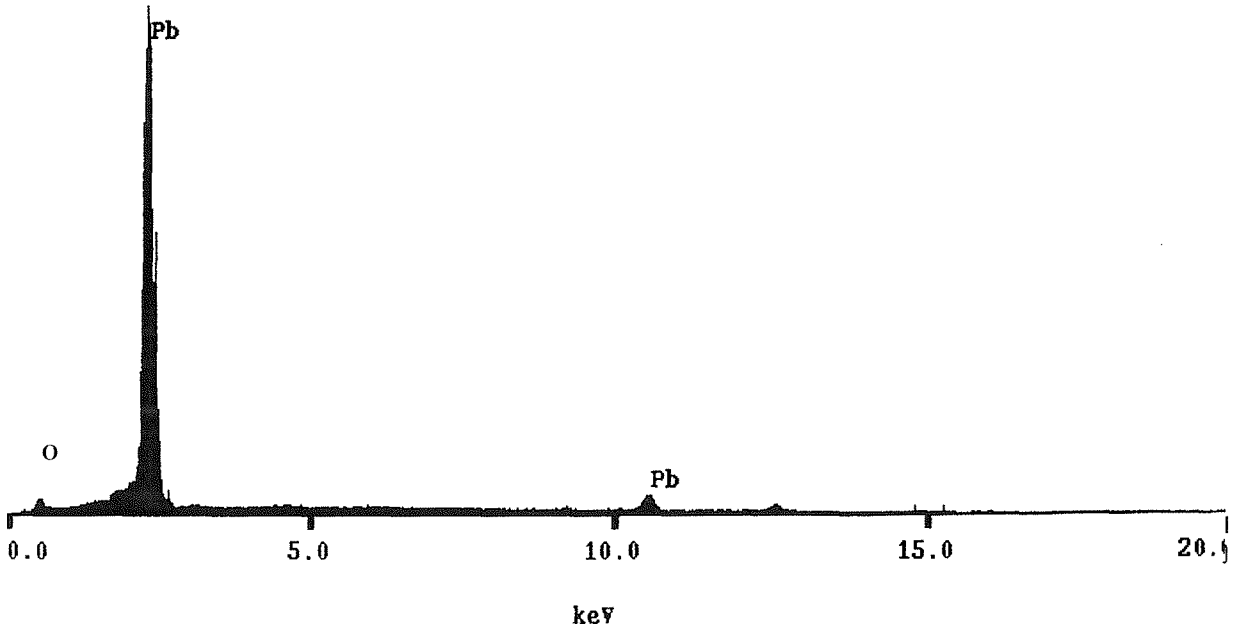

Figure 4.6 EDAX spectra of H_I Pb prepared while using thiourea as reducing agent.

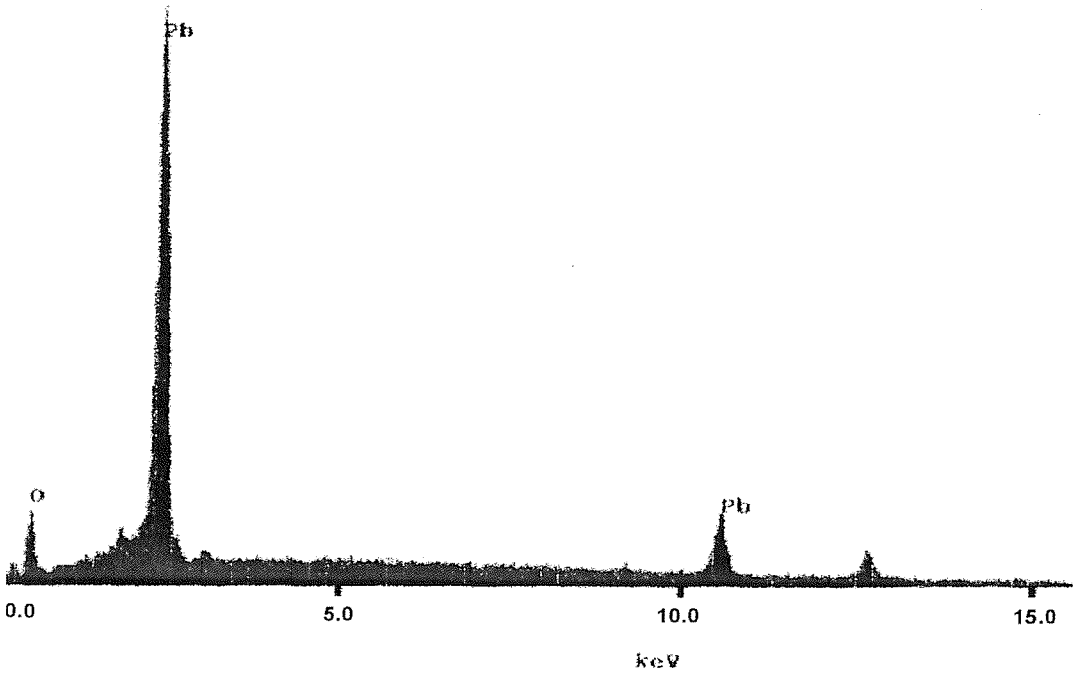

Figure 4.7 EDAX spectra of HI Pb prepared while using sodium borohydride as reducing agent.

4.3.2.4 Small angle XRD

In order to optimise the conditions for the chemical preparation of H_I lead using lead acetate and thiourea as reducing agent, small angle XRD were performed for various lead acetate/water/surfactant compositions before carrying out the reduction. The lead acetate concentration was kept constant at 3.5 M. Recognition of an ordered phase in terms of peak intensity, width at half height and repeat distance gave insight into the compositions to use to produce an ordered material.

Figure 4.7a) shows the small angle X- ray diffractogram of the H_I templating mixture lead acetate/water/Brij 76 where the amount of surfactant was fixed at 65 wt %.
In the small angle region, only one diffraction peak corresponding to an ordered H_I phase was observed. This corresponded to a repeat distance d_{100}= 6.7nm.
Figure 4.7b) shows the small angle XRD of the templating mixture lead acetate/water/ Brij 76 where the amount of surfactant was fixed at 70 wt %. In the small angle region, one diffraction peak corresponding to an ordered H_I phase with a lattice parameter of 6.9 nm was observed. When the amount of surfactant was fixed at 75 wt%, a lattice parameter of 7.2 nm was obtained (figure 4.7c).
Increasing the amount of surfactant in the templating mixture resulted in a slight increase of the lattice parameter. For the various compositions studied, small angle XRD confirmed the order of the H_I phase prior chemical reduction and their suitability for producing ordered materials as cast of the mesophase upon successful reduction and removal of surfactant.

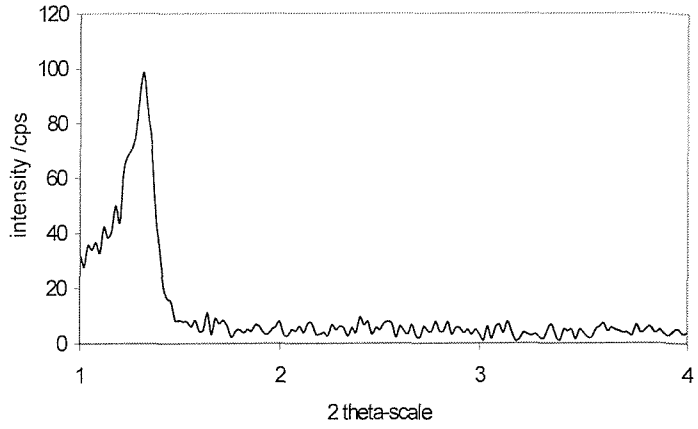

a) 65 wt% Brij 76: d_{100}= 6.7 nm.

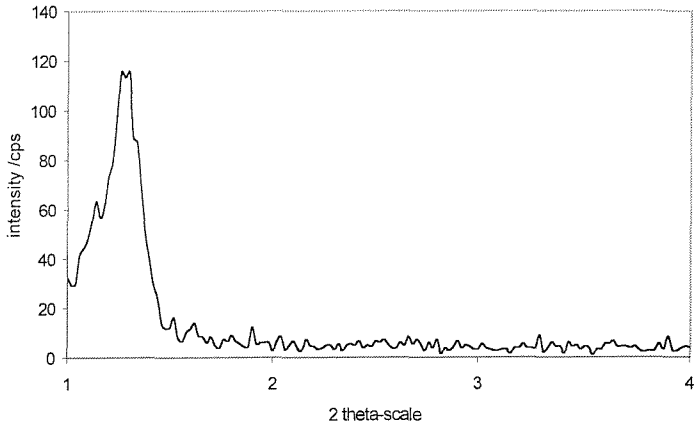

b) 70 wt% Brij 76: d_{100}= 6.9 nm.

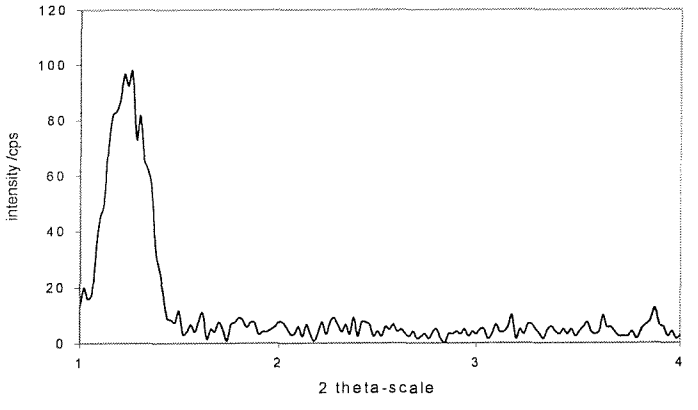

c) 75 wt% Brij 76: d100= 7.2nm.

Figure 4.7 Small angle X-ray diffractograms of the H_I templating mixture lead acetate/water/Brij 76 while varying the amount of surfactant.

Figure 4.8 shows the small angle X-ray diffractogram of the H_I Pb prepared by the chemical reduction of lead acetate dissolved in the H_I phase of Brij 76 by thiourea. Only a small inflection was observed in the diffraction pattern that corresponds to a weak 100 reflection (2θ = 1 degree) and confirmed the irregularity of the structure observed on the TEM micrographs.

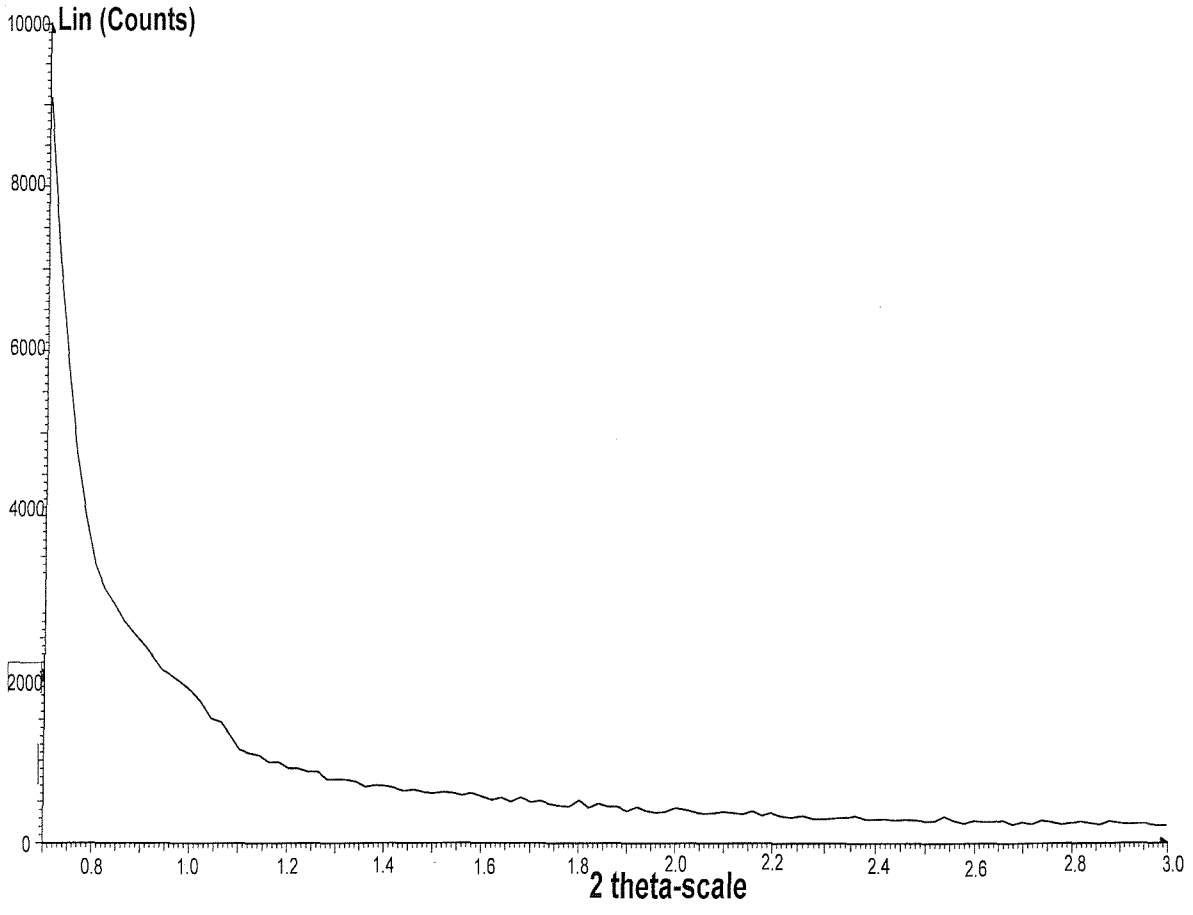

Figure 4.8 Small angle X-ray diffractogram of the mesoporous lead using thiourea as reducing agent. d_{100}= 90.4 Angstroms

4.3.2.5 Wide angle XRD

The wide angle X-ray diffractogram of mesoporous lead prepared using thiourea as reducing agent was recorded and compared to polycrystalline lead. The diffractogram depicted on figure 4.9 revealed the exact cubic crystal structure of the H_I lead powder prepared and was in excellent agreement with the ICDS values for polycrystalline cubic lead. The results are summarised in table 4.1.

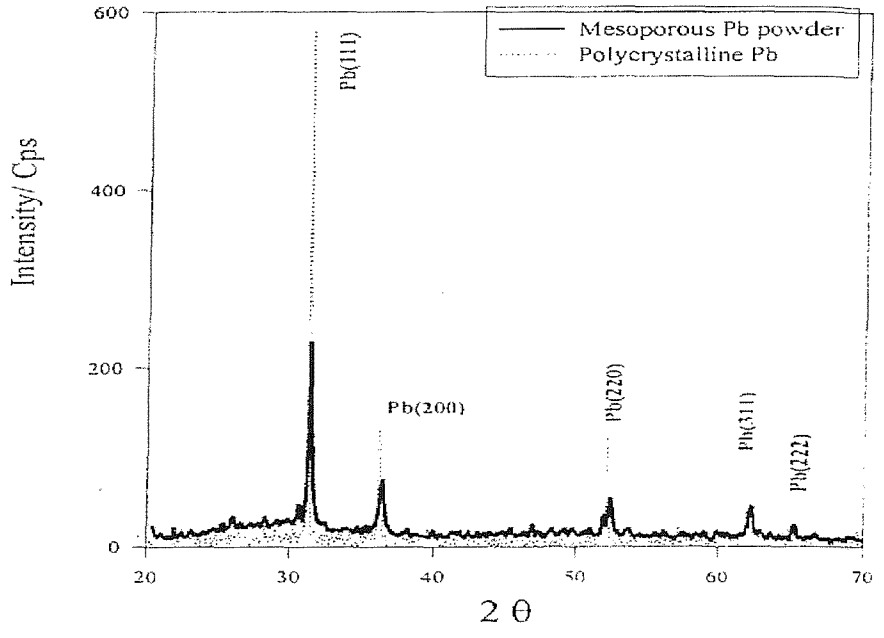

Figure 4.9 Wide angle x-ray diffractogram for mesoporous and polycrystalline lead powders.

Peaks (hkl)	ICDS Lead		Polycrystalline Lead		Mesoporous Lead	
	2θ /degrees	Relative Intensity	2θ /degrees	Relative Intensity	2θ /degrees	Relative Intensity
111	31.306	100	31.3	100	31.3	100
200	36.267	50	36.3	25	36.3	33
220	52.230	31	52.1	22.6	52.1	24
311	62.121	32	62.1	17.4	62.1	20
222	65.238	9	65.4	8.7	65.4	11

Table 4.1 XRD data for H_I Pb and polycrystalline Pb compared to ICSD values for crystalline cubic (Fm3m) lead.

4.3.2.6 BET Nitrogen adsorption

Nitrogen adsorption studies were carried out on the mesoporous lead prepared from Brij 76 and $C_{16}EO_8$ to study the surface area and the type of isotherms associated for different HI materials.

Figure 4.10 shows typical adsorption/desorption isotherms obtained for the mesoporous lead prepared by the chemical reduction of lead acetate in the H_I phase of Brij 76 (80 wt % Brij76, thiourea as reducing agent) which is characteristic of a material with only a small amount of mesoporosity that adsorbs at high relative pressures.

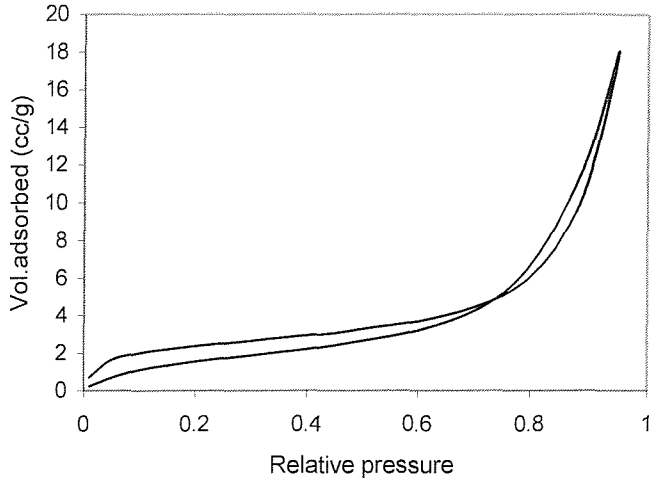

Figure 4.10 BET nitrogen adsorption/desorption isotherms for H_I Pb prepared using thiourea as reducing agent. Surface area = $9m^2g^{-1}$.

Figure 4.11 shows the nitrogen adsorption isotherms for the lead powders prepared using thiourea as reducing agent while varying the amount of Brij 76 in the initial templating mixture. For the samples prepared from 65 and 80 wt % Brij 76 in the templating mixture, the isotherms are characteristic of materials with lack of mesoporosity (adsorption only at high relative pressure, small surface area). For the materials prepared from 75 wt % in the initial mixture, an inflection in the isotherm was observed characteristic of a material with a small amount of mesoporosity (higher surface area observed 13 m^2g^{-1}, average of 3 measurements each made from a different batch).

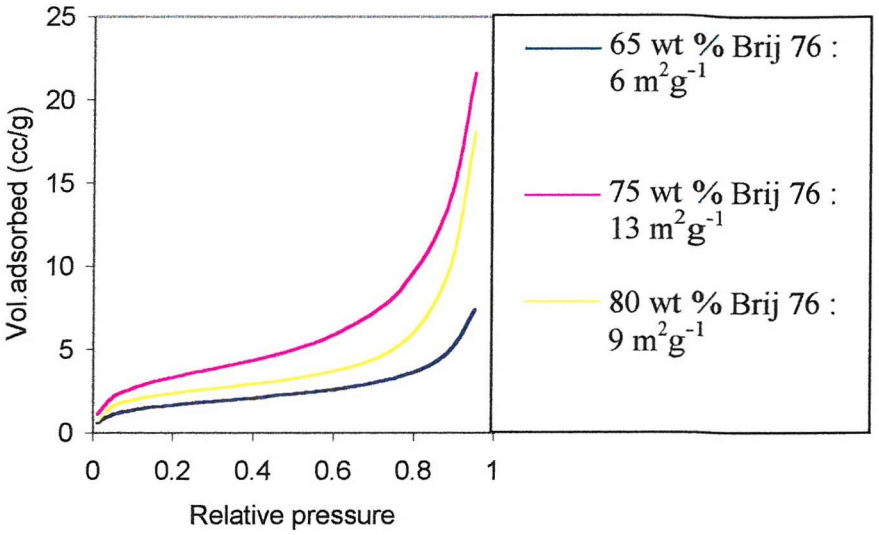

Figure 4.11 Nitrogen adsorption isotherms for different lead samples prepared while varying the amount of Brij 76 in the templating mixture.

Figure 4.12 shows the nitrogen adsorption isotherms for the lead powders prepared using thiourea as reducing agent while varying the amount of $C_{16}EO_8$ in the initial templating mixture.

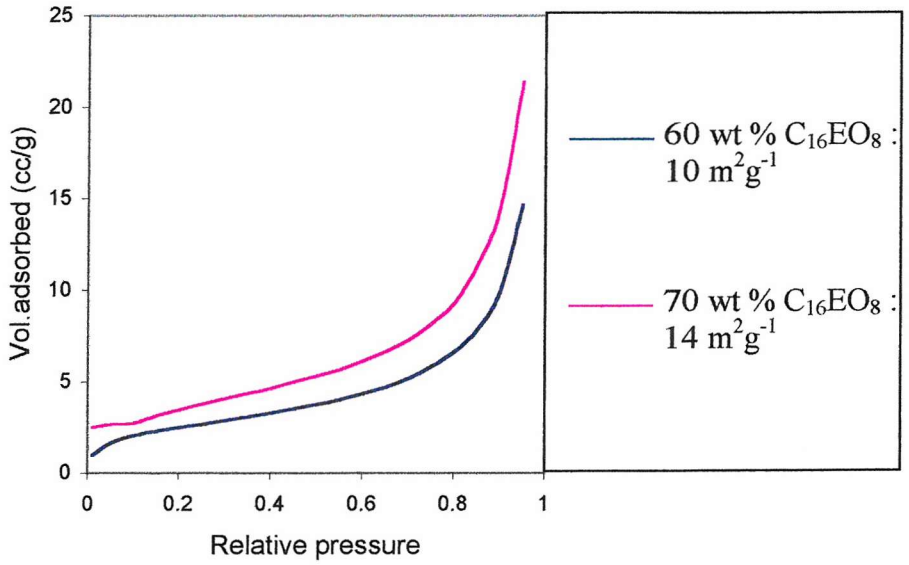

Figure 4.12 Nitrogen adsorption isotherms for different lead samples prepared while varying the amount of $C_{16}EO_8$ in the templating mixture.

The adsorption isotherms were similar to those observed for the materials prepared from Brij 76 and were characteristic of materials with only a small amount of mesoporosity (adsorption at relatively high relative pressure). An inflection in the isotherm was nevertheless observed for the material with the highest surface area measured prepared from 70 wt % $C_{16}EO_8$ (average of 3 measurements each made from different batch).

Figure 4.13 shows the nitrogen adsorption isotherms for the lead powders prepared using $NaBH_4$ as reducing agent while varying the amount of Brij 76 in the initial templating mixture.

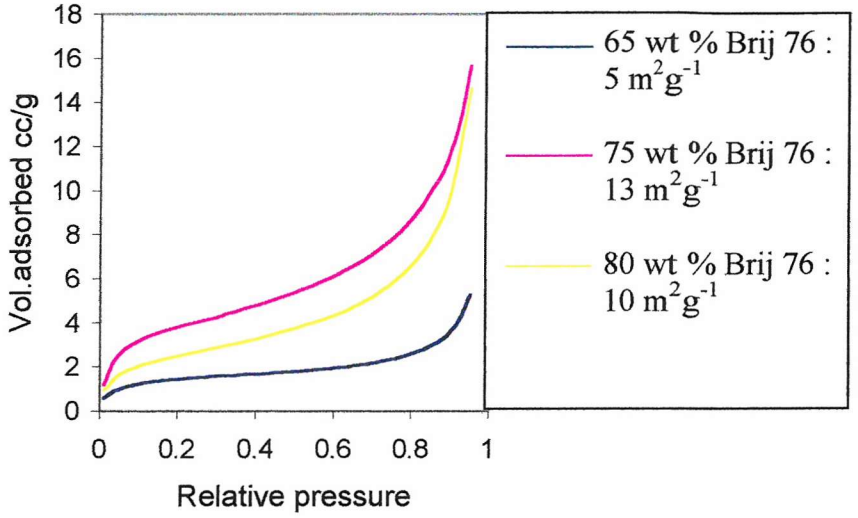

Figure 4.13 Nitrogen adsorption isotherms for different lead samples prepared while varying the amount of Brij 76 in the templating mixture.

The adsorption isotherms were similar to those obtained for the materials prepared while using thiourea as reducing agent characteristic of materials with only a small amount of mesoporosity (adsorption at relatively high relative pressure) even for the material with the highest surface area measured prepared from 75 wt % Brij 76 (13 m^2g^{-1} average of 3 measurements each made from different batch). Changing the reducing agent did not tend to affect the surface area of the lead powders prepared. When compared to the mesoporous platinum powders prepared previously, the materials were still characterised by small surface areas with a low degree of mesoporosity.

4.3.3 Investigations into the electrochemical preparation of mesoporous lead

The ability to electrodeposit platinum films that had an ordered mesoporous structure has led to considerable interest in investigating the preparation of other metals. Many papers have been devoted to the aqueous crystallization of lead on another metal. In weak acidic media, these deposits generally grow through a nucleation process which gives well-defined crystallites which are characterised by a cubic lattice (as determined by XRD) with different unit cell dimensions depending on the substrate metal [11,12]; the formation of metal layer observed in the electrodeposition of Pb on inert silver substrate from Cl^- solution was described for potentiostatic conditions; these results showed that in the complex study of the nucleation growth process, difficulties arise owing to the structure of the underlying metal itself [13]. The electrocrystallization of lead at a gold microelectrode has been reported in DMF solutions, the deposit grew through a 3D -nucleation diffusion -controlled process but the reduction mechanism of the divalent ion (Pb^{2+}) was not completely understood. In order to obtain mesoporous lead films, studies of the electrodeposition of lead in the presence of H_I phases have been undertaken. The characteristics of the electrodeposition from a solution containing the lead salt (i.e lead tetrafluoroborate PbTFB) and water are shown and compared with another solution containing the templating surfactant Brij 56, PbTFB and water. Simultaneously, the influence of using several types of gold substrates on the current transient is also shown. As for the chemical preparation of mesoporous Pb, XRD and TEM were used to analyse the regularity of the structure of the films obtained.

4.3.3.1 Cyclic voltammetry of the lead salt used for electrodeposition

The behaviour of the lead based solution was investigated by cyclic voltammetry. Lead tetrafluoroborate (50 % in water) was used as the lead precursor. Figure 4.14 shows a typical cyclic voltammogramm of 0.77 M PbTFB in water at a 1 mm Ø Au electrode. The potential was swept between 0 and -0.55 V (starting at 0 V) at 20 mV/s.

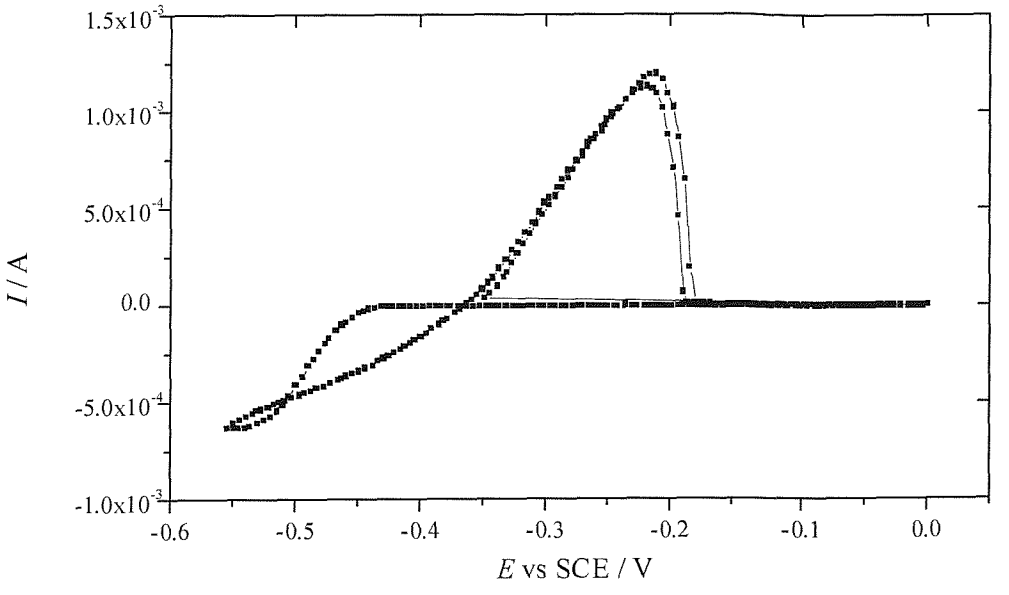

Figure 4.14 Cyclic voltammogram of 0.48 M PbTFB in water at 1mm Ø Au electrode. Cycled from 0 to -0.55V versus SCE at 20 mV/s. Room temperature.

It can be seen that hardly any current is passed on the cathodic scan until -0.4 V then the current increases suddenly around -0.45 V. The cathodic scan reveals the presence of a nucleation loop characteristic of the deposition of lead following the reduction Pb^{2+} to Pb^{O}.

Nucleation loops arise from the deposition of the material onto the electrode: deposition induces a physical change of the electrode surface and therefore the reactions at its surfaces are changed. This influences the current passed at the electrode. In this case, deposition of Pb onto Au occurs first, then when a monolayer of Pb has been deposited this is followed by the deposition of Pb onto Pb. Because the kinetics of the two reactions are different, the currents are different. When the cyclic voltammogram was stopped at -0.4V on the anodic scan and the electrode removed from the solution, it was shiny grey in appearance indicating the deposition of Pb on the surface. A positive current peak is present in the cyclic voltammogram during the anodic scan between -0.17 and -0.35 V which corresponds to the stripping of Pb from the electrode. As shown on figure 4.15, cyclic voltammetry of the same solution while sweeping the potential between 0 and -0.6V showed similar behaviour: the potential of the reduction of Pb^{2+} was the same, so was the magnitude of the current.

The main difference observed was a larger stripping peak, indicating that a greater amount of lead was deposited.

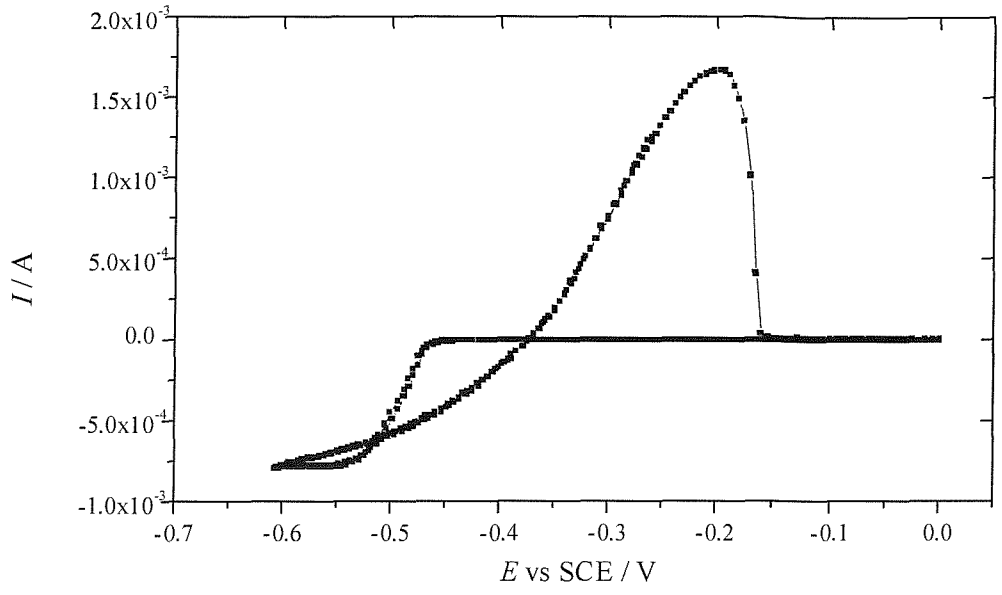

Figure 4.15 Cyclic voltammogram of 0.48 M PbTFB in water at 1mm Ø Au electrode. Cycled from 0 to -0.6 V versus SCE at 20 mV/s. Room temperature.

4.3.3.2 Cyclic voltammetry of the lead salt in the H_I phase of Brij 56

The lead precursor was mixed with the nonionic surfactant to produce the templating mixture used for the electrodeposition of the mesoporous films. The phase behaviour of Brij 56 in water was reported in chapter 2. For 55 wt % Brij 56, a stable H_I phase was observed from 25 °C to 62 °C. The phase behaviour of Brij 56 + PbTFB +water mixture (55 wt% surfactant) indicated that the lead precursor did not affect the H_I mesophase, the H_I phase was even present at higher temperature from 20 to 74 °C.

The templating mixture was firstly studied by cyclic voltammetry to investigate the effect of the addition of the surfactant on the cyclic voltammograms. Figure 4.16 shows a typical cyclic voltammogram of the H_I templating mixture made of 55 wt % Brij 56 and 45 wt % PbTFB (0.48 M solution in water) at a 1 mm Ø diameter Au electrode. The potential was swept between 0 and -0.5 V starting at 0 V at 20 mv/s.

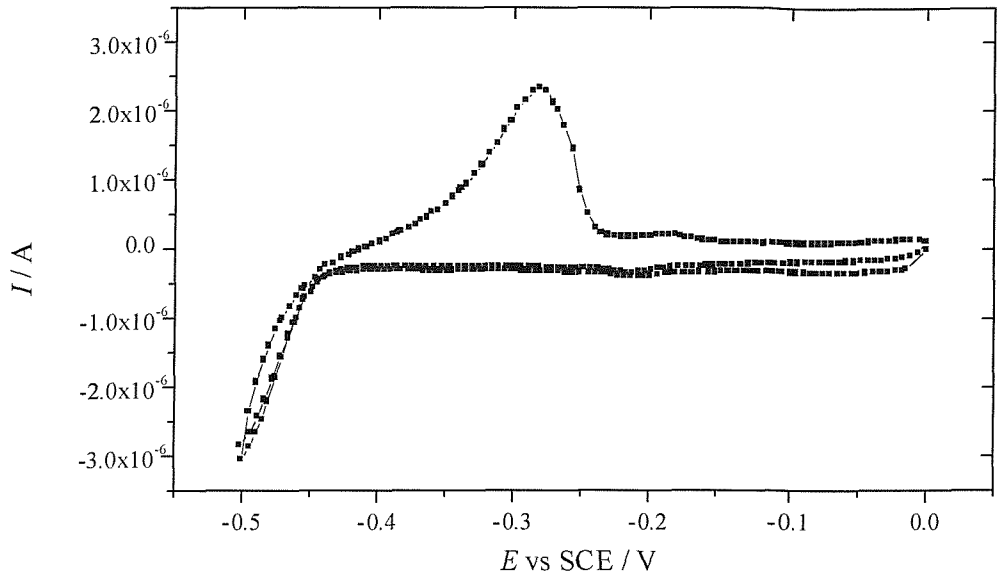

Figure 4.16 Cyclic voltammogram of the HI templating mixture made of 55 wt % Brij 56 and 45 wt% PbTFB (0.48 M in water) at 1mm Ø Au electrode.
Cycled from 0 to -0.5 V versus SCE at 20 mV/s. Room temperature.

It can be seen that hardly any current is passed on the on the cathodic scan until -0.45V then the current increases suddenly to reach a maximum value at -0.5V. Studies in solution showed that scanning towards a more reducing potential from -0.55 to -0.6 V for instance did not alter the shape of the voltammograms obtained.

As shown on figure 4.17 a different behaviour was observed in the presence of Brij 56: when the potential was scanned between 0 and -0.55 V, a nucleation loop was observed on the reduction peak (similar magnitude as before with a maximum at -0.52 V) but three stripping peaks were observed during the anodic scan between -0.2 and -0.4V. For the conditions reported, it is suggested that these stripping peaks observed correspond to different lead crystal structures deposited during the nucleation process which could be confirmed by wide angle XRD studies.

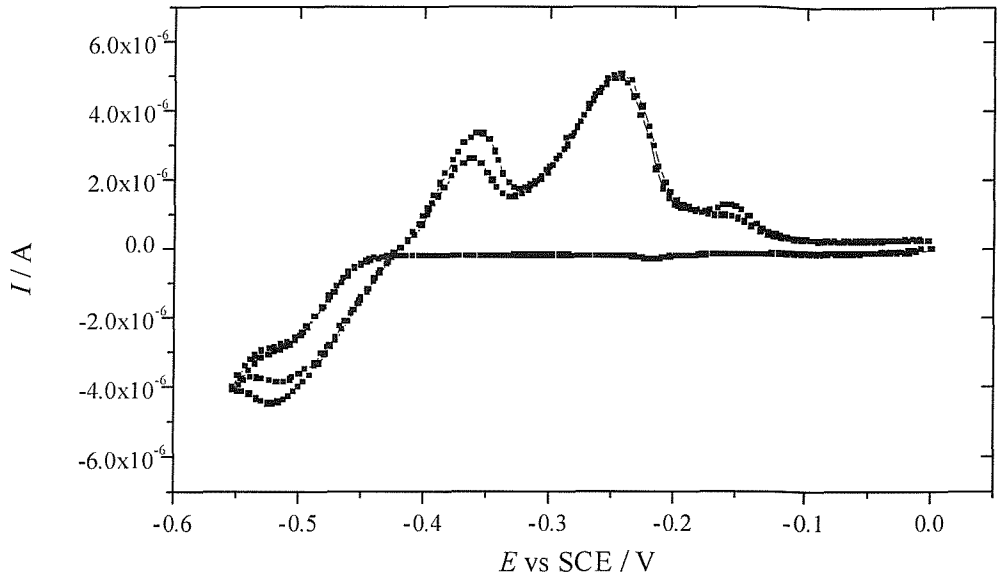

Figure 4.17 Cyclic voltammogram of the HI templating mixture made of 55 wt % Brij 56 and 45 wt% PbTFB (0.48 M in water) at 1mm Ø Au electrode.
Cycled from 0 to -0.55 V versus SCE at 20 mV/s.

When compared to the cyclic voltammogram in solution (figure 4.14) while sweeping the potential between the same upper and lower values (0 and -0.5V respectively), no loop was recorded in the presence of Brij 56 but the main difference is the magnitude of the reduction current which is much smaller (~1000 times smaller in the presence of surfactant). A positive current is present during the anodic scan between -0.25 and -0.4 V (stripping of Pb from the electrode) with a magnitude much smaller than the one recorded in the absence of surfactant.

Due to the much higher viscosity of the template mixture compared to the solution, slower diffusion through the lyotropic phase is thought to be responsible for the small current recorded. Similar behaviour was indeed reported during the electrodeposition of mesoporous palladium films from liquid crystal templates [2].

4.3.3.3 Aqueous electrodeposition from lead tetrafluoroborate solution

The electrodeposition of lead onto a 1mm Ø diameter Au disc electrode is described. From the cyclic voltammograms obtained in solution (0.77 M PbTFB in water), -0.5 V was selected as the potential to carry out the electrodeposition. Figure 4.18 shows a typical current transient obtained during the electrodeposition of Pb from 0.77 M PbTFB in water at room temperature. From the current transient, it can be seen that the reduction current rises sharply to -2 mA, as a result of double layer charging immediately after the potential step and then decreases quickly to -1.25 mA, where nucleation is believed to start. After 20 s, the reduction current increases gradually (~ plateau until 100s) then increases even more from 100 to 200 s. The rate of electrodeposition is still increasing in this region (no steady state reached in this short period of time) suggesting a rough deposit on the Au surface.

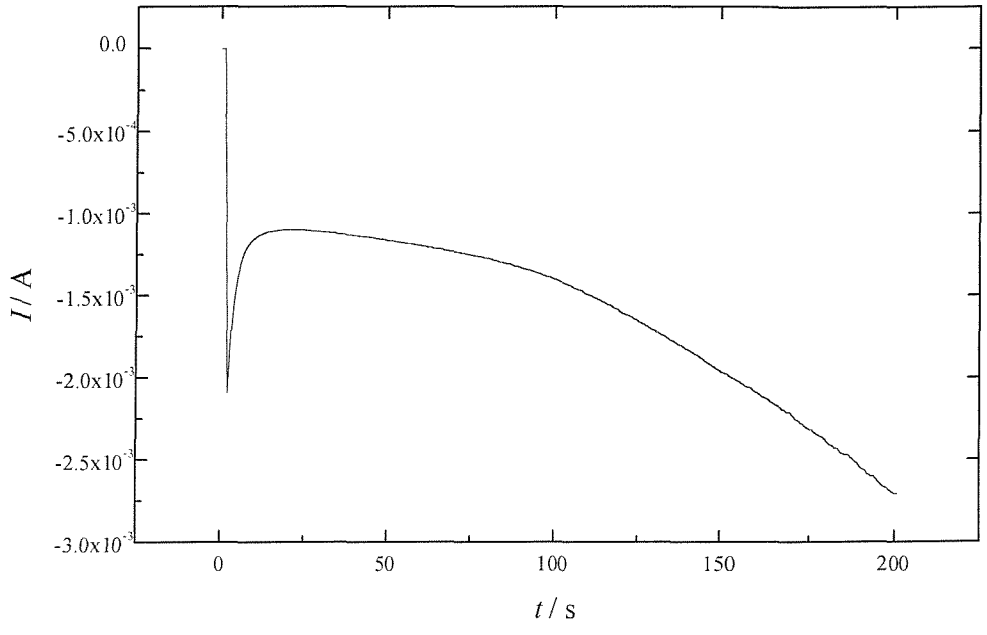

Figure 4.18 Typical current transient for the electrodeposition of Pb from 0.77 M PbTFB in water at -0.5 V/SCE on a 1mm Ø Au disc electrode at room temperature. Charge passed during deposition ca.4 mC

4.3.3.4 Electrodeposition of H_I Pb using the lyotropic hexagonal phase of Brij 56

The following describes the different lead electrodepositions carried out onto different substrates. The electrodeposition of mesoporous pb onto a 1mm Ø diameter Au disc electrode and onto Au evaporated on a glass substrate is described. The latter made the analysis by XRD and TEM possible. From the cyclic voltammograms obtained in the presence of Brij 56, -0.5 V was selected as the potential to carry out the depositions. In the presence of Brij 56, cycling between 0 and -0.5 V revealed only one stripping peak which was assumed to correspond to only one form of lead crystal structure deposited on the surface of the electrode.

Figure 4.19 shows a typical current transient obtained during the electrodeposition of Pb from a templating mixture containing 55 wt % Brij 56 and 45 wt % PbTFB (0.77 M in water) at -0.5V on a 1 mm Ø Au disc electrode. Knowing the surface area of the electrode (0.785 mm^2) a current density of 0.382 $mAcm^{-2}$ was measured.

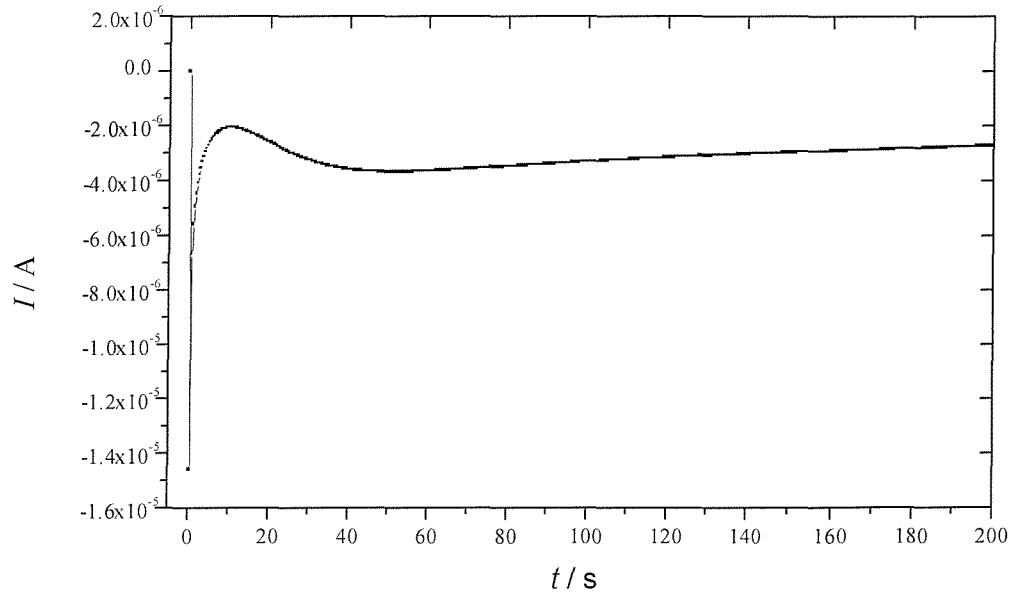

Figure 4.19 Typical current transient for the electrodeposition of mesoporous Pb from 55 wt % Brij 56 + 45 wt% (0.77M in water) at -0.5V/SCE on a 1 mm Ø Au electrode at room temperature. Charge passed during deposition ca. 0.5 mC

From the current transient, it can be seen that the reduction current rises to ca.-15 μA, as a result of the double layer charging immediately after the potential step and then decreases very sharply to -3μA, where nucleation is believed to start and finally reaches a plateau at -4μA after 40 s. After 200 s deposition, the electrode was covered by a shiny and adherent grey film visible on the surface. When comparing with the aqueous deposition on the same electrode, much smaller currents were recorded in the presence of the Brij 56 surfactant due to slower diffusion through the lyotropic H_I phase.

Figure 4.20 shows the current transient obtained during the electrodeposition of mesoporous Pb on gold evaporated on glass (1 cm^2 surface area). These substrates were used to carry out XRD and TEM studies. This time, the current rises quickly to a maximum at ca. -480 μA decreases quickly to -300μA over 500 s and then decreases to reach -150 μA after 3600s. For a 1 cm^2 surface area electrode, a current density of 0.25 $mAcm^{-2}$ was measured.

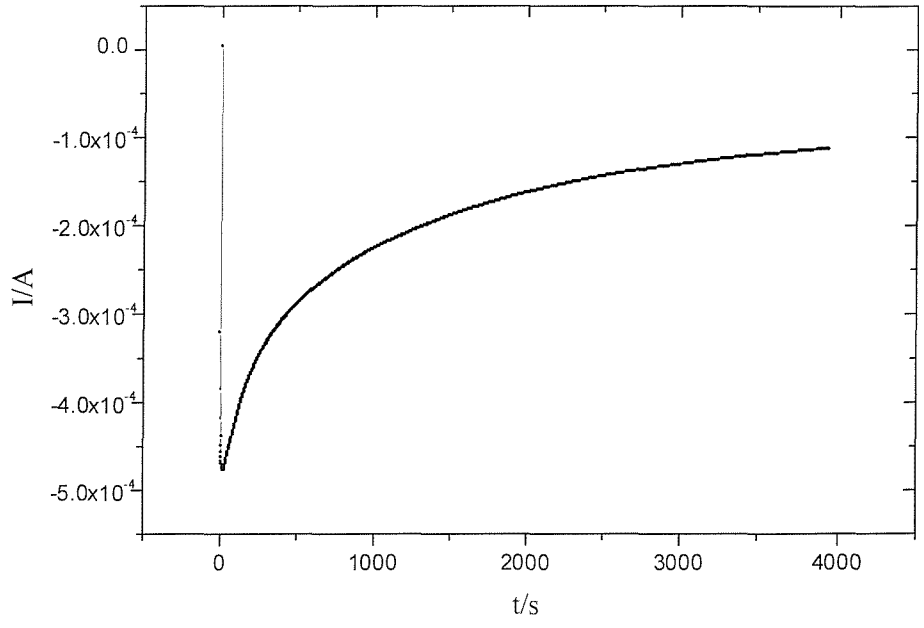

Figure 4.20 Typical current transient for the electrodeposition of mesoporous Pb from 55 wt % Brij 56 + 45 wt% (0.48 M in water) at -0.5V/SCE on an Au substrate made from evaporation of Au on glass. Electrode area 1cm^2.Charge passed during deposition ca.750 mC

The curve shown in figure 4.20 presents a noticeable difference to the one shown in figure 4.19 for the electrodeposition of H_I Pb on Au disc electrode. In both cases, the current minimum is reached very quickly following a huge drop but in the case of the disc electrode the current reaches a plateau very rapidly.

This can be explained by a slower nucleation and growth process ; alternatively the area covered could also account for this difference in the timescales.

4.3.3.5 Analysis of the films obtained

The lead deposit on gold has been stored under nitrogen atmosphere to prevent oxidation and then was analysed by XRD and TEM. The small angle XRD on figure 4.21 for the template mixture and the deposit obtained with Brij 56 shows only one diffraction peak in the small angle region with a lattice parameter of 6.2 nm (lead deposit).

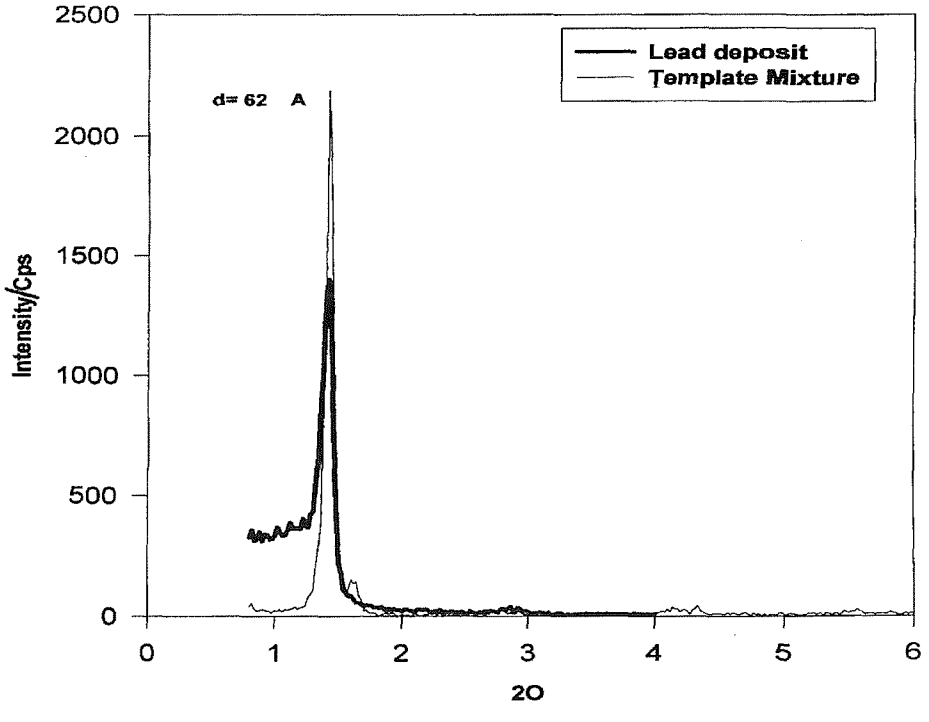

Figure 4.21 Small angle XRD H_I Pb and template mixture

d_{100}= 6.2 nm (lead deposit)

The TEM micrographs on figure 4.22 reveals the porosity of the material obtained using Brij 56 in the templating mixture.

Figure 4.22 TEM micrographs of H_I Pb electrodeposited from 55 wt % Brij 56 + 45 wt% (0.77 M in water) at -0.5V/SCE on an Au substrate made from evaporation of Au on glass.

4.3.4 Discussion on the preparation of H_I lead

4.3.4.1 Chemical preparation of H_I lead

The most successful method for preparing mesoporous H_I Pb was the reduction of lead acetate by thiourea. TEM studies of the material revealed a mesoporous structure with only a small amount of regularity (porous but disordered). The lack of long range regularity in the structure was shown by XRD where only a weak diffraction peak was observed in the small angle region. The surface area of the H_I lead powder prepared by thiourea (13 m^2g^{-1}) was considerably less than for example the analogous H_I platinum (46 m^2g^{-1}). Although similar surface area could be obtained using $NaBH_4$ as reducing agent, the structure of the lead powder obtained was more disordered as was revealed by TEM studies. There are two hypothesis as to why the different reduction methods produced different materials:

i) Rate of reduction:

The different methods that were tested reduced lead acetate at different rate. The sodium borohydride reduction was very fast compared to the thiourea reduction. When the lead is being produced very rapidly, the structure may grow regardless of the phase and produce a different material. Thiourea reduced the lead precursor moderately quickly and so the pore structure of the resulting lead powder was more ordered.

ii) Effect of reducing agent on the phase:

Although the phase behaviour of the polyoxyethylene surfactants in the presence of lead acetate was well known, the effect of the reducing agent was not characterised. For instance it would have been expected that sodium borohydride as a stong reducing agent might alter the phase behaviour of the surfactants investigated. Moreover, the gas evolved during the reduction process might also affect the template mixture.

4.3.4.2 Surface area of the chemically prepared H_I Pb

Nitrogen adsorption studies for the materials prepared from different surfactant systems revealed adsorption isotherms at high relative pressure which are characteristic of materials with only a small amount of mesoporosity. In the best cases, only a small inflection of the isotherms in the mesoporous domain was observed and the surface area (13 m^2g^{-1}) was smaller than expected. On the basis of lead being less dense than platinum for instance, the H_I lead powders should have an higher specific surface area. From the results obtained, a few hypotheses as to why the lead powders prepared have small surface area can be made:

i) Although for the material prepared from thiourea a nanoporous ordered structure was observed on the edge of the sample, majority of the particles analysed were nanoporous but disordered. This non regular distribution of pores can affect the resulting surface area of the material.

ii) Lead has a great tendency to oxidise readily to lead oxide as was shown from EDAX studies where oxygen was detected on the surface of the material. The oxide formation could lead to a blocking of the pore system resulting in a decrease of the surface area of the powders.

iii) BET nitrogen adsorption was used to characterise the surface area of the different H_I lead prepared. Although this technique is widely used for noble metals where the gas can be readily adsorbed and desorbed from the surface, nitrogen might not be as inert for a non-noble metal such as lead and might not be a suitable choice of adsorbant to characterise the surface area of the powders prepared. The porosity of these materials could be evaluated by argon as adsorbant to assess if any difference in surface area is noticeable.

4.3.4.3 Electrochemical preparation of H_I lead

Investigations on the electrochemical preparation of H_I Pb have shown it is possible to prepare mesoporous lead from Brij 56 lyotropic H_I phase. Lead tetrafluoroborate was shown to be a suitable precursor for the electrodeposition of a coherent and ordered mesoporous film on the surface of an Au supporting electrode. Cyclic voltammetry studies in solution and in the presence of the surfactant were necessary to evaluate the behaviour of the lead precursor and to select a correct potential for the potential step deposition. Although these studies were not exhaustive, the results reported the ability to produce ordered mesoporous films using this technique.

4.4 Conclusion and further work

The results reported in this chapter showed it is possible to chemically produce mesoporous lead using the lyotropic H_I phase of polyoxyethylene surfactants systems. Although TEM studies revealed some ordered nanostructure within the materials, small angle XRD revealed that this structure was not well ordered. The lead powders had a surface area of 13 $m^2 g^{-1}$. From the wide angle diffraction, the material obtained was polycrystalline and characterised by an exact cubic crystal structure in good agreement with the values for polycrystalline lead (ICDS database). Electrodeposition was shown to be a powerful technique to prepare coherent and nanostructured films: an adherent and homogeneous surface coverage of the supporting electrode was observed after an hour electrodeposition at room temperature. XRD revealed a single peak in the small angle region characteristic of an ordered periodic structure. TEM revealed the porosity of the material obtained. The results obtained during these investigations demonstrate the ability to use the templating method to produce nanostructured films.

Further work:

Although the study of the chemical preparation of mesoporous lead has been fairly exhaustive, there are still a number of issues to be addressed:

- Lead acetate was shown to be a suitable precursor for the production of H_I lead but other sources should be investigated. The suitable metal salt must be highly soluble in water but must not significantly affect the phase forming properties of the surfactant.
- The main difficulty encountered was to identify suitable methods of reducing the lead precursor without affecting the phase behaviour of the surfactant. The reduction must be carried out at a correct rate to replicate the aggregate structure of the template and the reaction by products must be easily removed. Other reducing agents should be investigated to optimise the process.
- To address the stability of the materials, oxidation should be prevented by keeping the lead material in a reducing environment.

Investigations into the electrochemical preparation of mesoporous lead were successful. The aim of the research was to show it is possible to use the direct templating method to prepare nanostructured lead films electrochemically. Although only one system was really investigated, electrodeposition was shown to be an attractive route as the rate of the reduction can be controlled and the reaction by-products are minimised because the reduction is electrochemical. Further work on the electrochemical preparation include:

- Investigating the phase behaviour of Brij surfactants + water + lead tetrafluoroborate using polarised light microscopy.
- Investigating different templating compositions at different temperatures. Increasing the lead precursor concentration and the reduction temperature should increase the deposition rate [14].
- Finally, the potential applications of the nanostructured lead deposit should be addressed: porous electrodes have a wide field of applications and are commonly used in batteries and fuel cells [15]. Due to their regularity of structure and porosity, the mesoporous films prepared could become of commercial importance in the lead -acid battery technology.

4.5 References

1. A H Whitehead, J M Elliott, J R Owen, G S Attard, *Chem.Commun.*,331 (1999).
2. S Guerin, PhD Thesis, Department of Chemistry, University of Southampton (1999).
3. M C Sneed, R C Brasted, Comprehensive Inorganic Chemistry, Vol.VII, The Elements and Compounds of Group IVA, D Van Nostrand Company Inc (1958).
4. J W Winckel, D M Rice, *J.of Power Sources*, **73**,3 (1998).
5. D Greninger, Lead Chemicals, International Lead Zinc Research Organisation Inc (1958).
6. B G Slay, B G Carbajal, *J.Electrochem.Soc.***113**, 306 (1993).
7. G N Glavee, K J Klabunde, *Inorg.Chem.*, **32**, 473 (1993).
8. G S Attard, P N Bartlett, N R B Coleman, J M Elliott, J R Owen, *Science*,**278**,838 (1997).
9. A T Kuhn, The Electrochemistry of Lead, Academic Press (1979).
10. D J Mitchell, G J T Tiddy, L Waring, T Bostock, M P Mc Donald, *J.Chem. Soc.Faraday Trans.* 1, **79**,975 (1983).
11. E Lojou, M Devaud, M Troupel, J Perichon,*J.Electochem.Soc.*140, **8**,2157,(1993).
12. S Fletcher, C S Halliday, D Gates, M Westcott, t Lwin, G Nelson, *J. Electroanal.Chem.*159,**183**, 267 (1983).
13. D J Astley, J A Harrison, H R Thirsk, *J.Electroanal.Chem.* **19**, 325, (1968).
14. J M Elliot, G S Attard, P N Bartlett, N R B Coleman, D A S Merckel, J R Owen, *Chem.Mater*,**11**, 3602 (1999).
15. G Lindbergh, *Electrochimica Acta*, 42,**8**,1239 (1997).

Chapter 5
The preparation of mesoporous alloys of platinum

5.1 Background and objectives

The ability to produce binary intermetallic materials that have a uniform dispersion of the constituents metals is of considerable importance for the development of new catalysts. In many cases, alloying affords materials whose catalytic activity/performance is enhanced significantly in comparison with that of the constituent metals [1]. Recent developments in fuel cell catalysis have shown that the modification of platinum by ruthenium in the form of an alloy does improve CO tolerance compared with pure platinum over a wide range of conditions [2-6]. Moreover the ruthenium alloyed catalyst exhibits lower overpotentials and extended lifetime compared to the platinum. In the control of automotive pollutants, Pt/Rh three-way catalysts were shown to be very effective to lower emissions from automobiles [7]. The performance of the Pt/Rh catalyst was described in terms of platinum-rhodium synergism [7]. Thus, it is reasonable to expect that the production of binary alloys of platinum that combine high specific areas, controllable pore diameters and a uniform distribution of metal species will impact on a wide range of catalytic processes.

The subject of the work presented in this chapter is a study of the chemical synthesis, characterisation and properties of mesoporous platinum based alloys from surfactant systems. The main focus was the preparation of mesoporous platinum-ruthenium (H_I - Pt/Ru) and platinum-rhodium alloys (H_I -Pt/Rh) alloys from Brij 76 surfactant. The objectives of the work are summarised below:

1- To investigate chemical methods of preparing mesoporous Pt-Ru alloys using the lyotropic hexagonal phase of Brij 76, while varying the amount of metal salts so as to produce alloys with various ratios of platinum to ruthenium.

2- To investigate chemical methods of preparing mesoporous Pt-Rh alloy using the same surfactant. The amounts of salts were chosen so as to produce an alloy with a nominal 1:1 atomic ratio of platinum to rhodium.

3- To investigate the electrochemical preparation of mesoporous Pt-Ru alloy in the H_I phase of Brij 76.

4- To characterise the mesoporous Pt-based alloys on a micron and nanometer scale, specificaly, surface area, regularity of the structure, crystal structure and evidence of alloy formations.

5.2 Experimental

The experimental work is divided into three sections. The first of these describes the chemical preparation of H_I -Pt/Ru and H_I -Pt/Rh alloys from Brij 76 where several methods were investigated. Following on from this, the electrochemical preparation of H_I -Pt/Ru is described and finally the characterization data for H_I -Pt/Ru and H_I -Pt/Rh materials are presented..

5.2.1Chemical preparation of H_I -Pt/Ru and H_I -Pt/Rh alloys

5.2.1.1 Background on chemical preparation of Pt-Ru and Pt-Rh

Several methods have been used for the preparation of platinum-ruthenium alloys. The most convenient method is the reduction of mixed salt solutions at low temperature to produce homogeneous alloys: Mc Kee *et al.* reported the chemical reduction of platinic acid and ruthenium chloride in water with a 5% solution of sodium borohydride ($NaBH_4$) added dropwise to the stirred mixtures [8]. The coagulated catalysts were washed to remove traces of chlorides, dried in air at 100 ^oC then reduced in flowing H_2 at 300 ^oC for 3 hours.In some cases, reduction was carried out using 85 wt % hydrazine hydrate solution. BET adsorption revealed surface area varying from 3 to 12 m^2g^{-1}. X-ray diffraction studies of the product showed the alloy preparation to be homogeneous and true solid solutions of ruthenium in platinum up to 50 wt % ruthenium [8]. Using the same metal precursors, formaldehyde mixed with potassium hydroxide was also reported as an effective reducing agent in the chemical preparation of Pt-Ru catalysts for the methanol electrode of methanol air fuel cell [9]. Bimetallic alloy particles supported on high surface area carbon find widespread applications as electrodes materials. The choice of precursor molecules and formation conditions in the preparation of the bimetallic Pt-Ru catalysts affect strongly the dispersion and the compositional homogeneity of the alloy clusters [10]. As mentioned in the introduction, Watanabe *et al.* reported the preparation of highly dispersed Pt-Ru alloy clusters based on the co-deposition of fine oxides of platinum and ruthenium followed by reduction with hydrogen bubbling. Pt and Ru oxides were precipitated from their respective chloride compounds with hydrogen peroxide as the oxidation agent.

This method produced supported Pt-Ru alloy clusters with specific surface areas of around $80m^2g^{-1}$ [11]. Radmilovic *et al.* reported similar preparations with the major difference being that both Ru and Pt were present in the impregnation solution as sulfite colloidal complexes [10].

5.2.1.2 Preparation of H_I -Pt/Ru alloys

Previous studies in our group showed that in spite of the polydispersity of the ethylene-oxide headgroup when compared to the more expensive C_{16} EO_8, the H_I liquid crystalline phase of Brij 76 can be used to produce high quality hexagonaly nanostructured silicas and metals [12]. Our approach to the synthesis of mesoporous bimetallic platinum alloys is very similar to the method reported for the synthesis of H_I Pt. The only modification was the co-reduction of two metals salts in the H_I phase of Brij 76.

Hexachloroplatinic acid hydrate, HCPA, (3.0g) and ruthenium trichloride (1.52g) were dissolved in 2.84 ml of deionised water contained in a sealable glass vial. The amounts of salts were initially chosen so as to produce an alloy with a nominal 1:1 atomic ratio of platinum to ruthenium. Brij 76 (9.0g) was added to the solution and the mixture was mixed vigorously using a plastic spatula. The vial was sealed, heated to ca 80°C using a hot air gun, and while hot was mixed using a vortex mixer. The heating/mixing process was repeated three times and the mixture was allowed to stand for 4 hours at room temperature. A sample was withdrawn from the clear dark grey-green mixture and viewed as a thin film under polarising microscope. The sample exhibited a uniform optical texture characteristic of the H_I phase of Brij 76. Sodium borohydride (0.3g dissolved in 6 ml water) was added dropwise to the mixture with vigorous stirring over a period of 20 minutes. The reaction mixture was sealed and allowed to stand at room temperature for 2 hours. The contents of the vial were transferred to a conical flask and stirred with 200 ml deionised water for 3 hours. Solids were isolated by centrifugation (2500 rpm for 20 min). The washing/centrifugation procedure was repeated six times, and after the final wash the solids were dried in an oven for 12 hours to afford a fine black powder. This material is refered to as H_I-Pt/Ru. In a separate experiment, HCPA (3.0g) and ruthenium trichloride (0.586g) were dissolved in 2.84g deionised water in a sealable glass vial so as to produce an alloy with 5:1 atomic ratio of platinum to ruthenium. Brij 76 (9g) was added to the solution and the same reduction method as before was used. In order

to prepare a 3:7 atomic ratio of platinum to ruthenium using the same reducing agent, 1.75 g ruthenium trichloride and 0.657g HCPA were dissolved in 2.84 g deionised water. Finally, using a nominal 1: 1 atomic ratio of platinum to ruthenium another reducing agent consisting of a mixture of 0.5g KOH in 2.5 ml deionised water mixed with 2.5 ml formaldehyde (40 % solution in water) was used in place of sodium borohydride.

5.2.1.3 Preparation of HI -Pt/Rh alloy

The synthetic procedure to produce the H_I -Pt/Rh alloy was identical to that for H_I-Pt/Ru alloy but employed rhodium sulfate (4.5g) instead of ruthenium trichloride. The amounts of salts were chosen so as to produce a 1:1 atomic ratio of platinum to rhodium. Sodium borohydride was used as reducing agent (0.3g dissolved in 6 ml water). Due to the cost of the metal salts precursors, one only one composition of the alloy was prepared.

5.2.2 Investigations on the electrochemical preparation of H_I -Pt/Ru

Electrochemistry experiments were performed with a three electrode system under potentiostatic control. The cyclic voltammograms and current transients were recorded by computer.All counter electrodes were made of platinum gauze. They were washed with deionised water and flamed over a bunsen flame just before use in order to remove any contaminants. The reference electrodes used were Saturated Calomel Electrodes (SCE). All electrochemical potentials are quoted with respect to the saturated calomel electrode. The working electrode consisted of a 1mm ∅ Au disc electrode for the cyclic voltammetry studies. These electrodes were polished using sand paper and alumina with particle size ranging from 25 μm to 3 μm. After polishing the electrodes were rinsed with deionised water. Electrodeposition (current transient experiments) were performed on these electrodes and also on 1 cm^2 Au electrodes that were made by evaporating a thin layer of gold onto a glass substrate.

5.2.2.1Cyclic voltammetry

For the cyclic voltammetry in solution, HCPA (0.1 M) and ruthenium trichloride (0.1M) in H_2SO_4 (2M) were used (nominal 1:1 atomic ratio of platinum to ruthenium). Cyclic voltammograms were recorded at room temperature at a scan rate of 20 mV/s.

5.2.2.2 Current transient experiments

During the electrodepositions, the current transients were recorded on isotropic solutions identical to the solutions used for cyclic voltammetry (HCPA (0.1 M) and ruthenium trichloride (0.1 M) in H_2SO_4 (2M)). Potential step depositions were then carried out on templating mixtures consisting of 65 wt % Brij 76 and 35 wt% (0.1M) $H_2PtCl_6/RuCl_3$ in H_2SO_4 2M at room temperature (nominal 1:1atomic ratio of platinum to ruthenium). When using higher surface area electrodes, electrodepositions were also carried out at 40 ^{0}C using the same templating mixture. Various deposition times depending on the geometry of the Au working electrode (surface area) were investigated.

5.2.3 Characterisation

Characterisation of the chemically prepared Pt alloys was carried out by TEM to determine the materials'structure on a nanometer level. Nitrogen adsorption/desorption was used to determine the specific surface areas of the powders prepared, small angle X-ray diffraction to deduce pore to pore distance and mesophase structure, wide angle X-ray diffraction and Extended X-ray Fine Structure Adsorption (EXAFS) were employed to conclude whether or not H_I-Pt/Ru and H_I-Pt/Rh were intermetallic materials.

For the electrochemical preparations, the thin films deposited on the Au electrode were analysed by cyclic voltammetry in 2M H_2SO_4. Small angle and wide angle X-ray diffraction were carried out to study the mesophase structure and crystal structure of the deposited film. Finally, the thin films were grounded and investigated by TEM to determine the structure on a nanometer level.

5.3 Results and discussion

This section contains the results that were obtained from the various analytical methods used to determine the nanostructure, porosity and chemical composition of the H_I Pt alloys.

5.3.1 Chemical preparations of H_I -Pt/Ru and H_I -Pt/Rh

5.3.1.1 TEM

Representative TEM micrographs obtained for the mesoporous H_I-Pt/Ru prepared using $NaBH_4$ as reducing agent with a 1:1 atomic ratio of platinum to ruthenium are depicted in figure 5.1.

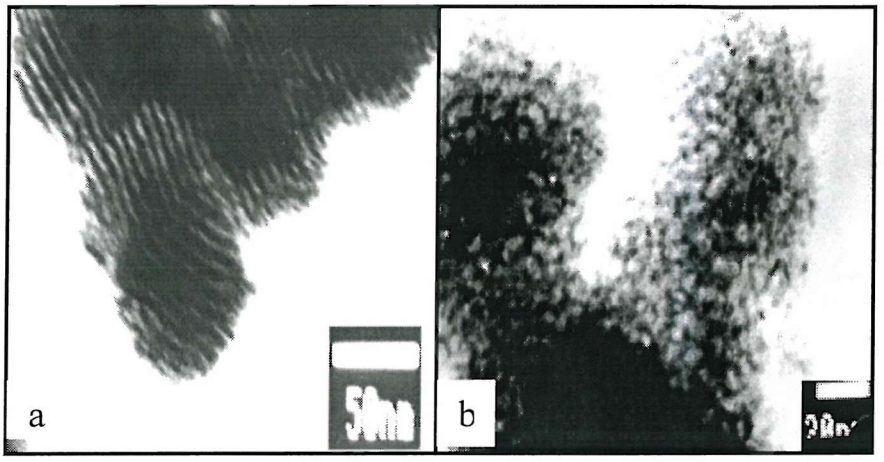

Figure 5.1 TEM micrographs of H_I-Pt/Ru prepared by $NaBH_4$, 1:1 atomic ratio of platinum to ruthenium.

Using $NaBH_4$ as reducing agent and a nominal 1:1 atomic ratio of platinum to ruthenium in the templating mixture, the material exhibits an ordered nanostructure consisting of cylindrical pores of uniform diameter disposed in an hexagonal arrangement with respect to one another.

Measurements taken from the micrographs indicate that H_I -Pt/Ru has a pore diameter of 17 (±1) Å and a wall thickness at the point of nearest contact between the pores of 34(±2) Å.

Figure 5.2 (a-b) show the TEM results for the H_I-Pt/Ru prepared using the same reducing agent while varying the atomic ratio of platinum to ruthenium.The results obtained from the H_I material prepared from HCHO+ KOH while using a nominal 1:1 Pt/Ru atomic ratio are also shown on figure 5.2 (c-d) for comparison.

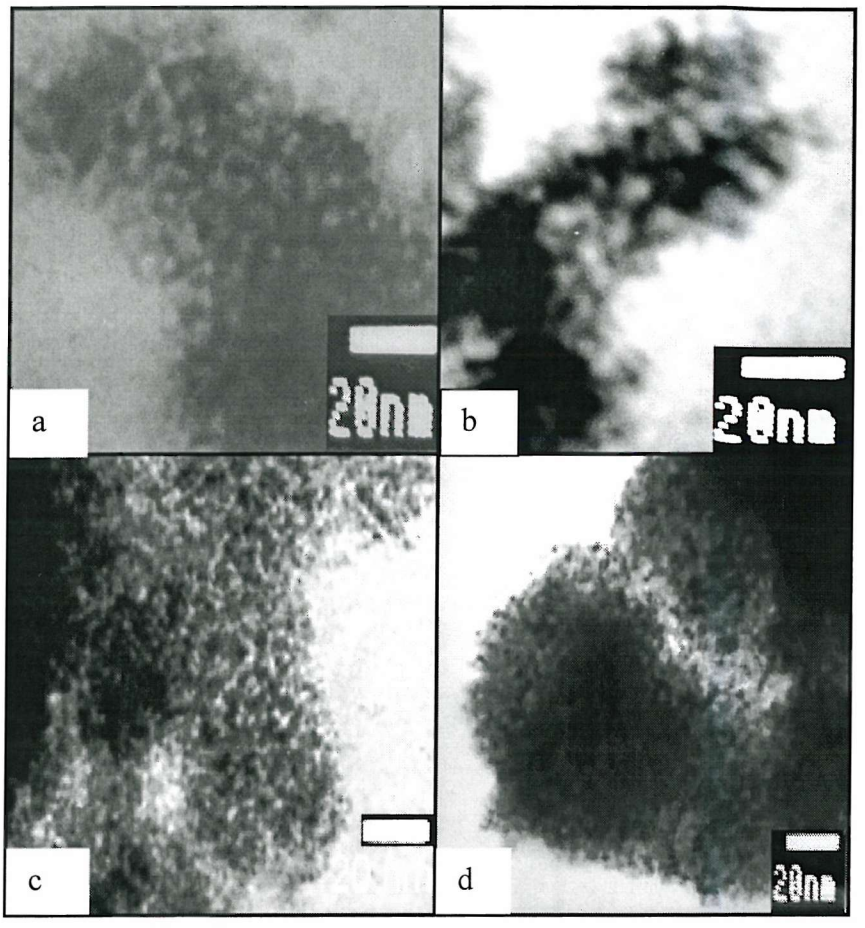

Figure 5.2 TEM micrographs of a) H_I -Pt/Ru 5:1 Pt/Ru atomic ratio, b) H_I-Pt/Ru 3:7 Pt/Ru atomic ratio. The 2 materials were prepared by $NaBH_4$ reduction. c,d) H_I-Pt/Ru 1:1 Pt/Ru atomic ratio prepared by HCHO+KOH reduction.

For a 5:1 atomic ratio of platinum to ruthenium, the micrograph in figure 5.2 a) reveals the porosity of the material obtained. Though porous, the material has a less ordered structure than that obtained for the alloy with a 1:1 ratio of platinum to ruthenium.

In a similar way, the porosity of the material prepared when increasing the amount of ruthenium in the initial mixture (3:7 atomic ratio of platinum to ruthenium) is evident

from figure 5.2 b) but the structure of the material is less ordered than the one obtained with a 1:1 Pt/Ru atomic ratio (figure 5.1).

For a 5:1 atomic ratio, measurements taken from the micrographs indicate that H_I Pt-Ru is characterised by a pore diameter of 20 (±2) Å and a wall thickness at the point of nearest contact of 40 (±2) Å whereas the catalyst prepared from a 3:7 Pt/Ru atomic ratio can be characterise by 25 (±2) Å diameter pores separated by 20 (±2)Å walls. Although for these 2 materials it is difficult to determine pore size with accuracy from the micrographs (very dark materials), the catalysts seems to become more porous as the ruthenium content in the initial mixture is increased.

The TEM results of the H_I Pt-Ru prepared from a nominal 1:1 atomic ratio of platinum to ruthenium using a mixture of HCHO + KOH (figure 5.2c and d) confirm the porosity of the material but are characteristic of a disordered structure.
TEM was also employed to visualise the nanostructure of the H_I Pt-Rh powders prepared from a nominal 1:1 atomic ratio of platinum to rhodium while using the same reducing agents as before .The results are shown in figure 5.3.

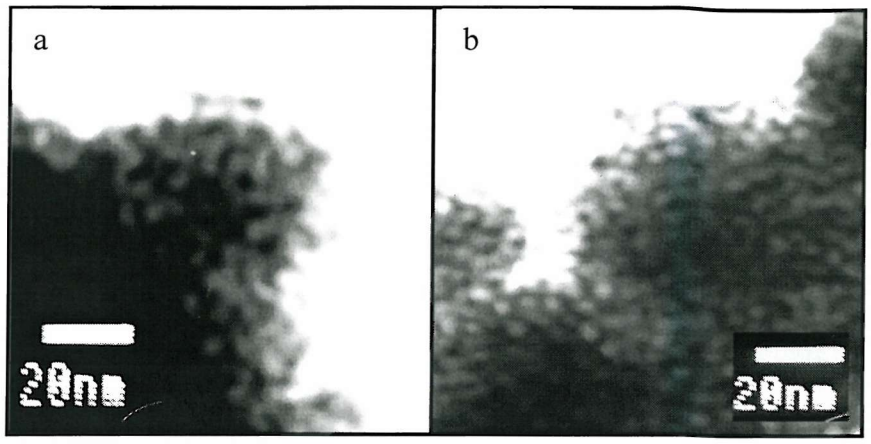

Figure 5.3 TEM micrographs of a) H_I -Pt/Rh prepared by Na BH_4 reduction, b) H_I -Pt/Rh prepared by HCHO+KOH reduction. For the 2 materials, the amount of salt was chosen so as to produce a nominal 1:1 Pt/Rh atomic ratio.

The TEM micrograph in figure 5.3a shows the porosity of the catalyst obtained using $NaBH_4$ as reducing agent. A more disordered structure than the one observed for H_I Pt-Ru (1:1 atomic ratio) is evident. Measurements taken from the micrograph indicate that H_I Pt-Rh has a pore diameter of 20 (±2) Å and a wall thickness at the point of nearest contact of 40 (±2) Å. Although porous, the H_I Pt-Rh prepared from HCHO+ KOH is characterised by a similar disordered structure with similar pore diameter 25 (±2) Å but the wall thickness is smaller 20 (±2) Å than the material prepared from $NaBH_4$ (figure 5.3b). Table 1 summarises pore diameters and wall thicknesses for the various H_I Pt/Ru and H_I Pt/Rh alloys prepared by varying the atomic ratio and reducing agent.

Alloy	Atomic ratio	Reducing agent	Pore diameter Å(± 2 Å)	Wall thickness Å(± 2 Å)
H_I Pt/Ru	1:1	$NaBH_4$	17	34
H_I Pt/Ru	5:1	$NaBH_4$	20	40
H_I Pt/Ru	3:7	$NaBH_4$	25	20
H_I Pt/Rh	1:1	$NaBH_4$	20	40
H_I Pt/Rh	1:1	HCHO + KOH	25	20

Table 1. Pore diameters and wall thicknesses for various H_I Pt/Ru and H_I Pt/Rh alloys chemically prepared by varying the atomic ratio and reducing agent. Measurements obtained from the TEM micrographs.

5.3.1.2 Small angle XRD

Small angle XRD was used to determine the repeat distance between pores and the order of the phase. For the H_I Pt-based catalysts described in this chapter, only one peak was observed in the diffraction patterns. This corresponds to the (100) reflection.

Before carrying out the reduction, small angle XRD were obtained from the "templating mixture" consisting of H_2PtCl_6/$RuCl_3$/Brij 76 (75 wt % in water).
The X-ray diffractogram (figure 5.4) exhibits only one diffraction peak in the small angle region corresponding to an ordered hexagonal phase with a lattice parameter of 7.2 nm.

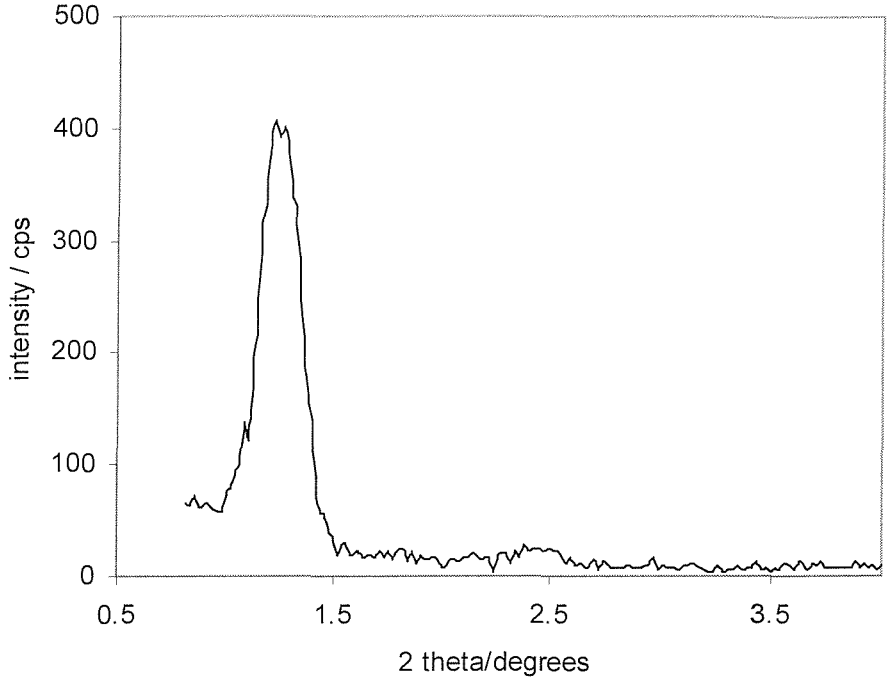

Figure 5.4. Small angle XRD : H_I phase templating mixture (75 wt % brij 76)
d_{100} = 7.2 nm

The product obtained by the chemical reduction of the templating mixture by $NaBH_4$ has also been characterised by small angle XRD to study the order of the structure of the material obtained. The X-ray diffractogram in figure 5.5 shows only one diffraction peak in the small angle region corresponding to an ordered hexagonal structure with a lattice parameter of 6nm.

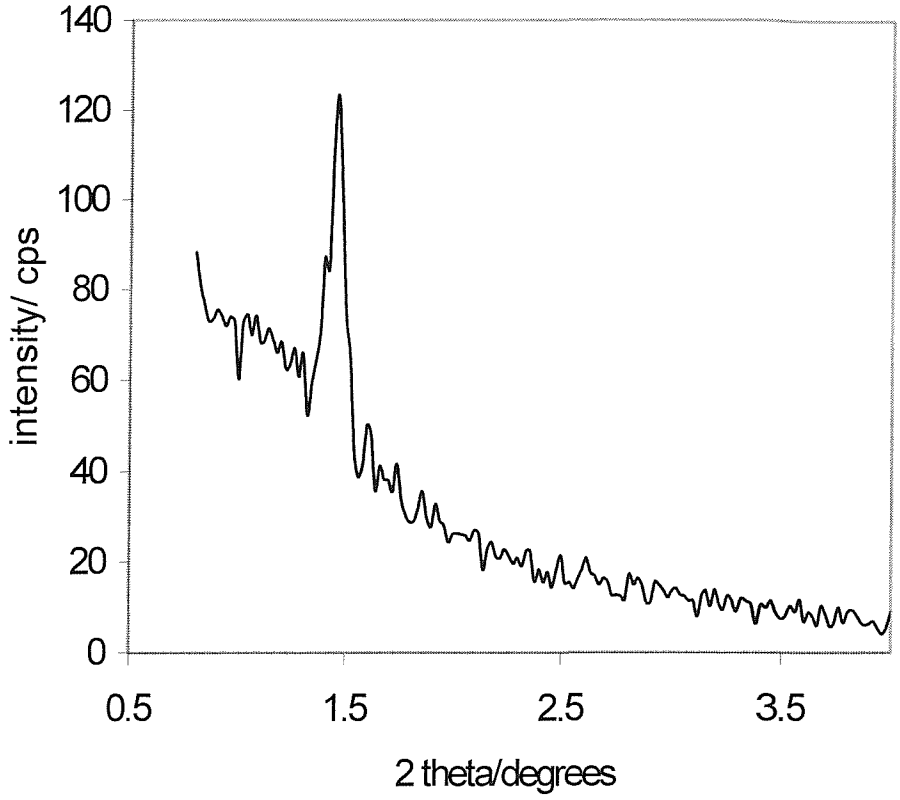

Figure 5.5. Small angle XRD of mesoporous Pt-Ru catalyst d_{100} = 6nm

The products obtained by the chemical reduction of the templating mixture by $NaBH_4$ (Pt/Ru=5/1and Pt/Ru=3/7 molar ratio) were also characterized by small angle XRD The X ray diffractogram in figure 5.6 for Pt/Ru=5/1(molar ratio) shows a broad diffraction peak in the small angle region with a smaller intensity than the one recorded for the nominal 1:1 material depicted in figure 5.5.The broad diffraction corresponds to a less ordered hexagonal structure which confirmed the less odered structure observed by TEM. The lattice parameter was estimated to be around 6.3 nm.

The X ray diffractogram in figure 5.7 (Pt/Ru=3/7) shows only one diffraction peak in the small angle region corresponding to an ordered hexagonal structure with a lattice parameter of 5.2 nm.

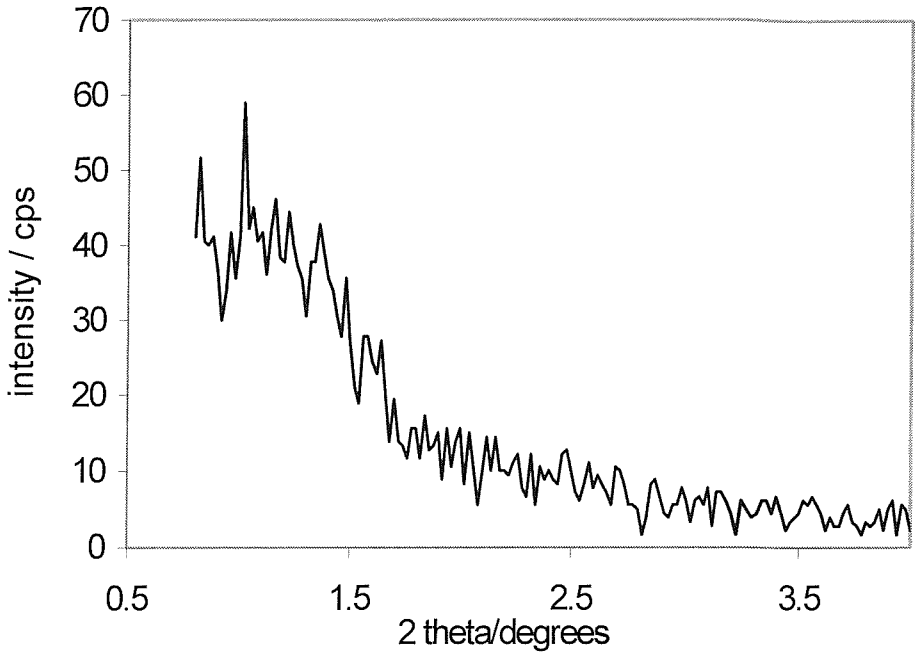

Figure 5.6. Small angle XRD of mesoporous Pt/Ru catalyst (Pt/Ru=5/1 molar ratio) d_{100}=6.3 nm.

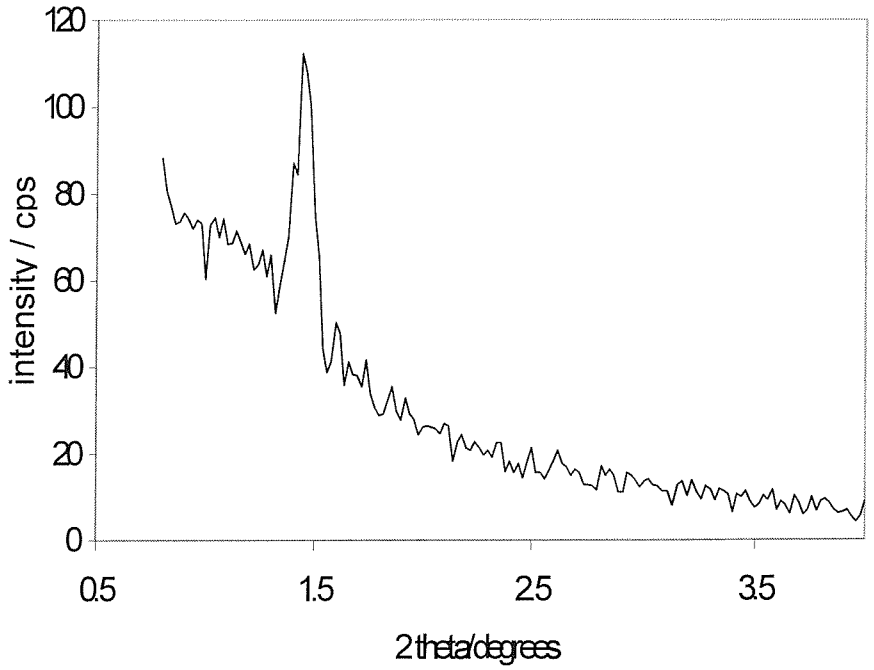

Figure 5.7. Small angle XRD of mesoporous Pt/Ru catalyst (Pt/Ru=3/7 molar ratio) d_{100}= 5.2 nm.

Small angle XRD results obtained on the materials prepared while varying the atomic ratio of platinum to ruthenium in the initial templating mixtures tend to show that, as the ruthenium content in the initial mixture increased, a contraction in the lattice parameter is observed. For comparison the H_I platinum prepared by steel reduction using the lyotropic H_I phase of Brij 76 (75 wt %) was also characterised by a single 100 small angle diffraction peak corresponding to a lattice parameter of around 6 nm. This result is very similar to the results obtained for the H_I -Pt/Ru materials prepared from $NaBH_4$ as reducing agent.

5.3.1.3 Wide angle XRD

Wide angle X-ray diffraction was employed to investigate whether or not H_I -Pt/Ru was indeed an intermetallic material. The diffractogram depicted in figure 5.8 for H_I -Pt/Ru (1:1 atomic ratio of platinum to ruthenium) shows four reflections that are in excellent agreement with those reported for nanoparticulate Pt/Ru alloy with a nominal Pt/Ru ratio of 1:1 which was prepared by co-reduction in an isotropic reaction mixture[13].

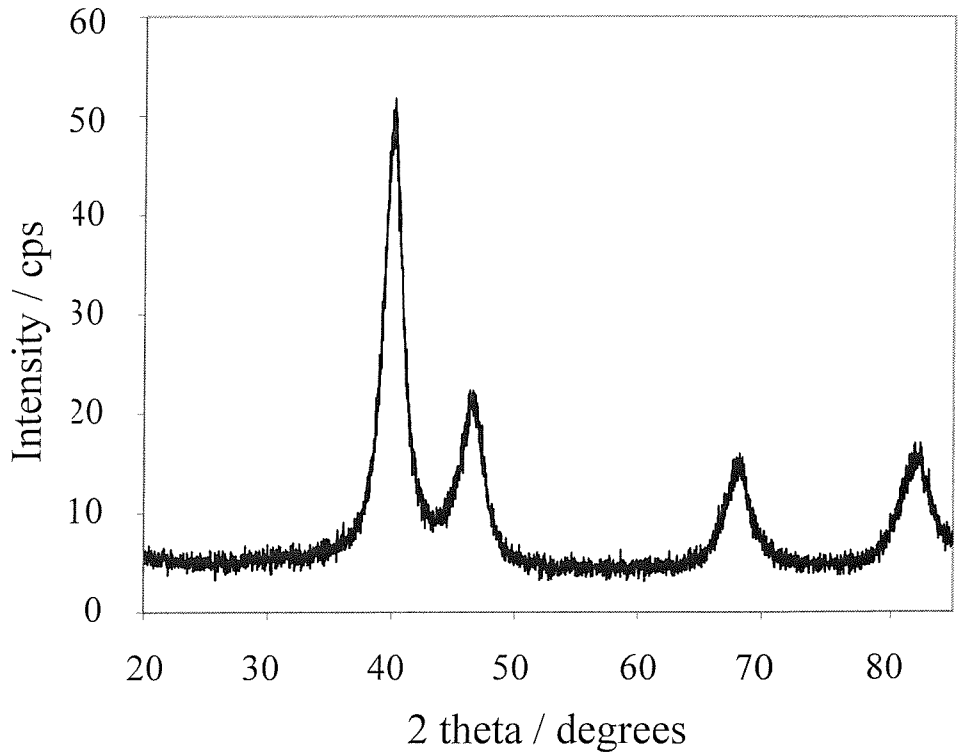

Figure 5.8. Wide angle XRD of mesoporous Pt/Ru catalyst (Pt/Ru =1:1 molar ratio) prepared from $NaBH_4$.

Comparison of the wide angle diffraction data of H_I Pt/Ru, with that of bulk platinum or platinum black indicates that H_I Pt/Ru has an fcc stucture (Fm3m space group). The X-ray diffraction data are summarised in table 2.

	Bulk platinum (Fm3m)		Platinum black		H_I-Pt		H_I- Pt/Ru	
hkl	d /Å	I/a.u.	d /Å	I/a.u.	d /Å	I/a.u.	d /Å	I/a.u.
111	2.2650	100	2.26	100	2.25	100	2.24	100
200	1.9616	53	1.96	54	1.96	54	1.95	48
220	1.3873	31	1.38	29	1.38	29	1.37	27
311	1.1826	33	1.18	31	1.19	31	1.18	30

Table 2. Summary of wide angle X-ray diffraction data obtained using Cu $K_{\alpha 1}$ radiation (λ = 1.5405 Å) for bulk platinum [14], platinum black, H_I-Pt and H_I-Pt/Ru. *I* denotes the intensity of the diffraction peaks, and *d* their position in real space.

The contraction in the lattice parameter, evidenced by the shift of the reflections to shorter distances, is consistent with the smaller size of ruthenium compared to platinum. Confirmation of the intermetallic nature of the H_I Pt/Ru material, as well as of the uniform distribution of the metallic components was achieved using EXAFS.

5.3.1.4 Extended X-ray Fine Structure Adsorption

Confirmation of the intermetallic nature of the H_I-Pt/Ru material, as well as of the uniform distribution of the metallic components was achieved using EXAFS. The k^3 weighted Fourier transforms of the Pt L_{III} and Ru K edge EXAFS data are shown in Figure 5.9 and 5.10 respectively. Structural parameters obtained by fitting the data are summarised in Table 2. The fit to the Pt L_{III} edge data H_I-Pt/Ru indicates that the first shell Pt-Pt co-ordination number is 5.4 (±0.3) while the first shell Pt-Ru co-ordination number is 2.9 (±0.2). The Pt-Pt co-ordination distance obtained from the fit is 2.737 (±0.002) Å, compared with a distance of 2.742 (±0.002) Å for H_I-Pt prepared from Brij76 (data not shown). This reduction in co-ordination distance on alloying is consistent with previous EXAFS investigations of Pt/Ru particles supported on carbon [15], and with the wide angle X-ray diffraction data.

The fit to the Ru K edge data indicates a Ru-Ru first shell co-ordination number of 3.2 (±0.3) and a Ru-Pt first shell co-ordination number of 2.7 (±0.4). The latter is in excellent agreement with the value obtained from the fit to the Pt L_{III} edge data, confirming that H_I-Pt/Ru consists of a well-mixed 1:1 alloy of the two metals.

The presence of an oxygen neighbour in the first co-ordination shell of Ru indicates that H_I-Pt/Ru is slightly oxidised, with the oxide forming preferentially at the ruthenium sites.

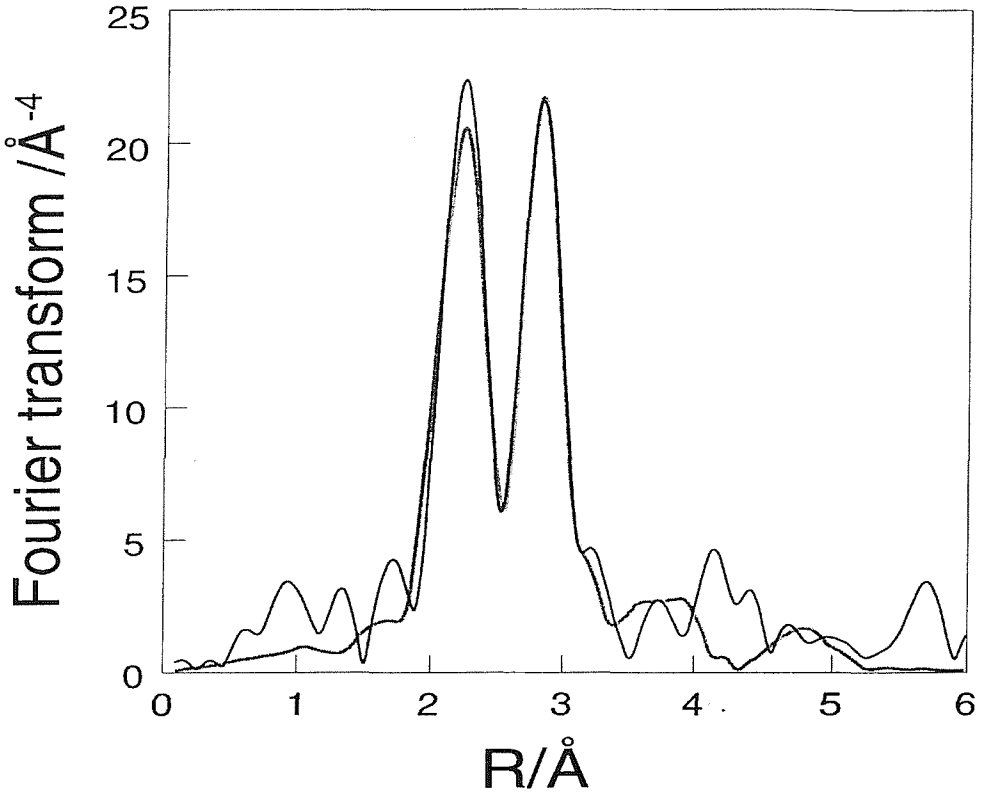

Figure 5.10 k^3 weighted ($\chi(k)$ x k^3) Fourier transform of Pt L_{III} EXAFS data for H_I-Pt/Ru (dark curves) and theoretical fits to data (pale curves); the fitting parameters are defined in the legend to Table 3. The Fourier transforms have been phase corrected for backscattering by the Pt and Ru near-neighbour contributions respectively. H_I-Pt/Ru powder was mixed with boron nitride in an amount which gave an edge step of 0.5 in the $\ln(I_o/I)$ plot at the Pt L_{III} edge. The mixture was pressed into a wafer which was mounted in a cryostat. XAS data were collected using the transmission data collection mode with the sample at liquid nitrogen temperature. All data were collected on Wiggler station 9.2 of the Synchrotron Radiation Source (SRC) at Daresbury, UK. The ring operated with 2.0 GeV energy and 100-250 mA current.

The station was operated with a Si(220) double crystal monochromator, which was detuned to 50% intensity for the Pt L_{III} edge and to 70% for the Ru K edge, to minimise the presence of higher harmonics. Three ion chambers, optimised for the appropriate edge energy, were used in series to measure the intensities of the incident beam (I_o), the beam transmitted by the sample (I_t) and the beam subsequently transmitted by a Pt foil or Ru powder sample (I_m). The reference materials were used for internal calibration of the X-ray beam energy.

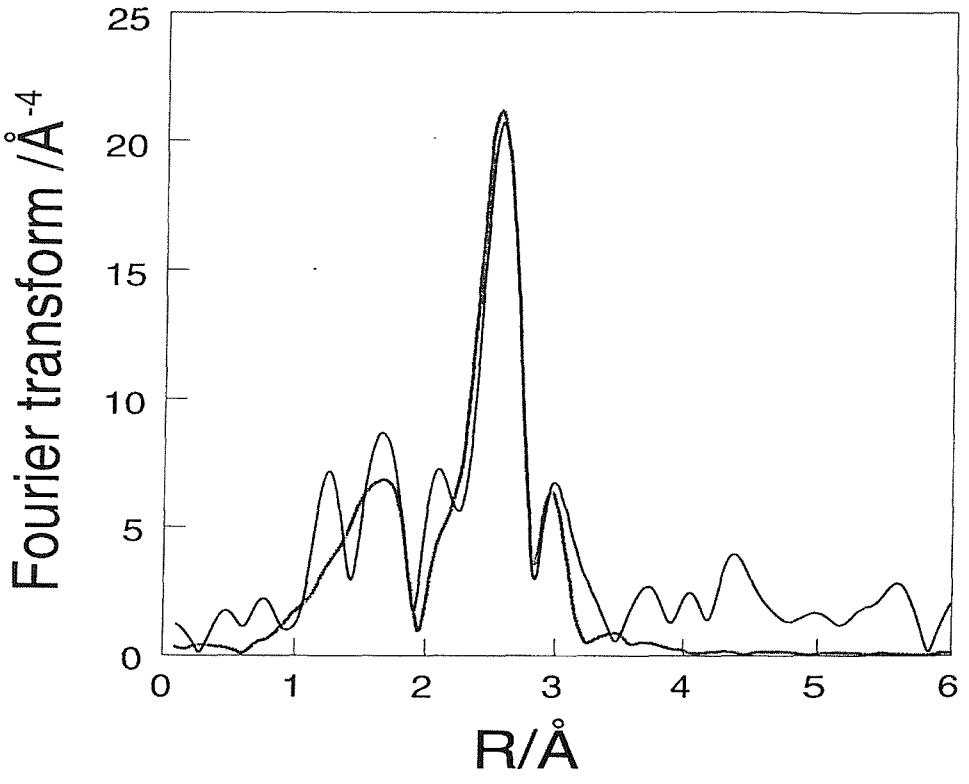

Figure 5.11. k^3 weighted ($\chi(k) \times k^3$) Fourier transform of the Ru K edge EXAFS data for H_I-Pt/Ru (dark curves) and theoretical fits to data (pale curves); the fitting parameters are defined in the legend to Table 3.

Sample (Edge)	Neighbour	N	R/Å	$2\sigma^2/Å^2$	E_f/eV	$R_{(EXAFS)}$/ %
H_I-Pt/Ru (Pt L_{III})	Pt-Pt	5.4 (±0.3)	2.737 (±0.002)	0.013	- 10.1	38
	Pt-Ru	2.9 (±0.2)	2.709 (±0.003)	0.014		
	Pt-Pt	1.4 (±0.7)	3.81 (±0.02)	0.015		
H_I-Pt/Ru (Ru K)	Ru-Ru	3.2 (±0.3)	2.668 (±0.006)	0.013	1.33	49
	Ru-Pt	2.7 (±0.4)	2.714 (±0.008)	0.014		
	Ru-O	1.2 (±0.3)	1.95 (±0.02)	0.011		

Table 3. Structural parameters for H_I-Pt/Ru obtained from theoretical fits of the EXAFS data. The absorption spectra were processed using EXBROOK [16]. The zero point energy scale was taken to be the point of inflection in the absorption edge. The pre-edge region was fitted by a straight line and extrapolated to zero energy. A polynomial spline was fitted to the non-oscillatory component of the post-edge region and was extrapolated to zero energy. The difference between the extrapolated values was taken to be the step height and the spectrum was normalised to this value. The EXAFS components $\chi(k)$ were then isolated from the absorption spectra and subsequently analysed using EXCURVE98 [*16*], a least squares fitting programme based on curved-wave theory, using a $Z+1$ 2p core hole approximation. N is the co-ordination number, R is the distance to the near neighbour, $2\sigma^2$ the Debye-Waller term, and E_f is the shift in the Fermi energy. It was assumed that the Hedin-Lundqvist potential accounted for any amplitude reductions due to absorption processess which do not result in EXAFS features. $R_{(EXAFS)}$, which is a measure of the goodness of the fit between the EXAFS data (χ^{exp}) and the theoretical model (χ^{th}), is defined as:

$$R_{(EXAFS)} = \left\{ \sum_{i}^{N} (|\chi_i^{exp} - \chi_i^{th}|)(\sigma_i^{exp})^{-1} \right\} \times 100$$

where N is the number of data points and σ_i^{exp} is the standard deviation for each data point.

5.3.1.5 BET Nitrogen adsorption

Nitrogen adsorption studies were carried out on H_I -Pt/Ru prepared from Brij 76 to study the surface area and type of isotherms. These results were compared with those obtained for Pt/Ru particles prepared by co-reduction from an isotropic reaction mixture using the same reduction method and the results are shown on figure 5.12.

a) Pt /Ru prepared by HCHO +KOH reduction

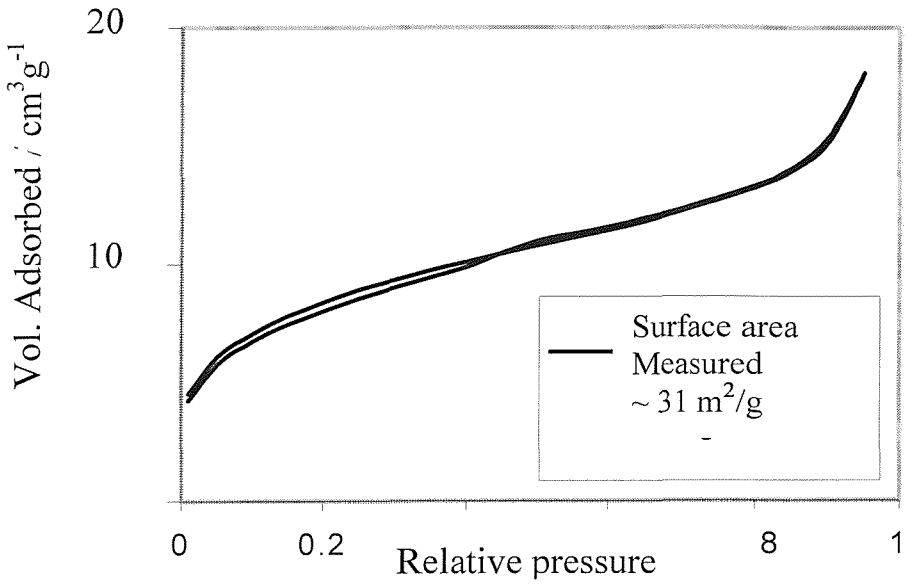

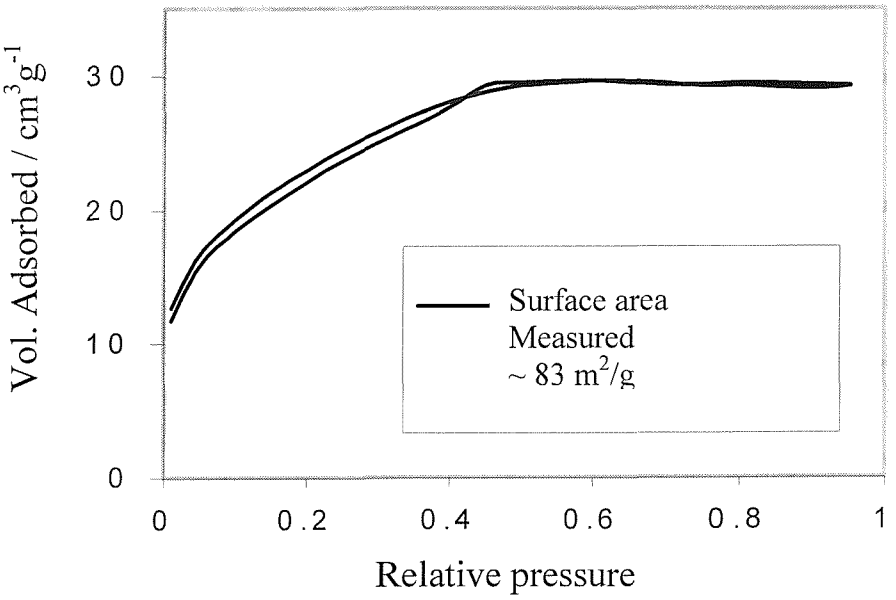

b) H_I Pt Ru prepared while using HCHO + KOH as reducing agent.

Figure 5.12 BET nitrogen adsorption/desorption isotherms on Pt/Ru materials prepared from HCHO +KOH mixtures.

The isotherms obtained for the material prepared from the isotropic reaction mixtures by HCHO + KOH reduction showed adsorption at high relative pressure. This type of isotherm is similar to the one obtained for macroporous solids that do not exhibit pore filling until high relative pressures. The surface area of the Pt/Ru particles was measured to be 31 m^2g^{-1}. By reducing with HCHO + KOH within the lyotropic H_I phase of Brij 76, a much higher surface area was obtained (83 m^2g^{-1}) and the isotherms were characteristic of a material with high degree of mesoporosity.The adsorption occurred mainly for small relative pressure (P/Po between 0 and 0.4) to reach a plateau at medium relative pressure.

Figure 5.13 shows the nitrogen adsorption isotherms for the H_I-Pt/Rh material prepared while using HCHO + KOH as reducing agent.

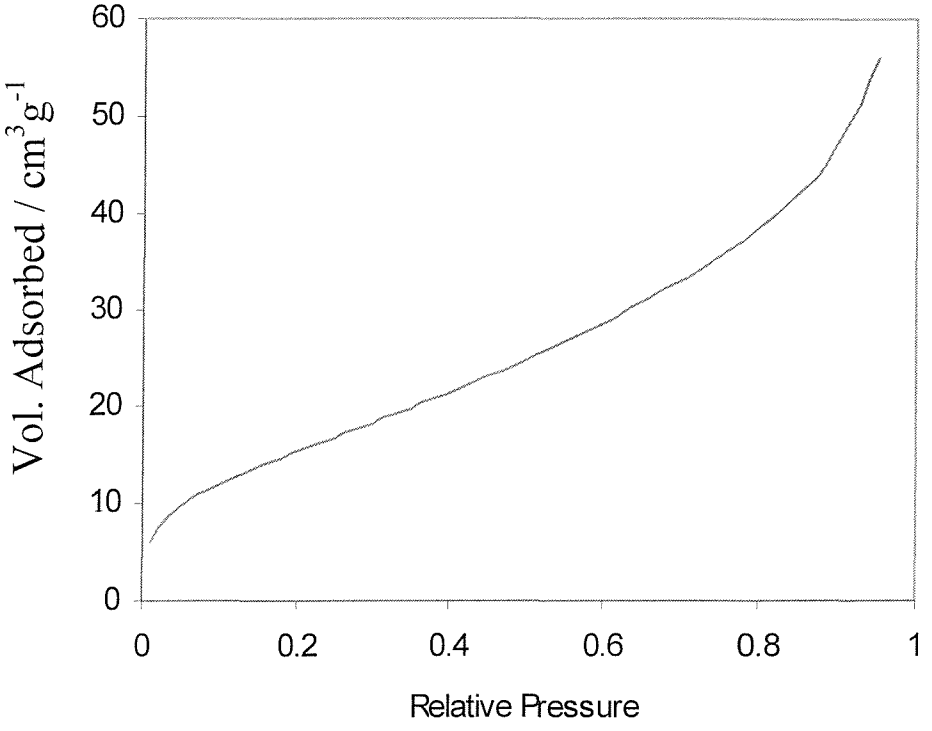

Figure 5.13 BET nitrogen adsorption isotherms on mesoporous Pt/Rh material prepared by HCHO + KOH reduction.

The adsorption isotherm depicted in figure 5.13 was typical of a mesoporous material with pore filling at intermediate relative pressures.

The isotherm was characterised by an inclination in the mesoporous domain and the surface area was measured as 58 m^2g^{-1}. It was interesting to note that both H_I -Pt/Ru and H_I -Pt/Rh materials prepared by HCHO +KOH mixtures exhibited higher surface areas than the H_I platinum materials prepared in chapter 2 by steel reduction. This might be explained by a more suitable method of reduction or simply because the alloy has a lower density than pure platinum (appendix 3). When comparing to the reduction of a single metal, a different mechanism of reduction might be involved during the co - reduction of the two metallic precursors and alloy formation.

5.3.1.6 Electrochemical characterisation of H_I -Pt/Ru catalyst

The influence of the ruthenium content on the electrochemical properties of the alloy was investigated by cyclic voltammetry using carbon fibre microdisc electrodes. Briefly, the metallic powder was rubbed onto the carbon fibre microdisc which was then immersed in 2 M sulfuric acid. The potential was cycled from - 0.26V to +1.3 V versus SCE at a sweep rate of 1 Vs^{-1}. The currents passed during the cycle were recorded.

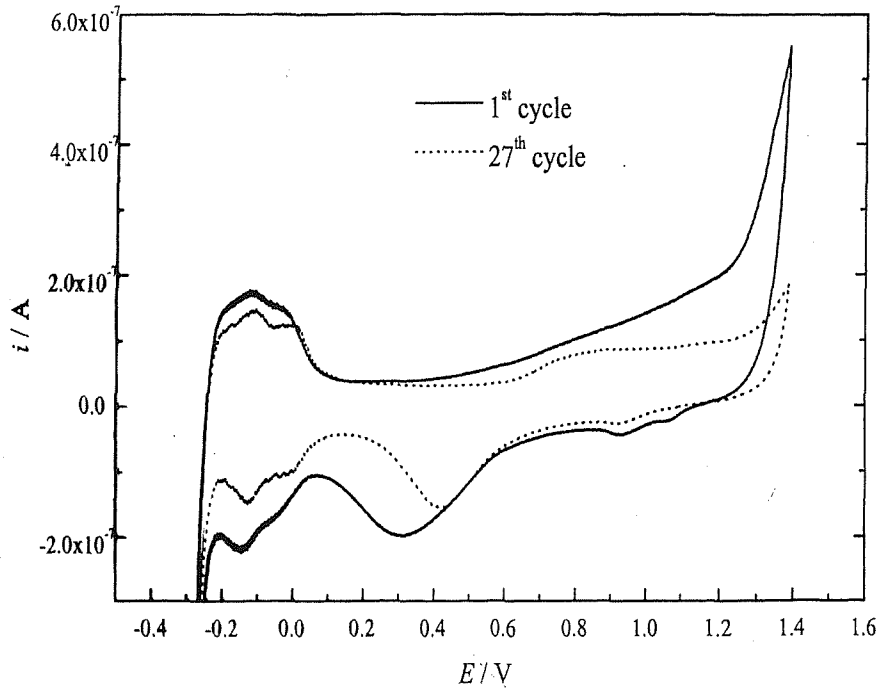

Figure 5.14 Cyclic voltammograms of nanostructured Pt/Ru alloy rubbed onto 7 μm diameter C-fibre microdisc in 2 M H_2SO_4 (ν=1 V/s).

The shape of the voltammogram was observed to change continuously as the material was cycled repeatedly in sulfuric acid (Figure 5.14). In particular, after some 27 cycles the trace is very similar in appearance to that obtained from H_I Pt. In the case of H1-Pt/Ru (first cycle) the peak corresponding to the stripping of the oxide layer occurs at +0.3 V and this shifts progressively to +0.42V, which compares with + 0.5V for the oxide stripping peak in H_I Pt. These observations are consistent with previous reports of the electrochemical behaviour of Pt/Ru alloys, in which cycling in sulfuric acid causes the ruthenium to leach out of the system [17].

5.3.2 Investigations into the electrochemical preparation of H_I -Pt/Ru

Platinum ruthenium electrodes have been known for a long time to exceed the electrocatalytic activity of pure platinum electrodes towards the electrooxidation of methanol in acid electrolytes. Even today, these electrodes are considered to be the most effective electrocatalysts for this reaction [18, 19]. Many different electrode materials have been tested for their activity towards the oxidation of methanol and several methods of preparations have been reported [19]. In their studies, Gasteiger *et al.* reported the catalytic activity of single phase polycrystalline Pt/Ru bulk alloys using sputter-cleaned and annealed alloys prepared in ultra high vacuum (UHV)[19]. In another approach, black platinum surfaces with adsorbed submonolayer equivalents of Ru adatoms were also reported. Lee *et al.* used in their preparation the deposition of Ru adatoms on Pt surfaces using an organometallic reaction between surface Pt-hydrides and a ruthenium-hydrocarbonyl compound dissolved in hexanes solutions at low temperature under 1 atmosphere of dihydrogen gas. The hydrogenation allowed for real time control over the equivalents of Ru adatoms deposited on platinum and provided a convenient method to generate platinum surfaces with known amounts of adsorbed Ru adatoms [20]. At present the electrochemical co-deposition of Pt-Ru electrodes is still extensively used with a vast amount of potentiodynamic and potentiostatic performances data of Pt-Ru alloys reported on methanol oxidation in the literature [19]. Pt-Ru electrodes are usually prepared by co electrodeposition on gold substrates. Platinic acid (H_2PtCl_6) and ruthenium trichloride ($RuCl_3$) are extensively used as metal precursors [21-23] and the depositions are usually carried out in acidic solution. Perchloric acid ($HClO_4$, 1M) was employed for example during the co electrodeposition of Pt/Ru on gold to prepare electrodes for the electrooxidation of ethanol [21], the use of sulfuric acid electrolytes (0.5M) to prepare similar electrodes for methanol electroxidation were also reported [22-23].

In order to obtain mesoporous Pt/Ru films, studies of the co electrodeposition of platinum and ruthenium have been undertaken. Platinic acid and ruthenium chloride were used as the metal salts precursors. For a nominal 1:1 atomic ratio of platinum to ruthenium in the initial mixture, the characteristics of the electrodepostion from a solution containing the platinum and ruthenium salts in 2M H_2SO_4 are shown and compared to the results obtained for the electrodeposition from a templating mixture

containing Brij 76 and the metal salts in 2M H_2SO_4. The influence of using several types of gold substrates on the current transient is also shown. As for the chemical preparation of mesoporous Pt-Ru alloys, XRD and TEM were used to analyse the regularity of the structure of the films obtained. X-ray microanalysis was also used to study the composition of the deposited films.

5.3.2.1 Studies in 2M H_2SO_4

The behaviour of the platinum-ruthenium based solution was investigated by cyclic voltammetry. Figure 5.15 shows a typical cyclic voltammogramm of 0.1M ($H_2PtCl_6/RuCl_3$) in 2M H_2SO_4 at a 1 mm Ø disc Au electrode. The potential was swept between 0.6 and -0.4 V starting at 0V at 20 mV/s.

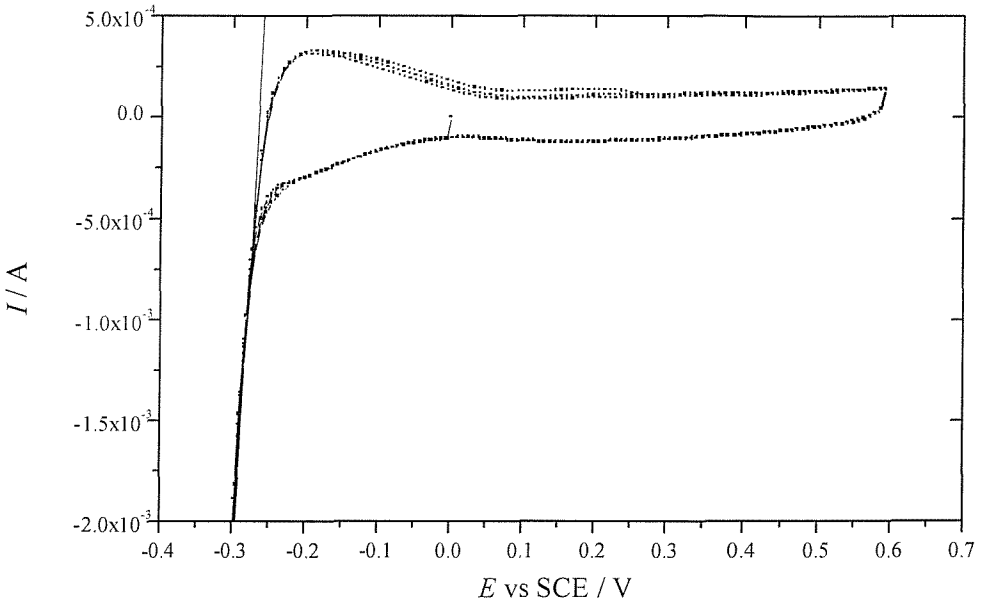

Figure 5.15 Cyclic voltammogramm 0.1 M ($H_2PtCL_6/RuCl_3$) in 2M H_2SO_4 at a 1 mm Ø disc Au electrode. Cycles between 0.6 to -0.3 V versus SCE at 20 mV/s.

It can be seen that a small current (-0.25 mA) is passed on the cathodic scan then the reduction current increases gradually around -0.1V to reach ~ -0.5 mA at -0.25V. A sharp increase to -2 mA was then recordered around -0.3 V. In the first sweep, no definite peak corresponding to the deposition of the metals on Au was observed.

After 10 min of cycling between 0.6V and -0.4V vs SCE the voltammogram depicted on figure 5.15 was similar to the first one recorded on the first cycle and was similar to the voltammogram of platinum and ruthenium electrodeposition from H_2PtCl_6 5mM and $RuCl_3$ 5mM on Au wire in H_2SO_4 1N [23]. The voltammogram shows the description of the hydrogen region overlapped with the double- layer resembling that one for ruthenium voltammetric response [23].

The following describes the results obtained during the potential step depositions on various Au substrates from a solution containing the platinum and ruthenium salts in 2M H_2SO_4.The electrodeposition of platinum and ruthenium onto a 1 mm Ø Au electrode was firstly investigated. From the cyclic voltammograms obtained in 2M H_2SO_4,-0.2 V was selected as the potential to carry out the electrodeposition. Figure 5.16 shows a typical current transient obtained during the electrodeposition of Pt and Ru from (0.1 M H_2PtCl_6,0.1M $RuCl_3$) in 2M H_2SO_4 at room temperature.

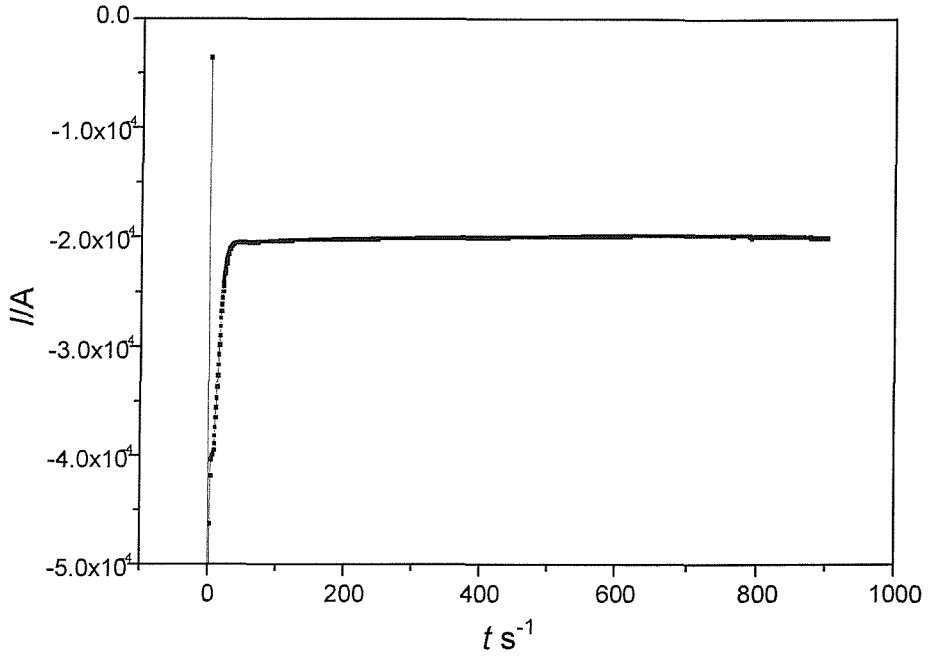

Figure 5.16 Typical current transient obtained during the electrodeposition of Pt and Ru from (0.1 M H_2PtCL_6,0.1M $RuCl_3$) in 2M H_2SO_4 at -0.2Vvs SCE (room temperature). 1mm diameter electrode. Charge passed = -1.8 mC.

From the current transient, it can be seen that the reduction current rises to ca. -0.5 mA, as a result of the double layer charging immediately after the potential step and then decreases very sharply to -0.4 mA where nucleation is believed to start. A sharp decrease of the current is then observed to -2 mA where the current reaches a plateau after 40 s . After 900 s deposition, the surface of the electrode was covered by a shiny and adherent grey film.

The potential step deposition was then carried out from the same intial mixture on 1 cm^2 Au electrode evaporated on glass. Figure 5.17 shows the current transient obtained during the electrodeposition of the 2 metal salts (0.1M) in H_2SO_4 2M on Au evaporated on glass (1 cm^2 surface area). These substrates were used to carry out EDAX and TEM studies. This time, the reduction current rises quickly to a maximum at ca. -21 mA decreases quickly to -14 mA where nucleation is believed to start and finally reaches -11 mA after 50s. A small increase in the reduction current is then observed to reach -12 mA after 600s. After 600s deposition, the surface of the electrode was fully covered by a shiny grey film.

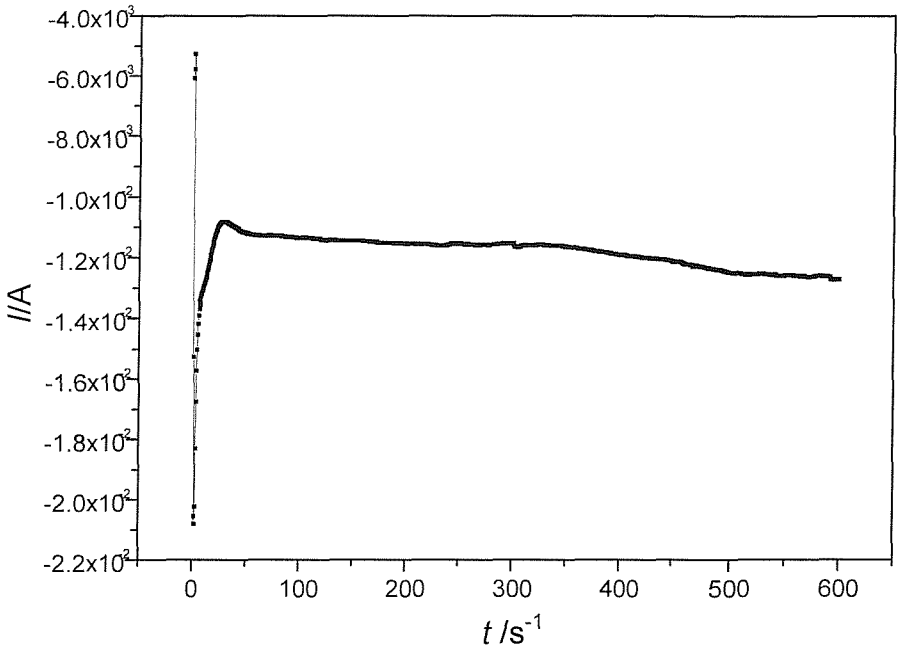

Figure 5.17 Typical current transient obtained during the electrodeposition of Pt and Ru from (0.1 M H_2PtCL_6, 0.1M $RuCl_3$) in H_2SO_4 2M on Au evaporated on glass (1cm^2 surface area). Deposition at -0.2Vvs SCE at room temperature.
Charge passed = -7.62 C.

The deposit obtained on the 1 mm Ø disc Au electrode as prepared above was then analysed by cyclic voltammetry in 2M H_2SO_4 and the results are shown on figure 5.18.

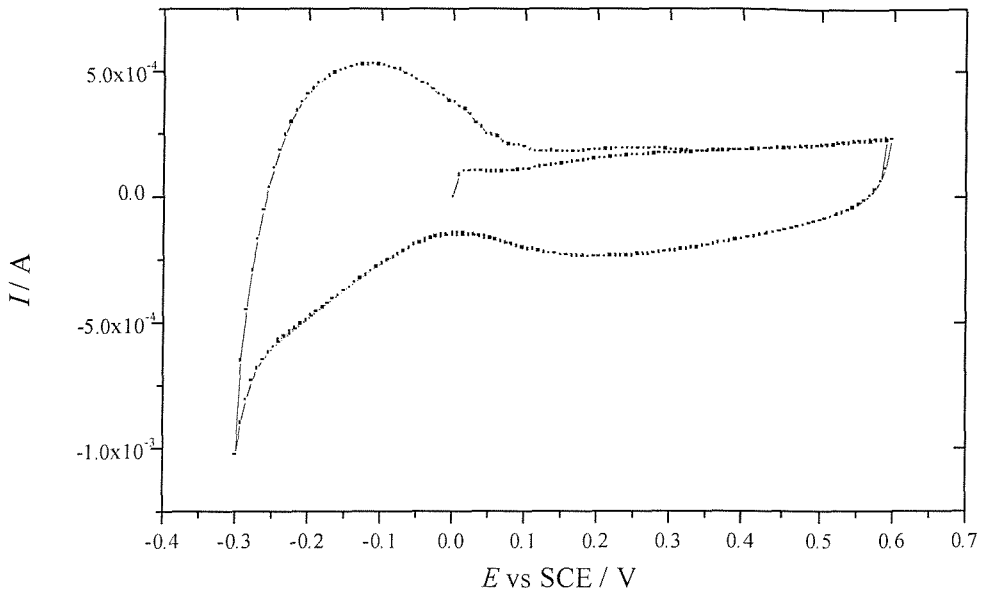

Figure 5.18 Cyclic voltammogram of PtRu deposit on 1 mm Ø Au electrode, scanning from 0.6 to -0.3 V versus SCE in 2M H_2SO_4 at 20 mV/s.

The potentiodynamic response attained a steady state after the first cycles and the overlap of hydrogen desorption and oxide formation region were observed. The voltammetry of the electrodeposits with 50 % ruthenium in the electrodeposition electrolyte did not show any features of platinum. The cyclic voltammograms obtained were similar the cyclic voltammograms of Pt/Ru electrodeposits prepared in solution at -0.2Vvs SCE in 0.5 M in H_2SO_4 with a 1:1 atomic ratio [23] where the "double layer" currents were also important and no distinct feature in the "hydrogen region" was observed [23]. These results were also confirmed by Richardz *et al.* who investigated the preparation and electrochemical characterisation of Pt -Ru alloys of different compositions electrodeposited on Au [22]. In their studies, after 1 hour potential step deposition at -0.2 V/SCE in H_2SO_4 0.5 M, the electrodes were characterised by cyclic voltammetry in H_2SO_4 0.5 M at 20 mV/s. Their results showed that the cyclic voltammograms changed slowly from pure ruthenium to pure platinum with increasing the platinum content in the deposition solution. The cyclic voltammograms were dominated by Ru -like structures up to relatively high amounts

of platinum in the solution [22]. For a nominal 1:1 Pt/Ru atomic ratio, the cyclic voltammograms exhibited the same characteristic behaviour (double layer current important, no distinct feature in the hydrogen region) as was observed in our studies. Cyclic voltammetry of the deposits obtained in 2M H_2SO_4 was the first evidence that the co reduction of the metal salts was successful.

5.3.2.2 Electrodeposition of H_I -Pt/Ru using the lyotropic H_I phase of Brij 76

The following describes the different electrodeposition of nanostructured platinum ruthenium carried out onto 1 cm^2 Au electrodes evaporated on glass substrates. These made the analysis by XRD, EDAX and TEM possible. The metal salts (0.1M in 2M H_2SO_4) were mixed with the non ionic surfactant to produce the templating mixture used for the electrodeposition (65 wt % Brij 76).

The templating mixture was firstly studied by cyclic voltammetry to investigate the effect of the addition of the surfactant on the cyclic voltammograms. Figure 5.19 shows a typical cyclic voltammogram of the H_I templating mixture made of 65 wt % Brij 76 and 35 wt % $H_2PtCl_6/RuCl_3$ (0.1 M) in H_2SO_4 2M at a 1mm Ø Au electrode. The potential was swept between 0.6 and -0.3 V starting at 0V at 20 mV/s.

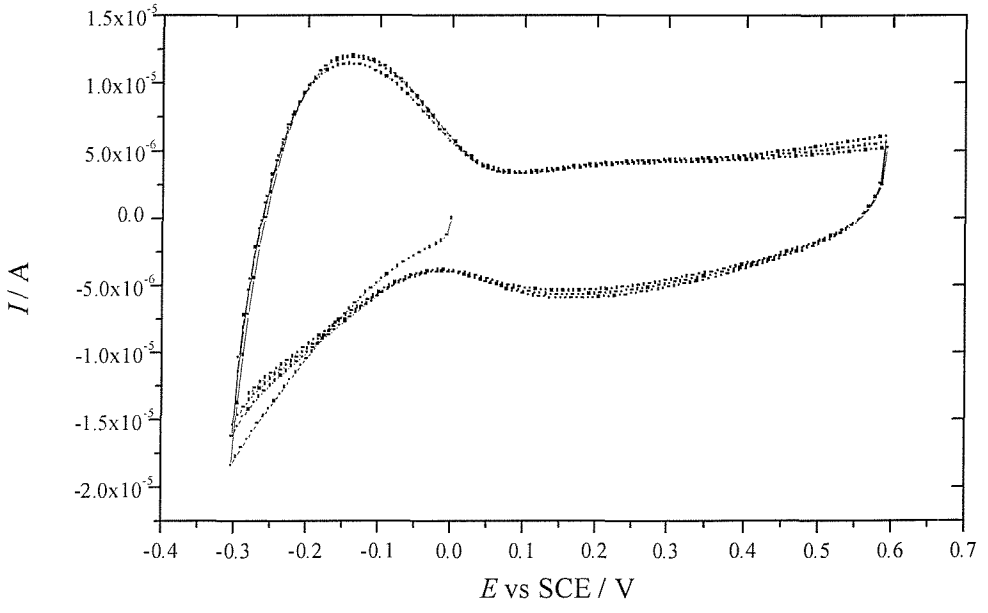

Figure 5.19 Cyclic voltammogramm of the H_I templating mixture made of 65 wt % Brij 76 and 35 wt % 0.1 M ($H_2PtCL_6/RuCl_3$) in H_2SO_4 2M at a 1 mm Ø Au electrode. Cycles between 0.6 to -0.3 V versus SCE at 20 mV/s.

When compared to the cyclic voltammogram in acidic solution (H_2SO_4 2M) reported on figure 5.15, the shape of the voltammogram was very similar but the main difference is the magnitude of the current which is much smaller (~100 to 1000 times smaller in the presence of Brij 76). Similar behaviour was observed during the electrochemical deposition of mesoporous lead reported in chapter 4 and palladium films from different surfactants systems [24]. The small intensity of the current recorded can be explained by a much slower diffusion through the highly viscous lyotropic phase.

From the cyclic voltammogram, -0.2 V was selected as the potential to carry out the electrodeposition (same potential as electrodeposition in solution). Potential step depositions were carried out at room temperature and at 40 ^{0}C to assess the effect of the temperature on the deposition process. Figure 5.20 shows a typical current transient obtained during the electrodeposition of platinum and ruthenium from a templating mixture containing 65 wt % Brij 76 and 35 wt % $H_2PtCl_6/RuCl_3$ (0.1 M) in 2M H_2SO_4 at -0.2V on a 1 cm^2 Au electrode.

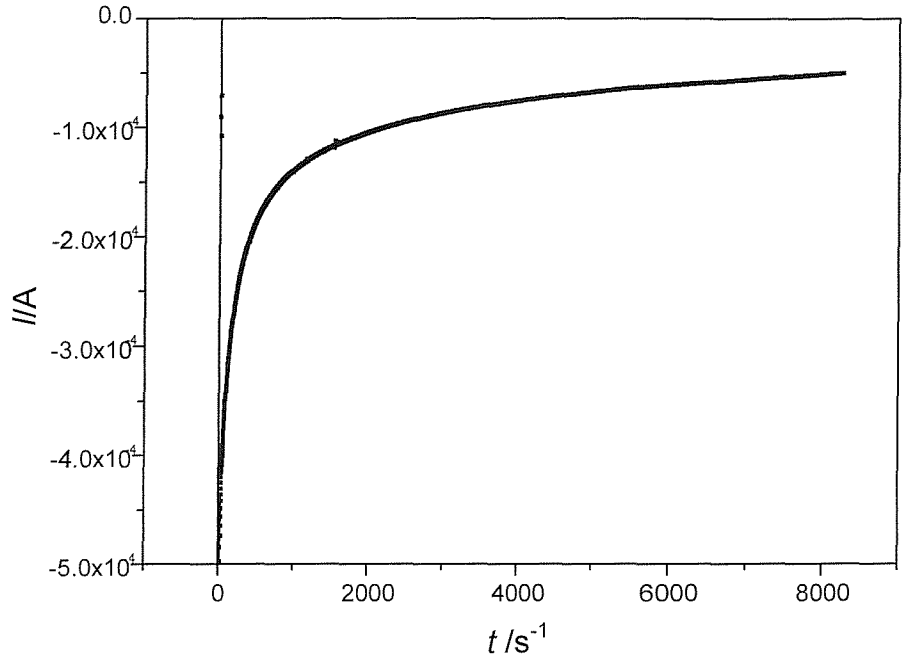

Figure 5.20 Typical current transient obtained during the electrodeposition of platinum and ruthenium from a H_I templating mixture containing 65 wt % Brij 76 and 35 wt % $H_2PtCl_6/RuCl_3$ (0.1 M) in H_2SO_4 2M at -0.2Vvs SCE on a 1 cm^2 Au electrode. Charge passed -5 mC.

From the current transient, it can be seen that the reduction current rises quickly to a maximum at ca. - 500 μA decreases quickly to -300 μA over 1000s, then decreases slowly with time to reach ~50 μA after 8000s. At room temperature, the transients obtained were reproducible (shape, magnitude of the current).

Using the same surface area electrode and templating mixture as before, current transients of the electrodepositions were recorded at 40 °C. Potential step deposition was carried out in exactly the same conditions as before (ie: deposition at -0.2 V, same deposition time) and a typical current transient is shown on figure 5.21.

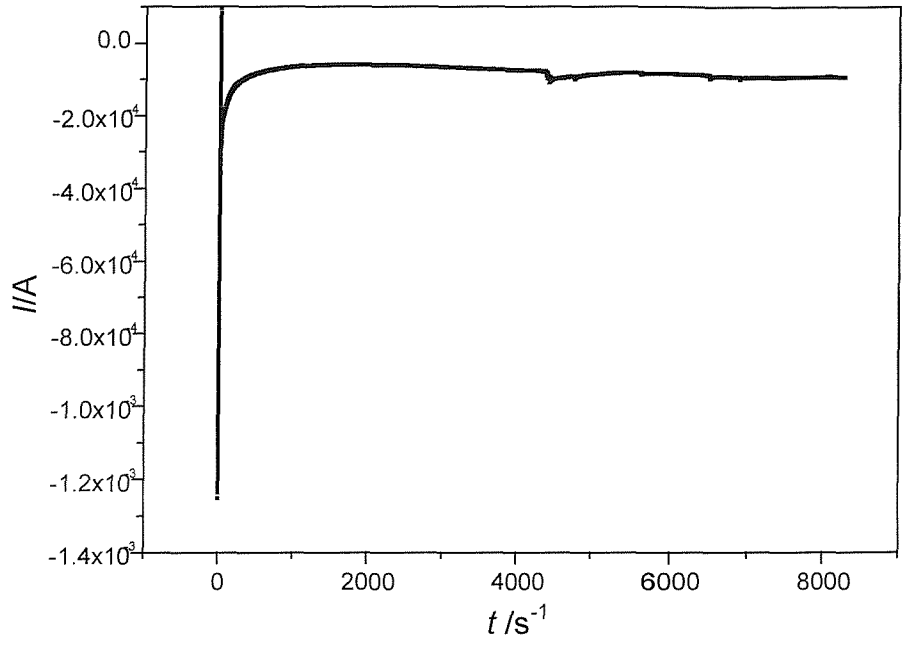

Figure 5.21 Typical current transient obtained during the electrodeposition of platinum and ruthenium at 40 °C from a H_I templating mixture containing 65 wt % Brij 76 and 35 wt % H_2PtCl_6/$Rucl_3$ (0.1 M) in 2M H_2SO_4 at -0.2Vvs SCE on a 1 cm^2 Au electrode. Charge passed -7 mC.

Immediately after the potential step, the reduction rises sharply to -1.2 mA as a result of the double layer charging and then decreases very sharply to -200 μA where nucleation is believed to start just after a few seconds. Finally the reduction current reaches a plateau at around -100 μA after only ~ 500s.

When comparing this current transient to the one obtained in sulfuric acid electrolyte at room temperature, differences can be found. At room temperature, after the potential step, the current decreases slowly with time and no plateau was observed.
At 40 °C, the current decreases and reaches an equilibrium very quickly. The current transients obtained at 40 °C were reproducible (shape, current magnitude) and were similar in shape to the typical current transient obtained in solution. This may be attributed to the decrease of the viscosity in the template mixture at higher temperature. Nevertheless, similar current magnitudes were obtained throughout the various depositions using the template mixture which were much smaller than the currents recorded in solutions.

5.3.2.3 Analysis of the film deposited from 65 wt % Brij 76

The film deposited from the templating mixture (65 wt % Brij 76, deposition at -0.2 V at room temperature) was analysed by XRD. The X ray diffractogram on figure 5.22 shows only one diffraction peak in the small angle region corresponding to an ordered H_I phase with a lattice parameter of 6 nm similar to the lattice parameter obtained for the chemically prepared H_I-Pt/Ru.

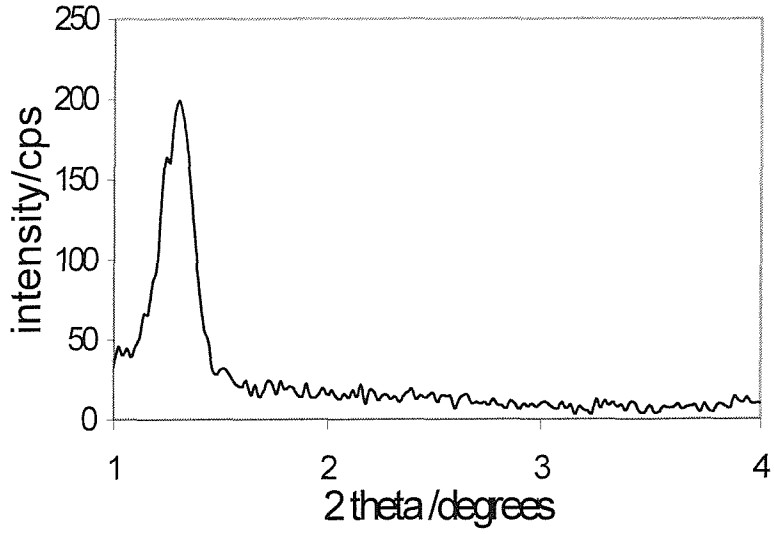

Figure 5.22 Small angle XRD of mesoporous Pt-Ru catalyst electrodeposited on 1 cm^2 Au electrode at room temperature.d_{100}= 6 nm.

The wide angle X-ray diffractogram of the mesoporous Pt/Ru film deposited on Au electrode was recorded and compared to the wide angle diffraction data obtained for the chemically prepared H_I -Pt/Ru alloy particles. The diffractogram depicted on figure 5.23 shows five reflections in the wide angle region studied. The biggest reflection observed for 2 theta = 38.2 degrees corresponds to a gold peak as confirmed by the ICDS database due to the thinness of the deposit. The four others reflections were in good agreement with those reported for the chemically prepared HI Pt-Ru particles. The X-ray diffraction data are summarised in table 4.

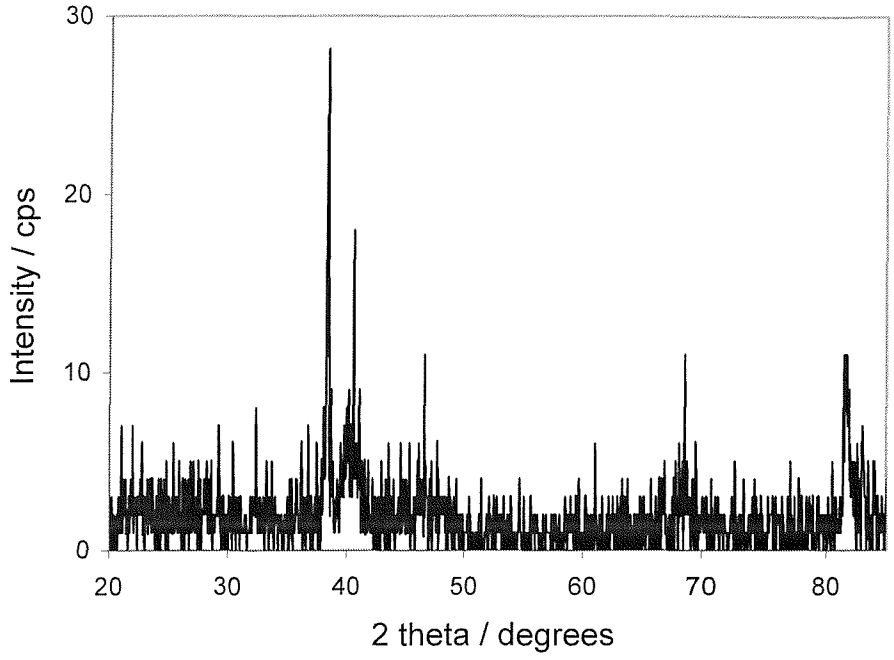

Figure 5.23 Wide angle diffraction XRD of mesoporous Pt-Ru film electrodeposited on Au electrode at -0.2 V/SCE (room temperature).

	H_IPt Chemically prepared (Steel reduction)		H_I- Pt/Ru Chemically prepared ($NaBH_4$ reduction)		H_I-ePt/Ru Electrochemically prepared	
hkl	d /Å	I/a.u.	d /Å	I/a.u.	d /Å	I/a.u.
111	2.25	100	2.24	100	2.23	100
200	1.96	54	1.95	48	1.94	61
220	1.38	29	1.37	27	1.37	61
311	1.19	31	1.18	30	1.18	61

Table 4. Summary of wide angle X-ray diffraction data obtained using Cu $K_{\alpha 1}$ radiation (λ = 1.5405 Å) for H_I Pt chemically prepared by steel reduction, H_I-Pt/Ru chemically prepared by $NaBH_4$ reduction, electrodeposited H_I -Pt/Ru (H_I -ePt/Ru) obtained by potential step deposition at -0.2 V vs SCE. *I* denotes the intensity of the diffraction peaks and *d* their position in real space.

X -Ray microanalysis was carried out on the Pt/Ru films deposited on Au electrode to confirm whether or not both metals were electrodeposited. Figure 5.24 shows the X-ray microanalysis of the films obtained by potential step deposition from the isotropic reaction mixture in acid solution at room temperature (-0.2 V, deposition time 600s). These results were compared to the X-ray microanalysis data (figure 5.25) obtained for the H_I Pt-Ru films deposited from the H_I phase of Brij 76 also in acid solution at room temperature (-0.2 V, deposition time 8000 s).

In both cases, EDAX spectra obtained confirmed that both platinum and ruthenium were deposited in the conditions reported but with different ratios (qualitative analysis). The presence of a Au peak for the films deposited from the lyotropic H_I phase of Brij 76 showed that the thickness of these films was small. This confirmed the wide angle XRD analysis where the presence of Au was also detected. Using the same initial concentrations of metal salts in the H_I phase of Brij 76, thicker deposits could be obtained by increasing the deposition time.

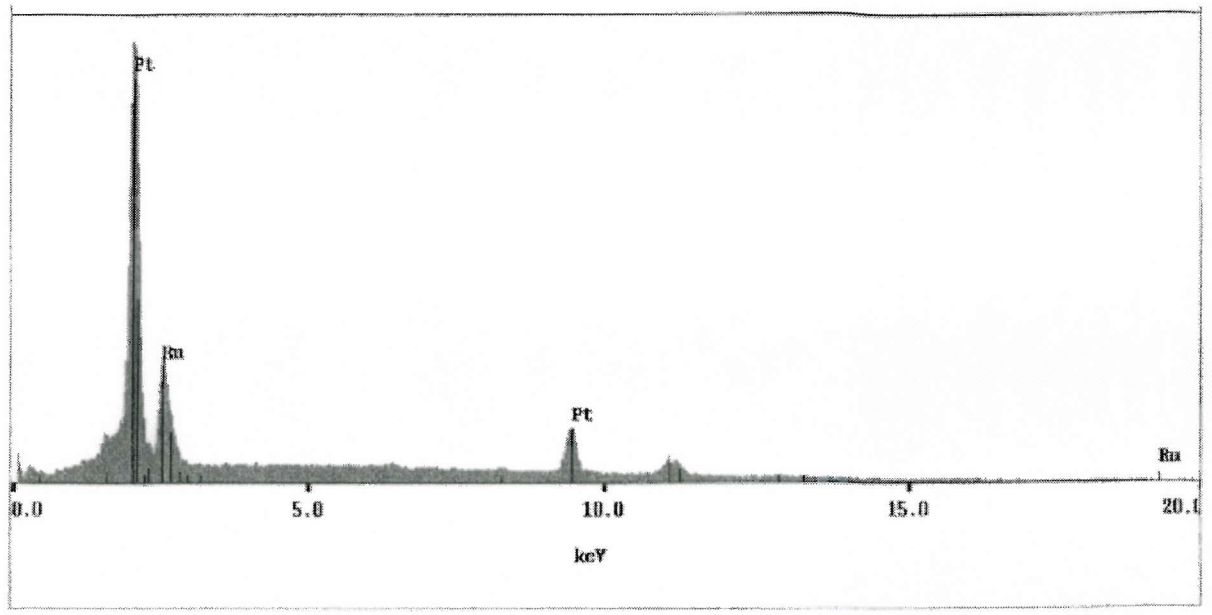

Figure 5.24 EDAX spectra of Pt-Ru film on 1 cm^2 Au electrode deposited at -0.2 V vs SCE for 600s at room temperature.

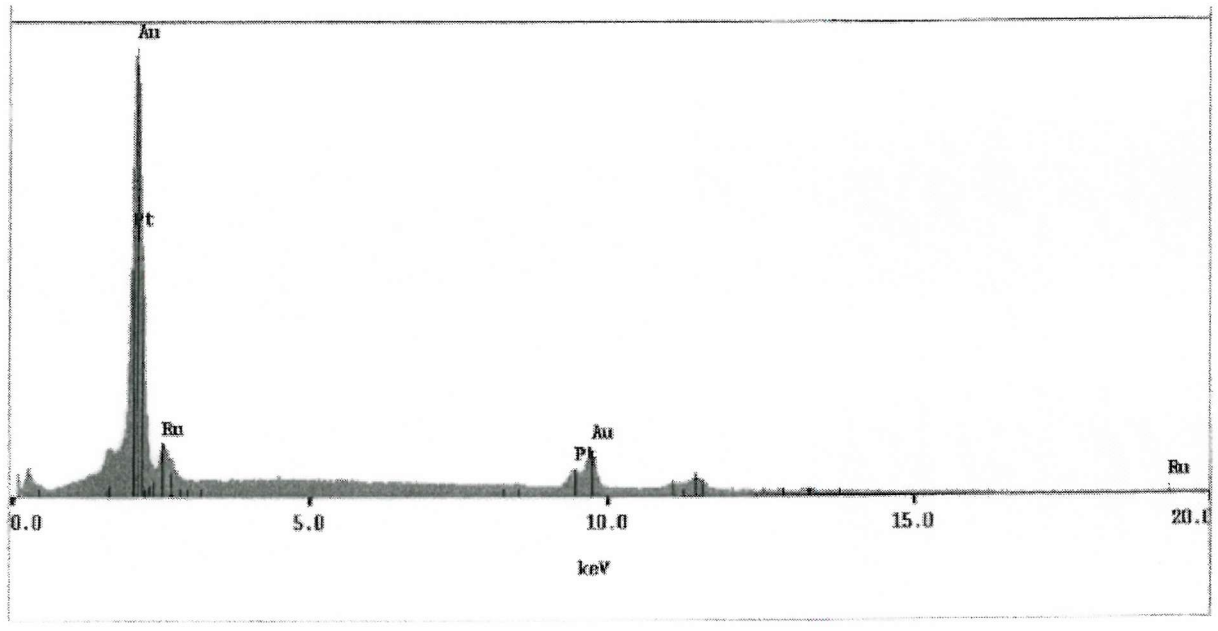

Figure 5.25 EDAX spectra of HI PtRu film deposited on 1 cm^2 Au electrode at -0.2Vvs SCE for 8000s at room temperature.

In table 4 and 5 are shown the corresponding compositions of the samples prepared from solutions and from the H_I phase of Brij 76 respectively (nominal 1:1 atomic ratio of platinum to ruthenium in the initial mixtures).

Pt-Ru Ratio in solution	Deposition time (s)	Analysis number	Atomic % Platinum	Atomic % Ruthenium	Atomic % Gold
1:1	600	1	76	23	1
1:1	600	2	73	25	2

Table 5. Sample compositions in at.% bases on SEM -EDAX analysis for Pt-Ru film on 1 cm^2 Au electrode deposited at -0.2 V vs SCE for 600s at room temperature.

Pt-Ru Ratio in H_I phase of Brij 76	Deposition time (s)	Analysis number	Atomic % Platinum	Atomic % Ruthenium	Atomic % Gold
1:1	8000	1	25	12	58
1:1	8000	2	28	20	52

Table 6. Sample compositions in at.% based on SEM -EDAX analysis for H_I Pt-Ru film on 1 cm^2 Au electrode deposited at -0.2 V vs SCE for 8000s at room temperature.

Electrodeposits obtained after 600s for a 1:1 atomic ratio of platinum to ruthenium in the isotropic reaction mixture showed that the gold surface was completely covered by a homogeneous electrodeposit with a composition of 76 % Pt and 23 % Ru (table 5). Although not in exactly the same experimental conditions, these results can be compared with the SEM-EDAX analysis reported for the co electrodeposition of platinum and ruthenium on Au wire from a 1:1 Pt-Ru ratio in acidic solution (H_2 $PtCl_6$ 5mM, $RuCl_3$ 5mM in H_2SO_4 0.5 M) [23]. After 15 mn deposition at room temperature, the gold surface was completely covered by an homogeneous electrodeposit with a composition of 74% Pt and 26 % Ru. The results obtained in our experiments were in good agreement and showed that platinum was preferentially deposited on the Au electrode (ratio of 3 Pt for 1 Ru deposited).

The sample compositions reported in table 6 for the H_I -Pt/Ru films showed that a large amount of Au was detected due to the thinness of the films. Electrodeposit obtained after 8000s were characterised by 25 % Pt, 12 % Ru and 58% Au composition (analysis1). Considering the two noble metals only, this corresponded to 59% Pt and 41 % Ru deposited on the Au surface. When comparing to the results obtained from isotropic reaction mixture in terms of amount of noble metal deposited,

the electrodeposition within the H_I phase of Brij 76 tend to produce films with higher content of ruthenium.

The H_I-Pt/Ru film deposited on Au electrode at room temperature was then analysed by TEM. The TEM micrograph on figure 5.26 revealed a non regular but porous structure. Although pore size measurement from the micrograph was difficult (very dark material), pore diameter was measured as 2.0 nm with 2.5 nm walls between the pores.

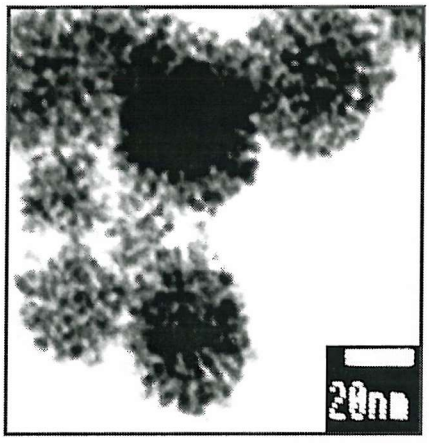

Figure 5.26 TEM micrograph of H_I -Pt/Ru electrodeposited from a H_I templating mixture containing 65 wt % Brij 76 and 35 wt % H_2PtCl_6/$Rucl_3$ (0.1 M) in 2M H_2SO_4 at -0.2Vvs SCE on a 1 cm^2 Au electrode at room temperature. Charge passed -5 mC.

5.3.3 Discussion on the preparation of H_I Pt/Ru and H_I Pt/Rh

5.3.3.1 Methods of preparation

For the preparation of H_I-Pt/Ru, the different reducing agents investigated (ie $NaBH_4$ and HCHO+ KOH mixtures) were successful in reducing the platinum and ruthenium precursors in the H_I phase of Brij 76 at room temperature. $NaBH_4$ reduction produced a material with a regular pore structure whereas the other method produced a porous but disordered structure. As for the preparation of H_I platinum reported in Chapter 2, hypotheses as to why the different reduction methods produced different materials can be made. The methods investigated reduced the metal salt precursors at different rates. Although it was not possible to visually assess the rapidity of the reduction, it can be assumed that $NaBH_4$ as a strong reducing agent reduced the salts more rapidly than the HCHO + KOH mixtures. If the co-reduction occurs slowly, then it is likely that the structures become more disordered as the surfactant molecules reorganise. Moreover, although the phase behaviour of Brij 76 in the presence of platinic acid and ruthenium chloride was checked by polarising microscope prior to reduction (stability of H_I phase at room temperature), the effect of the different reducing agents was unknown. Considering the dynamic states of all the species present in the reaction mixture further complicates the situation. During the co-reduction, the metal salts concentrations are depleted and reaction by-products formed. It is likely that the phase behaviour of the surfactant is changing throughout the reduction.

5.3.3.2 Alloy formation

Although the liquid crystal strategy has been used successfully to produce mesoporous platinum, the co-reduction of binary mixtures of metal compounds leading to intermetallic materials with a uniform distribution of the constituent metals was not certain. As is evident from the literature, reduction of binary mixtures does not necessarily produce intermetallic materials with an homogeneous distribution of metal atom. Even when alloying is achieved successfully, the metal distribution is often non uniform within a particle [25]. In our experiments, the amount of metal salts was chosen initially so as to produce an alloy with a nominal 1:1 atomic ratio of Pt to Ru. WAXRD and EXAFS analysis on the H_I -Pt/Ru materials obtained proved that the preparations were successful: intermetallic particles were obtained and H_I -Pt/Ru consisted of a well mixed 1:1 alloy of the two metals.

For the first time, the preparation of nanostructured mesoporous bimetallic alloy with a uniform distribution of the components was successfully achieved.

5.3.3.3 Discussion on the electrochemical preparations of H_I Pt/Ru

Investigations on the electrochemical preparation of HI Pt-Ru have shown it is possible to prepare mesoporous Pt-Ru from Brij 76 lyotropic H_I phase. Platinic acid and ruthenium chloride were shown to be suitable precursors for the co-deposition of a coherent and ordered film on the surface of an Au supporting electrode. As for the preparation of a mesoporous lead film on Au electrode described in chapter 4, cyclic voltammetry studies in solution and in the presence of the surfactant was necessary to assess the behaviour of the metal precursors and to select a correct potential for the potential step deposition. By increasing the deposition time, the production of thicker films on the Au electrodes could be obtained and ease the interpretation of the wide angle X-ray diffraction and EDAX analysis. Although the studies reported were not exhaustive, the results reported indeed the ability to produce ordered mesoporous films using the co -deposition of the two metallic precursors investigated.

5.4 Conclusion and further work

The work described in this chapter showed that it is possible to use the lyotropic H_I phase of Brij 76 as mould for the chemical preparation of mesoporous Pt/Ru alloys with high specific surface area (83 m^2g^{-1}). The material exhibit a nanostructure consisting of cylindrical pores of uniform diameter disposed in an hexagonal arrangement with respect to one another. Small angle XRD confirmed the order of the nanostructure with a lattice parameter of 60.3Å. For a 1:1 atomic ratio of platinum to ruthenium in the initial templating mixture, Wide angle XRD and EXAFS were used to confirm the alloy formation. XRD studies showed that H_I Pt/Ru had a fcc structure (Fm3m space group); the contraction in the lattice parameter evidenced by the shift to shorter distances, was consistent with the smaller size of the ruthenium compared with platinum. The intermetallic nature of the H_I Pt/Ru material as well as the uniform distribution of the metallic components was successfully demonstrated by EXAFS analysis: H_I Pt/Ru consists of a well mixed 1:1 alloy of the two metals.
The chemical preparation of HI Pt/Rh was also investigated for a 1:1 atomic ratio of platinum to rhodium; TEM analysis revealed the nanostructure of the material and high specific surface area of 58 m^2g^{-1} was measured by BET Nitrogen adsorption. EXAFS analysis confirmed that HI Pt/Rh consisted of a well mixed 1:1 alloy of the two metals.

Finally, electrodeposition was shown to be suitable for the preparation of coherent and nanostructured films by the simultaneous co depositions of the two metal precursors dissolved in the H_I phase of Brij 76. XRD revealed a single peak in the small angle region characteristic of an ordered periodic structure and TEM showed the porosity of the material obtained. Although the alloy formation could not be confirmed with certainty (EXAFS required), wide angle XRD and X-ray microanalysis on the films obtained showed that both metals were successfully deposited. The results obtained were indeed in good agreement with literature data obtained on the co deposition of Pt/Ru alloy from isotropic reaction mixtures. The similarities observed suggested that the films electrodeposited consisted of nanostuctured Pt/Ru intermetallic particles.

Further work

Although the study of mesoporous Pt /Ru alloy has been fairly exhaustive, numerous issues can still be addressed:

- H_2PtCl_6 and $RuCl_3$ were shown to be suitable precursors for the chemical preparation of the mesoporous Pt/Ru alloy but other sources should be investigated. The suitable metal salts must be highly soluble in water without affecting the phase forming properties of the surfactant. The ammonium salts of platinum and ruthenium could be investigated as precursors for example ($(NH_4)_2PtCl_6$ and $(NH_4)_2RuCl_6$ respectively).

- The H_I Pt/Ru materials prepared while varying the atomic ratio of platinum to ruthenium should be characterised by EXAFS to confirm the intermetallic and uniform distribution of the metallic components. Various other compositions could be prepared in a similar way.

- In our preparations, the H_I phase of Brij 76 (75 wt %) was used in the templating mixture. Other compositions or other surfactants from the Brij series could be employed for the production of nanostructured intermetallic alloys. Investigating other reduction temperatures could also improve the quality of the materials prepared.

The chemical preparation of mesoporous Pt-Rh materials should be addressed in more detail. Preliminary results obtained showed it was possible to prepare nanostructure Pt/Rh alloys particles but further characterisation is required (small angle and wide angle diffraction). As the rhodium precursor is very expensive, producing enough materials to be characterised was the main difficulty encountered. This could be overcome by preparing H_I -Pt/Rh marerials with a much smaller atomic ratio of ruthenium to platinum or using another rhodium precursor in the initial mixture. For three way catalysis applications for example, the amount of rhodium in the washcoat is minimum compared to the amount of platinum.

Investigations into the electrochemical preparation of H_I -Pt/Ru were successful. The aim of the research was to show it is possible to prepare nanostructured Pt/Ru films electrochemically and that the films obtained were made of intermetallic particles. Although only one system was investigated, potential step deposition was shown to be an attractive method as the rate of reduction can be controlled and the reaction by products are minimal. Further work on the electrochemical preparation include:

- Investigating different templating compositions at different temperatures.

- Increasing the metal salts concentrations and the reduction temperature should increase the deposition rate.

- Increasing the deposition time to produce thicker films to make the qualitative XRD analysis easier for example.

- Investigating other potentials to carry out the electrodepositions and compare the resulting compositions of the films obtained for a given initial ratio of platinum to ruthenium.

- Confirmation of the alloy formation by EXAFS analysis, this constitue the final evidence that intermetallic particles were obtained..

- Finally, the potential applications of the nanostructured Pt/Ru films should be assessed in the electrooxidation of methanol. Due to their regularity of structure and porosity, the mesoporous films prepared could become of commercial importance in this vast field of research.

5.5 References

1. Z Hu, F M Allen, *J.Catal.*,174,13 (1998).
2. H A Gasteiger, N Markovic, PN Ross Jr, EJ Cairns, *J.Phys.Chem.*, 98,617 (1994).
3. H A Gasteiger, N Markovic, PN Ross Jr, *J.Phys.Chem.*, 99, 16757 (1995).
4. K A Friedrich, K P Geizers, U Linke, U Stimming, J Stumper, *J.Electroanal.Chem.*, 402,123 (1996).
5. HF Oetjen, VM Schmidt, U Stimming, F Trila, *J.Electrochem.Soc.*, 143,3838 (1996).
6. M Iwase, S Kawatsu, *Proceedings of the Fist International Symposium on Proton Conducting Membrane Fuel Cells*, S Gottesfeld, G halpert, A Landgrebe (Eds), The Electrochemical Society, Pennington, NJ, Vol.95-23, p12.
7. Z Hu, *J.Chem.Soc.Chem.Commun.* 879 (1996).
8. D W Mc Kee, F J Norton, *J. Phys.Chem.*, 68,**3**,481 (1964).
9. T Horiba, K Tamura, *Denki Kagaku*, 57,**7**, 712 (1989).
10. V Radmilovic, H A Gasteiger, P N Ross Jr, *J.Catal.*,154,98 (1995).
11. M Watanabe, M Uchida, S Motoo, *J. Electroanal.Chem*, 229,395 (1987).
12. N R B Coleman, Ph D Thesis, Department of Chemistry, University of Southampton (1999).
13. M Watanabe, M Uchida, S Motoo, *J. Electroanal. Chem.* 229, 395 (1987).
14. T Barth, G Lunde, *Z. Phys. Chem. (Munich)* 121, 78 (1926).
15. J. Mc Breen, S. Mukerjee, *J.Electochem.Soc.*,142,3399 (1995).
16. N Binsted, "Excurv98: CCLRC Daresbury Laboratory Computer Programme" (CCLRC Daresbury Laboratory 1998).
17. H A Gasteiger, N Markovic, P N Ross, E J Cairns, *J. Phys. Chem.* 97,12020 (1993).
18. H A Gasteiger, N Markovic, P N Ross Jr,. E J Cairns, *J.Phys.Chem.*, 98, **2**, 617 (1994).
19. H A Gasteiger, N Markovic, P N Ross Jr,. E J Cairns, *J.Phys.Chem.*, 97,**46**,12020 (1993).
20. C E Lee, S H Bergens, *J.Phys.Chem.B*, 102,193 (1998).
21. J P I Souza, F J Botelho Rabelo, I R de Moraes, F C Nart, *J.Electroanal.Chem.*,420,17 (1997).

22. F Richardz, B Wohlmann, U Vogel, H Hoffschulz, K Wandelt, *Surface Science*,335,361 (1995).

23. B A Lopez De Mishima, H T Mishima, G Castro, *Electrochimica Acta*,40, **15**, 2491 (1995).

24. S Guerin, Ph D Thesis, Depatment of Chemistry, University of Southampton (1999).

25. F.C.M.J.M. vanDelft, B.E. Nieuwenhuys, J. Siera, R.M. Wolf, *ISIJ International* , **29**, 550 (1989).

Chapter 6

Catalytic activity of mesoporous metals

6.1 Background and objectives

As described in chapter 1, noble metals especially platinum and palladium are used extensively in heterogeneous catalysis. Because of their exceptional activity, particularly for reactions involving hydrogen, their uses are varied. In the catalytic processes, it is evident that adsorption on the surface and surface area of the catalysts are key factors for conversion or selectivity. The possibility of producing mesoporous metals with inherently high surface areas and high degree of porosity (concave and convexe surfaces) is particularly attractive in the vast field of heterogeneous catalysis.

Preliminary experiments aimed at assessing the catalytic activity of mesoporous platinum and platinum/ruthenium alloys in hydrogenation reactions were carried out. In the first set of experiments, we compared the activity of H_I Pt with that of commercial Pt black in the hydrogenation of 4,7 dimethyl-8-methoxycoumarine. The hydrogenation of this coumarine derivative at 1500 psi and 150 °C has been reported and provides a simple route to dihydrocoumarine and/or ethyl butanoate whereas lower pressures and temperatures tend to yield only the dihydrocoumarine [1]. The dihydrocoumarine is a key intermediate in the synthesis of a class of endothelin receptor antagonists under development by Smithkline Beecham [2]. A number of physiological responses are mediated by these endothelin receptors and their research aims at controlling certain detrimental human physiological responses by blocking these receptors [2]. In the second set of experiments, the activity of H_I Pt/Ru (1:1 atomic ratio) was compared to that of a commercial Pt/Ru black in the hydrogenation of 3,4,5,6 tetrahydrophtalinic anhydride. In both cases, the progress of the reactions were monitored by High Pressure Liquid Chromatography (HPLC).

The development of fuel cell technology has been intimately linked to the development of effective electrocatalyst technology. For the proton exchange membrane (PEM) fuel cell, the catalysts used in the membrane electrode assembly are carbon supported Pt based catalysts where the loading of active metal can be very high. For a cathode catalyst, this can range from 10 to 40 % Pt supported on a conductive carbon black substrate. The modification of platinum electrocatalytic properties by alloying with other metals is also well established for both anodic and cathodic applications[3-5]. Platinum modified by

ruthenium in the form of an alloy does improve CO tolerance compared with pure Pt over a wide range of conditions [6-10]; the ruthenium alloyed catalyst exhibits lower overpotentials and longer lifetimes compared to the platinum. The ability to produce high surface area mesoporous platinum and platinum based alloys with ordered pore systems make a very attractive alternative to current porous Pt based materials used in fuel cell technology.The final set of experiment was to assess the catalytic activity of mesoporous platinum in the formulation of electrodes for fuel cells applications. The electrodes prepared were compared with conventional electrodes in CO and MeOH electrooxidation.

6.2 Experimental

6.2.1 Hydrogenation of coumarine

The activity of H_I Pt (46 m^2g^{-1}) was compared with that of Pt black (25-30 m^2g^{-1}, Aldrich) in the hydrogenation of Coumarine. In these studies, 100mg of catalyst was added to 0.15 g of Coumarine dissolved in 10 ml ethyl acetate. The reaction vessels were purged with nitrogen and the hydrogenation was carried out under hydrogen at atmospheric pressure. The progress of the reactions depicted in figure 6.1 was determined by extracting 25 µl aliquots from each reaction mixture. Each aliquot was added to 975 µl of acetronitrile and eluted through an HPLC using a gradient of 0 to 100 % acetonitrile/trifluoroacetic acid over 20 minutes.

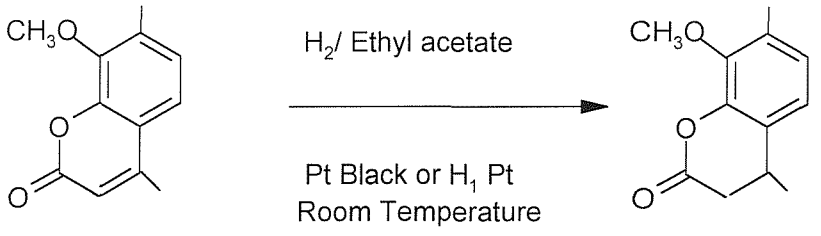

Figure 6.1. Hydrogenation of coumarine using Platinum as catalyst

6.2.2 Hydrogenation of 3,4,5,6 tetrahydrophtalinic anhydride

The activity of H_I Pt/Ru (1:1 atomic ratio, 83 m^2g^{-1}) was compared with that of a commercial Pt/Ru black (1:1 atomic ratio, specific surface area of 62 m2g-1, obtained from Alfa Aesar GmbH) in the hydrogenation of 3,4,5,6 tetrahydrophtalinic anhydride (obtained from Aldrich). In these studies, 50 mg of catalyst was added to 0.5 g of the anhydride dissolved in 10 ml ethyl acetate. The reaction vessels were purged with nitrogen and the hydrogenation was carried out under hydrogen at atmospheric pressure. The progress of the reaction depicted on figure 6.2 was determined by extracting 25 µl aliquots from each reaction mixture. Each aliquot was added to 975 µl of acetronitrile and eluted through an HPLC as mentioned before in the coumarine hydrogenation studies.

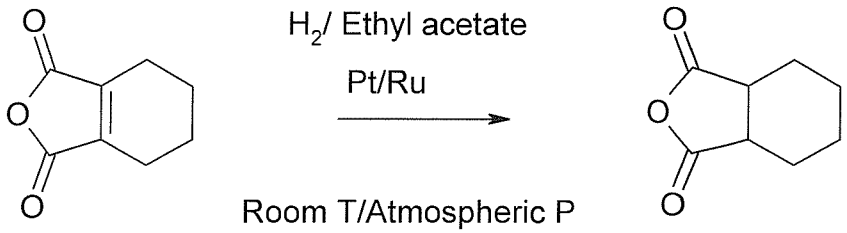

Figure 6.2 Hydrogenation of 3,4,5,6 tetrahydrophtalinic anhydride using Pt/Ru as catalyst.

6.3 Results and discussion

6.3.1 Hydrogenation of Coumarine

The progress of the reaction was monitored by extracting 25 μl aliquots from each reaction mixture. The HPLC chromatograms obtained were compared to the one obtained for the starting material and final product (retention time). Quantitative analysis (area %) of starting material and product was determined by HPLC to monitor the consumption of starting material and formation of product. Figure 6.3 and 6.4 show the HPLC chromatograms obtained for the starting material and final product characterised by only a single peak. The higher retention time obtained for the product in figure 6.4 was due to the less polar nature of the product (double bond being reduced).

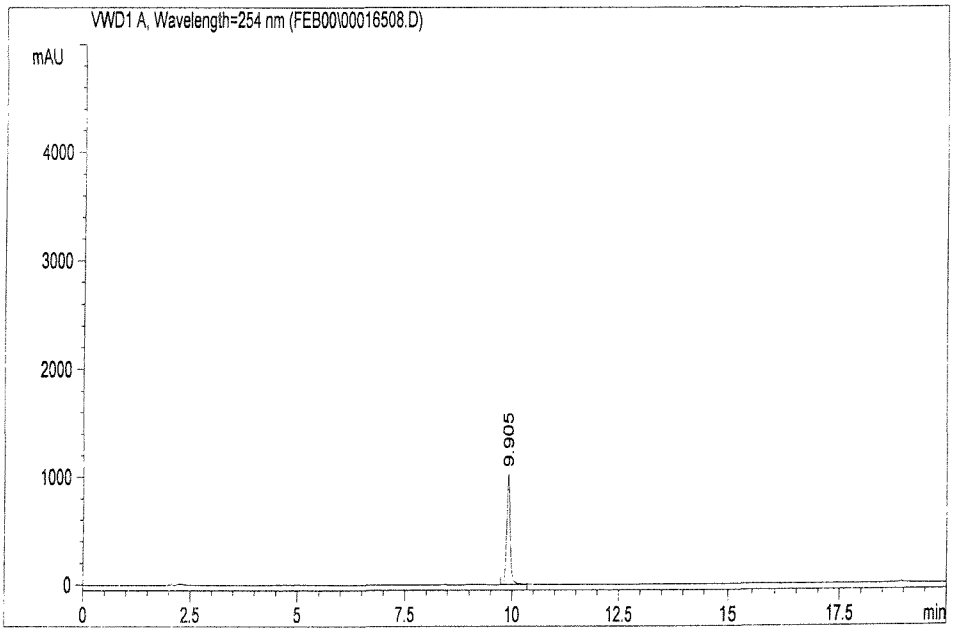

Figure 6.3 HPLC chromatogram of coumarine starting material

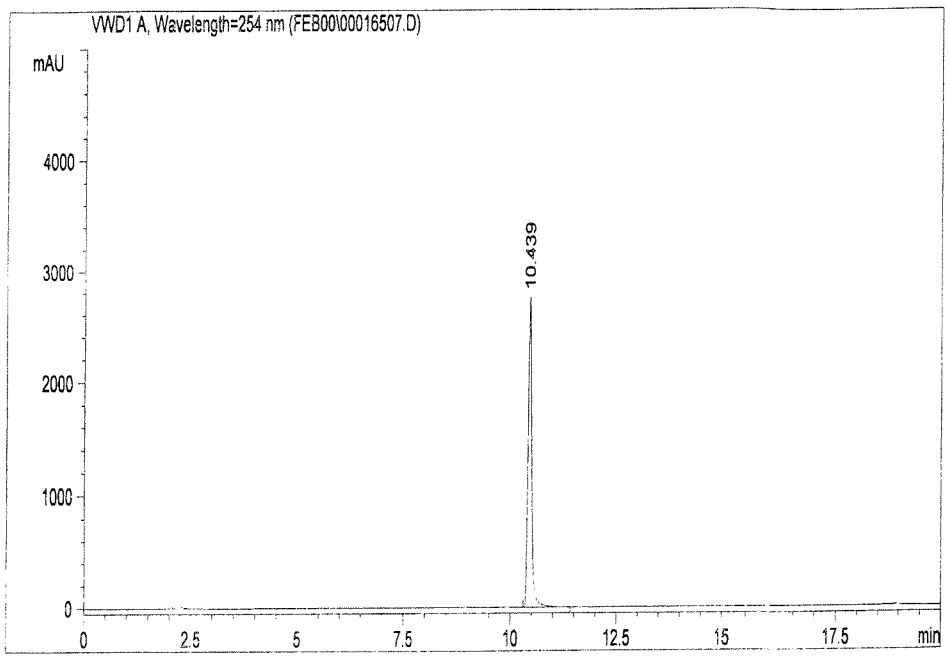

Figure 6.4 HPLC chromatogram of product

Figure 6.5 and 6.6 show the typical hplc chromatograms obtained after 2 hours hydrogenation at room temperature for the the reaction catalysed by H_I Pt and Pt black respectively. After 2 hours hydrogenation, the results showed that a much higher concentration of product was formed when mesoporous platinum was used (product to starting material ratio, area % compared for both catalysts).

The consumption of starting material and formation of product are shown on figure 6.7 and 6.8 respectively (quantitative yield determined by HPLC).

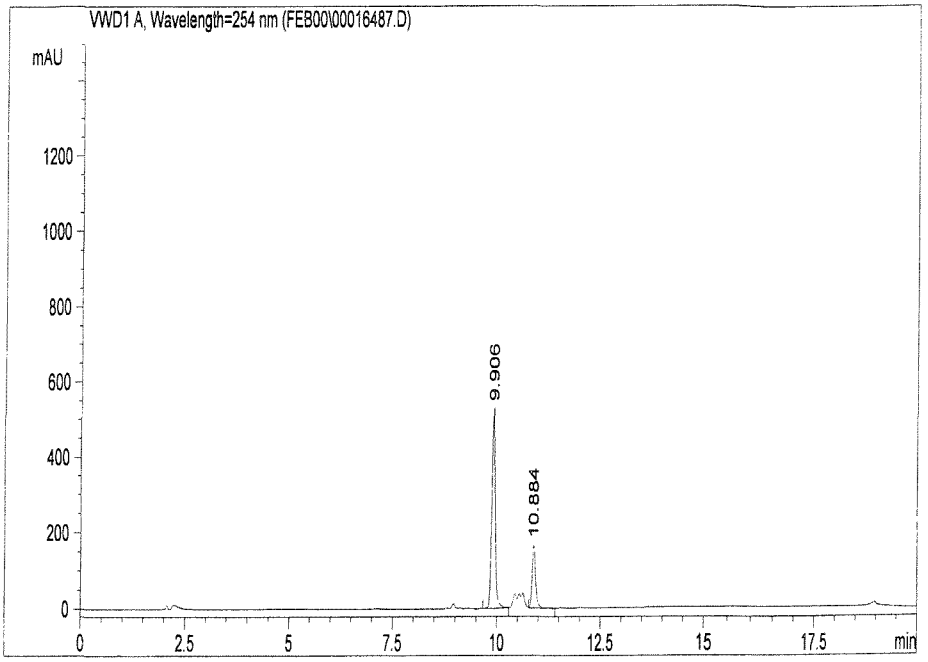

Figure 6.5 HPLC chromatogram of reaction mixture (starting material and product) after 2 hours hydrogenation at room temperature using H_1 Pt as catalyst.

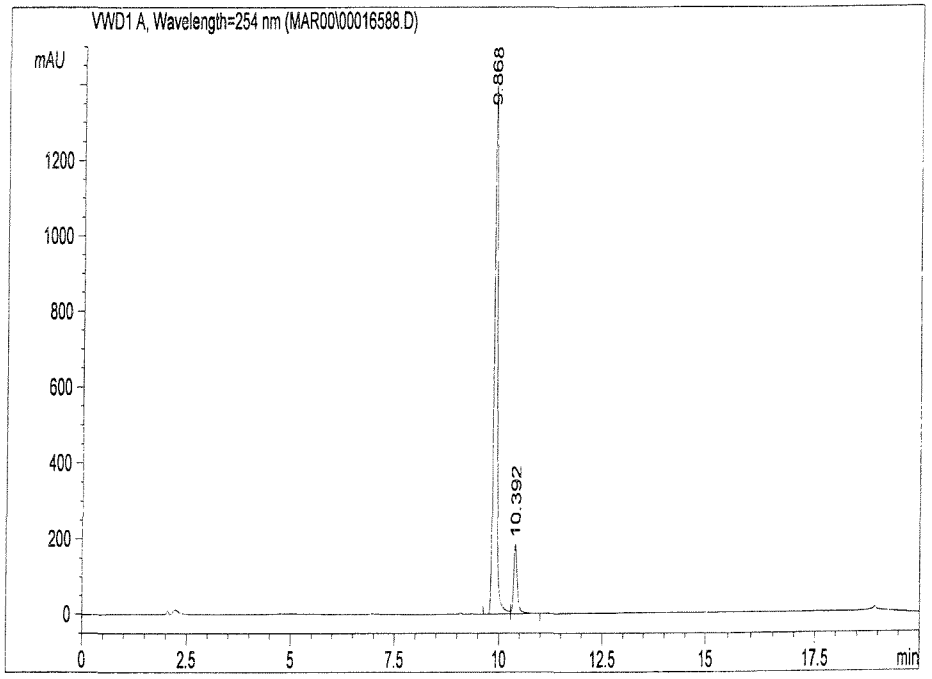

Figure 6.6 HPLC chromatogram of reaction mixture (starting material and product) after 2 hours hydrogenation at room temperature using Pt black as catalyst.

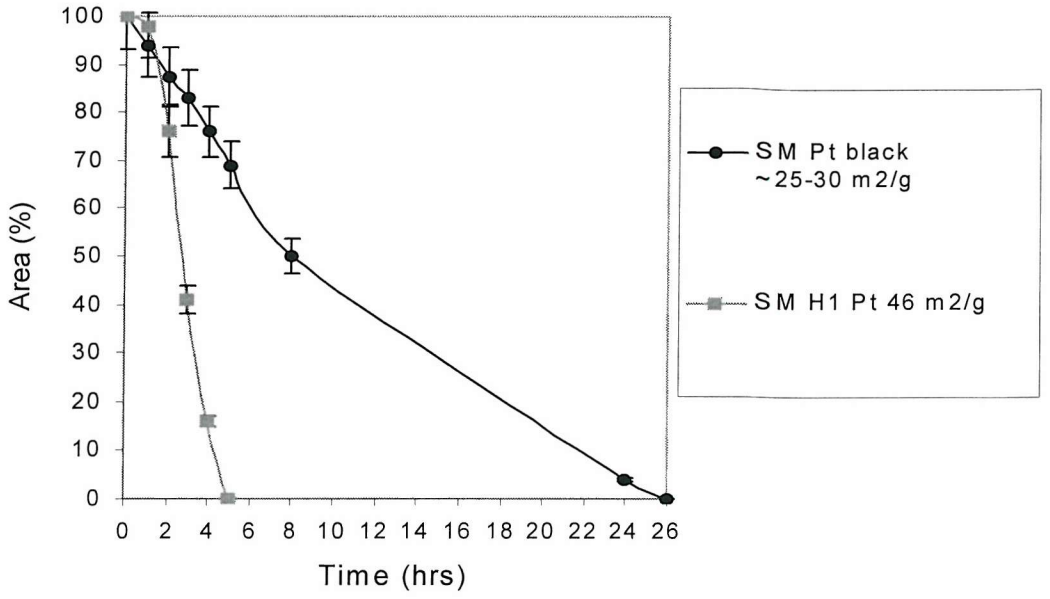

Figure 6.7 Change in concentration of coumarine starting material with time during the hydrogenation over platinum black and H_I Pt at room temperature (quantitative analysis determined by HPLC).

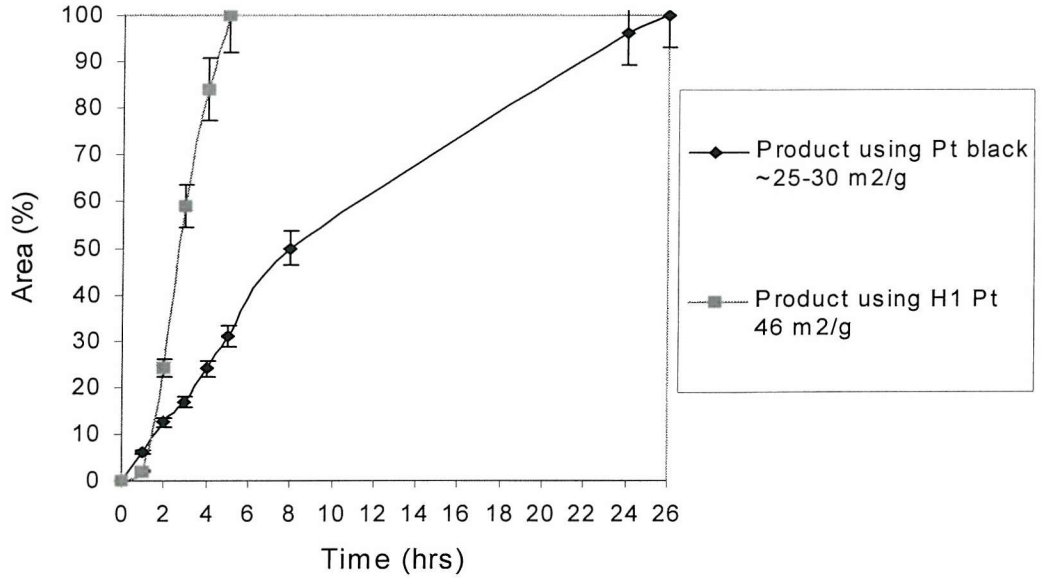

Figure 6.8 Change in concentration of coumarine product with time during the hydrogenation over platinum black and H_I Pt at room temperature (quantitative analysis determined by HPLC).

The results obtained showed that the reaction was much faster when H_I Pt was used as catalyst in place of platinum black. This may be attributed to H_I Pt having a higher surface area than platinum black After 5 hours hydrogenation over H_I Pt at room temperature, no starting material was detected (26 hours for platinum black).

The plot depicted on figure 6.9, ln (Ao/A) where Ao is the initial concentration of coumarine and A the concentration of coumarine after a given hydrogenation time, showed that both reactions followed first order kinetic (straight line observed after induction period).

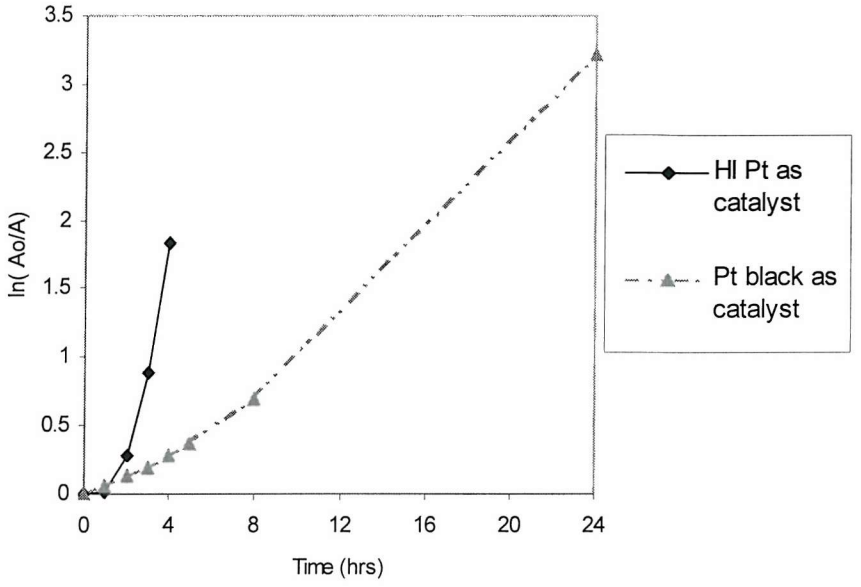

Figure 6.9 Plot showing the kinetics of the hydrogenations using H_I Pt and platinum black.

The rate constant for the reaction catalysed by H_I Pt was found to be 5.2 times larger than that for the reaction catalysed by platinum black. Furthermore, the induction period for the reaction was reduced from 3hours (Pt black) to 2 hours (H_I Pt). The final yield of the reactions were 67 % and 70 % for Pt black and H_I Pt respectively. These results suggest that the catalytic activity of H_I Pt is significantly different from that of the equivalent platinum black, and that this difference cannot be explained only by differences in specific surface area.

6.3.2 Hydrogenation of 3,4,5,6 tetrahydrophtalinic anhydride

As for the kinetic study of the coumarine hydrogenation, the progress of the anhydride hydrogenation was monitored by HPLC by extracting 25 µl aliquots from each reaction mixture. The HPLC chromatograms obtained after given hydrogenation times using the two catalysts were compared to the HPLC chromatogram obtained for the starting material depicted on figure 6.10. As can be seen, two distinct peaks were observed for the starting material that corresponded to the starting material anhydride and the starting material acid. Before hydrogenation, quantitative analysis showed indeed that 10 % of the anhydride reacted to form the corresponding acid in ethyl acetate (wet solvent).

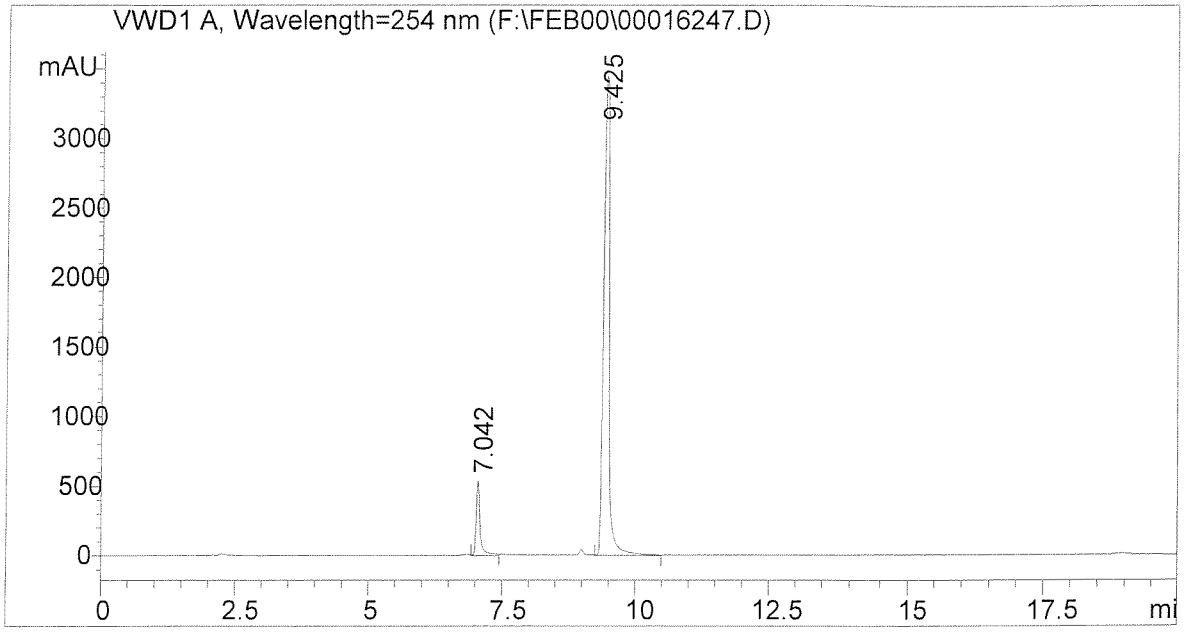

Figure 6.10 HPLC chromatogram of anhydride starting material showing two peaks corresponding to the starting material anhydride and the sarting material acid (smaller retention time).

Figure 6.11 and 6.12 show the typical HPLC chromatograms obtained after 72 hours hydrogenation using the two catalysts at room temperature. As shown on figure 6.11 for the H_I Pt/Ru catalyst, four peaks were observed on the chromatogram.

These correspond to the two forms of starting materials being reduced to two forms of products following the scheme:

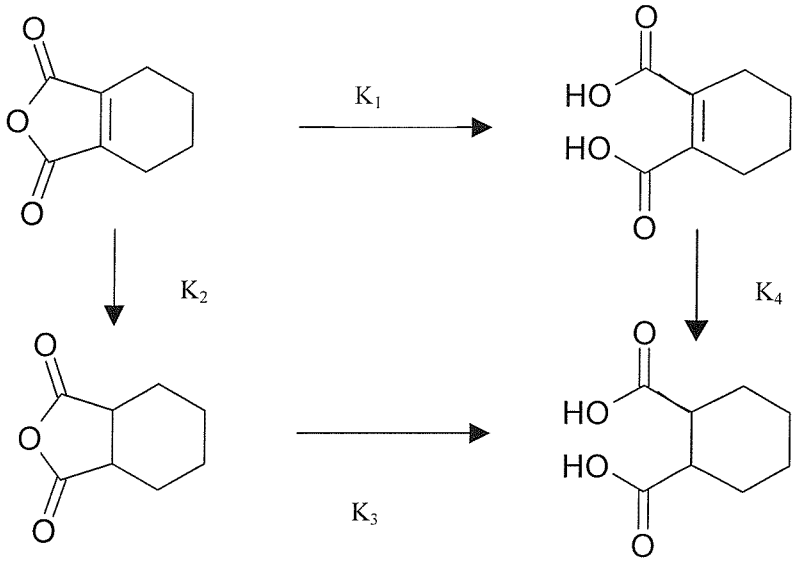

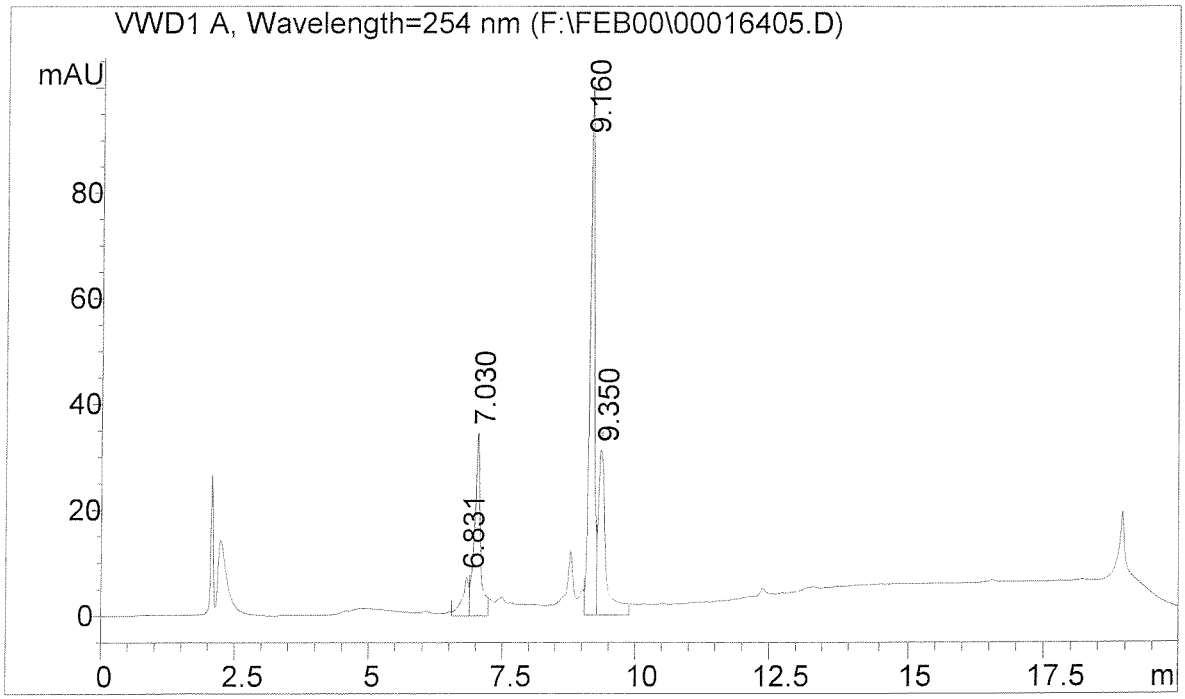

Figure 6.11 HPLC chromatogram of reaction mixture after 72 hours hydrogenation over H_I Pt/Ru catalyst (1:1 atomic ratio) at room temperature.

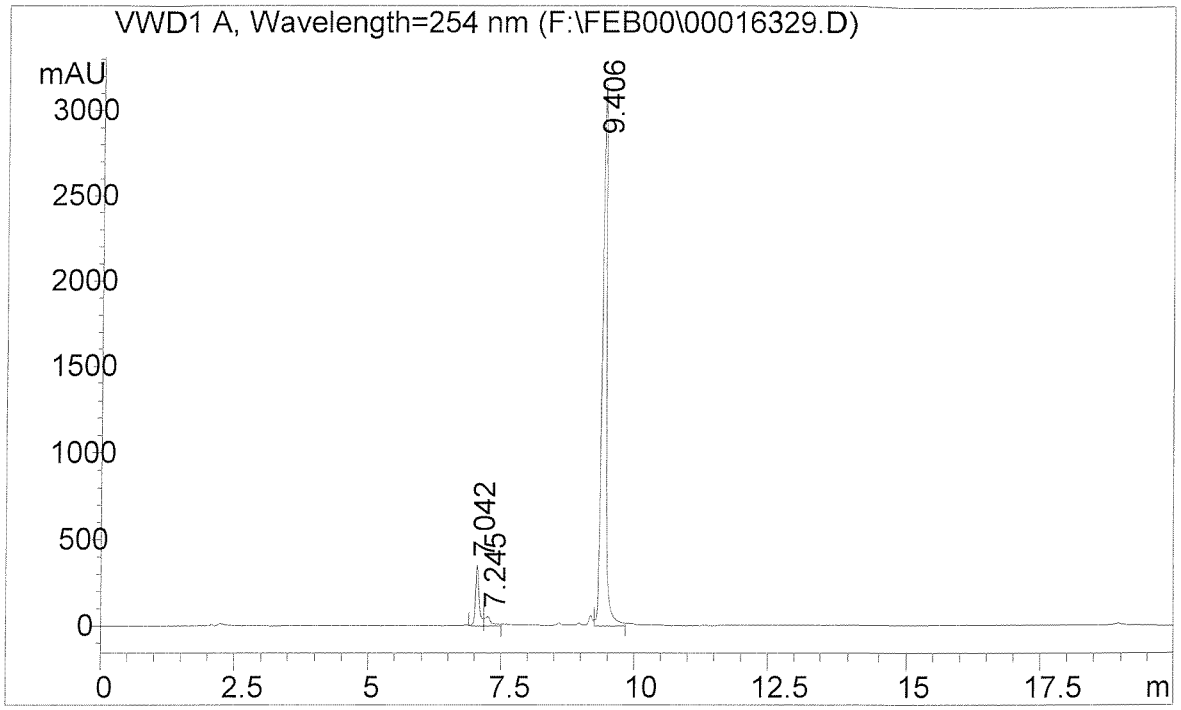

Figure 6.12 HPLC chromatogram of reaction mixture after 72 hours hydrogenation over commercial Pt/Ru catalyst (1:1 atomic ratio) at room temperature.

When comparing the chromatograms obtained after 72 hours for both catalysts, the conversion of the starting materials was much slower over the commercial catalyst: only a small amount of product acid was detected and the main two peaks corresponded to the starting materials (same retention time as peaks depicted on figure 6.10). After 72 hours hydrogenation, the chromatogram depicted on figure 6.11 showed that a much higher concentration of products was formed when H_I Pt/Ru was used. The HPLC data were summarized and the consumption of the starting materials and formation of products with time are shown for both systems on figure 6.13 and 6.14 (quantitative yield determined by HPLC).

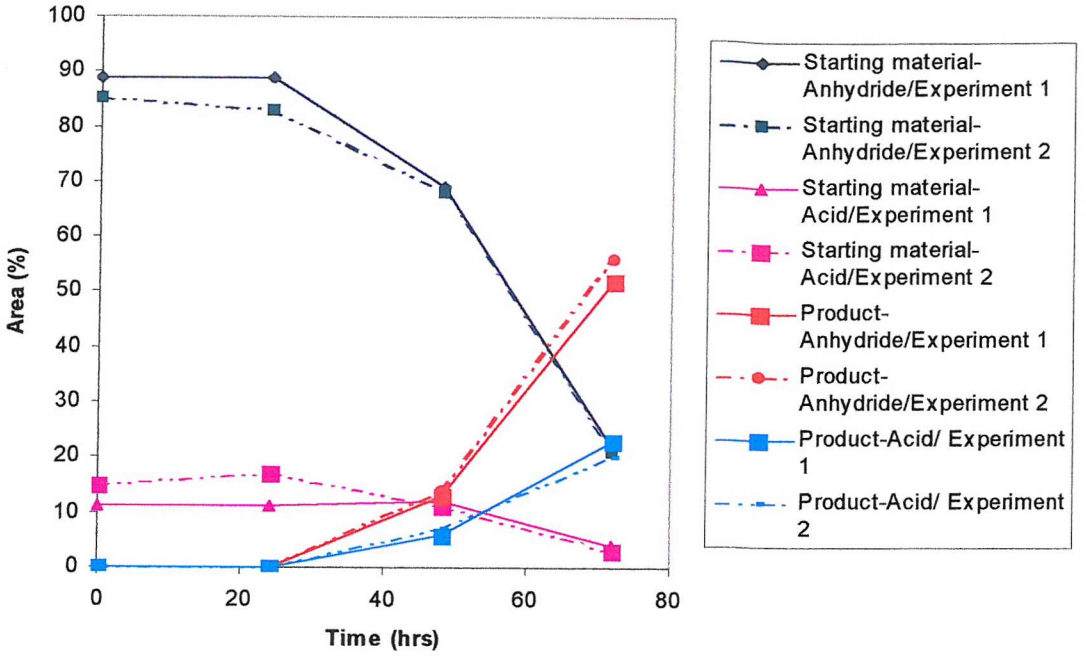

Figure 6.13 Changes in concentration with time for starting material (anhydride and acid) and product (anhydride and acid) over H_I Pt/Ru catalyst during hydrogenation at room temperature. Dotted lines: same experiment repeated in same conditions.

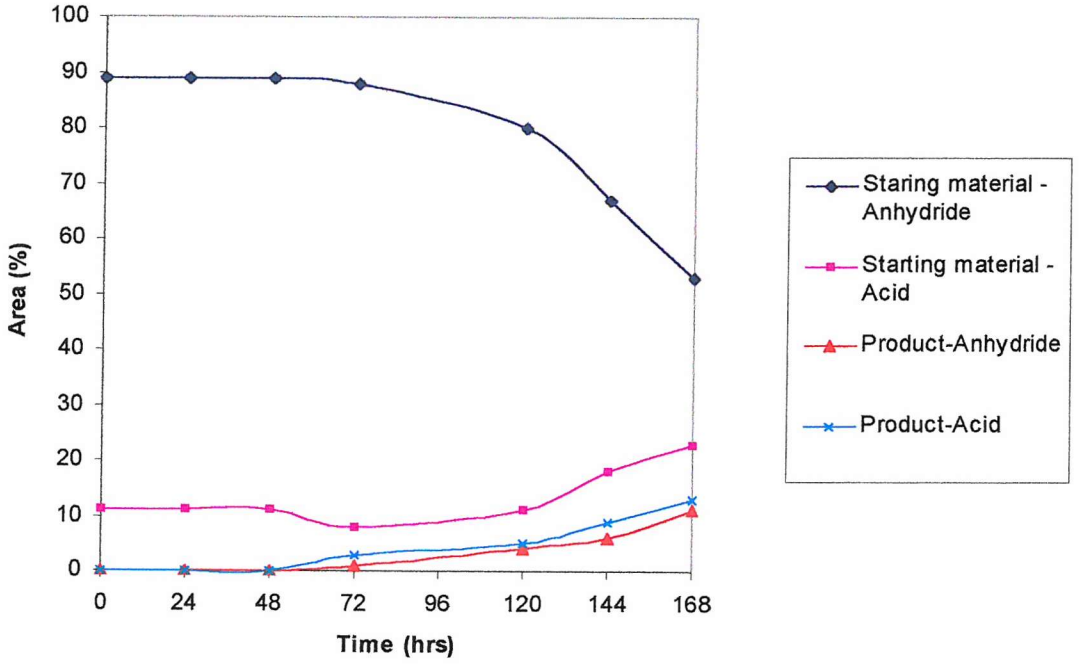

Figure 6.14 Changes in concentration with time for starting material (anhydride and acid) and product (anhydride and acid) over commercial Pt/Ru catalyst during hydrogenation at room temperature.

The rate constants for the reactions were determined as for the hydrogenation of coumarine by plotting ln (Bo/B) versus time. For the reaction catalyzed by commercial Pt/Ru, the results showed that the hydrogenation of the anhydride followed first order kinetics (straight line obtained after an induction period of 110 hours). Although not enough data points were collected in the case of H_I Pt/Ru , an approximate guide line was drawn and the hydrogenation of the anhydride was also assumed to follow first order kinetic with a much shorter induction period of 41 hours (figure 6.15).

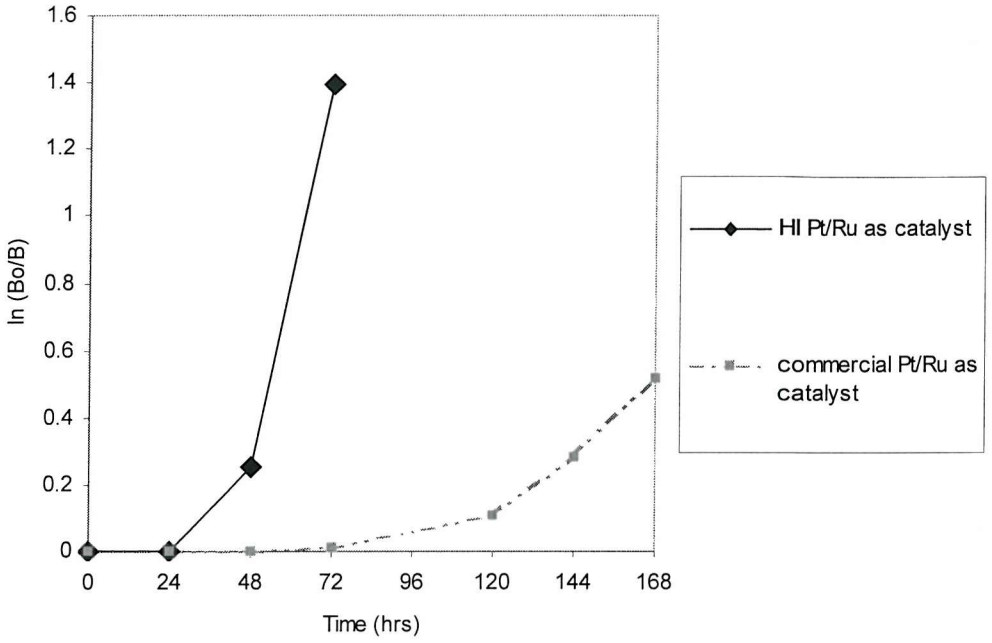

Figure 6.15 Plots showing the kinetics of the hydrogenations using H_I Pt/Ru and commercial Pt/Ru as catalysts.

The rate constant for the reaction catalysed by H_I Pt/Ru was found to be 5.7 (+/- 0.2) times larger than that for the reactions catalysed by the Pt/Ru black. These preliminary results suggest that the catalytic activity of the H_I Pt/Ru alloy may be different from that of the equivalent nanoparticulate alloy, and that the difference cannot be explained only by differences in the specific surface area.

6.4 Experimental procedures for CO and MeOH electroxidation

A set of preliminary experiments aimed at assessing the catalytic activity of H_I Pt (38 m^2g^{-1}) and H_I Pt/Ru (83 m^2g^{-1}) when prepared as composite electrodes for carbon monoxide and methanol oxidation were carried out. A commercial Pt catalyst supported on carbon (40 wt % Pt, Johnson Matthey XC 72-R) was used for direct comparison.

6.4.1 Electrode preparation

H_I Pt and H_I Pt/Ru was mixed with powdered carbon black (Vulcan XC-72), distilled water and Nafion ® (5 % solution in a mixture of lower aliphatic alcohols and water obtained from Aldrich) and dispersed in an ultrasonic bath for 2 hours until an ink- like paste was obtained.This paste was then spread onto carbon paper (E-Tek "A") and hot pressed at 76 kg cm $^{-2}$ for 3 mins at 100 ^{o}C. Exact compositions of the electrodes are reported with the results concerning the CO and MeOH oxidation experiments in table 1, appendix 4. Prior to the preparation of the electrodes, pretreatment of the H_I Pt and H_I Pt/Ru powders by presoaking in aqueous acid solutions ($HClO_4$, H_2SO_4) or proton conductors such as heptadecafluorooctanesulfonic acid was also investigated (exact compositions of the electrodes are reported in table 2, appendix 4).

6.4.2 Electrochemical testing

The three electrode type electrochemical cell used during cyclic voltammetry studies is shown in figure 6.16. Electrical contact to the working electrode was made by a platinum wire. A screw-on cap tightened on the electrode, holding it in position. The working electrode holder was mounted into the glass cell (of capacity 150 cm^3) which had an integrated water jacket for temperature control. A platinum gauze counter electrode was used and a mercury mercurous sulphate (MMS) with a luggin probe was used as a reference to measure the electrode potential. The tip of the luggin was positioned within 0.5 mm of the surface of the working electrode.

Cyclic voltammetry in 2 M H_2SO_4 was employed to determine the peak potential for carbon monoxide and methanol oxidation. For the CO oxidation, each electrode was held at a potential of -0.55 V (all potential are quoted relative to the mercury mercurous sulphate electrode, MMS) in 2M sulphuric acid at room temperature and the solution and

electrode were simultaneously purged to CO for 30 mins. The solution was then purged with nitrogen for 30 mins with the potential held at -0.55V. Following purging, cyclic voltammograms were recorded at a scan rate of 10 mV s^{-1} at room temperature. For the MeOH oxidations, cyclic voltammograms were recorded in the presence of 2 M methanol in 1M H_2SO_4 at 10 mV s^{-1} at room temperature.

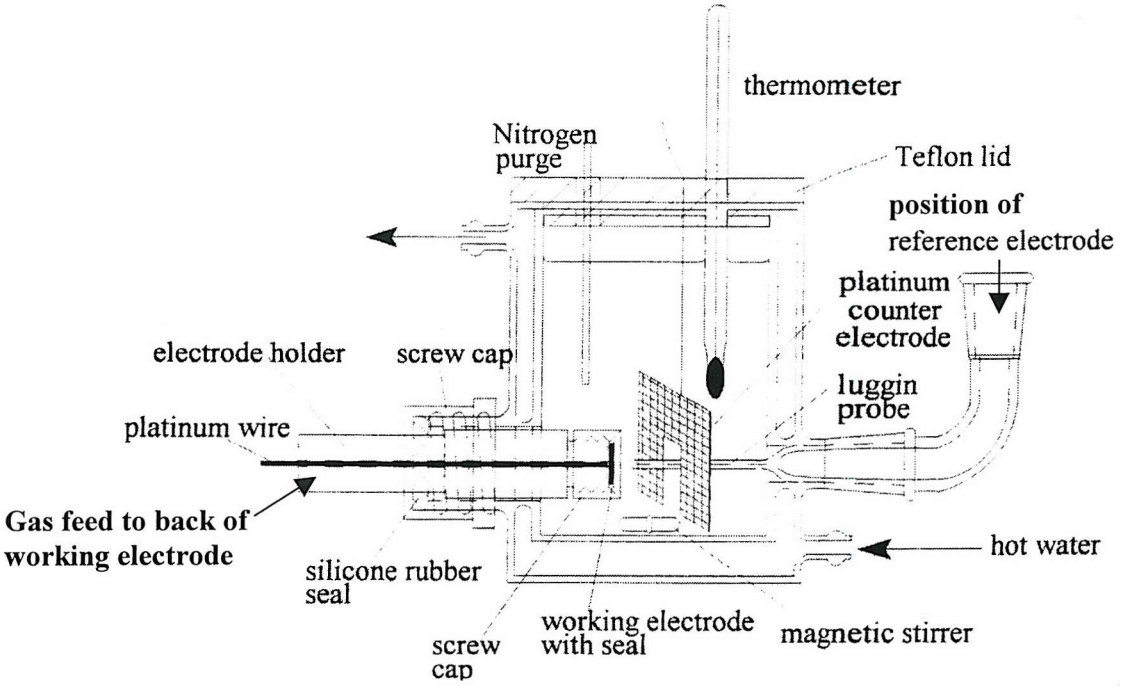

Figure 6.16 Three electrodes cell setting used during CO and MeOH electroxidation redrawn from reference [11].

6.5 Results and discussion for CO and MeOH electrooxidation experiments

Prior to Methanol or CO electrooxidation studies, each electrode prepared was cycled in 2 M H_2SO_4. Figure 6.17 shows a typical cyclic voltammogram of a H_I Pt electrode in 2 M H_2SO_4 recorded at room temperature at a scan rate of 10 mVs^{-1}. The mesoporous platinum was presoaked in 0.5 M H_2SO_4 before mixing with the carbon support and preparing as a composite electrode.

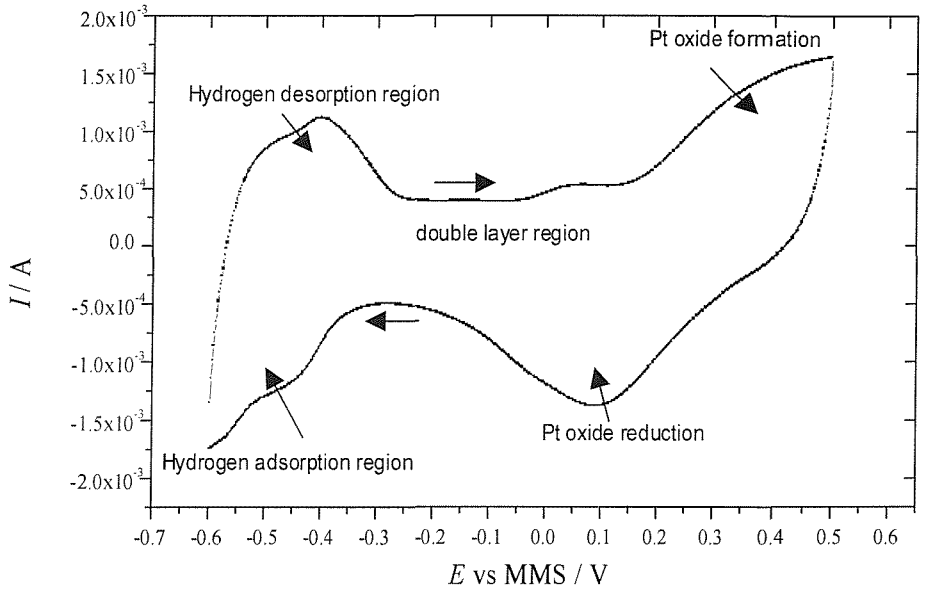

Figure 6.17 Cyclic voltammogram of H_I Pt/C electrode prepared by presoaking the mesoporous platinum in 0.5 M H_2SO_4 before electrode preparation and showing the typical features of a platinum voltammogram in sulfuric acid solution.
(Electrode area 1 cm^2)

6.5.1 Methanol oxidation results

Figure 6.18 gives a comparison of the methanol oxidation behaviour at conventional Pt/C electrode, H_I Pt non treated and H_I Pt electrodes prepared by presoaking the Pt catalyst in various H_2SO_4 concentrations. Similar platinum loadings (~ 2 mg $Ptcm^{-2}$) were used in the formulation of the electrodes for direct comparison (exact formulations and characteristics of the electrodes are summarised in table1, appendix 4).

The cyclic voltammograms of the platinum catalysts change dramatically in the presence of methanol. The hydrogen adsorption/desorption features are lost because the platinum surface is blocked by strongly bonded methanol fragments such as -C≡O [12]. On the forward sweep, the platinum surface remains poisoned with very little methanol oxidation taking place during the double-layer region. For the Pt/C catalyst for example, bulk methanol oxidation only begins at potential greater than 0 V when the surface intermediates are removed. However the oxidation peak soon reaches a maximum and then begins to decline as the surface is blocked by the formation of the oxide [12]. On the reverse sweep, oxidation of methanol begins at 0.3 V as the surface oxide is stripped to reveal a clean surface but reaches a maximum at 0.15 V after which strongly bonded surface intermediates begin to block the platinum surface [12].

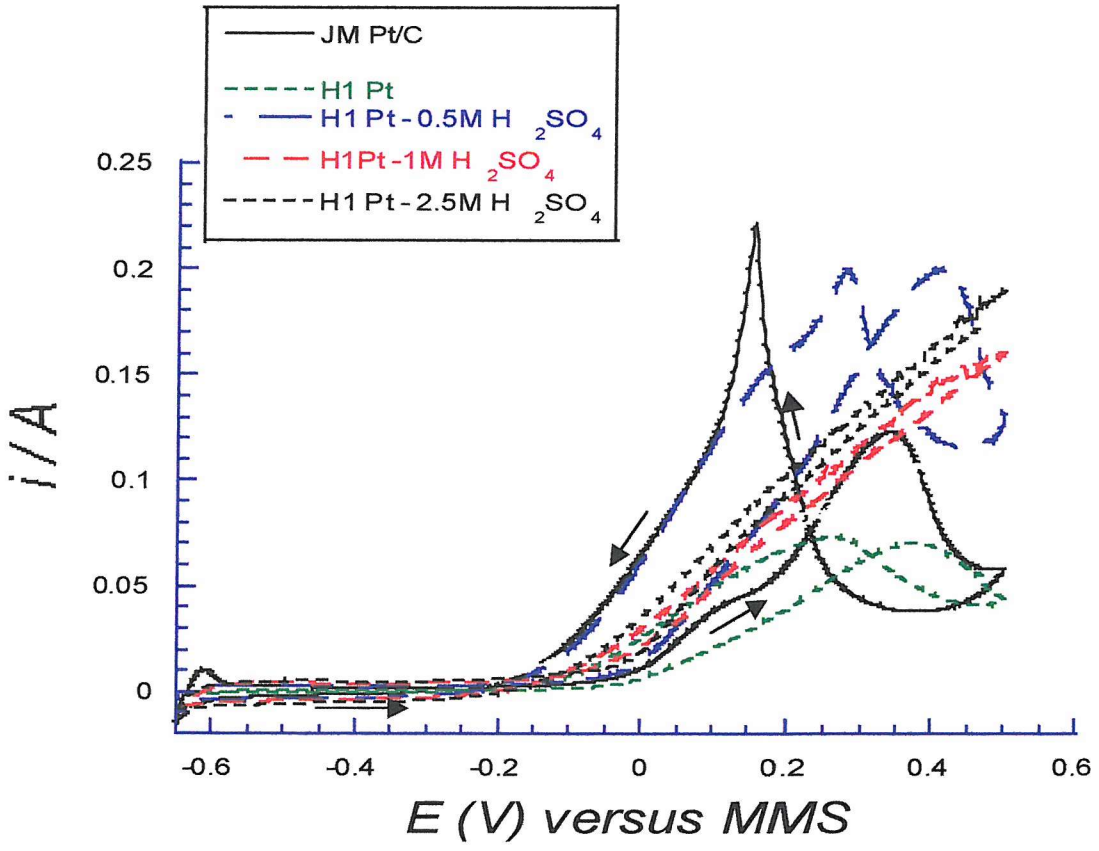

Figure 6.18 Comparison of cyclic voltammograms obtained for conventional Pt/C electrode, H_I Pt/C and H_I Pt presoaked in various H_2SO_4 concentrations before mixing with carbon. Scan rate 10 mVs^{-1} at room temperature.

When comparing the different cyclic voltammograms, the methanol oxidation peak is observed to be shifted to more positive potential (E_{onset}) and the oxidation peak intensity was much smaller at the H_I Pt electrode not pretreated than the one recorded for the conventional commercial catalyst or the H_I Pt presoaked prior to electrodes preparations. The potential for MeOH oxidation for the electrodes prepared while using the conventional Pt catalyst or the H_I Pt soaked in 0.5M acid was similar (E= 0 V) but the intensity of the oxidation current was slightly higher for the electrode prepared from H_I Pt pretreated in 0.5M H_2SO_4. In both cases, the shape of the voltammograms was in good agreement with the voltammetric response obtained for a polished platinum electrode (0.5 mm diameter) in 1 M methanol/1 M sulfuric acid at room temperature [13].

Although the preliminary results showed that the catalytic activity of the H_I Pt towards MeOH oxidation was not enhanced compared to conventional catalysts, the results showed that similar catalytic activity could be obtained by presoaking the H_I Pt in 0.5 M H_2SO_4. Increasing the concentration of H_2SO_4 in the pretreatment of H_I Pt did not lead to electrodes active at lower potential for MeOH oxidation and the oxidation currents recorded were smaller than those observed with the conventional catalyst (1 M and 2.5 M H_2 SO_4 as shown on figure 6.18). Without pretreatment, smaller oxidation currents were recorded when using the mesoporous platinum; the smaller conductivity obtained could be explained by either a pore blocking phenomenon or a lack of full hydration of the pores in the non-treated H_I Pt electrodes, both of which would result in a smaller apparent electrode area.

6.5.2 Carbon monoxide oxidation results

Figure 6.19 gives a comparison of the CO oxidation behaviour at the conventional Pt/C electrode, H_I Pt non-treated and H_I Pt electrodes treated by presoaking the platinum powder in 0.5M H_2SO_4 prior to preparation.

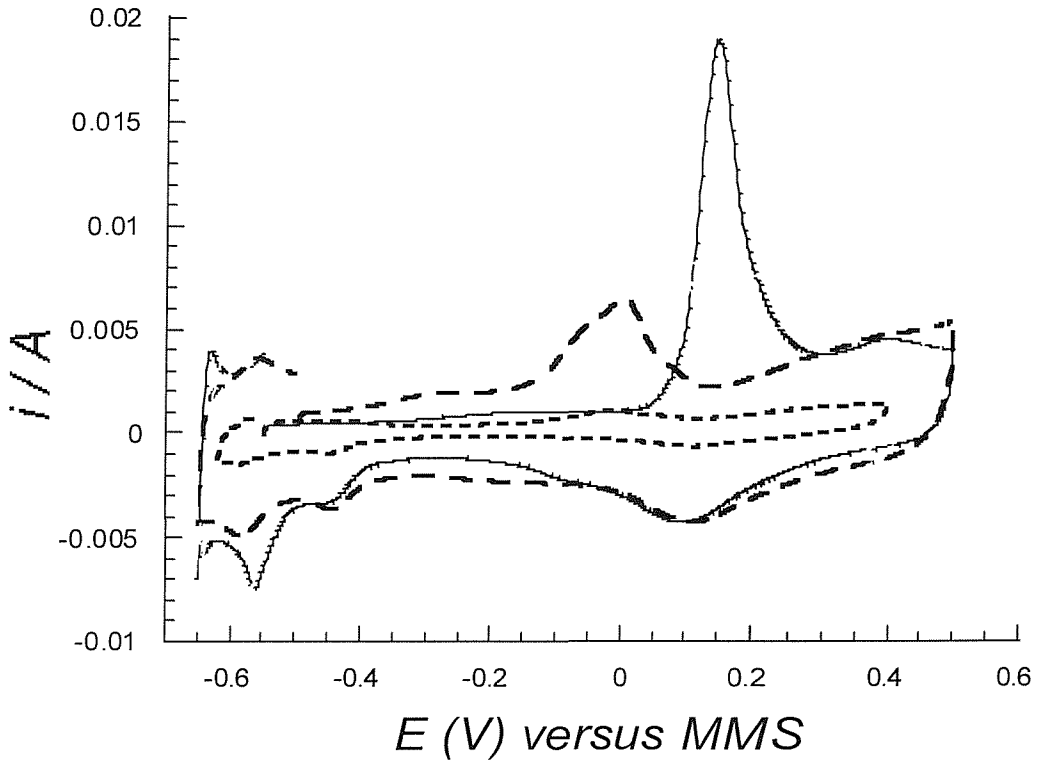

Figure 6.19 CO electrooxidation on conventional Pt/C electrode (——), H_I Pt/C (-----) and H_I Pt soaked in 0.5 M H_2SO_4 prior to mixing with carbon (-------). Scan rate 10 mVs^{-1} at room temperature.

For the electrode prepared with H_I Pt without pretreatment, the current recorded was very small (-------). Much higher CO oxidation currents were obtained with the conventional electrode (——) and the one prepared from H_I Pt soaked in 0.5M H_2SO_4 (------).

Although the CO oxidation peak intensity was lower when presoaking in 0.5M H_2SO_4 than the intensity recorded with Pt/C electrodes, the CO oxidation peak was observed to be significantly shifted to more negative potential when compared to the conventional Pt catalyst (-0.009V compared to 0.149 V for the commercial Pt/C catalyst). These results are significant in the context of fuel cell electrodes because they indicate that the oxidation of CO on the surface of the mesoporous platinum pretreated in acid is more facile than on the commercial Pt/C material.

Previous experiments have shown that interesting results could be obtained by presoaking the mesoporous platinum powders with additives prior to the preparation of electrodes. The last set of experiments aimed at preparing electrodes by presoaking the H_I Pt catalyst in other acids or proton conductors additives to further lower the CO oxidation potential and increase the efficiency of the process (peak intensity increased, geometric area of the electrodes for similar Pt loading of the electrodes).

Figure 6.20 and 6.21 shows the CO oxidation behaviour on electrodes prepared using H_I Pt pretreated by soaking the mesoporous Pt in 1 M $HClO_4$ and 1 M H_2SO_4 respectively for similar platinum loading (~2.7 mg Pt cm^{-2}). In both cases, the CO oxidation peak occurred at lower potential than that observed with Johnson Matthey's conventional Pt/C electrodes and higher peak intensities were also observed. When compared to the CO oxidation results obtained with conventional Pt/C electrodes, an additional feature in terms of a small pre-peak at -0.3 V before the main CO oxidation peak was observed (more pronounced in figure 6.20). This may be attributed to the CO oxidation starting at lower potential on different sites of the mesoporous catalyst (internal and external surface) and due to the different porous structure of the platinum material.

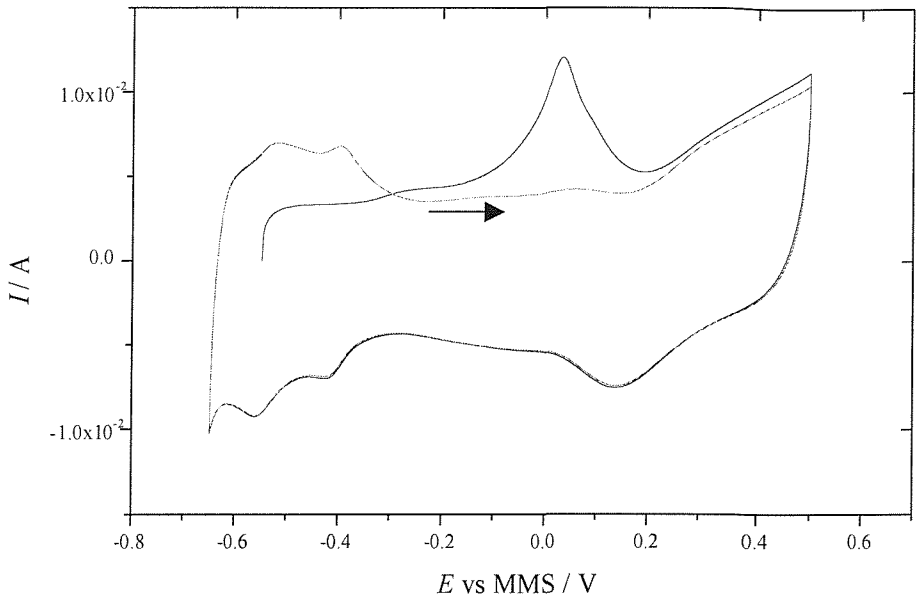

Figure 6.20 CO electrooxidation on H_I Pt soaked in 1 M $HClO_4$ prior to electrode preparation. Scan rate 10 mV s^{-1} at room temperature.

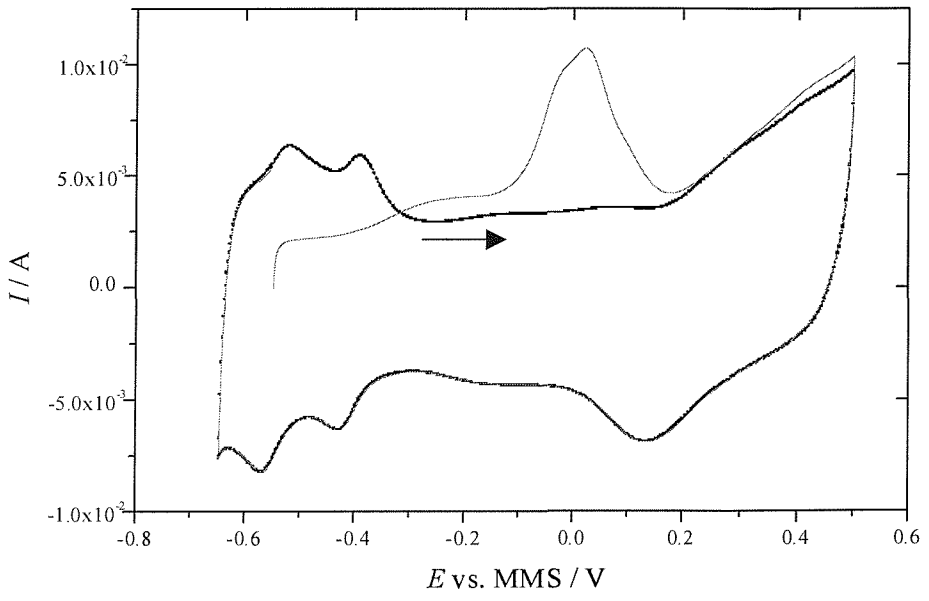

Figure 6.21 CO electrooxidation on H_I Pt soaked in 1M H_2SO_4 prior to electrode preparation. Scan rate 10 mVs^{-1} at room temperature.

Finally, the effect of another additive was assessed in CO electrooxidation reaction. The H_I Pt was pretreated by soaking in a 10 % weight solution of a perfluorosulfonic acid (proton conductor). The cyclic voltammogram depicted on figure 6.22 shows that the peak for CO oxidation occurs at a lower potential than that for conventional Pt/C (0.05 V compared to 0.145 V for Pt/C depicted in figure 6.19) and was similar to that obtained with the electrodes prepared by soaking the mesoporous platinum in perchloric or sulfuric acid prior to the electrodes preparations. The intensity of the CO oxidation peak reached a maximum at 5 mA, smaller than the intensity observed for the electrodes prepared from H_I Pt catalysts presoaked in aqueous acids (10 mA), the presence of a small pre-peak at -0.3 V was also noted.

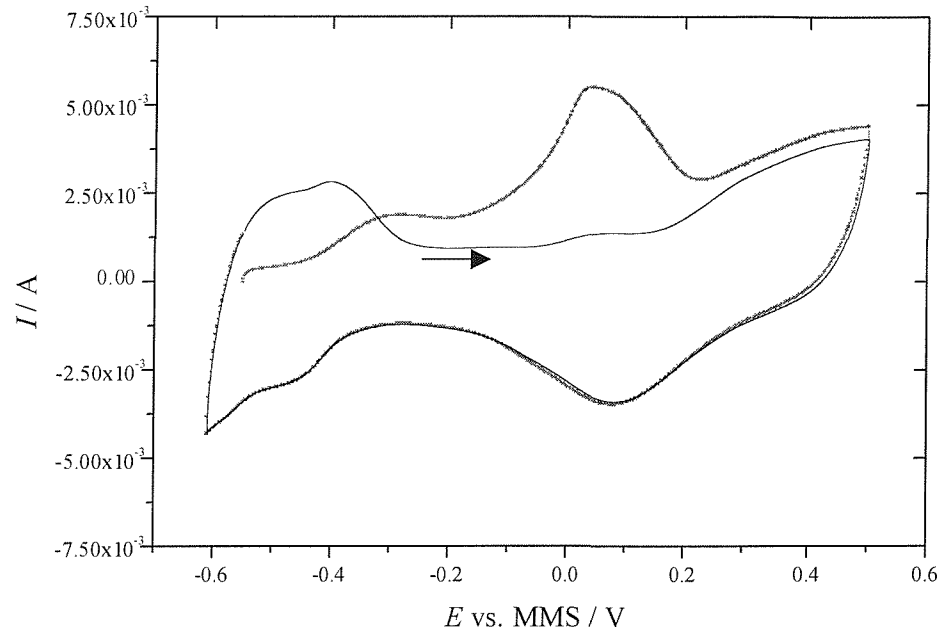

Figure 6.22 CO electrooxidation on H_I Pt soaked in 10 % heptadecafluorooctanesulfonic acid solution prior to electrode preparation. Scan rate 10 mVs^{-1} at room temperature.

Pt/Ru electrodes have been known for a long time to exceed the electrocatalytic activity of pure platinum electrodes towards the electrooxidation of methanol in acid electrolytes and even today they are considered to be the most active electrocatalysts for this reaction [ref3]. When mixed with platinum, ruthenium also exhibits synergestic effect towards rhe the CO oxidation. Gasteiger *et al.* measured the electrocatalytic activity of well characterised Pt/Ru alloy electrodes prepared in ultrahigh vacuum (UHV) towards the electrooxidation of CO in sulfuric acid electrolytes. In their results, the authors found that an alloy with a Ru surface composition of ~ 50 atomic % exhibited the highest activity with an approximate reduction of the oxidation overpotential of 0.25 V compared to pure platinum. The final set of data was collected by preparing electrodes with mesoporous Pt/Ru catalyst (1:1 atomic ratio) presoaked in 10 % weight solution of perfluorosulfonic acid. The cyclic voltammogram depicted in figure 6.23 shows that the CO oxidation occurs at much lower potential than the potential observed with the electrode prepared from conventional Pt/C (-0.125 compared to 0.149 V).

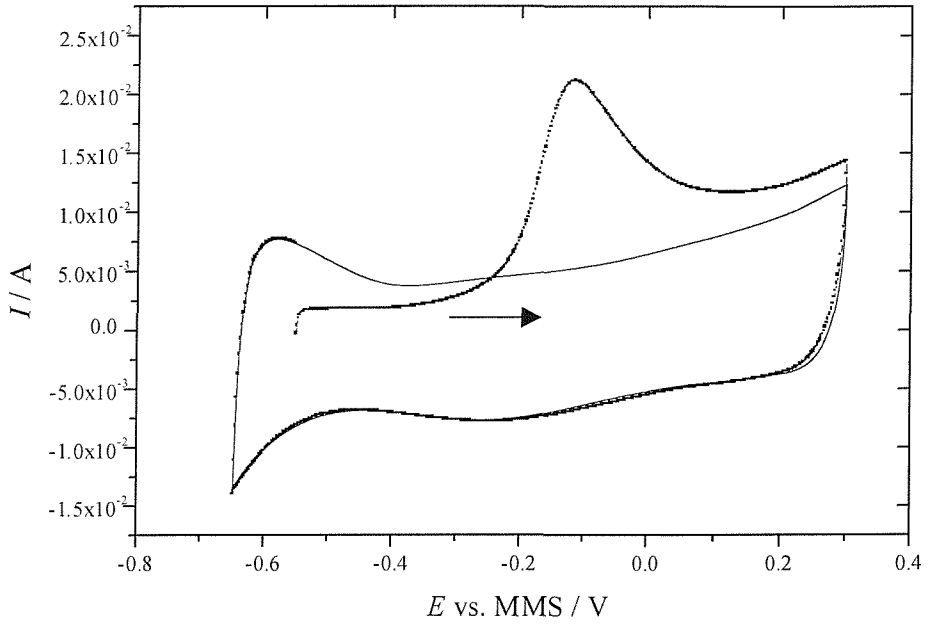

Figure 6.23 CO electrooxidation on H_I Pt/Ru soaked in 10 % heptadecafluorooctane - sulfonic acid solution prior to electrode preparation. Scan rate 10 mVs^{-1} at room temperature.

The CO oxidation occurs also at lower potential on the Pt/Ru catalyst than the potential recorded with the electrodes prepared with mesoporous Pt presoaked either in acid or proton conductors (-0.009 and 0.005 V respectively).The shift to lower potential observed for the CO oxidation while using H_I Pt/Ru is of considerable importance in the context of fuel cell because this indicates that the oxidation of CO on the surfaces of the mesoporous alloy is more facile than on either the commercial catalyst or the mesoporous platinum.

6.6 Conclusion and further work

The aim of the chapter was to assess the catalytic activity of mesoporous Pt and mesoporous Pt/Ru in hydrogenation reactions and in the formulation of electrodes for fuel cell applications. Noble metals, especially Pt and Pt based alloys, are extensively used in heterogeneous catalysis. The possibility of producing mesoporous Pt and Pt based alloy powders with inherently high surface areas is particularly attractive in the vast field of heterogeneous catalysis.

The results obtained from the catalytic hydrogenations carried out showed that H_I Pt and H_I Pt/Ru had higher catalytic activities than the commercial equivalent catalysts (higher rate constants, shorter induction periods for a given reaction). Preliminary data on the catalytic properties of these materials in hydrogenation reactions showed that these materials constituted a very attractive alternative to current catalysts used in heterogeneous catalysis.

Fuel cell technology is intimately linked to the development of effective electrocatalysts. Research over decades has shown that Pt or Pt containing catalysts are the best materials for low temperature proton exchange membrane fuel cells. Preliminary experiments aimed at assessing the catalytic activity of mesoporous Pt and Pt/Ru alloys in the formulation of electrodes for such fuel cells were also carried out. The results showed that by presoaking the H_I Pt in sulfuric acid solutions before preparing the electrodes, it was possible to greatly improve the efficiency of the electrodes in MeOH oxidation by increasing the oxidation current. Nevertheless, the onset potential for MeOH oxidation observed for the modified electrodes was the same as the one obtained using conventional Pt/C electrodes.

CO oxidation behaviour at conventional Pt/C, H_I Pt non treated and H_I Pt electrodes prepared by soaking the platinum catalysts in different additives prior electrodes preparations was finally studied. By pretreating in acid or solutions of proton conductors, a shift in the CO oxidation peak to some more negative potential was observed indicating that the CO oxidation on the surface of the mesoporous pretreated platinum was more facile. Optimal results were obtained by using H_I Pt/Ru catalysts also pretreated in proton conductor solutions; higher oxidation currents with a shift to lower potential were indeed

observed with these electrodes. These preliminary data illustrate that significant improvements in the context of fuel cell electrodes may be obtained by using mesoporous catalysts and demonstrate the viability of employing a liquid crystal templated route to produce catalysts that have enhanced performance over conventional catalysts.

Further work:

The use of mesoporous metals in heterogeneous catalysis has numerous applications; catalysts with long ranged porous nanostructure and hig specific areas are indeed particularly attractive. The catalytic behaviour of these catalysts should be assessed in selective hydrogenations or in reactions that can not be achieved using conventional catalysts.

Preliminary results showed that mesoporous Pt and Pt based alloys could play an important role in the development of effective catalysts for fuel cell technology. Experiments showed that presoaking the H_I materials in acid or proton conductors was important to improve their efficiency. Other pretreatments should be investigated to further optimise the electrode formulations. Finally, further tests at higher temperature are required to assess the viability of using these electrode assemblies for the development of fuel cell stacks.

6.7 References

1. F D Mills, *J.Heterocyclic Chem.*, **17**, 1597 (1980).
2. M A Mc Guire, S C Schilcrat, E Sorenson, *Tetrahedron Letters*, **40**, 3293 (1999).
3. P N Ross, K Kinoshita, A J Scarpelino, P Stonehart, *J. Electranal.Interfacial Electrochem.*,**59**,177 (1975).
4. V Jalan, D Landsman, US Patent 4,186,110
5. D Landsman, F Luckzak, US Patent 4,316,944
6. H A Gasteiger, N Markovic, PN Ross Jr, EJ Cairns, *J.Phys.Chem.*, **98**,617 (1994).
7. H A Gasteiger, N Markovic, PN Ross Jr, *J.Phys.Chem.*, **99**, 16757 (1995).
8. K A Friedrich, K P Geizers, U Linke, U Stimming, JStumper, *J.Electroanal.Chem.*, **402**,123 (1996).
9. H F Oetjen, VM Schmidt, U Stimming, F Trila, *J.Electrochem.Soc.*, **143**,3838 (1996).
10. M Iwase, S Kawatsu, *Proceedings of the Fist International Symposium on Proton Conducting Membrane Fuel Cells*, S Gottesfeld, G halpert, A Landgrebe (Eds), The Electrochemical Society, Pennington, NJ, Vol.95-23, p12.
11. M P Hogarth, PhD Thesis, Department of Chemistry, University of Newcastle upon Tyne (1995).
12. P A Christensen, A Hamnett, J Munk, G C Throughton, *J.Electroanal.Chem.*,**370**,251 (1994).
13. J M Elliott, G S Attard, P N Bartlett, J R Owen, N Ryan, G Singh, *J.New Mat.Electrochem.Systems*, 2,239 (1999).

Appendix 1Techniques

1A Polarised light microscopy and phase diagrams

Introduction

The polarised light microscope differs from a standard optical microscope in that the sample is observed through a pair of crossed, polaroid, filters. One of the filters (the analyser) is situated above the sample, which is sandwiched between two glass plates, and one below (the polariser). When there is no sample present, the image on the microscope appears black as no light is transmitted [1].

An isotropic liquid has no effect on plane polarised light as the refractive indices of the material are the same in all directions. However, in a liquid crystal system there is ordering of the molecules and in some cases this can result in anisotropy in the refractive index of the material. For lyotropic systems, hexagonal and lamellar phases have two different refractive indices at 90^{o} to each other. These liquid crystal phases are said to be birefringent and each has a particular optical texture under the polarising microscope. Figures 1 and 2 shows some optical textures for the commonly found liquid crystal phases of lyotropic systems. In cubic systems there is no birefringence as light interacts with the material in a similar manner whatever the orientation. Micellar solutions are isotropic and therefore, along with cubic phases, appear black under the polarising microscope.

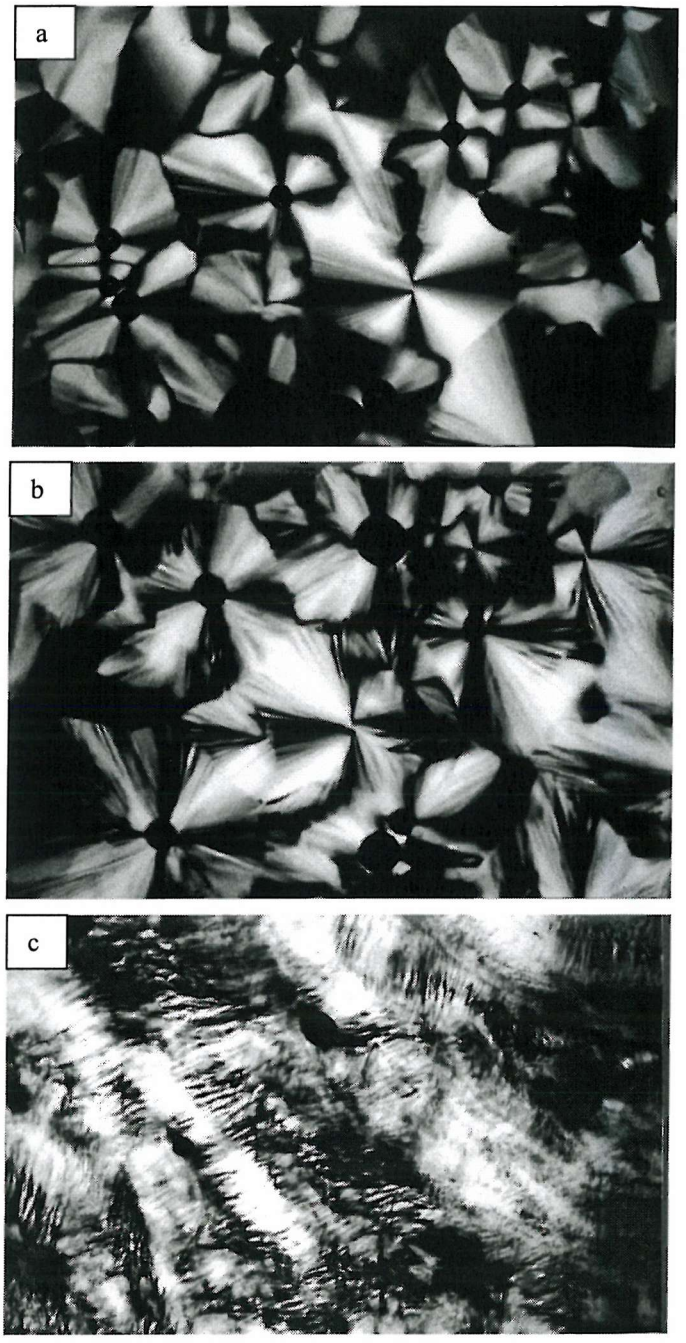

Figure 1 The optical textures of the hexagonal liquid crystal phase of $C_{16}EO_8$ in water a) A sample that has been cooled slowly from an isotropic micellar solution to a hexagonal phase. b) and c) show the hexagonal phase after the domains have been disturbed by rubbing the glass slide and cover slip across the sample. These pictures were reproduced from reference [2].

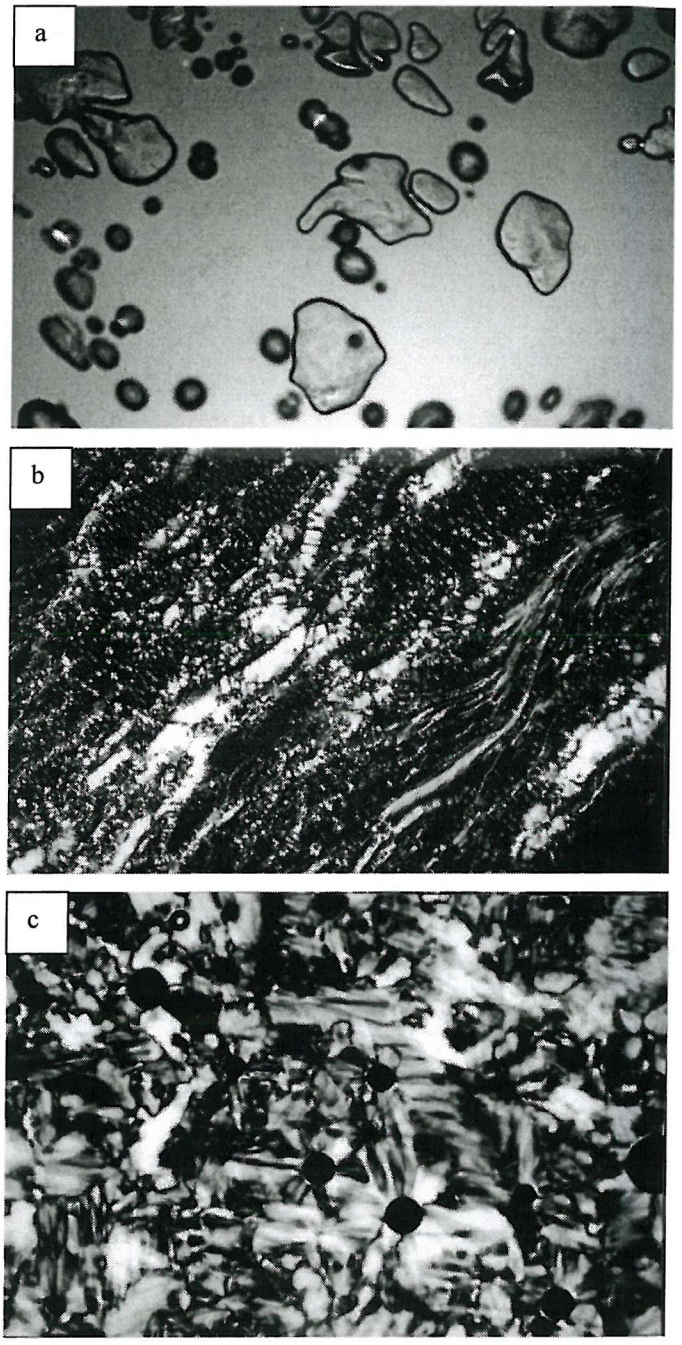

Figure 2. The optical textures of the a) cubic phase (V_1) and b-c) Lamellar phase (L_α) for $C_{16}EO_8$ + water mixtures.

Identification of the liquid crystal phase by polarised light microscopy is a combination of observations of optical textures and the viscosity of the phase [3]. The viscosity often helps to differentiate between systems that appear identical under the microscope. For example, cubic phases can be differentiated from micellar

solutions, as a cubic phase is very viscous with irregular shaped air bubbles trapped in the mixture whereas a micellar solution is very fluid. Another useful technique in identifying a phase is to observe the phases formed at the edge of the sample where water is lost upon heating. For example, a hexagonal phase will display a cubic phase followed by a lamellar phase at the edge of the sample where water has been lost. Table 1 provides some notes for identifying each individual phase.

Mixture	Optical texture	Viscosity	Notes
Micellar solution (L_1)	Isotropic (black)	Very fluid with circular air bubbles	
Phase seperated (L_1 + w)	Isotropic (black)	Very fluid with spherical regions rich in micelles	Turbid solution
Micellar cubic phase (I_1)	Isotropic (black)	Viscous phase sometimes containing angular air bubbles	Should observe an H_I phase at the edge of the sample upon heating.
Hexagonal phase (H_I)	Feather texture (figure 11a-c)	Viscous phase containing angular air bubbles	Should observe an V_I/L_α phase at the edge of the sample upon heating.
Cubic phase (V_1)	Isotropic (black) (figure 11a)	Very viscous phase containing angular air bubbles	Should observe an L_α phase at the edge of the sample upon heating.
Lamellar phase (L_α)	Mosaic texture (figure 12c) Sometimes this beomes string like upon heating. (figure 12b)	Fairly viscous but less viscous than an H_I phase – spherical air bubbles	The viscosity of the phase can drop dramatically with heating
Inverse micelles (L_2)	Isotropic (black)	Fluid with spherical air bubbles	No phases are observed at the edge of the sample upon heating

Table 1 Some pointers to identifying commonly found structures in lyotropic systems of ethylene oxide surfactants.

The construction of phase diagrams

The phase behaviour of the mixtures, described in this thesis, was investigated by polarised light microscopy using an Olympus BH-2 polarised light microscope equipped with a Linkam TMS90 heating stage and temperature control unit. Two techniques were used in order to determine the phase behaviour. The first of these was the contact method, which provided a quick analysis of the types of phases that the surfactant formed and their relative stabilities. The second method involved making up a large number of mixtures in order to determine exactly where the phase boundries existed for a given composition.

Contact method

For lyotropic materials the richness of phase behaviour can be determined using a contact preparation. This method simply involves making a thin film by melting the sample, sandwiched between a glass slide and cover slip, and adding a drop of water at the edge of the coverslip (figure 3a). As the water propagates through the sample, a range of compositions is formed, and the phase behaviour can be observed under the polarising microscope. A reverse effect is observed if a lyotropic phase is heated and water lost from the edge of the sample. The surfactant is more concentrated at the air interface and less concentrated towards the centre of the sample. Consequently the range of phases of the surfactant are observed under the polarised light microscope (figure 3b).

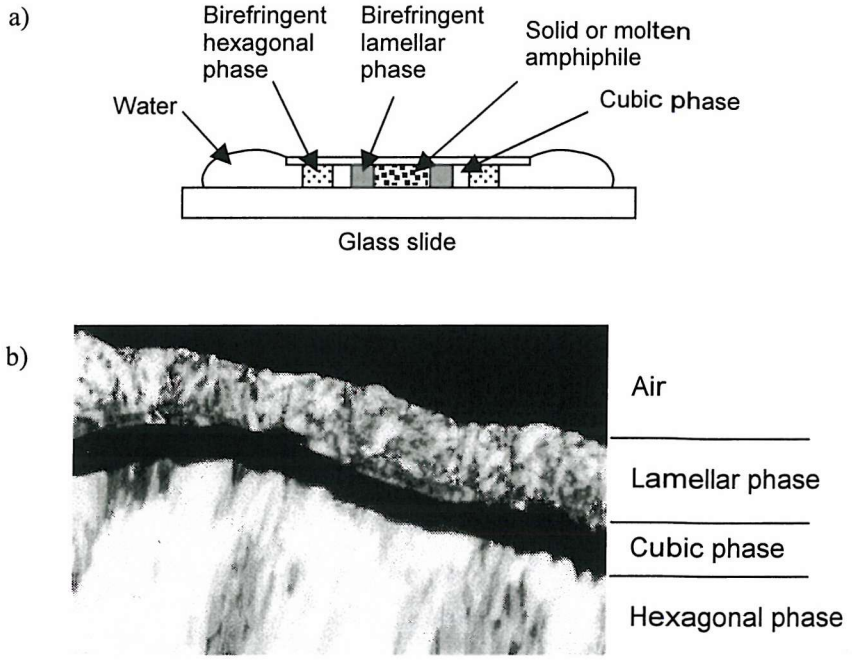

Figure 3 a) Studying phase behaviour using the contact method. b) The characteristic phase behaviour of polyoxyethylene based surfactants as water is lost from the edge of the sample upon heating.

Accurate phase boundary determination

Contact preparations only provide a qualitative method of phase determination. To accurately determine the phase behaviour of a lyotropic liquid crystal system it is necessary to make up a range of compositions and study each of them individually at a variety of temperatures.

For the phase diagrams constructed in this thesis it was important to ensure that the surfactant mixtures were homogeneous. Samples for study were prepared by accurately weighing out the required amount of surfactant and aqueous solution into a glass vial. After sealing the vial, mixing was achieved by at least four heating/cooling cycles where the sample was heated to 80°C and cooled to room temperature. In addition, during cooling the compositions were vigorously shaken using a vortex mixture. All mixtures were allowed to equilibrate at room temperature for at least 2 hours before analysis.

The phase behaviour of each mixture was characterised by placing a small sample between a glass slide and cover slip and viewing under a polarised light microscope. Phase transition boundaries were located to an accuracy of ± 2°C by using heating/cooling rates of 0.2°C/min across the boundary. Initially a regular series of mixtures was examined (e.g. 10 wt% increments in surfactant concentration) and a rough phase diagram constructed. From this further mixtures were prepared to better identify the positions of the boundaries.

1B Electron microscopy

Introduction

Light microscopy is limited by the wavelength of visible light making it impossible ever to see detail finer than 300 nm. By imaging a sample using electrons it is theoretically possible view structures as small as 0.002 nm.

In light microscopy the light falling on an object is reflected, transmitted, scattered, absorbed, or re-emitted at another wavelength. The main modes of light microscopy (reflected, transmitted, bright-field, dark field and fluorescence) result from these effects. In electron microscopy the possibilities are much wider, because the greater amount of energy carried by the illumination can cause a number of different effects to occur in the specimen. A range of microscopical and analytical modes are possible making electron microscopy a very powerful analytical tool. The types of beam-specimen interactions are summarised in figure 4.

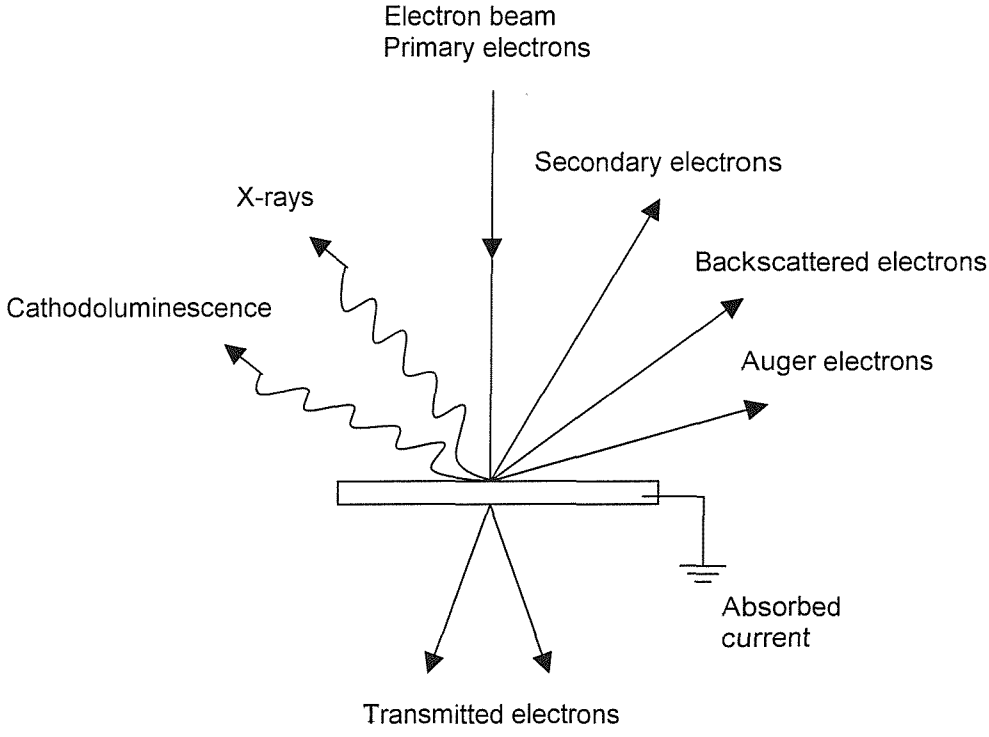

Figure 4 A schematic representation of the emissions resulting from the interaction between the electron beam and the specimen in an electron microscope.

The following list describes the various products of the interactions between the primary electron beam and the sample. Of these, c) are used for imaging in transmission electron microscopy (TEM) , a) and b) in scanning electron microscopy, whilst c) to g) can provide additional analytical information in either type of microscope,

a) Secondary electrons

Inelastic collisions on the surface of the sample result in outermost electrons being detached from the specimen atoms. These secondary electrons are used for imaging surfaces in the SEM.

b) Backscattered electrons

These are electrons from the primary beam that have been turned back out of the specimen again. The amount of backscattering increases with the atomic number of the elements in the specimen. Imaging using backscattered electrons, collected in the SEM, can be used to map elemental composition.

c) X-rays

Photons of x-radiation with wavelength and energy characteristic of the elements in the specimen are emitted under electron bombardment in the electron microscope. The spectrum of the radiation can be used for elemental identification, using either wavelength or energy (known as wavelength dispersive or energy dispersive x-ray spectroscopy, WDX and EDX respectively).

d) Auger electrons

The Auger electron is a result of a secondary electron process following the initial ejection of an electron from an inner shell by incident electron. Auger electrons can be used for analysing the composition of the surface of a specimen.

e) Cathodoluminescence

Specimens emit visible light under electron bombardment. Cathodoluminescence is widely utilised in TV screens.

f) Absorbed current

The net electron current remaining in the specimen after the electron emission or transmission processes makes up the absorbed current, which must be dissipated to earth. If the electron current is not dissipated the sample can charge-up causing repulsion of the electron beam. This is why samples must be conducting on the surface particularly in the SEM so that the charge can be earthed. The absorbed current can also be used to study the internal structure of semiconductors.

g) Transmitted electrons

If the specimen is thin enough some incident electrons penetrate through it and emerge as transmitted electrons. They may have been deflected from the line of the primary beam and may have lost energy by collisions. They carry information about the interior of the specimen and form the basis of the TEM.

Electron microscopy of the samples described in this thesis was carried out to determine the mesoporous structure, morphology on a micron scale and composition. TEM was used to study the pore structures and an SEM fitted with an EDX detector used to examine the surface at a micron level and carry out elemental analysis.

SEM and EDX

Scanning electron microscopy (SEM) is primarily used to study the topography of bulk specimens on a micron scale, but compositional information can also be extracted [4-5]. Figure 5 shows a schematic of the SEM. An electron beam is formed by a gun, which accelerates the electrons produced from a filament. The accelerating voltage that is applied can be varied depending on the sample of interest up to ~40 keV. Focusing and magnification is achieved using a series of electromagnetic lenses. The electron beam is focused onto the specimen by the condenser lenses and scanned across the sample surface. Detection of the secondary electrons is then used to build up a picture of the surface. Microanalysis (EDX) is also possible if the SEM has an additional x-ray detector. For the studies carried out in this thesis a JEOL JSM 6400 Analytical Scanning Electron Microscope was used.

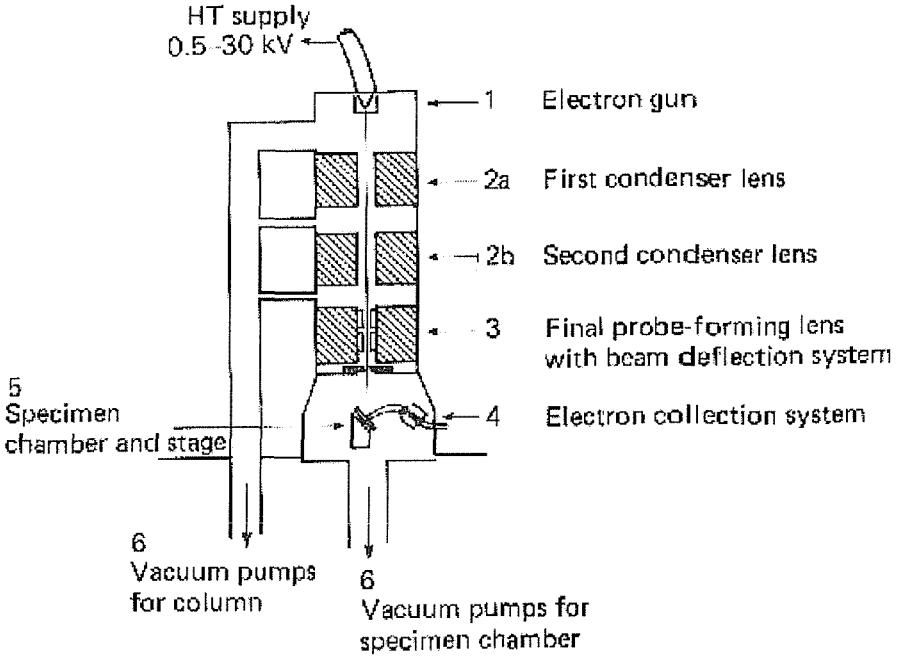

Figure 5 Schematic of a scanning electron microscope

Experimental parameters

The procedures followed for obtaining SEM images and carrying out microanalysis of the mesoporous materials are described below:

a) Sample preparation

All metal samples were prepared for the SEM by sticking them to an aluminium stub using double-sided sticky tape. These were fixed to the aluminium stubs using a double-sided carbon sticky tape.

b) Inserting samples into the vacuum system

Once the samples were supported on aluminium stubs they were inserted into the vacuum system of the microscope.

c) Image formation

A tungsten filament was used for obtaining the SEM images in this thesis and samples were examined at magnifications up to ×10,000.

d) EDX

Microanalysis was carried out by recording the x-ray spectrum from the sample and identification of the elements present done automatically by the software.

e) Photography

Photographs were taken using roll film, which was developed and printed.

TEM

Transmission electron microscopy is widely used to examine the nano-structure of inorganic materials [4-5]. As in the SEM an electron beam is formed by a gun, which accelerates the electrons produced from a filament. The accelerating voltage that is applied can be varied depending on the sample of interest. For most inorganic materials a relatively high accelerating voltage of 200kV is required so that the beam can penetrate the sample. However, in some cases this high voltage can cause local heating of the sample and destroy, over time, any microstructure that might be present. Focusing and magnification is achieved using a series of electromagnetic lenses. The electron beam is focused onto the specimen by the condenser lenses and magnification of the transmitted image is achieved using objective and projector lenses. Finally, the image is formed on a fluorescent screen. Figure 6 shows a schematic diagram of a transmission electron microscope. For the studies carried out in this thesis a JEOL 2000FX instrument was used.

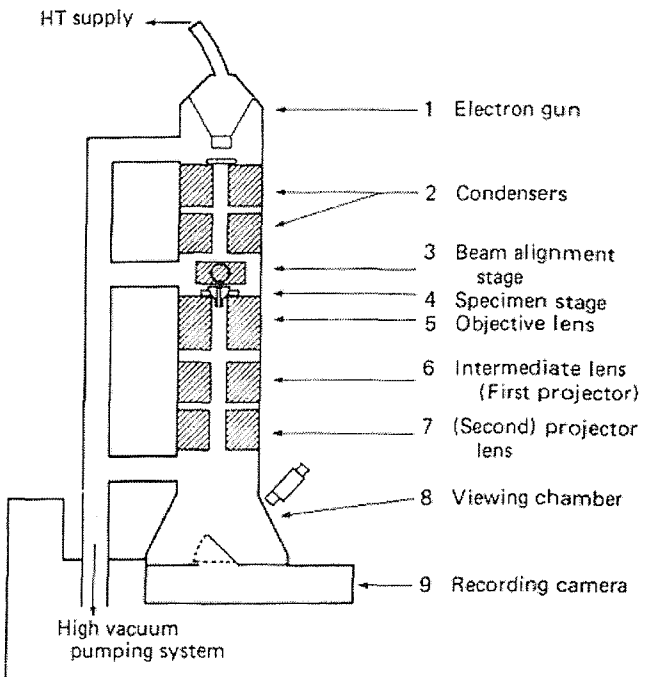

Figure 6 Schematic of a transmission electron microscope

Experimental parameters

The procedures followed for obtaining TEM images of the mesoporous materials using the JEOL 2000FX are described below:

a) Sample preparation

A dispersion of the material in water was dropped onto a circular, 3.05mm, 400 mesh copper grid that supported a carbon film (supplied by Agar Scientific). If the specimen was not a fine powder then it was ground up using an agate pestle and mortar. Dispersing the material in water was achieved by using an ultrasound bath for about 2 minutes. Once the grids were dried under ambient conditions any remaining water, trapped within the pores, was removed by placing them in a vacuum desiccator overnight.

b) Inserting samples into the vacuum system

Once dried, two grids were placed in the metal sample holder, which was inserted into the vacuum system. Typically, it took 10 minutes before a sufficient vacuum was re-established for the electron beam to be switched on.

c) Image formation

Both Lanthanum hexaboride (LaB_6) and Tungsten filaments were used for obtaining the TEM images in this thesis. The LaB_6 filament provided a much brighter source and consequently was better for imaging the nanostructure of the mesoporous metals. Also, the resolution of the images using the LaB_6 filament was better. Most of the samples were examined at a magnification of ×120,000, which was sufficient to observe the nanostructure. The stability of the samples under the electron beam was variable. In the case of the led samples, the mesoporous structure was destroyed within ~1 minute of exposure to the focused beam. For the mesoporous platinum samples, penetration of the beam through the sample was more of a problem. Usually, the mesostructure was only observed at the thin edges of particles or on very small particles.

d) Photography and digital image analysis

Underneath the viewing chamber was a camera that held a number of photographic plates. Once a suitable region of the sample had been found a plate was exposed and the image recorded. Typically about 5-10 representative pictures would be taken over a period of twenty minutes. Once the negatives have been removed from the vacuum system they were developed and in some cases printed.

Digitisation of the negatives was carried out using an AGFA Duoscan T1200 scanner attached to a PC. The Duoscan had a special transparency tray that was designed for scanning negatives and could produce high-resolution scans of the original negative in 12-bit greyscale. Adjustment of brightness and contrast of the scanned images was carried out using Corel Photopaint 8

Analysis of results

To properly assess the nature of any mesoporosity within a sample it was necessary to have a number of representative micrographs. In terms of order, the mesoporous materials could be placed into four categories:

1) The material did not have any mesoporosity
2) The material was mesoporous but disordered
3) The material was mesoporous and sufficiently ordered that the phase could be identified.
4) The material was mesoporous and the phase easily identifiable.

The repeat distance between the pores was measured by averaging across a number of pores. To ensure the scale bar on the micrograph was accurate the TEM was calibrated using asbestos fibres with known lattice spacings. In the case of the H_I materials there tended to be more particles, as might be expected, lying side on. Consequently, at first sight the material appeared lamellar but on further investigation the end on view of the hexagonally arranged pores was revealed [6]. Confirmation of a homogeneous hexagonal phase, throughout the material, could be obtained by measuring the ratio of the repeat distance of the pores, side on, to the repeat distance end on (figure 7).

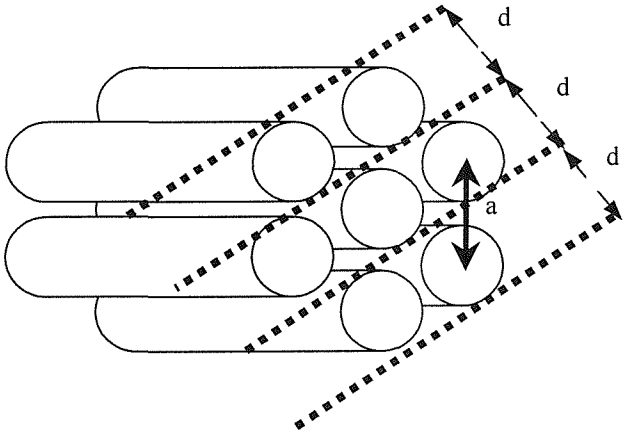

Figure 7 Representation of the H_I mesoporous structure. Note when the structure is viewed side on in the TEM the repeat distance d is observed and this is smaller than the true pore to pore distance.

1C Powder X-ray Diffraction

Introduction

Powder x-ray diffraction is routinely used to study polycrystalline solid state materials such as zeolites. It differs from single crystal x-ray diffraction in that the beam strikes a finely powdered sample, which ideally contains crystals, arranged randomly. The lattice planes of the crystals diffract the x-ray beam. Those planes oriented at the correct angle (Bragg angle 2θ) result in constructive interference of the x-ray beam providing a signal. The powder x-ray patterns, that are recorded, can be interpreted by using the Bragg equation $n\lambda=2d\sin\theta$. Where λ is the wavelength of the incident beam and d is the lattice spacing. Commonly a Cu $K_{\alpha 1}$ radiation source is used (λ=1.5406 Å) and detection of the scattered x-rays carried out by a scintillation counter. With such a setup the scattered x-rays result in Bragg reflections at wide angles (10-90°) for crystalline materials.

Characterisation of mesoporous materials by Powder x-ray diffraction has become the analytical method of choice for analysing the quality, phase and repeat distance of the structure [7]. The low angles reflections (2θ <10°) can be used to help identify the type of mesopore structure (H_1, V_1 and L_α). In addition, the sharper the Bragg peaks in the diffraction pattern, the better the long range order in the material

Equipment description

Data were collected using a conventional diffractometer, Siemens D5000, employing copper radiation passed through a single crystal monochromator giving only $K_{\alpha 1}$ radiation (figure 8). The monochromatic x-ray beam was then collimated through an aperture diaphragm and directed onto the sample, mounted flush in a recessed aluminium or plastic holder. Diffracted x-rays were detected by a standard scintillation counter. The sample goniometer was rotated at a constant angular velocity and the detector moved at twice this velocity to ensure the diffraction angle, 2θ. Diffraction data were recorded on a windows based PC.

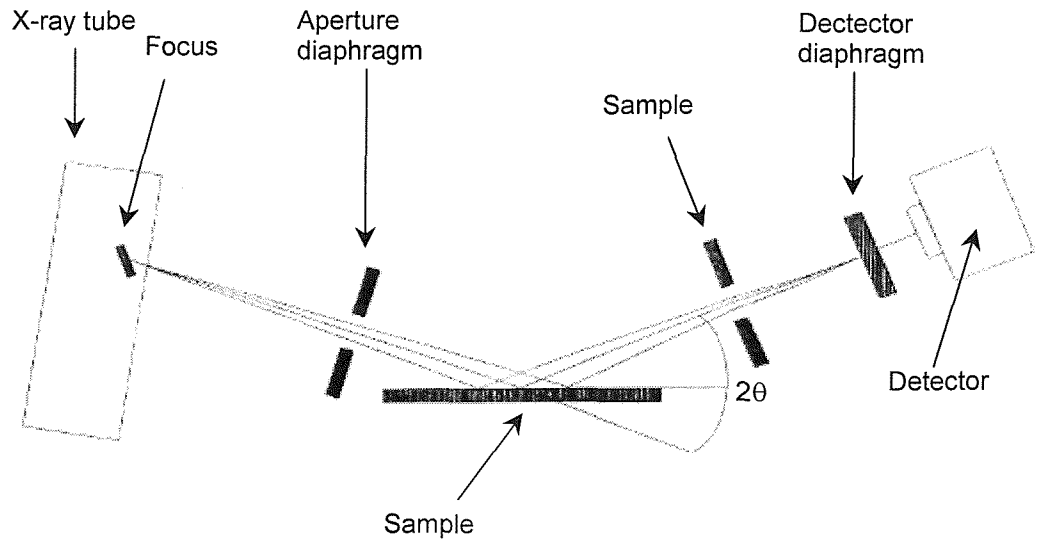

Figure 8 A Schematic representation of the Siemens D5000 diffractometer. Reproduced from reference 7

Experimental parameters

The fine metal powder was placed in a aluminium holder containing a circular indentation (ca. 30 mm in diameter and 1 mm deep), and the surface of the powder was made flush with the sides of the holder. Small angle XRD scans were recorded over a 2θ range of for 20 minutes. For the high angle XRD experiments a plastic holder was used rather than aluminium holder. This was to avoid confusion of the diffraction peaks for aluminium with those for platinum as both metals have the same crystal structure. High angle XRD patterns were recorded over a 2θ range of for 30 minutes.

Analysis of results

Small angle x-ray scattering

Small angle x-ray diffraction patterns were used to help identify the mesopore structure of the metal samples. Each order of diffraction has an associated reciprocal spacing, $S_{hkl}=1/d_{hkl}$. The ratio of the reciprocal spacings of the diffraction lines allow powder patterns to be indexed to a particular mesophase symmetry (lamellar, hexagonal or cubic for lyotropic systems).

The diffraction peaks for a lamellar phase are regularly spaced as $S_h = h$ {1, 2, 3, 4....}. For the 2D hexagonal liquid crystal phase $S_{hk} = (2/\sqrt{3})\ (h^2+k^2-hk)^{1/2}$ {1,$\sqrt{3}$, 2, $\sqrt{7}$, 3, $\sqrt{12}$, $\sqrt{13}$....} and for the cubic structures $S_{hkl} = (h^2+k^2+l^2)^{1/2}$ {1,$\sqrt{2}$, $\sqrt{3}$, 2, $\sqrt{5}$, $\sqrt{6}$, $\sqrt{8}$, 3....}. The various lyotropic cubic phases are further distinguished by characteristic systematic absences, which differ for each space group. The observed reflections and their corresponding positions are summarised in table 2.

In ordered to differentiate between the various liquid crystal phases a large number of orders of diffraction are necessary. This is particularly true of cubic materials where there are a variety of possible structures. Furthermore, powder XRD cannot differentiate between lattice planes that diffract at the same angle 2θ. Finally, the long range order in a mesoporous material is not nearly as high as the regular arrangement of atoms in a crystal. This means that the diffraction peaks, due to the mesoporous structure, are much less sharp than those observed for a crystal. The combination of all these factors means that a great deal of care must be taken when recording and interpreting XRD data of mesostructures. It is possible to improve the quality of the diffraction data by using equipment specifically designed for low angle measurements. Other improvements include the use of a highly monochromatic source of x-rays (e.g. synchrotron radiation) and the collection of data over a long period of time.

All the mesoporous materials described in this thesis produced at least one diffraction peak (*100*). The peak width of the *100* peak dramatically increased for more disordered structures and the peak width at half height was used as a measure of disorder in the system. The lower the long-range order in the mesoporous structure the broader the diffraction peak.

Phase	Space group	Selection rules n = 1, 2, 3, 4	*hkl* list	spacing ratios
Lamellar (L_α)		*h*00: $h = n$	*100* *200* *300*	1 2 3
Hexagonal (H_I)	P6mm	*hk*0: $h + k = n$	*100* *110* *200* *210*	1 √3 2 √7
Cubic (V_I)	Pm3n (223)	*h, k, l* permutable *hhl*: $l = 2n$ *h*00: $h = 2n$	*110* *200* *210* *211* *220* *310* *222*	√2 2 √5 √6 √8 √10 √12
	Pn3m (224)	*h, k, l* permutable *hhl*: $l = 2n$ *h*00: $h = 2n$	*110* *111* *200* *211* *220* *221* *310* *311* *222*	√2 √3 2 √6 √8 3 √10 √11 √12
	Fm3m (225)	*h, k, l* permutable *hkl*: $h+k, h+l, l+k = 2n$ 0*kl*: $k+l = 2n$ *hhl*: $h+l = 2n$ *h*00: $h = 2n$	*110* *200* *220* *311* *222*	√2 2 √8 √11 √12
	Fd3m (227)	*h, k, l* permutable *hkl*: $h+k = 2n$ *and* $h+l, l+k = 2n$ 0*kl*: $k+l = 4n$ and $k, l = 2n$ *hhl*: $h+l = 2n$ *h*00: $h = 4n$	*111* *220* *311* *222*	√3 √8 √11 √12
	Im3m (229)	*h, k, l* permutable *hkl*: $h+k+l = 2n$ 0*kl*: $k+l = 2n$ *hhl*: $l = 2n$ *h*00: $h = 2n$	*110* *200* *211* *220* *310* *222*	√2 2 √6 √8 √10 √12
	Ia3d (230)	*h, k, l* permutable *hkl*: $h+k+l = 2n$ 0*kl*: $k, l = 2n$ *hhl*: $2h+l = 4n$ *h*00: $h = 4n$	*110* *200* *211* *220* *310* *222*	√2 2 √6 √8 √10 √12

Table 2 Selection rules for the space groups associated with lyotropic liquid crystal phases and the relative spacings of the first Bragg reflections. Note that only a selection of the cubic space groups are given for the more commonly found phases in lyotropic systems. Information obtained from the international tables of cystallography.

Wide angle x-ray scattering

Wide/high angle XRD was used to determine the crystal structure of the platinum materials. By comparing the recorded XRD patterns with the literature crystal data for platinum [8] it was possible to identify the materials as fcc platinum (space group Fm3m). Also, by measuring the broadening of the diffraction peaks it was possible to determine crystallite size using the Scherrer equation [9].

1D EXAFS

EXAFS (Extended X-ray absorption fine structure) refers to the sinusoidal variation of the X-ray absorption coefficient as a function of X-ray photon energy, which occurs after each absorption edge of an element and extends for up to 1500 eV further. This phenomenon forms the basis of the analytical technique of EXAFS spectroscopy, which can be used to obtain structural information about molecules without the need for obtaining single crystals.

Basic EXAFS Theory

Atoms in molecules can absorb x-rays. Generally, the proportion of x-rays absorbed (the absorption coefficient) will decrease as their energy increases, but at certain values of energy, specific to each element, a sudden increase in the amount of energy absorbed is observed. These energies are known as absorption edges. The energies correspond to the ejection of an electron from the atom in question (*i.e.* ionisation). The ejected electron can be considered as a wave, travelling outwards from the central absorbing atom. The increase in absorption at the edge occurs when the energy of the incident x-rays is equal to the threshold energy necessary to eject an electron.

Simple models of X-ray absorption predict a gradual monotonic decrease in the absorption coefficient with increasing energy away from the absorption edge. Such behaviour is observed in spectra of isolated atoms, *e.g.* noble gases (Xe, Kr *etc.*), but for atoms either in a molecule or a condensed phase, the presence of other atoms around the absorber causes oscillations in the absorption coefficient near the edge (figure 9). These oscillations in the post edge region arise from the back-scattering of the emitted electron wave off neighbouring atoms and so the structure of the post edge region of the x-ray absorption spectrum is related to the radial distribution of atoms in the sample. Hence, by analysing this structure (the frequency and amplitude of the oscillations), information about the local environment of the absorbing element can be derived.

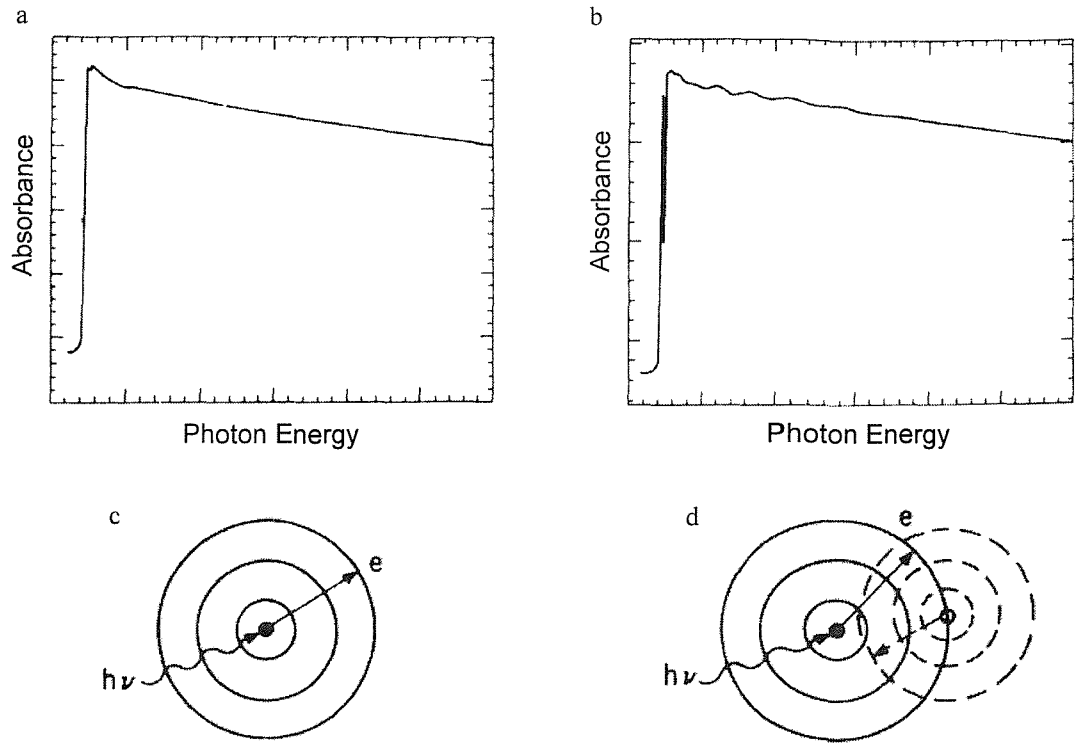

Figure 9 Rationalisation of the absence and presence, respectively, of the EXAFS in a monatomic gas such as Kr (a and c) and a diatomic gas such as Br_2 (b and d). Reproduced from reference 10.

The EXAFS effect (the oscillations in the post edge absorption coefficient) is small compared to the absorption resulting from the electron ejection (ionisation), hence a strong x-ray source is required to produce features sufficiently intense to be analysed. Synchrotron x-ray sources meet this requirement; they produce x-ray radiation by accelerating pulses of electrons to a speed approaching that of light, in a circular path of *ca.* 20 metres radius. Because of the complexity of the equipment necessary to achieve this, there are only a small number of such sources in existence. The only facility in the UK is the Daresbury synchrotron source, located near Liverpool, but there are about 30 more elsewhere in the world.

Energy dispersive EXAFS on station 9.3 at the Daresbury synchrotron radiation source

The Energy dispersive EXAFS experiments described in chapter 5 on platinum-ruthenium samples were carried out at the Wiggler Station 9.2 of the synchrotron radiation source at Daresbury (UK). Standard EXAFS were used and the station was operated with a Si (220) double crystal monochromator. Each scan was carried out for 35 minutes on Station 9.2.

Analysis of EXAFS data

A detailed description of EXAFS analysis is beyond the scope of this thesis and is explained elsewhere [10, 12]. At a simple level, analysis involves extracting the EXAFS data from the background and building a model to match this data. The Fourier transform of the extracted EXAFS data provides information on the average separation of atoms within the sample and if a sensible model can be fitted to the data then coordination numbers and types of nearest neighbours can also be obtained.

Background subtraction was obtained using EXBROOK and curve fitting of the EXAFS data was carried out using EXCURVE 98 [13] programme. The quality of the fitted models was determined in EXCURVE 98. The quality of the fit may be judged by the R-factor (The percentage difference between theoretical EXAFS data and the experimental data).

The author would like to thank Dr Andrea Russell and Stephanie Maniguet for running the EDE experiments and for their help with analysing the EDE data.

1E Nitrogen adsorption/desorption experiments

Introduction

Studying the adsorption/desorption of an inert gas, such as nitrogen, on the surface of a material can provide information about the surface area and pore size distribution of the material, and reveal any pore blocking within the structure. Routine surface area analysis is carried out by using commercialy available instruments that record the adsorption and desorption of nitrogen before calculating a surface area form the collected data. Nitrogen adsorption/desorption studies are widely used in the study of mesoporous inorganic oxide and have become a standard technique for characterising surfactant templated materials [14].

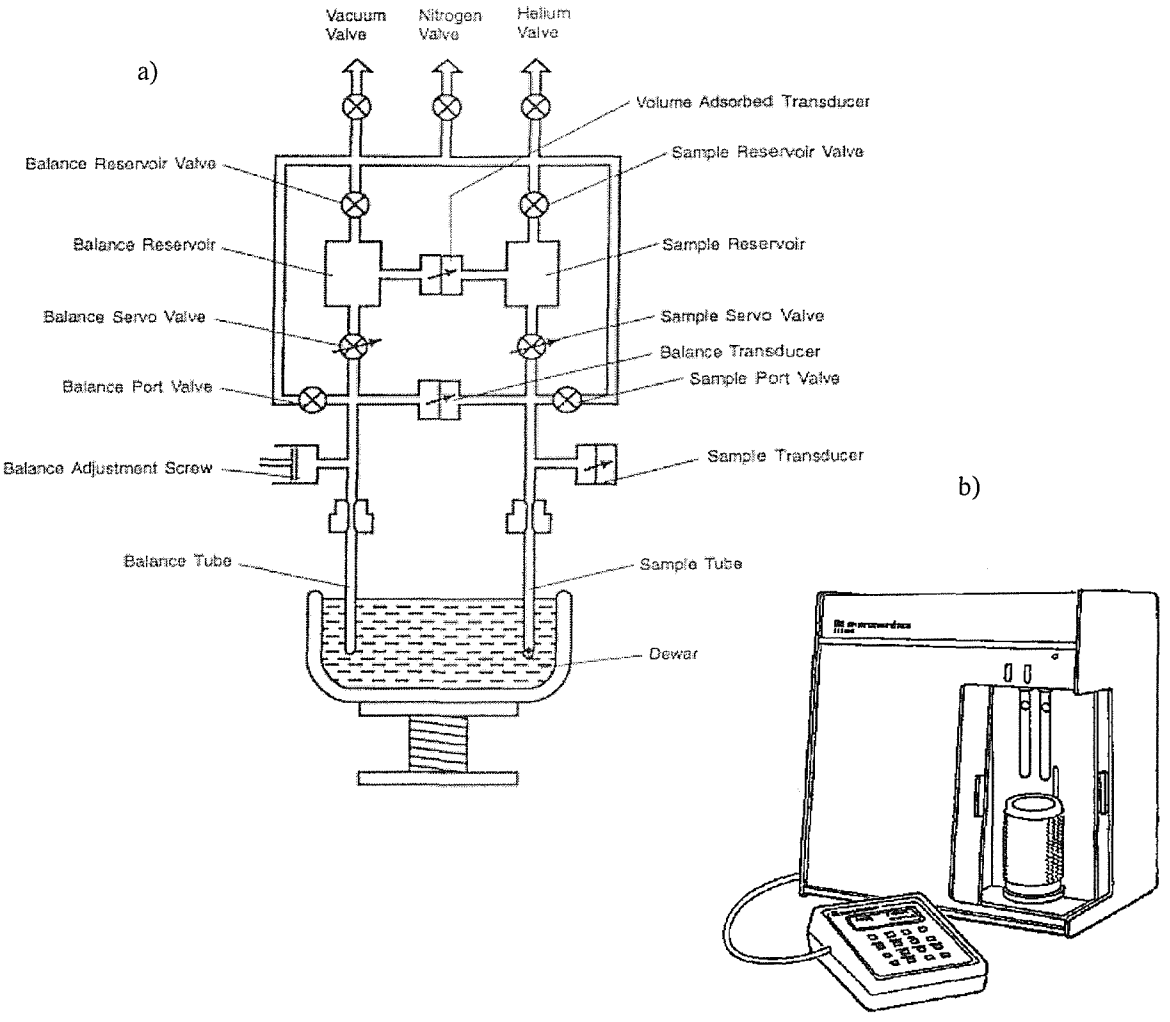

Figure 10 The Gemini III 2375 analyser a) general overview and b) plumbing diagram. Reproduced from the Micrometrics operating manual.

Nitrogen adsorption/desorption experiments were carried out using a Micrometrics Gemini III 2375 Surface Area Analyser. The Gemini instrument automates the process of obtaining nitrogen adsorption/desorption curves and BET surface areas. It works by analysing the difference in the volume of nitrogen adsorbed by a tube containing the sample of interest and an empty reference tube. Both tubes are immersed in a single liquid nitrogen bath, which maintains isothermal conditions. Figure 10 shows a schematic of the components of the Gemini's plumbing system.

Experimental parameters

For all the nitrogen adsorption/desorption experiments described in this thesis the following procedure was adopted:

1. Sample tubes were cleaned by washing in an ultrasound bath of deionised water for 1 minute and rinsed with acetone before drying in an oven, at 60°C, overnight.
2. Samples were weighed out accurately (~200mg for mesoporous metals) into the anlysis tube.
3. The instrument was set-up with the following parameters before starting the analysis:
    - 40 adsorption points between P/P_0 0.01-0.95 and 32 desorption points.
    - Sample weight (see above)
    - Saturation pressure P_0 – 760 mmHg
    - Evacuation rate 500 mmHg/min
    - Evacuation time 30 min
4. The automated BET analysis was carried out on adsorption points at relative pressures (P/P_0) between 0.05 and 0.30.
5. Pore volumes were obtained at a relative pressure (P/P_0) of ~0.95

Analysis of results

Nitrogen/adsorption desorption curves

The quantity of nitrogen adsorbed by a solid is proportional to the mass of the solid, the pressure and the nature of the solid at a given temperature. For a given temperature and solid, the relationship between the amount of nitrogen adsorbed and the relative pressure can be expressed as:

$$V = f(P/P_o)_{T,gas,solid} \qquad (1)$$

V is the amount or volume of nitrogen adsorbed by the solid, P is the vapour pressure and P_o is the saturated vapour pressure. Adsorption isotherms, such as those in figure 7 were constructed by plotting the amount adsorbed V against the relative pressure P/P_o.

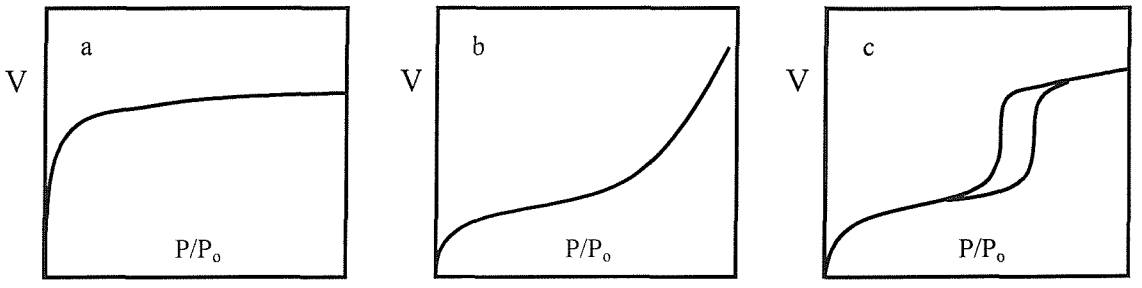

Figure 11 Typical adsorption isotherms for a) microporous solids such as zeolites, b) non-porous solids or macroporous solids and c) mesoporous solids.

At very low relative pressures, a monolayer of nitrogen molecules forms on the surface of the solid. As the limit of monolayer coverage is reached, nitrogen begins to condense and fill in the very smallest pores of the sample. Further increases in the relative pressure result in the filling of steadily larger pores. If a sample has a narrow range of pore sizes then when a certain relative pressure is reached the adsorption isotherm will contain a step as nitrogen is rapidly adsorbed into the pores. Microporous solids such as zeolites have very large internal surface areas compared to their external surface areas and filling of the pores occurs at low relative pressures (figure 11a). At the other extreme a macroporous solid does not exhibit pore filling until high relative pressures (figure 11b). A mesoporous material exhibits pore filling at intermediate relative pressures and is often characterised by a hysteresis loop associated with capillary condensation (figure 11c). Generally, the presence of hysteresis indicates that the pore size and shape is not well defined.

For the mesoporous materials described in this thesis nitrogen adsorption/desorption curves of V against P/P_o were plotted using the output from the Gemini analyser. Many of the silicas produced isotherms that were characteristic of mesoporosity with varying degrees of hysteresis (figure 11c).

Pore size analysis of nitrogen desorption isotherms

It was mentioned in the previous section that the size of pores that are present and the range of pore sizes determine the form of a nitrogen adsorption/desorption isotherm. Pore size analysis takes this principle one step further by applying a mathematical analysis of the form of the isotherm to deduce a pore size distribution. A number of methods have been described in the literature for calculating pore size distributions [15-17]. In essence they are all based on the Kelvin equation (2) which relates the relative pressure to the pore radius.

$$\ln P/P_o = \frac{-2\gamma V}{r_K RT} \qquad (2)$$

Where γ is the surface tension of adsorbate
V is the molar volume of adsorbate
R is the gas constant
T is the absolute temperature
r_K is the capillary condensate radius
P/P_o is the relative pressure

Unfortunately, the Kelvin equation only accounts for capillary condensation and does not consider the adsorption of nitrogen multi-layers on the surface of the pores. For an accurate pore size determination the multi-layers must also be taken into account. When the capillary liquid is lost, multi-layers are left on the walls, and thus the radius of the meniscus of the capillary condensate is less than the actual radius of the pores (r_p) by the amount t (3).

$$r_K = r_p - t \qquad (3)$$

The method of determining t, the geometry of the pores and the pore size add to the complexity of pore size analysis and have been discussed in a number of publications. For the pore size analyses described in this thesis a calculation described by Dollimore and Heal was employed [16]. This is based on the method of Barrett *et al.*,

(commonly known as the BJH method [17] but uses an improved route to determining multi-layer desorption. Equation 4 was used as the basis for determining the pore size distribution and from this a spreadsheet was drawn up as described by Dollimore and Heal.

$$\Delta V_p = R_n(\Delta V_n - \Delta t_n \Sigma S_p + 2\pi t_n \Delta t_n \Sigma L_p) \qquad (4)$$

Where ΔV_p is the change in pore volume between two relative pressures

ΔV_n is the change in volume of the adsorbate between two relative pressures

$R_n = (r_p)^2/(\underline{r}_K+\Delta t_n)^2$ ($\underline{r}_K$ – average capillary radius between two relative pressures)

Δt_n = change in multi-layer thickness between two relative pressures

$S_p = 2\Delta V_p/r_p$ (surface area of the pores)

$L_p = S_p/(2\pi r_p)$ (length of the cylindrical pores)

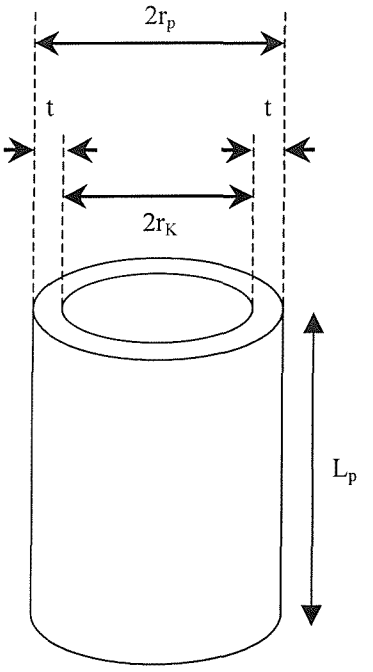

Figure 12 The cylindrical model used in pore size analysis and the multilayers of adsorbed nitrogen, of thickness t, that have to be considered.

The spreadsheet for the pore size analysis of mesoporous silica is shown in table 1. The pore size distributions given in this thesis were obtained by plotting the values of $\Delta V_p/\Delta r$ (dV_p/dr) against r_p for the desorption branch of the isotherm.

A	B	C	D	E	F	G	H
P/P_o	V_{des} mlg^{-1}	V_{liq} ml	ΔV/ ml	t Å	Δt Å	r_K Å	r_p Å
A1	B1	B1*0.00155	C2-C1	$-4.3[(5/\ln A1)^{1/3}]$	E2-E1	-9.53/lnA1	E1+G1
A2	B2	B2*0.00155	C3-C2	$-4.3[(5/\ln A2)^{1/3}]$	E3-E2	-9.53/lnA2	E2+G2
A3	B3	B3*0.00155	C4-C3	$-4.3[(5/\ln A3)^{1/3}]$	E4-E3	-9.53/lnA3	E3+G3
.	.	.	.	.	.	.	.
A_m	B_m	B_m*0.00155	C_m-C_{m+1}	$-4.3[(5/\ln A_m)^{1/3}]$	E_m-E_{m+1}	-9.53/lnA_m	E_m+G_m

I	J	K	L	M	N	O
<t> Å	U $Å^2$	<r_p> Å	<r_K> Å	R_n	$\Delta t*\Sigma S_p$ ml	$U*\Sigma(2\pi L_p)$ ml
(E2+E1)/2	F1*I1	(H2+H1)/2	(G2+G1)/2	$(H1)^2/(L1+F1)^2$	F1*S1	J1*U1
(E3+E2)/2	F2*I2	(H3+H2)/2	(G3+G2)/2	$(H2)^2/(L2+F2)^2$	F2*S2	J2*U2
(E4+E3)/2	F3*I3	(H4+H3)/2	(G4+G3)/2	$(H3)^2/(L3+F3)^2$	F3*S3	J3*U3
.	.	.	.	.	.	.
$(E_{m+1}+E_m)/2$	F_m*I_m	$(H_{m+1}+H_m)/2$	$(G_{m+1}+G_m)/2$	$(H_m)^2/(L_m+F_m)^2$	F_m*S_m	J_m*U_m

P	Q	R	S	T	U
ΔV_p ml	$\Sigma\Delta V_p$ ml	S_p m^2	ΣS_p m^2	$2\pi L_p = S_p/r_p$ $m\times10^{10}$	$\Sigma 2\pi L_p$ $m\times10^{10}$
(D1-N1+O1)*M1	SUM(P1:P_m)	2P1/H1	SUM(R1:R_m)	R1/H1	SUM(T1:T_m)
(D2-N2+O2)*M1	SUM(P2: P_m)	2P2/H2	SUM(R2:R_m)	R2/H2	SUM(T1:T_m)
(D3-N3+O3)*M1	SUM(P3:P_m)	2P2/H2	SUM(R3:R_m)	R3/H3	SUM(T1:T_m)
.	.	.	.	.	.
$(D_m-N_m+O_m)*M_m$	P_m	$2P_m/H_m$	R_m	R_m/H_m	T_m

W	X
$\Delta V_p/\Delta r$ ml $Å^{-1}$	Pore diameter Å
$[P1/(H2-H1)]/C_m$	2*K1
$[P2/(H3-H2)]/C_m$	2*K2
$[P3/(H4-H3)]/C_m$	2*K3
-	.
$[P_m/(H_{m+1}-H_m)]/C_m$	2*K_m

Table 3 The Spreadsheet used for calculating pore size distributions from nitrogen adsorption data. As some of the equations are recursive the data has to be inputted line by line. Columns A and B are obtained from the nitrogen desorption experiment and column W is plotted against X to obtain the pore size distribution

BET surface area analysis

The BET (Brunauer-Emmett-Teller) technique has been widely used as the standard procedure for determination of the surface area of solids, nonporous as well as porous [18]. In this technique gas adsorption is carried out by exposing a solid (the adsorbent) to an adsorptive gas (the adsorbate) at different relative pressures and at the liquid temperature of the adsorbate. Nitrogen is the preferred adsorbate gas for BET measurements as it is relatively insensitive to the chemical nature of the surface.

The surface area of a solid can be obtained by applying the BET model to the adsorption data. The hypothesis of a monolayer coverage on the solid is the basis of the BET method. The rate of adsorption onto the adsorptive sites of the solid is assumed to be equal to the desorption rate of the gas from the occupied sites. Thus, a linear equation can be derived, usually called the 'BET equation':

$$\frac{P}{V(P_o - P)} = \frac{1}{V_m C} + \frac{(C-1)P}{V_m C P_o} \qquad (2)$$

V_m is the volume of gas required for monolayer coverage per gram of solid and C is the BET constant. A BET curve is obtained by plotting the left-hand side of equation (2) as a function

$$\text{slope} = \frac{(C-1)}{V_m C} \qquad (3)$$

of P/P_o. V_m and C values can be calculated from the slope and the y intercept of the linear part of the BET curve.

$$\text{intercept} = \frac{1}{V_m C} \qquad (4)$$

From the volume of gas adsorbed for monolayer coverage per gram of solid V_m and the average area occupied by one nitrogen molecule in the monolayer a_m, the specific surface area of the solid can be calculated SA:

$$SA = \frac{V_m L a_m}{22.4 \times 10^{-3}} \qquad (5)$$

The Gemini instrument automated the process of obtaining the surface areas given in this thesis by measuring the amount of nitrogen adsorbed at a number of relative pressures and carrying out a BET calculation on the results. BET analysis was carried out on the measurements between relative pressures of 0.05 and 0.30.

1F Electrochemical techniques

This section describes the basic elctrochemical techniques used in this thesis. More complete and theoretical treatments may be found elsewhere [19,20].

Cyclic voltammetry

Voltammetry is a useful technique available to study the redox reaction mechanism in electrochemical cells. The simplest approach involves two electrodes -a working electrode and a reference electrode. The working electrode is where the reaction of interest occurs and the reference electrode provides a stable and fixed potential. A third electrode, the counter electrode, is used so that when a voltage is applied between the working electrode and the reference electrode, the difference is well defined. Hence all potentials quoted are with respect to the respect electrode. The current is monitored between the working electrode and the counter electrode.

Potential sweep techniques, in particular cyclic voltammetry, are a common procedure for preliminary mechanistic investigations. An " electrochemical spectrum" indicating the potentials at which surface processes occur can be rapidly obtained, while from the sweep rate dependance the involvement of coupled homogeneous reactions is readily identified, and other components such as adsorption can be recognised.

The potential-time wave -form used for sweep measurements is shown in figure 14.

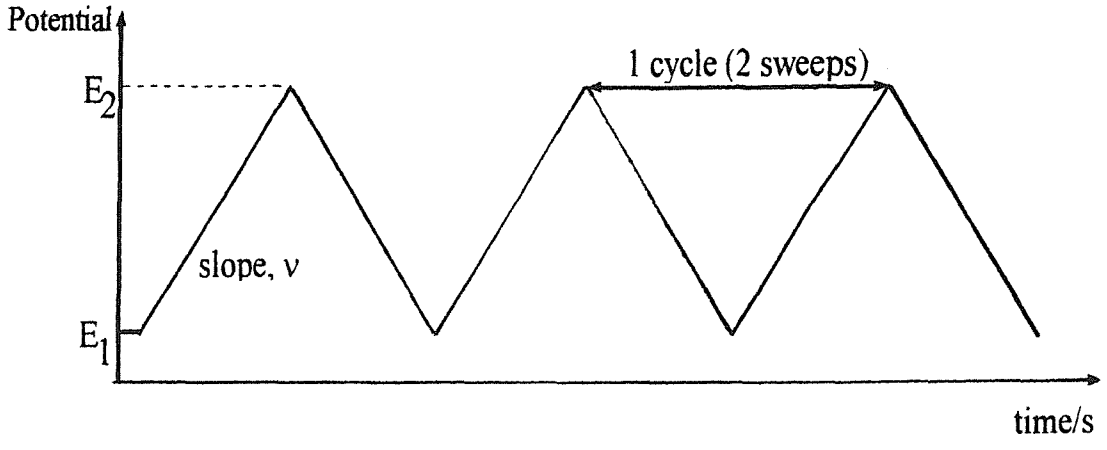

Figure 13 Potential-time profiles for cyclic voltammetry.

The cyclic voltammetry technique (CV) technique involved sweeping the electrode potential continuously between two pre-set limits (E_1 and E_2) at a known sweep rate (υ). As the electrode was cycled, its current response was measured as a function of potential; scan rates can vary from a few mV/s to few hundred V/s depending on the experiments.

Potential step techniques

Many important electrode reactions involve the formation of a solid phase, either as a result of the ions in solution, as in the case of metal deposition, or by oxidation of the electrode and subsequent reactions with anions to form an anodic film. The term electrocrystallisation is used to describe electrode processes of this kind [20].
In potential step experiments, the potential of the working electrode is changed instantaneously, and either the current time response or the charge time response is recorded. These techniques are known respectively as chronoamperometry and chronocoulometry. In these methods, the system is perturbed from its equilibrium and electrochemical information is obtained from the relaxation in the time domain to the new steady state condition.
Assuming an electrode reaction as described by equation 1 and that initially only O is present in the solution.

$$O + n\,e^- \rightleftharpoons R \qquad (1)$$

A potential time profile as shown in figure 15 is then applied to the working electrode .E1 is chosen such that no reduction of O, or indeed any other reaction occurs. Then at time t = 0 the potential is instantaneously changed to a new value E2, where the reduction of O occurs at a diffusion controlled rate [20].

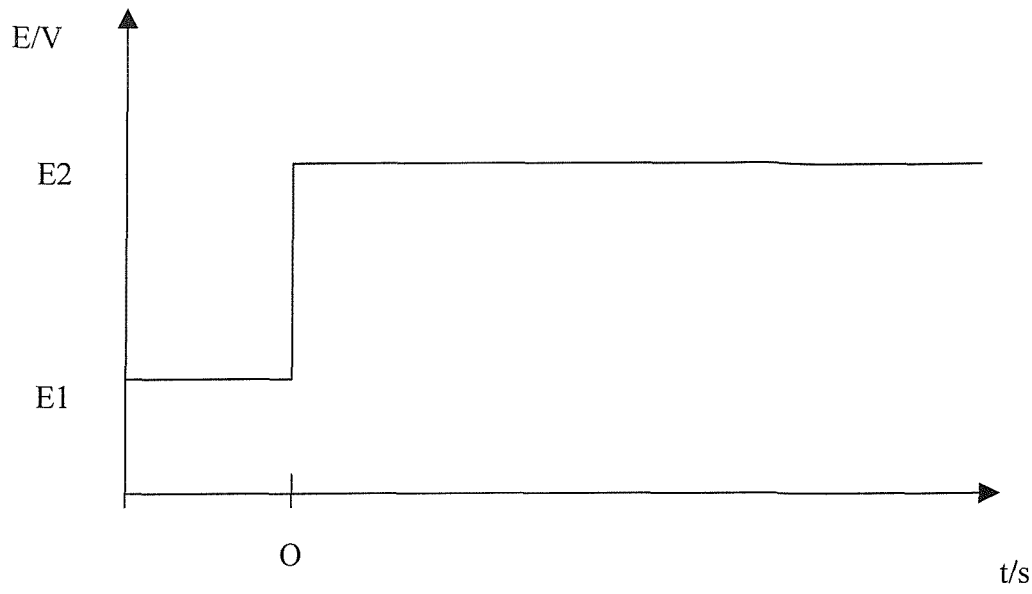

Figure 14. The potential time profile for a single potential step chronoamperometric experiment.

The mesoporous Pb and Pt/Ru films electrodeposited in this thesis were obtained by potential step depositions.

References

1 P J Collings and M Hird, *Introduction to Liquid Crystals* (Taylor and Francis, London, 1997).

2 N R B Coleman, PhD Thesis, Department of Chemistry, University of Southampton (1999).

3 R G Laughlin, *The Aqueous Phase Behaviour of Surfactants*, Appendix 4, 521-546 (Academic Press, London, 1994).

4 P J Goodhew and F J Humphreys, *Electron Microscopy and Analysis*, 2nd edition (Taylor and Humphreys, London, 1988).

5 I M Watt, *The principles and practice of electron microscopy*, 2nd edition (Cambridge University Press, Cambridge, 1997).

6 A Chenite, Y LePage, A Sayari, *Chem. Mater*, **7**, 1015 (1995).

7 R L Needs, *Ph.D thesis*, department of Chemistry, University of Southampton (1997).

8 F H Allen, G Bergerhoff, R Sievers, crystallographic databases, (1987), The Inorganic crystal structure database (ICSD), Daresbury Laboratory, Warrington, UK.

9 A R West, X-ray diffraction in *Solid State Chemistry and its Applications*, (Wiley, Trowbridge, 1995).

10 B T Keo, *EXAFS: Basic Principles and Data Analysis,* (Springer, Berlin, 1986).

11 N Binsted, *PAXAS - Programme for the Analysis X-ray Absorption Spectroscopy*, University of Southampton, 1988.

12 S G Fiddy, M A Newton, A J Dent, G Salvani, J M Corker, S Turin, T Campbell, J Evans, *J. Chem. Soc. Chem. Commun.,* 851 (1999)

13 N Binsted, Excurv98: CCLRC Daresbury Laboratory Computer Programme (CCLRC Daresbury Laboratory 1998)

14 M. Jaroniec, M Kruk, A Sayari, *Stud. Surf. Sci. Catal.* **117**, 325 (1998).

15 K S W Sing, D H Everettt, R A W Haul, L Moscou, R A Pierotti, J Rouquerol, T Siemieniewska, *Pure. and Appl. Chem.,* **57**, No. 4, 603 (1985).

16 D Dollimore, G R Heal, *J. Appl. Chem.*, 109 (1964).

17 E P Barrett, L G Joyner, P P Halender, *J. Am. Chem. Soc.*, **57**, 373 (1951).

18 H Lao and C Detellier, Microporosimetry, in *Comprehensive Supramolecular chemistry,* Volume 8: Physical Methods in Supramolecular Chemistry, chapter 6 (Elsvier Science, Oxford, 1996).

19 A J Bard L R Faulkner, Electrochemical Methods: fundamentals and applications, John Wiley, New York (1980).

20 The Southampton Electrochemistry Group, Instrumental methods in Electrochemistry (Ed T J Kemp) Ellis Horwood (1985).

Appendix 2 Phase diagram compositions

2A Phase diagram reported in chapter 2:

The compositions for the phase diagram of Brij 76 + water shown in chapter 2:

Brij 76 /g	water/ g	wt% Brij 76
0.25	0.75	25
0.30	0.70	30
0.35	0.65	35
0.40	0.60	40
0.45	0.55	45
0.50	0.50	50
0.55	0.45	55
0.60	0.40	60
0.65	0.35	65
0.70	0.30	70
0.75	0.25	75
0.80	0.20	80
0.85	0.15	85
0.90	0.10	90

HCPA + water + surfactant compositions

The compositions for the phase diagram of Brij 76 + HCPA + water shown in chapter 2 (fixed concentration of HCPA):

$H_2PtCl_6.6H_20$ /g	water /g	Brij 76 /g	total water /g †	wt% Brij 76*
0.25	0.20	0.05	0.25	17
0.25	0.20	0.10	0.25	29
0.25	0.20	0.15	0.25	38
0.25	0.20	0.20	0.25	44
0.25	0.20	0.25	0.25	50
0.25	0.20	0.30	0.25	56
0.19	0.15	0.30	0.19	61
0.13	0.10	0.30	0.13	70
0.09	0.08	0.30	0.10	75
0.06	0.05	0.30	0.06	83
0.03	0.02	0.30	0.03	91

† total water content includes the water of hydration of HCPA

* wt% Brij 76 is given as a percentage of the total water + Brij 76 content and does not include the HCPA.

The compositions for the phase diagram of Brij 76+ HCPA + water shown in chapter 2 (40 wt% surfactant with respect to the total water content):

$H_2PtCl_6.6H_20$ /g	water /g	Brij 76 /g	total water /g †	mole fraction H_2PtCl_6*
0.050	0.040	0.040	0.050	0.035
0.040	0.042	0.040	0.050	0.026
0.030	0.044	0.040	0.050	0.022
0.020	0.046	0.040	0.050	0.014
0.010	0.048	0.040	0.050	0.007

† total water content includes the water of hydration of HCPA

* mole fraction of H_2PtCl_6 calculated from the total number of moles of water and HCPA

The compositions for the phase diagram of Brij 76+ HCPA + water shown in chapter 2 (75 wt% surfactant with respect to the total water content):

$H_2PtCl_6.6H_20$ /g	water /g	Brij 76 /g	total water /g †	mole fraction H_2PtCl_6*
0.066	0.037	0.146	0.051	0.043
0.059	0.038	0.153	0.050	0.039
0.053	0.039	0.156	0.050	0.036
0.046	0.040	0.150	0.050	0.031
0.039	0.042	0.155	0.050	0.026
0.032	0.043	0.159	0.050	0.022
0.010	0.023	0.075	0.025	0.014
0.005	0.024	0.075	0.025	0.007

† total water content includes the water of hydration of HCPA

* mole fraction of H_2PtCl_6 calculated from the total number of moles of water and HCPA

2 B Phase diagrams reported in chapter 3:

The compositions for the phase diagram of Brij 76 + ammonium tetrachloropalladate + water shown in chapter 3 (fixed concentration of ATCP 1.1M):

$(NH_4)_2$ $PdCl_6$ /g	water /g	Brij 76 /g	wt% Brij 76*
0.1	0.325	0.081	20
0.1	0.325	0.139	30
0.1	0.325	0.217	40
0.1	0.325	0.325	50
0.1	0.325	0.487	60
0.1	0.325	0.758	70
0.1	0.325	1.300	80
0.1	0.325	2.925	90

* wt% Brij 76 is given as a percentage of the total water + Brij 76 content and does not include the ATCP.

The compositions for the phase diagram of Brij 76 + palladium acetate + water shown in chapter 3 (fixed concentration of palladium acetate 0.26 M):

$Pd(Oac)_2$/g	water /g	Brij 76 /g	wt% Brij 76*
0.40	7.00	1.75	20
0.40	7.00	3.00	30
0.40	7.00	4.65	40
0.40	7.00	7.00	50
0.40	7.00	10.50	60
0.40	7.00	16.30	70
0.20	3.50	14.00	80
0.05	0.88	7.88	90

* wt% Brij 76 is given as a percentage of the total water + Brij 76 content and does not include the palladium acetate.

2 C Phase diagrams reported in chapter 4:

The compositions for the phase diagram of Brij 76 + lead acetate + water shown in chapter 4 (fixed concentration of lead acetate 3.5 M):

$Pd(Oac)_2$/g	water /g	Brij 76 /g	wt% Brij 76*
0.50	0.40	0.10	20
0.50	0.40	0.17	30
0.50	0.40	0.27	40
0.50	0.40	0.40	50
0.50	0.40	0.50	55
0.50	0.40	0.60	60
0.50	0.40	0.93	70
0.50	0.40	1.60	80
0.50	0.40	3.60	90

* wt% Brij 76 is given as a percentage of the total water + Brij 76 content and does not include the lead acetate.

Appendix 3 Surface area model for H_I materials

By considering an H_I material as an infinitely sized particle with a perfect hexagonal pore structure it was possible to obtain a theoretical surface area for the material.

Fundamental unit

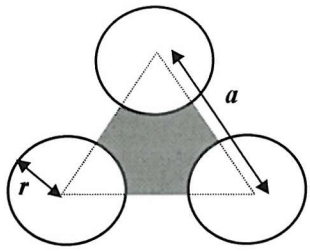

Tube length = l
Density of the material = ρ

Surface area of unit = $\pi r l$

Area occupied by material (shaded area) = $\frac{1}{2}a^2 \sin 60 - \frac{1}{2}\pi r^2$

Mass of material = $\rho l\left(\frac{\sqrt{3}}{4}a^2 - \frac{1}{2}\pi r^2\right)$

Specific surface area of fundamental unit,

$$S_f = \frac{\text{Surface area}}{\text{mass}} = \frac{4\pi r}{\rho(\sqrt{3}a^2 - 2\pi r^2)} \quad (1)$$

The specific surface area of an H_I material is dependent on the density (ρ) of the material, the distance between the holes (a) and the size of the holes (r). Table 1 shows some theoretical surface areas based on pore geometries obtained experimentally for mesoporous platinum and platinum-ruthenium. Comparison of the specific surface areas for platinum and platinum ruthenium showed that the theoretical value was approximately 5 times smaller than the experimental value. The model reflected the relative changes in surface area with pore geometry and density but the absolute values were always lower for the model compared to the experimental data.

The model did not take into account some of the properties that were observed for the real materials:

- The surface area was not just due to the hexagonal pore structure but also had a contribution from the micropores within the samples.
- The pore walls were not totally smooth, particularly in the platinum materials, roughness of the pore walls added to the experimental surface area.
- Defects in the pore structure also effected the surface area.
- The external surface area of the particles was not accounted for and this made a large contribution to the H_I platinum materials as the particles were only micron sized.

	H_I platinum templated from $C_{16}EO_{8*}$	H_I platinum-ruthenium templated from Brij 76
Density (ρ) / gcm^{-3}	21.5	16.9
Pore radius (r) / nm	1.5	0.85
Repeat distance (a) / nm	6.8	5.1
Surface area (based on model) / m^2g^{-1}	13	16
Surface area (experimental) / m^2g^{-1}	60	83

Table 1 Some theoretical and experimental values for the surface areas of H_I platinum templated from $C_{16}EO_8$ (*as described by NRB Coleman, PhD thesis University of Southampton (1999)), H_I Platinum/Ruthenium (nominal 1:1 atomic ratio) templated from Brij 76.

Assuming that the amount of disorder and microporosity was the same for both H_I platinum and platinum-ruthenium then it was possible to estimate a value for the surface area of H_I platinum/ruthenium by using the experimental value for H_I platinum templated from $C_{16}EO_8$.

From (1)

$$H_I \text{ Platinum/ruthenium surface area} = \frac{S_f \text{ of } H_I \text{ Pt/Ru}}{S_f \text{ of } H_I \text{ Pt}} \times \text{experimental value for platinum}$$

$$= (13/16) \times 60 = \underline{49\ m^2g^{-1}}$$

This recalculated value for the surface area of H_I platinum/ruthenium was still lower than the experimental value.

In summary, the model proposed here was a useful guide to predicting the relative magnitudes of surface areas for various pore geometries and different materials of known densities. However, factors such as microporosity, pore wall roughness and external surface were not accounted for by the model and as a result the absolute surface areas calculated from the model were lower than the experimental values.

Catalyst	**Pt loading mg Pt/cm^2**	Catalyst composition %Pt/C	Nafion % wt.eq.cat	CO charge C	Geometric Area cm^2	E peak (CO) V/MMS	H(ads) Charge C	Geometric area cm^2	E onset (MEOH) V/MMS	Pretreatment
H_I Pt	2.31	14.2	10.6	$5.77*10^{-2}$	137.5	0.004	1.18*10-1	561.9		0.5 M H_2SO_4
H_I Pt	2.8	18.9	9.6	$8.15*10^{-2}$	194.1	0.003	6.37*10-2	303.2	-0.1	1 M H_2SO_4
H_I Pt	1.98	17.9	6.2	$9.53*10^{-2}$	226.9	0.031	7.66*10-2	364.8		2.5 M H_2SO_4
H_I Pt	2.28	20	10.5	$6.63*10^{-3}$	15.7	-0.009	1.91*10-2	91.1		
Pt/C	1.2	40	19.2	$1.16*10^{-1}$	275.5	0.145	1.06*10-1	504.8		

Table1. Methanol and CO electrooxidation/ H_2SO_4 soaking

Catalyst	**Pt loading mgPt/cm^2**	Catalyst composition %Pt/C	Nafion % wt.eq.cat.	Pretreatment
H_I Pt 38 m^2g^{-1}	2.64	19.7	6.3	1 M $HClO_4$
H_I Pt 38 m^2g^{-1}	2.8	18.9	9.6	1 M H_2SO_4
H_I Pt 38 m^2g^{-1}	2.9	13.8	8.4	Perfluorosulfonic acid 10 % solution
H_I Pt/Ru 83 m^2g^{-1}	2.7	15.8	9.7	Perfluorosulfonic acid 10 % solution

Table 2. CO electrooxidation/ H_2SO_4 and proton conductor soaking